

Tuning the Photophysical and Biological Properties of a Series of Ruthenium-Based Chromophores and Chromophore Coupled Cisplatin Analogs with Substituted Terpyridine Ligands

Avijita Jain

Dissertation submitted to the faculty of the Virginia Polytechnic Institute and State University
in partial fulfillment of the requirements for the degree of

Doctor of Philosophy

In

Chemistry

Prof. Karen J. Brewer, Chair

Prof. Brenda S. J. Winkel

Prof. Gordon T. Yee

Prof. Brian M. Tissue

Prof. John H. Robertson

(December 4, 2008)

Blacksburg, VA

Keywords: cisplatin; chromophore; supramolecular; bridging ligand; DNA photocleavage;
photodynamic therapy; antibacterial

Tuning the Photophysical and Biological Properties of a Series of Ruthenium-Based Chromophores and Chromophore Coupled Cisplatin Analogs with Substituted Terpyridine Ligands

Avijita Jain

Abstract

The goal of this research was to develop an understanding of the impact of component modifications on spectroscopic properties, DNA interaction, and bioactivity of tridentate, terpyridine containing ruthenium-based chromophores and chromophore coupled cisplatin analogs. The coupling of a light absorbing unit to a bioactive site offers the potential for developing supramolecules with multifunctional interactions with DNA and other biomolecules. A series of supramolecular complexes of the form $[(TL)RuCl(dpp)](PF_6)$ and $[(TL)RuCl(BL)PtCl_2](PF_6)$ with the BL (bridging ligand) = 2,3-bis(2-pyridyl)pyrazine (dpp) and varying TL (terminal ligand) (tpy = 2,2':6',2''-terpyridine, MePhtpy = 4'-(4-methylphenyl)-2,2':6',2''-terpyridine, or ^tBu₃tpy = 4,4',4''-tri-tert-butyl-2,2':6',2''-terpyridine) have been designed and developed. The investigations described in this thesis were focused on the design and development of multifunctional supramolecules with improved DNA interaction and antibacterial properties. The impact of component modifications on photophysical and biological properties of the designed the supramolecular complexes was investigated.

A series of supramolecular complexes of the type, $[(TL)RuCl(dpp)](PF_6)$ and $[(TL)RuCl(dpp)PtCl_2](PF_6)$, have been synthesized using a building block approach. Electronic absorption spectroscopy of these types of complexes displayed intense ligand-based $\pi \rightarrow \pi^*$ transitions in the UV region and metal to ligand charge transfer (MLCT) transitions in the visible region. The $Ru(d\pi) \rightarrow dpp(\pi^*)$ MLCT transitions in $Ru^{II}Pt^{II}$ bimetallic complexes were found to be red-shifted relative to the monometallic synthons. The MLCT transitions for $[(TL)RuCl(dpp)](PF_6)$ and $[(TL)RuCl(dpp)PtCl_2](PF_6)$ were centered at ca. 520 and 545 nm, in CH₃CN respectively. The $Ru^{II}Pt^{II}$ bimetallic complexes with (TL = tpy, MePhtpy, and ^tBu₃tpy) displayed reversible $Ru^{II/III}$ couples at 1.10, 1.10, and 1.01 V vs. Ag/AgCl, respectively. The

tpy^{0/-} reductions occurred for TL = tpy, MePhtpy, and ^tBu₃tpy at -1.43, -1.44, and -1.59 V vs. Ag/AgCl, respectively. The Ru^{II}Pt^{II} complexes displayed a more positive potential for the dpp^{0/-} couples (-0.50 -0.55, -0.59 V for tpy, MePhtpy, and ^tBu₃tpy, respectively) relative to their monometallic synthons (-1.15, -1.16, and -1.22 V), consistent with the coordination of electron deficient Pt(II) metal center.

This research also presents first extensive DNA photocleavage studies of these relatively unexplored tridentate, tpy-containing chromophores. The DNA binding and photocleavage properties of a series of homoleptic and heteroleptic chromophores and Ru^{II}Pt^{II} bimetallic complexes were investigated using agarose gel electrophoresis and equilibrium dialysis experiments. The heteroleptic complexes, [(MePhtpy)RuCl(dpp)](PF₆), [(tpy)RuCl(dpp)](PF₆), and [^tBu₃tpy)RuCl(dpp)](PF₆), were found to photocleave DNA more efficiently than homoleptic complexes, [Ru(MePhtpy)₂]²⁺, [Ru(tpy)₂]²⁺, and [Ru(^tBu₃tpy)₂]²⁺, in the presence of oxygen. Coupling of [(TL)RuCl(BL)] subunit to a *cis*-Pt^{II}Cl₂ site provides for the application of typically shorter lived Ru^{II}(tpy) based chromophores in DNA photocleavage. The [(TL)RuCl(dpp)PtCl₂]⁺ complexes displayed covalent binding to DNA and photocleavage upon irradiation with visible light modulated by TL identity.

The impact of component modifications on antibacterial properties of the designed molecules was explored for the first time. Both the Ru^{II}Pt^{II} bimetallic complexes and their monometallic analogs displayed antibacterial properties. [(MePhtpy)RuCl(dpp)](PF₆) was found to be the most efficient antibacterial agent in the series of monometallic and Ru^{II}Pt^{II} bimetallic complexes, displaying cell growth inhibition at 0.05 mM concentration compared to 0.1 mM concentration of [(MePhtpy)RuCl(dpp)PtCl₂](PF₆) needed to display the similar effect. A direct correlation was found to exist between the DNA interaction and bactericidal properties of the designed supramolecules. The effects of light on antibacterial properties of [(MePhtpy)RuCl(dpp)](PF₆) were also briefly examined. This complex represents the first inorganic chromophore-based photodynamic antibacterial agent.

Thesis Statement

The goal of this research is to develop an understanding of the impact of component modifications on spectroscopic properties, DNA interaction, and bioactivity of tridentate, terpyridine containing ruthenium-based chromophores and chromophore coupled cisplatin analogs.

Dedication

This dissertation is dedicated to the victims of the Bhopal gas tragedy

Acknowledgments

I am deeply indebted to my advisors, Prof. Karen J. Brewer and Prof. Brenda S. J. Winkel, for giving me the opportunity to work with them. It is an unforgettable experience in my life to work under their inspiring guidance. They have read and responded to the drafts of papers and dissertation more quickly than I could have hoped. I thank them for their support, guidance, insightful critique, and constant encouragement.

Next, I would like to thank my advisory committee members, Prof. Gordon T. Yee, Prof. Brian M. Tissue, and Prof. John H. Robertson, for their valuable time, guidance, and helpful suggestions.

I thank Jared Brown for his help with construction of LED setup. I thank Dr. Hugo F. Azurmendi for his help with ^{195}Pt NMR experiments. I thank Dr. Carla Slebodnick for her help with crystal structure determination.

I am particularly thankful to Samantha Hopkins, Jessica Knoll, Dr. Shamindri Arachchige, and Joan Zapiter, for reading some portions of this dissertation and providing me with very useful input. I thank Sanghamitra Sen and Ran Miao for useful discussions.

At last, I want to thank my family for their love and encouragement. I thank my parents, Santosh and Kalpana Jain, who have always believed in me and helped me reach my goals. I thank my husband, Prakash Kumar, for his love, patience, and encouragement.

Table of Contents

Thesis Statement.....	iv
Dedication.....	v
Acknowledgments.....	vi
Table of Contents.....	vii
List of Figures.....	xii
List of Tables.....	xx
List of Abbreviations.....	xxii
Preface.....	xxiii
I. Introduction.....	1
1.1. Cancer.....	1
1.2. Structure of DNA.....	2
1.2.1. DNA binding modes.....	3
1.2.1.1. Electrostatic interaction/ Ionic binding.....	3
1.2.1.2. Groove Binding.....	4
1.2.1.3. Intercalation.....	4
1.2.1.4. Covalent binding.....	4
1.3. Cisplatin.....	5
1.3.1. Cisplatin: Mode of action.....	6
1.3.2. Limitations of cisplatin.....	7
1.3.3. Cisplatin analog research.....	7
1.4. Photodynamic therapy.....	9
1.4.1. PDT: History and mechanism of action.....	9
1.4.2. Inorganic complexes as PDT agents.....	11
1.4.3. Ruthenium based light absorbers.....	12
1.4.3.1 Spectroscopic and electrochemical properties.....	12
1.4.3.2. DNA interaction properties.....	16
1.4.4. Photodynamic antibacterial therapy.....	18
1.4.4.1. Ruthenium metal complexes: Antibacterial properties.....	19
1.4.5. Limitations of PDT.....	19

1.5. Combination therapy.....	20
1.5.1. Coupling of a cisplatin analog to a PDT agent.....	20
1.5.1.1. Coupling of ruthenium chromophores to a cis-PtCl ₂ moiety by a non communicative bridging ligand.....	22
1.5.1.1.1. Spectroscopic and electrochemical properties.....	22
1.5.1.1.2. DNA and protein interaction properties.....	23
1.5.1.2. Coupling of ruthenium chromophores to a cis-PtCl ₂ moiety by a communicative bridging ligand.....	24
1.5.1.2.1. Spectroscopic and electrochemical properties.....	24
1.5.1.2.2. DNA interaction studies.....	31
1.5.1.2.2.1. Gel electrophoresis as an assay of the DNA-MC interaction...	32
1.6. Project description.....	34
1.6.1. Design of Ru ^{II} Pt ^{II} bimetallic complexes.....	35
1.6.2. Understanding DNA-metal complex interaction.....	36
1.6.3. To explore antibacterial properties.....	36
1.6.4. To explore photodynamic antibacterial properties.....	37
2. Materials and Methods.....	38
2.1. Materials.....	38
2.1.1. Materials, synthesis.....	38
2.1.2. Materials, DNA interaction studies.....	38
2.1.3. Materials, cell culture studies.....	38
2.2. Methods.....	39
2.2.1. Column chromatography.....	39
2.2.2. Mass spectroscopy.....	39
2.2.3. Crystal structure determination.....	39
2.2.4. NMR spectroscopy.....	40
2.2.5. Electrochemistry.....	40
2.2.6. Electronic absorption spectroscopy.....	40
2.2.7. Emission spectroscopy.....	41
2.2.8. Quantum yield measurements.....	42

2.2.9. Excited state lifetime measurements.....	42
2.2.10. Partition coefficient determination.....	43
2.2.11. Photolysis with 1000W xenon arc lamp.....	44
2.2.12. Agarose gel electrophoresis.....	46
2.2.12.1. DNA photocleavage studies.....	47
2.2.12.2. DNA binding studies.....	47
2.2.12.3. R_f value determination.....	47
2.2.13. Equilibrium dialysis.....	48
2.2.14. Electroporation.....	49
2.2.15. Cell culture studies.....	50
2.2.16. DNA extraction.....	50
2.2.17. Cell lysis in the wells of electrophoresis gel.....	51
2.2.18. Construction of LED for cell culture studies.....	52
2.2.19. Determination of spectral output of designed LED.....	53
2.2.19.1. Physical actinometry.....	54
2.2.20. Synthesis and purification of metal complexes.....	56
2.2.20.1. [(tpy)RuCl(dpp)](PF ₆).....	56
2.2.20.2. [(MePhpty)RuCl(dpp)](PF ₆).....	56
2.2.20.3. [(^t Bu ₃ tpy)RuCl(dpp)](PF ₆).....	57
2.2.20.4. [Ru(tpy) ₂](PF ₆) ₂	58
2.2.20.5. [Ru(MePhpty) ₂](PF ₆) ₂	58
2.2.20.6. [Ru(^t Bu ₃ tpy) ₂](PF ₆) ₂	58
2.2.20.7. [Pt(DMSO) ₂ Cl ₂].....	59
2.2.20.8. [(tpy)RuCl(dpp)PtCl ₂](PF ₆).....	59
2.2.20.9. [(MePhpty)RuCl(dpp)PtCl ₂](PF ₆).....	60
2.2.20.10. [(^t Bu ₃ tpy)RuCl(dpp)PtCl ₂](PF ₆).....	60
3. Results and discussion.....	61
3.1. Synthesis.....	61
3.2. Crystal structure determination.....	63

3.3. Mass spectrometry.....	66
3.4. NMR spectroscopy.....	69
3.5. Electrochemical properties.....	70
3.5.1. Electrochemical properties: heteroleptic and homoleptic complexes.....	72
3.5.2. Electrochemical properties: Ru ^{II} Pt ^{II} heterobimetallic complexes.....	75
3.5.3. Comparison of electrochemical properties of Ru ^{II} Pt ^{II} bimetallic complexes with their monometallic precursors.....	78
3.6. Electronic absorption properties.....	79
3.6.1. Electronic absorption properties: Heteroleptic complexes.....	79
3.6.2. Comparison of electronic properties of homoleptic and heteroleptic complexes.....	80
3.6.3. Electronic absorption spectroscopy: Ru ^{II} Pt ^{II} bimetallic complexes.....	82
3.6.4. Comparison of electronic absorption properties of monometallic and bimetallic complexes.....	83
3.7. Comparison of electrochemical and spectroscopic Properties.....	84
3.8. Emission spectroscopy.....	88
3.8.1. Emission spectroscopy: Heteroleptic complexes.....	88
3.8.2. Emission spectroscopy: Homoleptic complexes.....	90
3.9. Excited state lifetime.....	92
3.9.1. Excited state lifetime: Heteroleptic complexes.....	92
3.9.2. Comparison of photophysical properties of homoleptic and heteroleptic complexes.....	93
3.10. Partition coefficient determination.....	95
3.11. DNA-MC binding constant determination.....	96
3.12. DNA interaction studies.....	98
3.12.1. DNA photocleavage properties: homoleptic complexes.....	98
3.12.2. DNA photocleavage properties: heteroleptic complexes.....	100
3.12.3. DNA photobinding properties: [(MePhtpy)RuCl(dpp)]Cl.....	102
3.12.4. DNA binding properties: bimetallic complexes.....	104
3.12.5. R_f value determination.....	105

3.12.5. DNA photocleavage properties: Ru ^{II} Pt ^{II} bimetallic complexes.....	107
3.13. Antibacterial properties.....	109
3.13.1. Antibacterial properties: Cisplatin.....	111
3.13.2. Antibacterial properties: [(tpy)RuCl(dpp)PtCl ₂](PF ₆) and its monometallic precursor.....	112
3.13.3. Antibacterial properties: [(MePhtpy)RuCl(dpp)PtCl ₂](PF ₆) and its monometallic precursor.....	114
3.13.4. Antibacterial properties: [(^t Bu ₃ tpy)RuCl(dpp)PtCl ₂](PF ₆) and its monometallic precursor.....	117
3.13.5. Comparisons of antibacterial properties of Ru ^{II} Pt ^{II} complexes.....	119
3.14. Photodynamic antibacterial chemotherapy.....	121
3.15. Mechanism of cell growth inhibition.....	125
3.15.1. DNA extraction using Quagen kit.....	125
3.15.2. DNA Extraction using lysis in the gel well protocol.....	127
4. Conclusions and future work.....	130
4.1. Conclusions.....	130
4.2. Future work.....	134
References.....	137
Appendix.....	A-1

List of Figures

Figure 1.1. Structure of DNA double helix showing major and minor grooves. Green spheres represent the phosphate backbone and purple spheres display the bases.....	2
Figure 1.2. Structure of DNA nucleotides (C = cytosine, G = guanine, A = adenine, T = thymine). N-7 position on guanine is indicated. Dashed lines indicate hydrogen bonds between base pairs.....	3
Figure 1.3. Schematic showing different DNA binding modes exhibited by $[\text{Ru}(\text{Ph}_2\text{phen})_3]^{2+}$ ($\text{Ph}_2\text{Phen} = 4,7\text{-diphenyl-}1,7\text{-phenanthroline}$). Top: Ionic binding of Λ isomer to sugar phosphate backbone. Middle: Intercalation of isomer into the double helix. Bottom: Steric inhibition of intercalation of Δ isomer into the helix.....	5
Figure 1.4. Structure of <i>cis</i> -diamminedichloroplatinum(II) (cisplatin).....	5
Figure 1.5. Cisplatin-DNA binding modes (a) interstrand cross-link, (b) 1,2-intrastrand cross-link, (c) 1,3-intrastrand cross-link, (d) protein-DNA cross-link.....	6
Figure 1.6. Crystal structure of cisplatin bound DNA fragment (T = thymine, G = guanine, C = cytosine, A = adenine, numeric figures represents the residue number).....	7
Figure 1.7. Structures of carboplatin (A), Oxaliplatin (B), and Nedaplatin (C).....	8
Figure 1.8. Structure of BBR3464.....	8
Figure 1.9. Jablonski diagram showing the origin of Type I and Type II Photodynamic therapy.	10
Figure 1.10. Chemical structures of hematoporphyrin derivatives and teraphenylchlorin...	11
Figure 1.11. Block diagram of molecular orbitals of a d^6 octahedral complex and some its possible transitions (IL = interligand, MLCT = metal to ligand charge transfer, and LF = ligand field). Shaded blocks denote filled orbitals and unshaded blocks denote unfilled orbitals.....	13
Figure 1.12. Representation of $[\text{Ru}(\text{bpy})_3]^{2+}$ ($\text{bpy} = 2,2'\text{-bipyridine}$).....	14
Figure 1.13. Jablonski diagram for $[\text{Ru}(\text{bpy})_3]^{2+}$. ($\text{bpy} = 2,2'\text{-bipyridine}$; GS = ground state; MLCT = metal-to-ligand charge-transfer; k_r = rate constant for radiative decay; k_{nr} = rate constant for non-radiative decay; and k_{isc} = rate constant for intersystem crossing).....	15
Figure 1.14. Representation of $[\text{Ru}(\text{tpy})_2]^{2+}$ ($\text{tpy} = 2,2':6',2''\text{-terpyridine}$).....	15
Figure 1.15. Jablonski diagram for $[\text{Ru}(\text{tpy})_2]^{2+}$ ($\text{tpy} = 2,2':6',2''\text{-terpyridine}$; GS = ground state; MLCT = metal-to-ligand charge-transfer; k_r = rate constant for radiative decay; k_{nr} = rate constant for non-radiative decay; and k_{isc} = rate constant for intersystem crossing).....	16
Figure 1.16. Representative terminal ligands (($\text{bpy} = 2,2'\text{-bipyridine}$, $\text{phen} = 1,10\text{-phenanthroline}$, $\text{Me}_2\text{phen} = 3,4\text{-methyphenanthroline}$, ${}^t\text{Bu}_2\text{tpy} = 4,4'\text{-di-tert-butyl-}2,2'\text{-}$	

bipyridine, tpy = 2,2':6',2''-terpyridine, MePhtpy = 4'-(4-methylphenyl)-2,2':6',2''-terpyridine, ^tBu₃tpy = 4,4',4''-tri-tert-butyl-2,2':6',2''-terpyridine)..... 21

Figure 1.17. Representative polyazine bridging ligands (dpp = 2,3-bis(2-pyridyl)pyrazine, dpq = 2,3-bis(2-pyridyl)quinoxaline, dpb = 2,3-bis(2-pyridyl)benzoquinoxaline, bpm = 2,2'-bipyrimidine, Me₂bpm = 5,5'-dimethyl-2,2'-bipyrimidine, tppz = 2,3,5,6-tetrakis(2-pyridyl)pyrazine)..... 22

Figure 1.18. Structures of Ru^{II}Pt^{II} bimetallic complexes, [(tpy)Ru(dtdeg)PtCl]³⁺, [tpyRu(PEt₂Ph)(dpp)PtCl₂]⁺, [(bpy)₂Ru(dpq)PtCl₂]²⁺, [(bpy)₂Ru(bpy(CONH(CH₂)₃NH₂)₂)PtCl₂]²⁺, and [(bpy)₂Ru(bpy(phenNHCO(COOHbpy)PtCl₂)]²⁺ (where bpy = 2, 2'-bipyridine, dpq = 2,3-bis(2-pyridyl)quinoxaline, dpp = 2,3-bis(2-pyridyl)pyrazine, dtdeg = bis[4'-(2,2':6',2''-terpyridyl)]diethyleneglycoether)..... 28

Figure 1.19. Structures of ligand 2,2':3',2'':6'',2'''-quaterpyridine (AB) and [(bpy)₂Ru(AB)PtCl₂](PF₆)₂ (bpy = 2,2'-bipyridine)..... 29

Figure 1.20. Structure of [{(bpy)₂Ru(dpp)}₂Ru(dpp)PtCl₂](PF₆)₆ (where bpy = 2,2'-bipyridine, and dpp = 2,3-bis(2-pyridyl)pyrazine)..... 31

Figure 1.21. Schematic showing agarose gel electrophoresis..... 33

Figure 1.22. A typical 0.8% agarose gel illustrating the electrophoretic migration of three different forms of plasmid DNA (A), covalent binding using linear pUC18 DNA (B), and DNA photocleavage using circular pUC18 DNA (C) The lanes from left to right are as follows: λ is a Lambda DNA/*Hind*III digest molecular weight marker (kbp = 1,000 base-pairs), I is circular plasmid DNA containing native supercoiled (Form I) and open-circular (Form II) plasmid DNA, and II is linear plasmid DNA (Form III), 1 is linear plasmid DNA control, 2 represent covalent binding of the metal complex to DNA, 1* represents circular plasmid DNA control, 2* represents DNA photocleavage (conversion of supercoiled to open circular form)..... 34

Figure 1.23. Mixed-metal Ru(II)-Pt(II) complexes of the form TL-LA-BL-BAS with hydrogens omitted for clarity (TL = terminal ligand, LA = light absorber, BL = bridging ligand, BAS = bioactive site, tpy = 2,2':6',2''-terpyridine, MePhtpy = 4'-(4-methylphenyl)-2,2':6',2''-terpyridine, ^tBu₃tpy = 4,4',4''-tri-tert-butyl-2,2':6',2''-terpyridine) and dpp = 2,3-bis(2-pyridyl)pyrazine..... 36

Figure 2.1. Hamamatsu 1527 photomultiplier response profile..... 41

Figure 2.2. Schematic for emission lifetime measurements using a PTI PL 2300 nitrogen laser with a PL 201 dye chamber showing the excitation source, the beam path, beam stop, trigger, sample, emission monochromater, photomultiplier tube, and oscilloscope..... 43

Figure 2.3. Representation of shake flask method to determine partition coefficient of [(MePhtpy)RuCl(dpp)]Cl (MePhtpy = 4'-(4-methylphenyl)-2,2':6',2''-terpyridine, and dpp = 2,3-bis(2-pyridyl)pyrazine)..... 44

Figure 2.4. Schematic of experimental design for photolysis using 1000 W xenon arc lamp including H ₂ O UV and IR filter, and cutoff pass filter and focusing lens to focus the collimated light onto the cell and a thermostated cell holder.....	45
Figure 2.5. Graph showing the photon flux of light from a xenon arc lamp filtered with a 450 nm cutoff filter.....	45
Figure 2.6. Graph showing the absorption profile of a 450 nm cutoff filter.....	46
Figure 2.7. Schematic displaying major component of electroporator.....	49
Figure 2.8. Schematic of LED setup used for light activated antibacterial cell culture studies.....	52
Figure 2.9. Spectral out measurement of designed LED. The fiber optic sensor from ocean optics diode array spectrophotometer oriented towards LED.....	53
Figure 2.10. LED spectral output with rectangles overlaid representing the right endpoint approximation determining area. The step size used was 0.2 nm.....	54
Figure 3.1. Building block method used to prepare mixed-metal supramolecular complex, [^t Bu ₃ tpy]RuCl(dpp)PtCl ₂](PF ₆) (^t Bu ₃ tpy = 4,4',4''-tri-tert-butyl-2,2':6',2''-terpyridine) and dpp = 2,3-bis(2-pyridyl)pyrazine).....	62
Figure 3.2. Perspective view of [(MePhtpy)RuCl(dpp)] ⁺ with atomic numbering (MePhtpy = 4'-(4-methylphenyl)-2,2':6',2''-terpyridine and dpp = 2,3-bis(2-pyridyl)pyrazine). The PF ₆ anion, toluene solvent molecules, and H-atoms have been omitted for clarity and thermal ellipsoids are shown at 50% probability level	64
Figure 3.3. Packing diagram of [(MePhtpy)RuCl(dpp)] ⁺ (MePhtpy = 4'-(4-methylphenyl)-2,2':6',2''-terpyridine and dpp = 2,3-bis(2-pyridyl)pyrazine).....	64
Figure 3.4. ¹⁹⁵ Pt NMR of [(TL)RuCl(dpp)PtCl ₂](PF ₆) in d ₆ -DMSO (TL = MePhtpy (A), tpy (B), and ^t Bu ₃ tpy (C) (tpy = 2,2':6',2''-terpyridine, MePhtpy = 4'-(4-methylphenyl)-2,2':6',2''-terpyridine, ^t Bu ₃ tpy = 4,4',4''-tri-tert-butyl-2,2':6',2''-terpyridine), and dpp = 2,3-bis(2-pyridyl)pyrazine). Spectra were taken at 600 MHz and chemical shifts are reported relative to K ₂ PtCl ₆	70
Figure 3.5. Cyclic voltammograms of [(tpy)RuCl(dpp)](PF ₆) (A), [(MePhtpy)RuCl(dpp)](PF ₆) (B), and [(^t Bu ₃ tpy)RuCl(dpp)](PF ₆) (C) in 0.1 M Bu ₄ NPF ₆ in CH ₃ CN and reported vs. Ag/AgCl (tpy = 2,2':6',2''-terpyridine, MePhtpy = 4'-(4-methylphenyl)-2,2':6',2''-terpyridine, ^t Bu ₃ tpy = 4,4',4''-tri-tert-butyl-2,2':6',2''-terpyridine), and dpp = 2,3-bis(2-pyridyl)pyrazine).....	73
Figure 3.6. Cyclic voltammograms of [(tpy) ₂ Ru](PF ₆) (A), [(MePhtpy) ₂ Ru](PF ₆) (B), and [(^t Bu ₃ tpy) ₂ Ru](PF ₆) (C) in 0.1 M Bu ₄ NPF ₆ in CH ₃ CN and reported vs. Ag/AgCl (tpy = 2,2':6',2''-terpyridine, MePhtpy = 4'-(4-methylphenyl)-2,2':6',2''-terpyridine, ^t Bu ₃ tpy = 4,4',4''-tri-tert-butyl-2,2':6',2''-terpyridine).....	75

Figure 3.7. Cyclic voltammogram of $[(^t\text{Bu}_3\text{tpy})\text{RuCl}(\text{dpp})\text{PtCl}_2](\text{PF}_6)$ (A), $[(\text{MePhtpy})\text{RuCl}(\text{dpp})\text{PtCl}_2](\text{PF}_6)$ (B), $[(\text{tpy})\text{RuCl}(\text{dpp})\text{PtCl}_2](\text{PF}_6)$ (C) in 0.1 M Bu_4NPF_6 in CH_3CN and reported vs. Ag/AgCl (tpy = 2,2':6',2''-terpyridine, MePhtpy = 4'-(4-methylphenyl)-2,2':6',2''-terpyridine, $^t\text{Bu}_3\text{tpy}$ = 4,4',4''-tri-tert-butyl-2,2':6',2''-terpyridine), dpp = 2,3-bis(2-pyridyl)pyrazine)..... 77

Figure 3.8. Electronic absorption spectroscopy of $[(^t\text{Bu}_3\text{tpy})\text{RuCl}(\text{dpp})](\text{PF}_6)$ (—), $[(\text{MePhtpy})\text{RuCl}(\text{dpp})](\text{PF}_6)$ (—) and $[(\text{tpy})\text{RuCl}(\text{dpp})](\text{PF}_6)$ (—) in CH_3CN at room temperature (tpy = 2,2':6',2''- terpyridine, MePhtpy = 4'-4-methylphenyl)-2,2':6',2''-terpyridine, $^t\text{Bu}_3\text{tpy}$ = 4,4',4''-tri-tert-butyl-2,2':6',2''- terpyridine), and dpp = 2,3-bis(2-pyridyl)pyrazine)..... 80

Figure 3.9. Electronic absorption spectroscopy of heteroleptic complex, $[(\text{tpy})\text{RuCl}(\text{dpp})](\text{PF}_6)$, (—) and homoleptic complex, $[(\text{tpy})_2\text{Ru}](\text{PF}_6)_2$ (.....) in CH_3CN at RT (tpy = 2,2':6',2''- terpyridine and dpp = 2,3-bis(2-pyridyl)pyrazine)..... 82

Figure 3.10. Electronic absorption spectroscopy of $[(^t\text{Bu}_3\text{tpy})\text{RuCl}(\text{dpp})\text{PtCl}_2](\text{PF}_6)$ (—), $[(\text{MePhtpy})\text{RuCl}(\text{dpp})\text{PtCl}_2](\text{PF}_6)$ (—) and $[(\text{tpy})\text{RuCl}(\text{dpp})\text{PtCl}_2](\text{PF}_6)$ (—) in CH_3CN at room temperature (tpy = 2,2':6',2''- terpyridine, MePhtpy = 4'-4-methylphenyl)-2,2':6',2''-terpyridine, $^t\text{Bu}_3\text{tpy}$ = 4,4',4''-tri-tert-butyl-2,2':6',2''- terpyridine), and dpp = 2,3-bis(2-pyridyl)pyrazine)..... 83

Figure 3.11. Electronic absorption spectroscopy of $[(\text{tpy})\text{RuCl}(\text{dpp})\text{PtCl}_2](\text{PF}_6)$ (—) and its monometallic precursor $[(\text{tpy})\text{RuCl}(\text{dpp})](\text{PF}_6)$ (—) in CH_3CN at room temperature (tpy = 2,2':6',2''- terpyridine and dpp = 2,3-bis(2-pyridyl)pyrazine)..... 84

Figure 3.12. The ΔE_{redox} versus ΔE_{MLCT} plot for a series of tpy-containing ruthenium chromophores (■) and $\text{Ru}^{\text{II}}\text{Pt}^{\text{II}}$ bimetallic complexes (■) in CH_3CN at RT..... 87

Figure 3.13. The ΔE_{redox} versus ΔE_{MLCT} plot for a series of tpy-containing ruthenium chromophores and $\text{Ru}^{\text{II}}\text{Pt}^{\text{II}}$ bimetallic complexes in CH_3CN at RT..... 87

Figure 3.14. The emission spectra of the complexes, $[(\text{tpy})\text{RuCl}(\text{dpp})](\text{PF}_6)$ (.....) $[(\text{MePhtpy})\text{RuCl}(\text{dpp})](\text{PF}_6)$ (—), in degassed CH_3CN at RT, where each emission data corrected for instrument response (λ^{ex} = 520 nm, PMT = Hamamatsu 1527 red sensitive photomultiplier tube) (tpy = 2,2':6',2''-terpyridine, MePhtpy = 4'-(4-methylphenyl)-2,2':6',2''-terpyridine, and dpp = 2,3-bis(2-pyridyl)pyrazine)..... 90

Figure 3.15. The 77 K emission spectrum for homoleptic complexes $[\text{Ru}(\text{MePhtpy})_2](\text{PF}_6)_2$ (—) $[\text{Ru}(^t\text{Bu}_3\text{tpy})_2](\text{PF}_6)_2$ (—) and $[\text{Ru}(\text{tpy})_2](\text{PF}_6)_2$ (—) (tpy = 2,2':6',2''- terpyridine, MePhtpy = 4'-(4-methylphenyl)-2,2':6',2''-terpyridine $^t\text{Bu}_3\text{tpy}$ = 4,4',4''-tri-tert-butyl-2,2':6',2''- terpyridine; and dpp = 2,3-bis(2-pyridyl)pyrazine) in 4:1 Ethanol:methanol mixture (λ^{ex} = 480 nm, PMT = Hamamatsu 1527 red sensitive photomultiplier tube)..... 92

Figure 3.16. Jablonski diagram for $[\text{Ru}(\text{TL})_2]^{2+}$ (tpy = 2,2':6',2''-terpyridine; GS = ground state; MLCT = metal-to-ligand charge-transfer; k_r = rate constant for radiative decay; k_{nr} = rate constant for non-radiative decay; k_{isc} = rate constant for intersystem crossing)..... 94

Figure 3.17. Jablonski diagram for $[(\text{tpy})\text{RuCl}(\text{dpp})]^+$ (tpy = 2,2':6',2''-terpyridine; GS =

ground state; MLCT = metal to ligand charge-transfer; k_r = rate constant for radiative decay; k_{nr} = rate constant for non-radiative decay; k_{isc} = rate constant for intersystem crossing)..... 94

Figure 3.18. Representative Scatchard plot of binding isotherm for [(MePhtpy)RuCl(dpp)]Cl with calf thymus DNA in buffer at room temperature, where r is the ratio of bound metal complex to nucleotide concentrations and c is the concentration of the free metal complex. The solid line is the best fit to the McGhee and von Hippel equation..... 97

Figure 3.19. Representative Scatchard plot of binding isotherm for [(tpy)RuCl(dpp)]Cl with calf thymus DNA in buffer at room temperature (A). Plot B represents the Scatchard plot of binding isotherm for [(tpy)RuCl(dpp)]Cl with calf thymus DNA in buffer at room temperature with lower values of r/C_f (r is the ratio of bound metal complex to nucleotide concentrations and c is the concentration of the free metal complex). The solid lines are the best fits to the McGhee and von Hippel equation..... 97

Figure 3.20. DNA photocleavage by Ru(II) terpyridine complexes assayed with 0.8% agarose gel electrophoresis using circular plasmid pUC18 DNA (MePhtpy = 4'-(4-methylphenyl)-2,2':6',2''-terpyridine, dpp = 2,3-bis(2-pyridyl)pyrazine, tpy = 2,2':6',2''-terpyridine, ¹Bu₃tpy = 4,4',4''-tri-tert-butyl-2,2':6',2''-terpyridine). λ is the molecular weight standard (24, 9.4, 6.6, 4.4, 2.2, 2.0 kb), C is the DNA control, MC is 5:1 base pair (BP):metal complex (MC) kept in the dark at room temperature, O₂ is 5:1 BP/MC photolyzed with 450 nm –1000 nm light for 2 hr under atmospheric conditions, Ar is 5:1 BP/MC photolyzed with 450 nm –1000 nm light for 2 hrs..... 100

Figure 3.21. DNA photocleavage by heteroleptic complexes, assayed with 0.8% agarose gel electrophoresis using circular plasmid pUC18 DNA (MePhtpy = 4'-(4-methylphenyl)-2,2':6',2''-terpyridine, dpp = 2,3-bis(2-pyridyl)pyrazine, tpy = 2,2':6',2''-terpyridine, ¹Bu₃tpy = 4,4',4''-tri-tert-butyl-2,2':6',2''-terpyridine). λ is the molecular weight standard (24, 9.4, 6.6, 4.4, 2.2, 2.0 kb), C is the DNA control, MC is 5:1 base pair (BP):metal complex (MC) kept in the dark at room temperature, O₂ is 5:1 BP/MC photolyzed with 450–1000 nm light for 2 hrs under atmospheric conditions, Ar is 5:1 BP/MC photolyzed with 450–1000 nm light for 2 hrs..... 101

Figure 3.22. DNA photobinding assay of [(MePhtpy)RuCl(dpp)]Cl complex using calf thymus DNA at 5:1 BP:MC ratio. Plot displays the absorbance at 520 nm of remaining [(MePhtpy)RuCl(dpp)]Cl in the solution followed by photolysis and selective precipitation of DNA versus time. A 5 W, 455 nm LED was used for photolysis. Sample points (●) were compared with that of dark control (■)..... 103

Figure 3.23. DNA binding study for [(TL)RuCl(dpp)PtCl₂](PF₆) by agarose gel electrophoresis using linearized pUC18 DNA (dpp = 2,3-bis(2-pyridyl)pyrazine, TL = terminal ligand (tpy = 2,2':6',2''-terpyridine, MePhtpy = 4'-(4-methylphenyl)-2,2':6',2''-terpyridine, ¹Bu₃tpy = 4,4',4''-tri-tert-butyl-2,2':6',2''-terpyridine). Lane 1 is the molecular weight standard (9.4, 6.6, 4.4, 2.3, and 2.0 kbp), lane 2 is the DNA control, lane 3 is the 5:1 base pairs (BP):metal complex (MC) ratio, lane 4 is the 10:1 BP:MC ratio, and lane 5 is the 20:1 BP:MC ratio..... 104

Figure 3.24. CAChe figure displaying DNA interaction of $[(^t\text{Bu}_3\text{tpy})\text{RuCl}(\text{dpp})\text{PtCl}_2](\text{PF}_6)$ (dpp = 2,3-bis(2-pyridyl)pyrazine, $^t\text{Bu}_3\text{tpy}$ = 4,4',4''-tri-tert-butyl-2,2':6',2''-terpyridine). A = ball and cylinder model showing proximity of DNA and metal complex, B = ball and cylinder model displaying the sterics associated with the interaction of $[(^t\text{Bu}_3\text{tpy})\text{RuCl}(\text{dpp})\text{PtCl}_2](\text{PF}_6)$ with DNA and C = space filling model displaying the sterics associated with the interaction of $[(^t\text{Bu}_3\text{tpy})\text{RuCl}(\text{dpp})\text{PtCl}_2](\text{PF}_6)$ with DNA. All the atoms of $[(^t\text{Bu}_3\text{tpy})\text{RuCl}(\text{dpp})\text{PtCl}_2](\text{PF}_6)$ are shown as green balls in order to achieve a better picture of DNA-MC interaction..... 107

Figure 3.25. DNA binding and photocleavage study for $[(\text{TL})\text{RuCl}(\text{dpp})\text{PtCl}_2](\text{PF}_6)$ by agarose gel electrophoresis using circular pUC18 DNA (dpp = 2,3-bis(2-pyridyl)pyrazine, TL = terminal ligand (tpy = 2,2':6',2''-terpyridine, MePhtpy = 4'-(4-methylphenyl)-2,2':6',2''-terpyridine, $^t\text{Bu}_3\text{tpy}$ = 4,4',4''-tri-tert-butyl-2,2':6',2''-terpyridine). λ is the molecular weight standard (9.4, 6.6, 4.4, 2.3, and 2.0 kbp), C is the DNA control, RT is the 20:1 BP:MC incubated at room temperature for 2 hrs, 37 is the 20:1 BP:MC incubated at 37°C for 2 hrs, O₂ is 20:1 base pair (BP): metal complex (MC) photolyzed with 450 nm–1000 nm light for 2 hrs under atmospheric conditions, and Ar is 20:1 BP:MC photolyzed with 450 nm –1000 nm light for 2 hrs in the absence of oxygen..... 108

Figure 3.26. Growth curves of *E. coli* JM109 (pBluescript) at different concentrations of DMSO (DMSO = dimethylsulphoxide). Cells were grown in the presence of 1% (■), 2% (▲), 3% (▼), 4% DMSO (◀), and Control (●) 111

Figure 3.27. Growth curves of *E. coli* JM109 (pBluescript) at different concentrations of cisplatin. Cells were grown in the presence of 0.2 mM cisplatin (▲), 0.4 mM cisplatin (■), and Control (●)..... 112

Figure 3.28. Growth curves of *E. coli* JM109 (pBluescript) at different concentrations of $[(\text{tpy})\text{RuCl}(\text{dpp})\text{PtCl}_2](\text{PF}_6)$ (where dpp = 2,3-bis(2-pyridyl)pyrazine and tpy = 2,2':6',2''-terpyridine). Cells were grown in the presence of 0.2 mM $[(\text{tpy})\text{RuCl}(\text{dpp})\text{PtCl}_2](\text{PF}_6)$ (◆), 0.4 mM $[(\text{tpy})\text{RuCl}(\text{dpp})\text{PtCl}_2](\text{PF}_6)$ (■), 0.6 mM $[(\text{tpy})\text{RuCl}(\text{dpp})\text{PtCl}_2](\text{PF}_6)$ (▲), and Control (●)..... 113

Figure 3.29. Growth curves of *E. coli* JM109 (pBluescript) at different concentrations of $[(\text{tpy})\text{RuCl}(\text{dpp})](\text{PF}_6)$ (where dpp = 2,3-bis(2-pyridyl)pyrazine and tpy = 2,2':6',2''-terpyridine). Cells grown in the presence of 0.4 mM $[(\text{tpy})\text{RuCl}(\text{dpp})](\text{PF}_6)$ (▲), 0.6 mM $[(\text{tpy})\text{RuCl}(\text{dpp})](\text{PF}_6)$ (■), and Control (●)..... 114

Figure 3.30. Growth curves of *E. coli* JM109 (pUC18 KS+) at different concentrations of $[(\text{MePhtpy})\text{RuCl}(\text{dpp})\text{PtCl}_2](\text{PF}_6)$ (where dpp = 2,3-bis(2-pyridyl)pyrazine and MePhtpy = 4'-(4-methylphenyl)-2,2':6',2''-terpyridine). Cells grown in the presence of 0.05 mM $[(\text{MePhtpy})\text{RuCl}(\text{dpp})\text{PtCl}_2](\text{PF}_6)$ (●), 0.1 mM $[(\text{MePhtpy})\text{RuCl}(\text{dpp})\text{PtCl}_2](\text{PF}_6)$ (▲), and Control (■)..... 115

Figure 3.31. Growth curves of *E. coli* JM109 (pBluescript) at different concentrations of $[(\text{MePhtpy})\text{RuCl}(\text{dpp})](\text{PF}_6)$ (where dpp = 2,3-bis(2-pyridyl)pyrazine and MePhtpy = 4'-(4-methylphenyl)-2,2':6',2''-terpyridine). Cells grown in the presence of 0.025 mM $[(\text{MePhtpy})\text{RuCl}(\text{dpp})](\text{PF}_6)$ (▲), 0.05 mM $[(\text{MePhtpy})\text{RuCl}(\text{dpp})](\text{PF}_6)$ (●), and Control

(■).....	117
Figure 3.32. Growth curves of <i>E. coli</i> JM109 (pUC18) at different concentrations of [(^t Bu ₃ tpy)RuCl(dpp)](PF ₆) (where dpp = 2,3-bis(2-pyridyl)pyrazine and ^t Bu ₃ tpy = 4,4',4''-tri-tert-butyl-2,2':6',2''-terpyridine). Cells grown in the presence of 0.05 mM [(^t Bu ₃ tpy)RuCl(dpp)](PF ₆) (●), 0.1 mM [(^t Bu ₃ tpy)RuCl(dpp)](PF ₆) (▲), and Control (■).....	118
Figure 3.33. Growth curves of <i>E. coli</i> JM109 (pUC18) at different concentrations of [(^t Bu ₃ tpy)RuCl(dpp)PtCl ₂](PF ₆) (where dpp = 2,3-bis(2-pyridyl)pyrazine and ^t Bu ₃ tpy = 4,4',4''-tri-tert-butyl-2,2':6',2''-terpyridine). Cells grown in the presence of 0.05 mM [(^t Bu ₃ tpy)RuCl(dpp)PtCl ₂](PF ₆) (●), 0.1 mM [(^t Bu ₃ tpy)RuCl(dpp)PtCl ₂](PF ₆) (▲), and Control (■).....	119
Figure 3.34. Growth curve of <i>E. coli</i> JM109 (pUC18 KS+) done with continuous exposure to LED light. Cells were grown under photolysis conditions (●), and Control (no photolysis) (■).....	122
Figure 3.35. Growth curve of <i>E. coli</i> JM109 (pUC18) at 0.05mM [(MePhtpy)RuCl(dpp)](PF ₆) in the presence and absence of 5W LED (where dpp = 2,3-bis(2-pyridyl)pyrazine, MePhtpy = 4'-(4-methylphenyl)-2,2':6',2''-terpyridine). Cells were grown in dark with 0.05 mM [(MePhtpy)RuCl(dpp)](PF ₆) complex (●), under continuous photolysis conditions with 0.05 mM [(MePhtpy)RuCl(dpp)](PF ₆) complex (▲), and Control without [(MePhtpy)RuCl(dpp)](PF ₆) complex (■).....	123
Figure 3.36. Growth curve of <i>E. coli</i> JM109 (pUC18) at 0.05mM [(MePhtpy)RuCl(dpp)](PF ₆) under intermittent photolysis conditions (where dpp = 2,3-bis(2-pyridyl)pyrazine and MePhtpy = 4'-(4-methylphenyl)-2,2':6',2''-terpyridine). Bacterial cell cultures done under intermittent photolysis conditions (●), and Control (■). The inset figure shows reversible photoactivity with intermittent photolysis conditions. Green balls represents the time at which LED was turned on.....	124
Figure 3.37. Agarose gel electrophoresis studies on DNA extracted from bacterial cells using quagen kit, when cells were grown in the presence of no metal complex (lane C), 0.025 (lane 0.025), 0.05 (lane 0.05), 0.1 (lane 0.1) and 0.2 mM (lane 0.2) [(MePhtpy)RuCl(dpp)PtCl ₂](PF ₆). Lane λ represent molecular weight marker	126
Figure 3.38. Agarose gel electrophoresis studies on DNA extracted from bacterial cells grown in the presence of different concentrations of [(MePhtpy)RuCl(dpp)](PF ₆) under no photolysis and photolysis conditions (where dpp = 2,3-bis(2-pyridyl)pyrazine and MePhtpy = 4'-(4-methylphenyl)-2,2':6',2''-terpyridine). After extraction DNA was diluted 100 times. DNA extracted from the culture, done in the presence of 0.05 mM [(MePhtpy)RuCl(dpp)](PF ₆) (lane 3), 0.05 [(MePhtpy)RuCl(dpp)](PF ₆) with continuous photolysis (lane 4). Lane 2 represents DNA extracted from control culture. Lane λ represents molecular weight marker.....	127
Figure 3.39. Agarose gel electrophoresis studies on DNA extracted from bacterial cells by lysis in gel well. Cells were grown in the presence of 0.05 mM [(MePhtpy)RuCl(dpp)](PF ₆) under no photolysis and photolysis conditions (where dpp = 2,3-bis(2-pyridyl)pyrazine, MePhtpy = 4'-(4-methylphenyl)-2,2':6',2''-terpyridine). Lane λ	

represents molecular weight marker, Lane C represents DNA extracted from cell culture done in the absence of metal complex, Lane MC represents DNA extracted from the culture done in the presence of 0.05 mM [(MePhtpy)RuCl(dpp)](PF₆) (lane 3), lane (hv MC) represents DNA extracted from the culture done in the presence of 0.05 mM [(MePhtpy)RuCl(dpp)](PF₆) with continuous photolysis (lane 4). Lines are drawn to show the relative positions of the bands in the gel..... 128

Figure 4.1. Proposed florescent sensors..... 136

List of Tables

Table 1.1. Electrochemical and spectroscopic properties of Ru(II)/Os(II)-Pt(II) mixed metal bimetallic metalcomplexes.....	26
Table 2.1. Protocol for protoplast buffer	51
Table 2.2. Protocol for Lysis Solution	51
Table 3.1. Crystal data and summary of data collection and refinement for [(MePhtpy)RuCl(dpp)](PF ₆).C ₇ H ₈	65
Table 3.2. FAB MS spectral data for [(MePhtpy)RuCl(dpp)PtCl ₂](PF ₆) (MePhtpy = 4'-(4-methylphenyl)-2,2':6',2"-terpyridine and dpp = 2,3-bis(2-pyridyl)pyrazine).....	66
Table 3.3. ESI MS spectral data for [(tpy)RuCl(dpp)PtCl ₂](PF ₆) (tpy = 2,2':6',2"-terpyridine and dpp = 2,3-bis(2-pyridyl)pyrazine).....	67
Table 3.4. ESI MS spectral data for [(^t Bu ₃ tpy)RuCl(dpp)PtCl ₂](PF ₆) (^t Bu ₃ tpy = 4,4',4"-tri-tert-butyl-2,2':6',2"-terpyridine) and dpp = 2,3-bis(2-pyridyl)pyrazine)	68
Table 3.5. ESI MS spectral data for [(TL)RuCl(dpp)](PF ₆) (tpy = 2,2':6',2"-terpyridine, MePhtpy = 4'-(4-methylphenyl)-2,2':6',2"-terpyridine, ^t Bu ₃ tpy = 4,4',4"-tri-tert-butyl-2,2':6',2"-terpyridine), and dpp = 2,3-bis(2-pyridyl)pyrazine).....	69
Table 3.6. Cyclic voltammetric data for [(TL)RuCl(dpp)PtCl ₂](PF ₆) and monometallic synthons (TL = terminal ligand (tpy = 2,2':6',2"-terpyridine, MePhtpy = 4'-(4-methylphenyl)-2,2':6',2"-terpyridine, ^t Bu ₃ tpy = 4,4',4"-tri-tert-butyl-2,2':6',2"-terpyridine), dpp = 2,3-bis(2-pyridyl)pyrazine).....	71
Table 3.7. Cyclic voltammetric data for [(TL)RuCl(dpp)PtCl ₂](PF ₆) and monometallic synthons (TL = terminal ligand (tpy = 2,2':6',2"-terpyridine, MePhtpy = 4'-(4-methylphenyl)-2,2':6',2"-terpyridine, ^t Bu ₃ tpy = 4,4',4"-tri-tert-butyl-2,2':6',2"-terpyridine), dpp = 2,3-bis(2-pyridyl)pyrazine).....	81
Table 3.8. Electrochemical and spectroscopic properties of a series of ruthenium complexes incorporating tridentate, 2,2',6',2"-terpyridine (tpy) terminal ligand (bpy = 2,2'-bipyridine, tpp = 2,3,5,6-tetrakis(2-pyridyl)pyrazine, dpp = 2,3-bis(2-pyridyl)pyrazine, dpq = 2,3-bis(2-pyridyl)quinoxaline, dpb = 2,3-bis(2-pyridyl)benzoquinoxaline, MePhtpy = 4'-4-methylphenyl)-2,2':6',2"-terpyridine, ^t Bu ₃ tpy = 4,4',4"-tri-tert-butyl-2,2':6',2"-terpyridine).....	86
Table 3.9. Electrochemical and spectroscopic properties of a series of Ru ^{II} Pt ^{II} bimetallic complexes incorporating tridentate, 2,2',6',2"-terpyridine (tpy) terminal ligand (tpp = 2,3,5,6-tetrakis(2-pyridyl)pyrazine, dpp = 2,3-bis(2-pyridyl)pyrazine, dpq = 2,3-bis(2-pyridyl)quinoxaline, dpb = 2,3-bis(2-pyridyl)benzoquinoxaline, MePhtpy = 4'-4-methylphenyl)-2,2':6',2"-terpyridine, ^t Bu ₃ tpy = 4,4',4"-tri-tert-butyl-2,2':6',2"-terpyridine, and ΔE _{redox} = E _{ox} - E _{red}).....	86

Table 3.10. Electrochemical and spectroscopic properties of a series of Ru ^{II} Pt ^{II} bimetallic complexes incorporating tridentate, 2,2',6',2''-terpyddine (tpy) terminal ligand (tpp = 2,3,5,6-tetrakis (2-pyridyl)pyrazine, dpp = 2,3-bis(2-pyridyl)pyrazine, dpq = 2,3-bis(2-pyridyl)quinoxaline, dpb = 2,3-bis(2-pyridyl)benzoquinoxaline, MePhtpy = 4'-(4-methylphenyl)-2,2':6',2''-terpyridine, ^t Bu ₃ tpy = 4,4',4''-tri-tert-butyl-2,2':6',2''-terpyridine).....	89
Table 3.11. Log P values for homoleptic and heteroleptic complexes.....	96
Table 3.12. R _f values of Ru ^{II} Pt ^{II} bimetallic complexes and standard cisplatin. The R _f values were calculated by dividing the distance traveled by the DNA-MC adduct by the distance traveled by the 2.0 kb band of the molecular weight standards (dpp = 2,3-bis(2-pyridyl)pyrazine, tpy = 2,2':6',2''- terpyridine, MePhtpy = 4'-(4-methylphenyl)- 2,2':6',2''-terpyridine, ^t Bu ₃ tpy = 4,4',4''-tri-tert-butyl-2,2':6',2''-terpyridine).....	106
Table 3.13. Comparison of antibacterial and DNA interaction properties shown by [(TL)RuCl(dpp)PtCl ₂](PF ₆).....	120

Table of Abbreviations

Abbreviations	
BAS	Bioactive site
BL	Bridging ligand
bpy	2,2'-bipyridine
CV	Cyclic voltammetry
DAP	1,12-diazaperylene
DIP	4,7-diphenyl-1,7-phenanthroline
DNA	Deoxyribonucleic acid
dpb	2,3-bis(2-pyridyl)benzoquinoxaline
dpp	2,3-bis(2-pyridyl)pyrazine
dppz	dipyridio[3,2'-a:2,3'-c]phenazine
dpq	2,3-bis(2-pyridyl)quinoxaline
GS	Ground state
HOMO	Highest occupied molecular orbital
IL	Intraligand
LA	Light absorber
LED	Light emitting diode
LF	Ligand field
LUMO	Lowest unoccupied molecular orbital
Me ₂ bpm	5,5'-dimethyl-2,2'-bipyrimidine
Me ₂ phen	3,4-methyphenanthroline
MePhtpy	4'-(4-methylphenyl)-2,2':6',2"-terpyridine
MLCT	Metal to ligand charge transfer
PHBI	2-(2-benzimidazole)-1,10-phenanthroline
phen	1,10-phenthroline
PHNI	2-(2-napthoimidazole)-1,10-phenanthroline
Pydppz	3-(pyrid-2'-yl)dipyrido(3,2-a:2',3'-c]phenazine)
SWV	Square wave voltammetry
^t Bu ₂ tpy	4,4'-di-tert-butyl-2,2'-bipyridine
^t Bu ₃ tpy	4,4',4"-tri-tert-butyl-2,2':6',2"-terpyridine
TL	Terminal ligand
tmen	<i>N,N,N',N'</i> -tetramethylethylenediamine
tppz	2,3,5,6-tetrakis(2-pyridyl)pyrazine
tpy	2,2':6',2"-terpyridine

Preface

As a graduate student at Virginia Tech, I have been involved with number of projects, resulting into several publications, which go beyond the scope of this dissertation. Following is the list of publications to date resulting from my graduate work.

Jain, A.; Winkel, B. S. J.; Brewer, K. J. *In vivo* inhibition of *E. coli* growth by a Ru(II)/Pt(II) supramolecule [(tpy)RuCl(dpp)PtCl₂](PF₆). *J. Inorg. Biochem.* **2007**, 101(10), 1525-1528.

Prussin, A. J., II; Zigler, D. F.; Jain, A.; Brown J. R.; Winkel, B. S. J.; Brewer, K. J. Photochemical Methods to Assay DNA Photocleavage using Supercoiled pUC18 DNA and LED or Xenon Arc Lamp Excitation. *J. Inorg. Biochem.* **2008**, 102(4), 731-739.

Jain, A.; Slebodnick, C.; Winkel, B. S. J.; Brewer, K. J. Enhanced DNA photocleavage properties of Ru(II) terpyridine complexes upon incorporation of methylphenyl substituted terpyridine and/or the polyazine bridging ligand dpp (2,3-bis(2-pyridyl)pyrazine) *J. Inorg. Biochem.* **2008**, 102, 1854-1861.

Arachchige, S. M.; Brown, J. R.; Chang, E.; Jain, A.; Zigler, D. F.; Rangan, K.; Brewer, K. J. Design considerations for a system for photocatalytic hydrogen production from water employing mixed-metal photochemical molecular devices for photoinitiated electron collection. *Inorg. Chem.* **2008**, In press.

Prussin A. J.; Zhao S.; Jain A.; Winkel B. S. J.; Brewer K. J. DNA interaction studies of a new class of tridentate bridged Ru(II)-Pt(II) mixed metal supramolecules. *J. Inorg. Biochem.* **2008**, Accepted for publication.

Jain, A.; Macshaw, E.; Winkel B. S. J.; Brewer K. J. Tuning DNA interactions of a series of multifunctional Ru-Pt mixed metal supramolecular complexes with substituted terpyridine ligands. *Inorg. Chem.* **2008**, Manuscript in preparation.

Jain A.; Ockyere, B.; Thelwel, B.; Winkel B. S. J.; Brewer K. J. DNA photocleavage and photobinding studies of mixed-metal supramolecular complexes containing Ru and Rh metal centers. *J. Inorg. Biochem.* **2008**, Manuscript in preparation.

Chapter 1: Introduction

1.1. Cancer

According to the American Cancer Society (ACS), cancer is the second leading cause of death in the United States.¹ For this reason, there has been a vast interest in the development of efficient anticancer drugs with minimal side effects. The oldest description of cancer was documented in Egypt dates in approximately 5000 B.C.^{2,3} Hippocrates, Galen, and Morgagni were among the first to describe cancer.⁴ Most of the physical evidence of early cancers has come from the examination of the remains of skeletons like fossilized bone and human mummies. Bone remains of the mummies have revealed growths suggestive of the bone cancer, osteosarcoma.

In the 20th century we saw tremendous improvement in our understanding of the cellular mechanisms related to cell growth and division.⁵ Cancer is characterized by uncontrolled cell division and the capability of these cells to invade other tissues. The development of cancer is commonly referred as carcinogenesis. It is a multi-step process that involves a series of genetic mutations in critical growth regulatory genes. Cancer cells often travel to other parts of the body where they replace normal cells. This process, called metastasis, occurs as the cancer cells move into the bloodstream or lymph vessels of the body. Chemicals, viruses, and heredity are the known causes of cancer.

There are three main approaches currently used to treat cancer: surgery, radiation, and chemotherapy. Depending on the disease, they can be used alone or in combination. Chemotherapy is most effective against tumors with rapidly dividing cells such as leukemia and lymphoma. Most chemotherapeutic drugs work by interfering with transcription or translation, or by blocking other essential cellular functions. Cisplatin (*cis*-diamminedichloroplatinum(II)), one of the most widely-used chemotherapeutic drugs, inhibits DNA replication and transcription by binding to DNA through chloride ligand exchange.⁶⁻⁸

1.2. Structure of DNA

DNA is the hereditary molecule in all cellular life forms.⁹ It is a polyanion made up of a chemically linked chain of nucleotides, each of which consists of a sugar (deoxyribose), a phosphate, and a nucleobase (purine and pyrimidine) (Figure 1.1). The purine bases are guanine and cytosine and the pyrimidine bases are adenine and thymine. DNA consists of two polynucleotide strands that wind about a common axis to form ~20 Å diameter double helix.⁹ The two strands run in opposite direction to each other and are therefore antiparallel. The bases occupy the core of the helix and the sugar-phosphate chains are coiled about its periphery, thereby minimizing the repulsion between the charged phosphate groups. Each base is hydrogen bonded to the base on the opposite strand to form a planar base pair (Figure 1.2). Base pairs are stacked one above the other and are nearly perpendicular to the long axis of the molecule. The stability of double stranded DNA is due to the stacking interactions between the base pairs. The helical arrangement gives rise to the major and minor grooves (Figure 1.1). Within each groove, the functional groups on the edges of the base pair are exposed to water and are chemically indistinguishable.

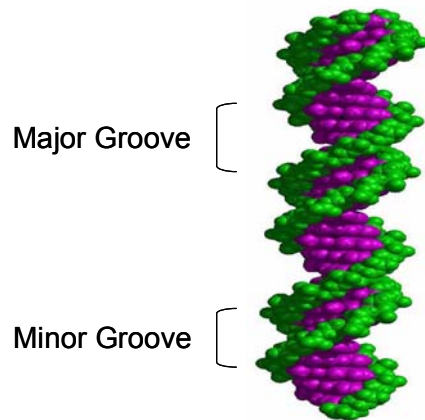


Figure 1.1. Structure of DNA double helix showing major and minor grooves. Green spheres represent the phosphate backbone and purple spheres display the bases.

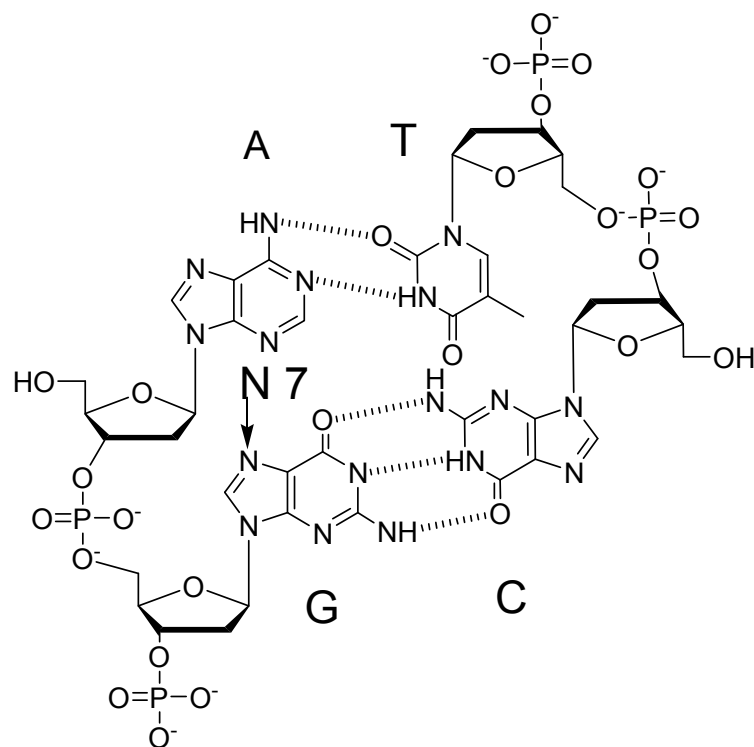


Figure 1.2. Structure of DNA nucleotides (C = cytosine, G = guanine, A = adenine, T = thymine). The N-7 position on guanine is indicated. Dashed lines indicate hydrogen bonds between base pairs.

1.2.1. DNA Binding Modes

DNA plays an important role in the synthesis of proteins (transcription) as well as its own replication and therefore is a major target for metal complexes (MC), especially for anticancer and antibiotic action. The four principal ways of DNA-MC interactions include electrostatic binding, groove binding, intercalation, and covalent binding. The mode of interaction of a metal complex to DNA depends upon its shape, size, chirality, and hydrophobic nature.¹⁰

1.2.1.1. Electrostatic Interaction/ Ionic Binding

DNA molecules have a single negative charge per nucleotide in an aqueous solution. Structurally compact metal complexes with large positive charge have been shown to display strong electrostatic interactions or ionic binding with DNA.¹¹ For example, the prototypical transition metal complex, $[\text{Ru}(\text{bpy})_3]^{2+}$ (bpy = 2,2'-bipyridine) exhibits ionic binding to DNA.¹⁰

1.2.1.2. Groove Binding

The ability of a metal complex to groove bind DNA is controlled by the lipophilicity and molecular shape of the complex. Groove binding involves an association of a species with the hydrophobic pocket formed between the sugar-phosphate backbones of each strand. The $[\text{Ru}(\text{Me}_4\text{phen})_3]^{2+}$ (Me_4phen = 3,4,7,8-tetramethylphenanthroline) complex is a well known groove binder.¹² The methyl substituents on the phen ligands contribute to the complex's overall lipophilicity and help in groove binding.¹²

1.2.1.3. Intercalation

Intercalation is a non-covalent association in which a planar, heteroaromatic molecule slides between the base pairs of DNA. Intercalation is stabilized by π - π stacking between the DNA base pairs and the metal complex. This leads to the unwinding of the helical backbone and an increase in helix length and rigidity. Barton and coworkers have shown that the complex Δ - $[\text{Ru}(\text{Ph}_2\text{phen})_3]^{2+}$ (Ph_2phen = 4,7-diphenyl-1,10-phenanthroline), binds strongly to DNA via intercalation. In contrast, no intercalation was observed with the Λ - $[\text{Ru}(\text{Ph}_2\text{phen})_3]^{2+}$ enantiomer due to steric repulsion of the bulky ancillary ligands with the sugar-phosphate backbone of DNA.¹² The different binding modes of the $[\text{Ru}(\text{Ph}_2\text{phen})_3]^{2+}$ complex are shown in Figure 1.3. Ruthenium polyazine complexes containing extended planar ligands such as dppz = dipyrido[3,2'-a:2,3'-c]phenazine, have been shown to intercalate between the base pairs of DNA.¹³

1.2.1.4. Covalent Binding

The fourth mode of binding involves the formation of covalent bonds between the metal complexes and the nucleophilic bases of DNA. Cross-linking of metal complexes with the bases of DNA is irreversible and causes a deformation of the overall DNA structure. Cisplatin, one of the most widely used anticancer drugs, covalently binds to DNA through the N-7 atom of the guanine base.⁸

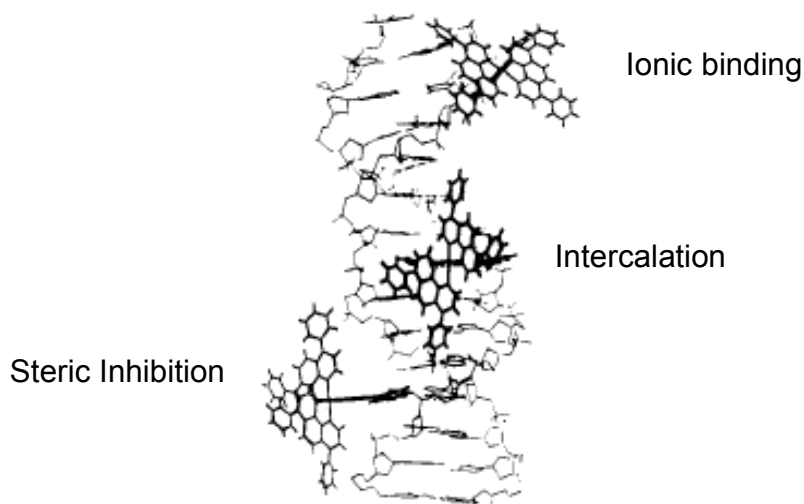


Figure 1.3. Schematic showing different DNA binding modes exhibited by $[\text{Ru}(\text{Ph}_2\text{phen})_3]^{2+}$ ($\text{Ph}_2\text{phen} = 4,7\text{-diphenyl}11,10\text{-phenanthroline}$). Top: Ionic binding of Λ isomer to sugar phosphate backbone. Middle: Intercalation of isomer into the double helix. Bottom: Steric inhibition of intercalation of Δ isomer into the helix. Adapted from Ref. 10.

1.3. Cisplatin

Cisplatin (*cis*-diamminedichloroplatinum(II)) (Figure 1.4) and its analogs are a class of widely used anti-tumor drugs. Although cisplatin has been known since 1844, its anti-tumor activity was discovered accidentally by Rosenberg while investigating the influence of an electric field on the growth of *E. coli* in 1965.^{14,15} In 1978, cisplatin was approved for the treatment of testicular and ovarian cancer. Cisplatin is now used in the treatment of variety of cancers including head, neck, bladder, and cervical cancer. It is also used in the treatment of melanoma, lymphoma, oropharyngeal and bronchogenic carcinoma, osteosarcoma, and neuroblastoma.^{6,7}

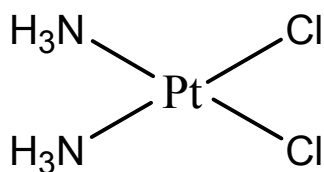


Figure 1.4. Structure of *cis*-diamminedichloroplatinum(II) (cisplatin)

1.3.1. Cisplatin: Mode of Action

The anti-tumor properties of cisplatin originate from its binding to DNA and formation of covalent cross-links.^{6-8,16} Early studies showed that cisplatin coordinates with DNA mainly through the N-7 atom of the guanine base due to its basicity and location on the surface of the major groove of DNA.^{17,18} ¹⁹⁵Pt NMR studies have revealed that cisplatin-DNA binding occurs in two steps.^{19,20} The first, rate determining step involves the replacement of one chloride atom by water, followed by monofunctional binding to either an adenine or a guanine base. The loss of the second chloride atom then occurs, leading to the binding to a purine base on the same strand (intrastrand cross-link) or on the other strand (interstrand cross-link) of DNA. Among various binding modes (Figure 1.5), intrastrand binding to the adjacent guanine bases or 1,2-intrastrand cross-links accounts for 60-70% of overall binding modes while binding with adjacent guanine and adenine (interstrand cross-link) bases accounts for 20-25% of overall binding modes.^{17,21} X-ray crystallographic studies of a cisplatin bound duplex DNA segment revealed that the covalent binding of the cisplatin to the adjacent guanine distorts the DNA double helix, causing a bend towards the major groove and flattening and broadening of the minor groove.²² The crystal structure of the DNA fragment bound to cisplatin is shown in Figure 1.6. The distortion caused by cisplatin leads to the compression of the sugar phosphate backbone, which then causes the sugar residues on the 5' side of the platinum lesion to pucker. These distortions inhibit DNA replication and transcription.

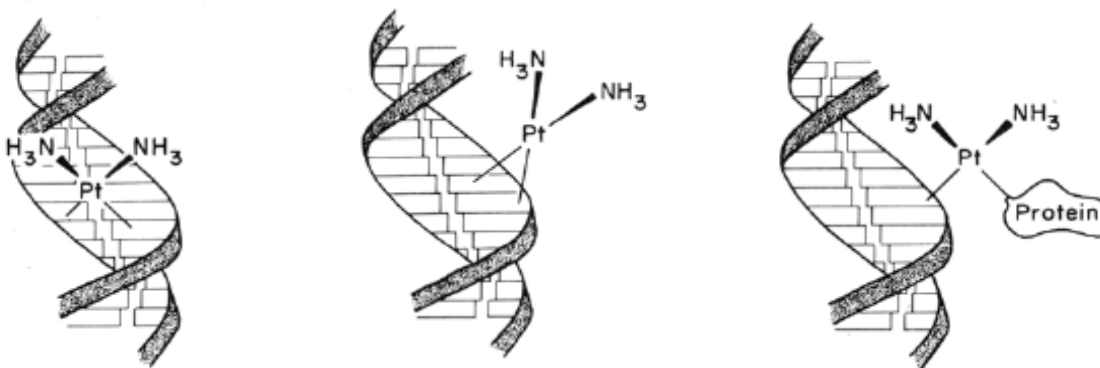


Figure 1.5. Cisplatin-DNA binding modes (a) interstrand cross-link, (b) 1,2-intrastrand cross-link, (c) protein-DNA cross-link. Adapted from Ref. 17.

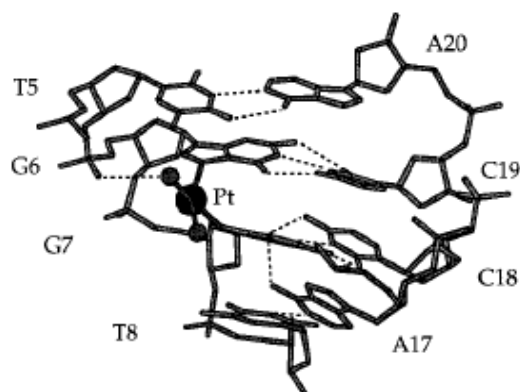


Figure 1.6. Crystal structure of cisplatin bound DNA fragment (T = thymine, G = guanine, C = cytosine, A = adenine, numeric figures represents the residue number). Adapted from Ref. 22.

1.3.2. Limitations of Cisplatin

Although cisplatin is used to treat a number of different cancers, its use as an anti-cancer agent does have limitations. An important limitation of cisplatin is the development of tumor resistance.⁷ Cisplatin can also only be administered intravenously due to its limited solubility in water. Cisplatin is not tumor selective and is cytotoxic in nature, with its main side effects including kidney toxicity, nausea, vomiting, hearing loss, low white blood cell count, and bone marrow depression.²¹ Investigators have demonstrated that the cytotoxicity induced by the Pt(II) complexes is attributed to the production of a glutathione-conjugates, formation of a reactive oxygen species, or disruption of intracellular calcium homeostasis.²³

1.3.3. Cisplatin Analog Research

In spite of the widespread success of cisplatin, the search for new cisplatin analogs continues in order to address the side effects, toxicity, and resistance associated with cisplatin. To date, only one second generation Pt(II) compound, diammine[1,1-cyclobutanedicarboxylato(2-)]-O,O'-platinum(II) (carboplatin), has received worldwide approval. Carboplatin is less toxic than cisplatin and can be administered in higher doses.²⁴ The lower toxicity of carboplatin has been attributed to the slower hydrolysis of the cyclobutanedicarboxylato ligand in comparison to the *cis*-chlorides on cisplatin.²⁴, *trans* 1,2-

diaminocyclohexaneoxalatoplatinum(II) (Oxaliplatin) has been approved in France for the treatment of colorectal cancer, while *cis*-diammine-glycolato-O,O'-platinum(II) (nedaplatin) has received approval in Japan.²⁵ The structures of carboplatin, oxaliplatin and nedaplatin are shown in Figure 1.7.

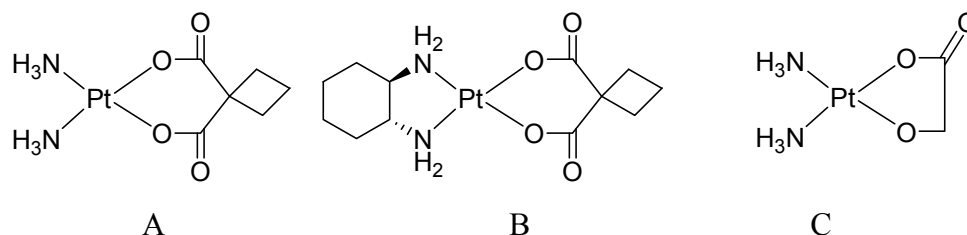


Figure 1.7. Structures of carboplatin (A), Oxaliplatin (B), and Nedaplatin (C).

Farrell and coworkers have developed multinuclear platinum complexes containing two or more platinum centers with the general formula $[\mu\text{-H}_2\text{N-R-NH}_2\text{-}\{\text{PtCl}_n(\text{NH}_3)_{3-n}\}]^{[(2-m)+(2-n)]+}$ ($m = 0, n = 2, 4$).^{26,27} These multinuclear Pt complexes primarily form interstrand cross-links rather than intrastrand cross-links with DNA. $[\{\text{trans-PtCl}(\text{NH}_3)_2\}\mu\text{-}\{\text{trans-Pt}(\text{NH}_3)_2(\text{H}_2\text{N}(\text{CH}_2)_6\text{NH}_2)_2\}](\text{NO}_3)_4$ (BBR3464) (Figure 1.8) is the first multinuclear platinum complex to enter into a clinical trial.^{28,29} This complex has been found to be more active than cisplatin and has an optimal dose of 0.4 mg/kg for human carcinoma, tumor model H460 compared to 6 mg/kg for cisplatin. BBR3464 binds to DNA primarily through long range 1,4 interstrand cross-links.²⁸ Although thousands of anticancer compounds have been discovered after the serendipitous discovery of cisplatin, the search continues for orally active, tumor specific compound.

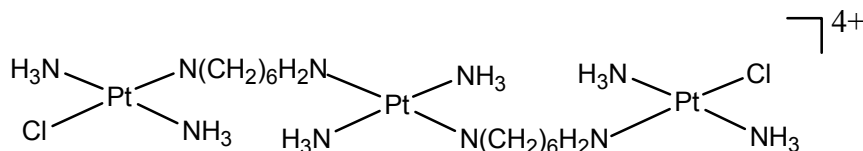


Figure 1.8. Structure of BBR3464.

1.4. Photodynamic Therapy (PDT)

1.4.1. PDT: History and Mechanism of Action

Photodynamic therapy (PDT) is a treatment in which activation of a sensitizer by light of the appropriate wavelength leads to the destruction of cancer cells. Light has been used as a therapeutic agent by ancient Chinese, Egyptians, and Indians to treat skin diseases including psoriasis, rickets, vitiligo, and skin cancer. The lethal effects of the combination of acridine dyes and red light was first reported by Oscar Raab.³⁰ R. L. Lipson and S. Schwartz began the modern era of PDT at the Mayo Clinic in 1960.³¹ PDT is used in the treatment of breast cancer, gynecological tumors, intraocular tumors, brain tumors, head, and neck tumors.^{32,33} The mitochondria, lysosome, plasma membrane, and nuclei of tumor cells have been identified as potential targets of PDT agents.³⁴

In PDT, light of appropriate wavelength is absorbed by a photosensitizer, giving the excited-triplet state via a short-lived excited singlet state. The excited singlet-state undergoes intersystem crossing (ISC) and the spin of the excited electron inverts its spin to form a long lived excited triplet state (Figure 19). The excited triplet-state can undergo two types of reactions: electron transfer reaction (Type I) and energy transfer reaction (Type II). The Type I mechanism involves electron transfer directly from the excited triplet-state of the photosensitizer to a substrate such as plasma membrane to form radicals. These radicals react rapidly with molecular oxygen producing a reactive oxygen species. The Type I mechanism involves reductive quenching of an excited photosensitizer by DNA, as described by Foote.³⁵ The Type II mechanism involves the energy transfer from the excited triplet state of the sensitizer to the triplet oxygen species which results in the ground state sensitizer and the singlet oxygen. The singlet oxygen reacts with the plasma membrane, lysosome, mitochondria, and DNA, resulting in cell death through apoptosis and necrosis. Recently, a Type III mechanism of PDT has also been proposed.^{36,37} In this type of PDT the excited triplet state of sensitizer interacts with (doublet) free radicals generated by cells with diffusion controlled rate constants.³⁷ This mechanism have been proposed to take place by both electron transfer and energy transfer.³⁸ It has been suggested that the Type III mechanism might compete with the Type II mechanism during

photosensitization processes under *in vivo* conditions when an enhanced steady state concentration of “native” free radicals (generated in the cells) is established.³⁹

Ideal PDT agents absorb light in the red and far-red region of the visible spectrum. Generally, longer wavelengths of light penetrate the tissue more efficiently than shorter wavelengths, with strong reduction up to 580 nm largely due to the absorption by hemoglobin present in the body. The photosensitizer is activated by precise illumination to provide selective treatment. The main advantage of PDT is the selectivity of drug accumulation in the tumor tissues and the absence of systemic toxicity of the drug in the absence of light. Hematoporphyrin (HPD) derivatives are the first sensitizers to receive regulatory approval in the United States.³⁰ Most of the photosensitizers used in the treatment of cancer are based on the tetrapyrrole nucleus, for example, porphyrins (HPD), chlorins, bacteriochlorins, and pthalocyanines (Figure 1.10).

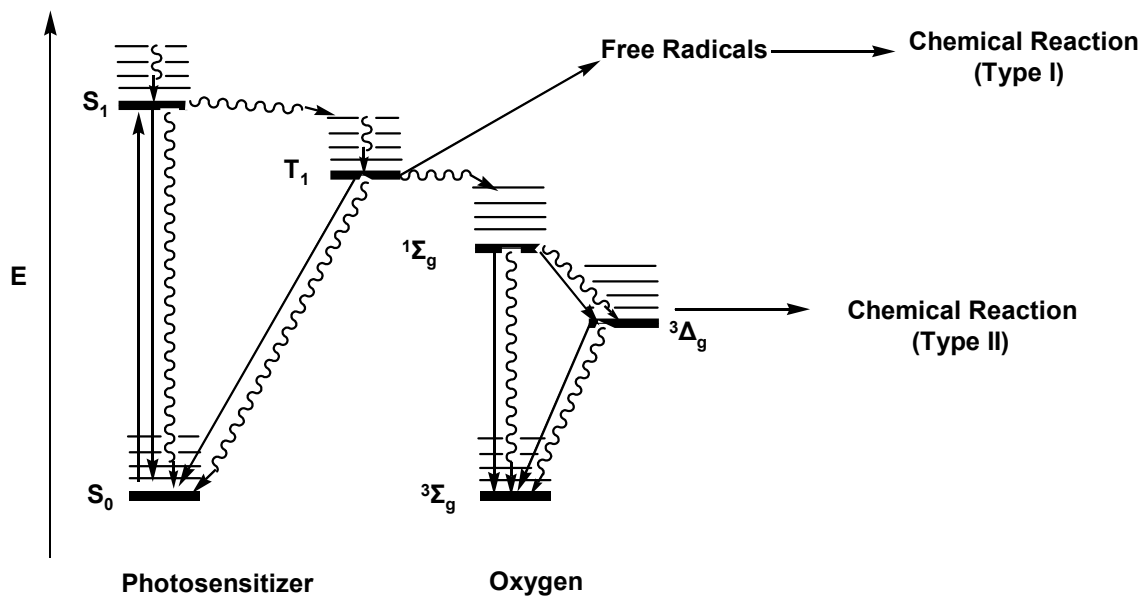


Figure 1.9. Jablonski diagram showing the origin of Type I and Type II photodynamic therapy.

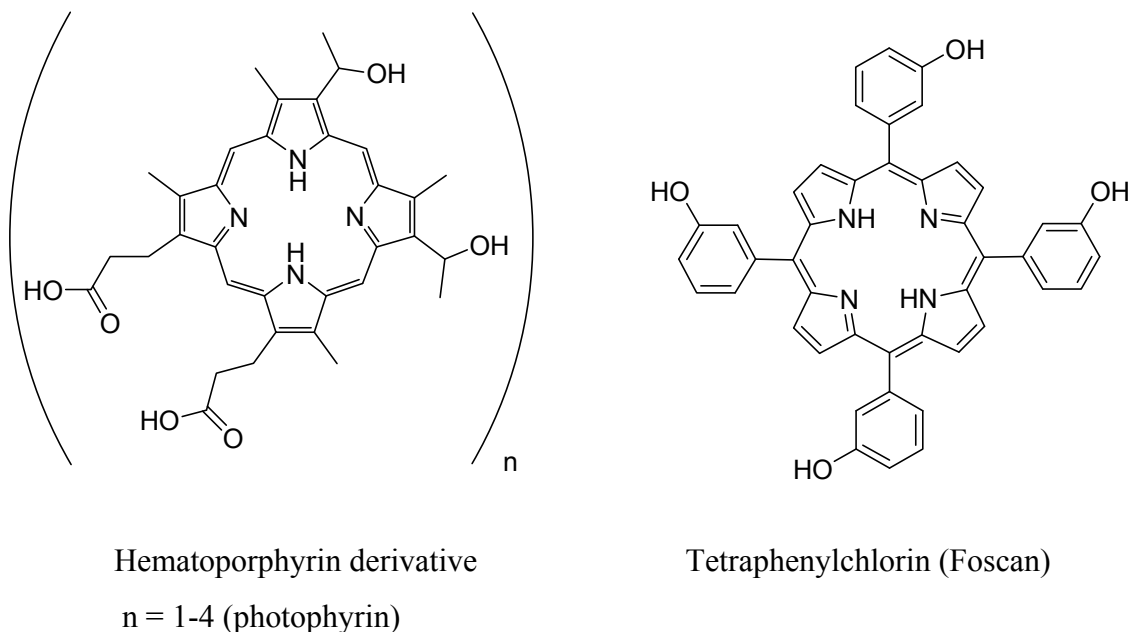


Figure 1.10. Chemical structures of hematoporphyrin derivatives and teraphenylchlorin.

1.4.2. Inorganic Complexes as PDT Agents

During the past decade research on PDT action of transition metal supramolecular complexes has seen extraordinary progress. The octahedral d^6 transition metal complexes containing polypyridyl ligands are widely used as light absorbers.⁴⁰ These complexes are generally photostable and under many circumstances are able to undergo excited state energy and electron transfer. The advantages of using inorganic chromophores to build supramolecular assemblies over organic chromophores include the following: (1) diverse bonding angles imparted by the transition metal centers and high directionality of the bonding between ligands and metals provide superior features over weak electrostatic, van der Waals, and π - π interactions, (2) involvement of the d orbitals offers more binding modes and geometric symmetries than simple organic molecules, (3) electronic and steric properties can be tuned by the use of various ancillary bridging and terminal ligands, (4) size can be easily varied by changing the lengths of bridging and terminal ligands, (5) positively charged metal complexes can exhibit ionic binding, (6) planar aromatic ligands can improve the interactions of metal complexes with DNA by intercalation, and (7) incorporation of transition metals can provide distinct spectral, magnetic, redox, photochemical, and photophysical properties.⁴¹

1.4.3. Ruthenium Light Absorbers

The light absorbing properties of ruthenium polypyridyl complexes have been extensively studied.^{40,42-46} These complexes possess highly versatile photophysical, photochemical, and redox properties and play an important role in electron and energy transfer processes.⁴⁰ The prototypical ruthenium polypyridyl complex, $[\text{Ru}(\text{bpy})_3]^{2+}$ (where bpy = 2,2'-bipyridine), is well studied due to its long excited state lifetime and interesting photophysical and redox properties.

1.4.3.1. Spectroscopic and Electrochemical Properties

The spectroscopic and electrochemical properties of Ru^{II} polypyridyl complexes are described in terms of the localized molecular orbital (MO) approximation. Figure 1.11 shows the block molecular orbital diagram of the ruthenium metal complex using a linear combination of atomic orbitals (LCAO) description. In this approach, each molecular orbital is a combination of one or more atomic orbitals. The boxes in the diagram represent a set of orbitals of slightly varied energy, where shaded boxes denote filled orbitals and unshaded boxes represent unfilled orbitals. In these complexes, the highest occupied molecular orbital (HOMO) is located on the ruthenium-based $d\pi$ orbital and the lowest unoccupied molecular orbital (LUMO) is located on the ligand-based π^* orbital. Upon absorption of light, the major electronic transitions that occur in the ruthenium polypyridyl complexes are ligand-based $\pi \rightarrow \pi^*$ (IL), metal to ligand charge transfer (MLCT), and ligand field (LF) transitions. The intensity of a transition is determined by selection rules. In order for a transition to be fully allowed, it must be both Laporte and spin allowed.

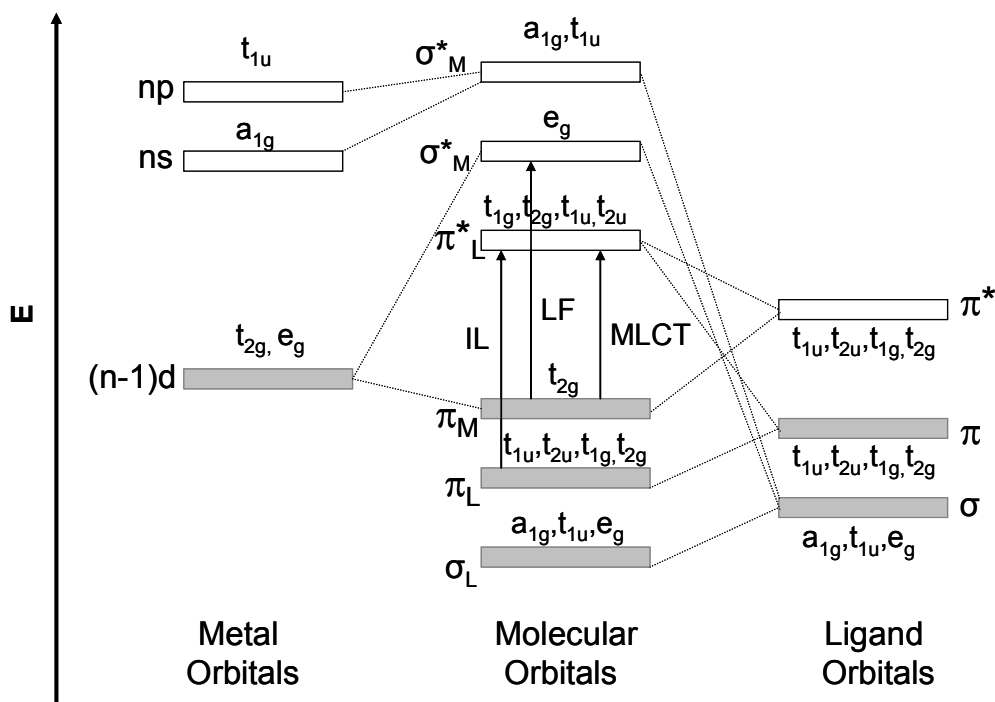


Figure 1.11. Block diagram of molecular orbitals of a d^6 octahedral complex with π backbonding ligands and some its possible transitions (IL = intraligand, MLCT = metal to ligand charge transfer, and LF = ligand field). Shaded blocks denote filled orbitals and unshaded blocks denote unfilled orbitals.

Electrochemical processes involve the addition (reduction) and removal (oxidation) of electrons. Therefore, the electrochemical properties of a metal complex can also be understood from a molecular orbital diagram. The oxidations are typically metal-based and indicate the energy of the HOMO. The reductions are typically ligand-based and indicate the energy of the LUMO.

The prototypical ruthenium polypyridyl complex, $[\text{Ru}(\text{bpy})_3]^{2+}$ (Figure 1.12), is a well studied light absorber.^{40,47,48} This complex shows intense intraligand $\pi \rightarrow \pi^*$ (IL) transitions in the UV region and MLCT transitions in the visible region. Upon optical excitation at 450 nm, population of the $\text{Ru}(d\pi) \rightarrow \text{bpy}(\pi^*)$ $^1\text{MLCT}$ occurs. The excited electron rapidly undergoes spin flip, known as intersystem crossing (isc) to populate the $^3\text{MLCT}$ state with unit efficiency (Figure 1.13). The non radiative decay (excited state deactivation) is represented by wavy lines in the energy diagram. The radiative decay from the triplet state to the ground state is represented

by a straight line and is known as phosphorescence. The $^3\text{MLCT}$ of $[\text{Ru}(\text{bpy})_3]^{2+}$ is relatively long-lived and emissive ($\lambda_{\text{max}}^{\text{em}} = 605 \text{ nm}$, excited state lifetime of the $^3\text{MLCT}$, $\tau = 860 \text{ ns}$ in acetonitrile, and $\Phi^{\text{em}} \approx 0.10$).⁴⁹ The excited state lifetime (τ) is defined as the inverse of the sum of all the rate constants for deactivation of the excited state in the absence of a quencher and is given by:

$$\tau = \frac{1}{k_r + k_{nr}} \quad 1.1$$

The quantum yield, Φ^{em} , for an excited state process is given by the ratio of the rate constants for the process of interest, divided by the sum of all the rate constants for the deactivation of a state for a directly populated state. The quantum yield, Φ^{em} of emission from the $^3\text{MLCT}$ state of $[\text{Ru}(\text{bpy})_3]^{2+}$, in the absence of a quencher is given by

$$\Phi^{\text{em}} = \Phi_{^3\text{MLCT}} \frac{k_r}{k_r + k_{nr}} \quad 1.2$$

where $\Phi_{^3\text{MLCT}}$ is the quantum efficiency for generation of the $^3\text{MLCT}$ state.

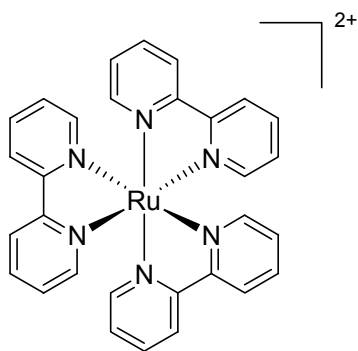


Figure 1.12. Representation of $[\text{Ru}(\text{bpy})_3]^{2+}$ (bpy = 2,2'-bipyridine).

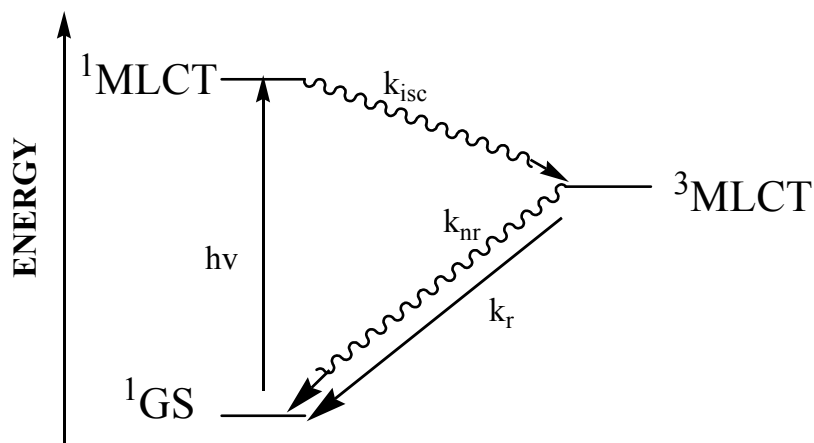


Figure 1.13. Jablonski diagram for $[\text{Ru}(\text{bpy})_3]^{2+}$. (bpy = 2,2'-bipyridine; GS = ground state; MLCT = metal-to-ligand charge transfer; k_r = rate constant for radiative decay; k_{nr} = rate constant for non-radiative decay; and k_{isc} = rate constant for intersystem crossing).

Applications of ruthenium (II) bis-tridentate polypyridyl light absorbers are more limited than the highly studied ruthenium (II) tris-bidentate polyazine chromophores. The $[\text{Ru}(\text{tpy})_2]^{2+}$ complex (where tpy = 2,2':6',2''-terpyridine) (Figure 1.14) exhibits less favorable photophysical properties than $[\text{Ru}(\text{bpy})_3]^{2+}$, exhibiting a very short lived $^3\text{MLCT}$ ($\tau = 0.25$ ns, $\Phi^{em} \approx 5.0 \times 10^{-6}$ in CH_3CN) excited state due to the thermal population of the ^3LF excited state.⁵⁰⁻⁵³ The thermal accessibility of the ^3LF state is due to the lower energy of this state as a result of the unfavorable bite angle for octahedral coordination associated with tpy type ligands.⁵³ The low lying ^3LF state quenches the emission of the normally emissive $^3\text{MLCT}$ state (Figure 1.15). However the use of terpyridine ligands provides the distinct advantage of allowing stereochemical control, eliminating the Δ and Λ isomeric mixtures the characteristic of tris-bidentate systems.

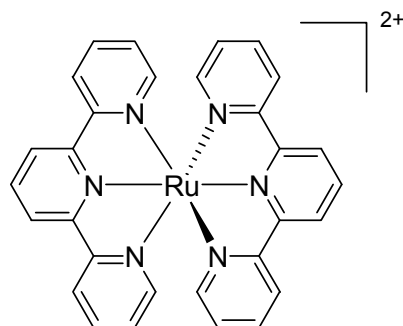


Figure 1.14. Representation of $[\text{Ru}(\text{tpy})_2]^{2+}$ (tpy = 2,2':6',2''-terpyridine).

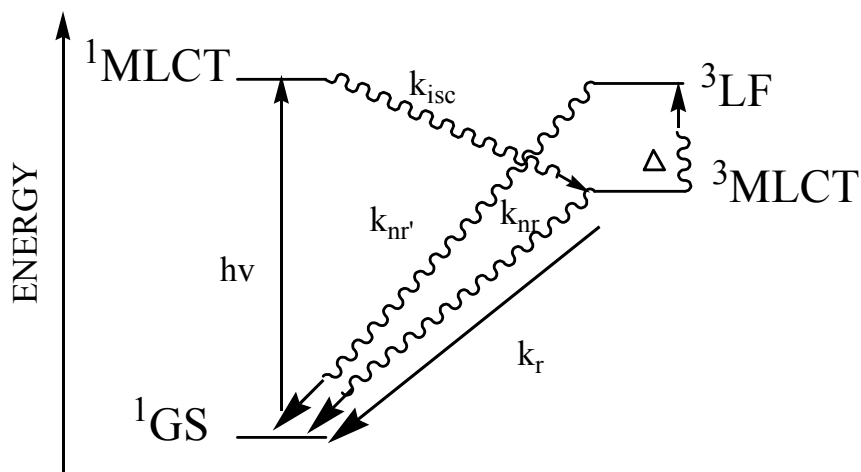


Figure 1.15. Jablonski diagram for $[\text{Ru}(\text{tpy})_2]^{2+}$ (tpy = 2,2':6',2''-terpyridine; GS = ground state; MLCT = metal to ligand charge transfer; k_r = rate constant for radiative decay; k_{nr} = rate constant for non-radiative decay; and k_{isc} = rate constant for intersystem crossing).

The photophysical properties of Ru(II) bis-tridentate polypyridyl metal complexes can be tuned by the introduction of various substituents on the tridentate ligand. Electron-withdrawing groups stabilize the LUMO, while electron-donating groups destabilize the HOMO.⁵⁴⁻⁶⁰ Stabilization of the lowest $^3\text{MLCT}$ state results in lower thermal population of the ^3LF state.^{58,61} Balzani and coworkers have reported increased excited state lifetime and emission quantum yield of $[\text{Ru}(\text{tpy})_2]^{2+}$ type molecules upon incorporation of a methylphenyl group at the 4' position of the terpyridine ring.⁵⁴ The 4'-methyl-sulphonyl substituted bis-terpyridine complexes have been shown to have prolonged room temperature luminescence lifetimes, $([\text{Ru}(\text{MeSO}_2\text{-tpy})_2](\text{PF}_6)_2$, 25 ns; $([\text{MeSO}_2\text{-tpy}]\text{Ru}(\text{tpy-OH}))(\text{PF}_6)_2$, 50 ns), due to the strong electron-withdrawing ability of the methyl-sulfonyl group compared to $[\text{Ru}(\text{tpy})_2]^{2+}$, 0.25 ns.⁵⁸

1.4.3.2. DNA Interaction Properties

Ruthenium polyazine complexes have been reported to interact with DNA through electrostatic interaction, intercalation, and groove binding.^{10,11,62,63} The DNA photocleavage activity of ruthenium polyazine complexes is well known.⁶⁴⁻⁶⁶ These types of complexes have been shown to photocleave DNA via singlet oxygen ($^1\text{O}_2$) generation. The $^3\text{MLCT}$ state of these

complexes undergoes energy transfer to molecular oxygen ($^3\text{O}_2$) to generate $^1\text{O}_2$, which reacts with DNA, cleaving the backbone. Thummel and coworkers have reported that the complex, $[\text{Ru}(\text{bpy})_2(\text{DAP})]^{2+}$ (DAP = 1,12-diazaperylene), photocleaves DNA upon irradiation with visible light via $^1\text{O}_2$ generation.⁶⁷ A ruthenium (II) complex with two sequentially linked viologen units has also been reported to photocleave DNA both in the presence and in the absence of oxygen.⁶⁸ This oxygen independent reactivity was thought to involve guanine oxidation by a photogenerated Ru(III) center. Complexes incorporating tridentate tpy ligands have been reported to interact with DNA through electrostatic interaction, intercalation, and groove binding. Turro and coworkers have recently reported the DNA photocleavage activity of $[\text{Ru}(\text{tpy})(\text{pydppz})]^{2+}$ (pydppz = 3-(pyrid-2'-yl)dipyrido(3,2-a:2',3'-c)phenazine) in the presence of oxygen.⁶⁹ Thorp and coworkers have examined the DNA cleavage activity of $[\text{Ru}(\text{tpy})(\text{tmen})(\text{OH}_2)]^{2+}$ (tmen = *N,N,N',N'*-tetramethylethylenediamine) by cyclic voltammetry.⁶⁶ The heteroleptic complexes, $[\text{Ru}(\text{tpy})(\text{PHBI})]^{2+}$ and $[\text{Ru}(\text{tpy})(\text{PHNI})]^{2+}$ (PHBI = 2-(2-benzimidazole)-1,10-phenanthroline and PHNI = 2-(2-naphthoimidazole)-1,10-phenanthroline), have been reported to interact with DNA via electrostatic interaction and intercalation, respectively.⁶⁶ Recently, the $^1\text{O}_2$ generation and DNA photocleavage ability of an aryl (naphthalene, anthracene) modified ruthenium bis-terpyridine complexes has been reported.⁷⁰ The aryl-substituted terpyridines have been shown to interact with DNA through intercalation of the aryl tail group between the DNA bases.

Ruthenium polyazine complexes have also been reported as luminescent markers of DNA in an aqueous solution. According to Barton, the complex, $[\text{Ru}(\text{phen})_2(\text{dppz})]^{2+}$ (phen = 1,10-phenanthroline), shows no luminescence in an aqueous solution due to quenching by hydrogen bonding between water and phenazine nitrogen of the ligand.¹³ Upon binding, interaction between DNA and the ligand protects the phenazine ligand from water, leading to an intense emission. The complex, $[\text{Ru}(\text{phen})_2(\text{dppz})]^{2+}$, functions as a molecular “light switch” for DNA. The “light switch effect” can be used to detect DNA binding spectroscopically. The luminescence properties, DNA interaction properties, and proposed “light switch” behavior of these types of inert coordinatively-saturated water soluble molecules makes them excellent complexes as diagnostic and therapeutic agents.

1.4.4. Photodynamic Antibacterial Therapy

Recently, bacterial resistance against antibiotics has become a threatening health issue. Bacteria replicate very rapidly, and a mutation that facilitates microbe survival in the presence of an antibiotic drug can quickly become predominant in the microbial population. Due to the resistance developed to the already existing antibiotics, there has been a constant demand for effective antibacterial agents and alternative chemotherapeutics.

PDT has been proposed as an alternative antibacterial therapy to combat the worldwide increase in antibiotics resistance.⁷¹⁻⁷⁷ Visible light irradiation can kill microorganisms like bacteria, viruses, and fungi by treatment with an appropriate photosensitizer. It has been shown that Gram positive bacteria are susceptible to PDT in contrast to Gram negative bacteria, which are resistant against commonly used photosensitizers.⁷⁸ The high susceptibility of Gram positive bacteria is explained by their physiology, as their cytoplasmic membrane is surrounded by a relatively porous layer of peptidoglycan and lipoteichoic acid that allows photosensitizers to cross the membrane.⁷⁸ Similarly, the resistance of Gram negative bacteria to PDT can be explained by the fact that their cell wall consists of an inner cytoplasmic membrane and an outer membrane that are separated by the peptidoglycan-containing periplasm. The outer membrane forms a barrier between the cytoplasm and the outer environment of the cell. To overcome the resistance of Gram negative bacteria, cationic photosensitizers and conjugates of photosensitizers with cationic polymers have been used.⁷² According to Hartman and coworkers, if singlet oxygen is generated in sufficient quantities near the bacterial outer membrane, it can diffuse into the cell to cause damage to the vital intracellular components.⁷⁹

There are two mechanisms that can lead to photodynamic inactivation of bacteria: (i) DNA damage and (ii) cytoplasmic membrane damage.⁷⁵ Exposure to light in the presence of a photosensitizer can cause breaks in both single and double stranded DNA. It has also been shown that photosensitizers can intercalate into DNA and cause distortion in the DNA double helix.^{80,81} Photooxidation of guanine residues has also been reported.⁸¹ Nitzan and coworkers have reported disruption of cell wall synthesis and the appearance of a multilamellar structure near the septum

of dividing cells, along with the loss of potassium ions from the cells in the presence of a photosensitizer on irradiation with the visible light.⁸²

1.4.4.1. Ruthenium Metal Complexes: Antibacterial Properties

Development of metal-containing antibiotics is an emerging area of research. Numerous metal containing complexes have been reported to possess interesting toxicological and pharmaceutical properties.⁸³⁻⁸⁸ Metalloantibiotics can interact with several kinds of biomolecules, including DNA, RNA, proteins, and lipids, interfering with their unique and specific bioactivity. Ruthenium polypyridine complexes have been reported to inhibit bacterial cell growth.^{67,89-92}

Ruthenium complexes have shown a great potential as anti-bacterial and anti-tumor agents and remain the subject of interest.^{67,89-92} Ruthenium complexes possessing 2-hydroxyl-1-naphthaldehyde thiosemicarbazone as a ligand have been studied for their antifungal and antimicrobial properties.⁹¹ Recently, protein binding sites of the $[(\eta^6\text{-p-cymene})\text{RuCl}_2(\text{DMSO})]$ complex in *E. coli* were identified using combined multidimensional liquid chromatography and ESI tandem mass spectrometry.⁹³ Although there are a number of reports on DNA photolyase properties of ruthenium polypyridyl complexes, the photodynamic inhibition of bacterial cell growth has yet to be studied.

1.4.5. Limitations of PDT

Although PDT has shown promise against various cancers, its use as an anti-cancer therapy does have limitations. One of the main side effects of PDT agents is prolonged light sensitivity.⁹⁴ Skin and eyes remain sensitive to light for some 6 weeks after treatment.⁹⁵ Exposure to light can cause burns, swelling, pain, scarring, itchiness, blisters, and skin infections. PDT is not suitable for all kinds of tumors, especially for large tumors because of the lack of light activation of photosensitizers deep inside the tumor. PDT can only be used to treat tumors that are located on the skin or just below the skin. The average penetration depth at 630 nm, the wavelength used for clinical treatment with Photofrin, an FDA approved photosensitizer for

PDT, is 1-3 mm. Photofrin reacts with a wide variety of biomolecules and is cleared from the body relatively slowly.⁴¹ The medical dye lasers used for illumination are expensive and delivering the proper amount of light to a particular area is a complex process.

1.5. Combination Therapy (Cisplatin + PDT)

The development of new cancer treatments has been an area of active research for many years due to the side effects associated with current therapies. Drugs with different modes of action could be combined to achieve additive effects and to avoid side effects. It has been reported that administering cisplatin in combination with a PDT agent increases the effectiveness of the treatment against tumors.⁹⁶⁻⁹⁸ Coupling of a PDT active chromophore to a cisplatin analog leads to a combination of PDT and chemotherapy.⁹⁹⁻¹⁰² The chromophore-coupled cisplatin analogs have been shown to preferentially accumulate in the tumor tissue due to the presence of a photosensitizer and can inhibit transcription due to the presence of a cisplatin moiety.

1.5.1. Coupling of a Cisplatin Analog to a PDT Agent

The cytotoxic effect of cisplatin and, upon irradiation additional photodynamic effect of the chromophore, is achieved by coupling a ruthenium-based chromophore to a cisplatin moiety.^{103,104} The ruthenium chromophores provide the light absorbing properties and add overall positive charge to the metal complex. The coupling of a light absorbing unit to a cisplatin moiety provides photoactivation along with covalent binding and increases the water solubility of the complex. Positively charged metal complexes show additional electrostatic attraction towards DNA. The chromophoric properties of ruthenium chromophores can provide a handle to assay the DNA binding properties spectroscopically. Ruthenium complexes, being less reactive, on coupling with a cisplatin analog, can impart reactivity to a particular DNA sequence and cross-linking with a unique protein. The coupling of a light absorbing metal with directed charge transfer to the remote platinum site could impart interesting photochemical properties to these metal complexes.

A chromophore unit consists of a ruthenium metal center and the terminal ligands,

(Figure 1.16) which can be coupled to a cisplatin moiety by communicative and non-communicative bridging ligands (BLs) (Figure 1.17). Non-communicative BLs do not allow for electronic communication between the two units, thus individual units in a supramolecular assembly maintain their intrinsic redox properties. On the other hand, communicative BLs allow for electronic communication between two units, thus the redox properties of the individual units are not maintained. The polyazine bridging ligands are communicative in nature, are good π -acceptors, and impart interesting redox and physical properties to the polymetallic complexes. These bridging ligands bind to the metal by coordinate covalent bonds, where nitrogen acts as a Lewis base while the metal center acts as a Lewis acid. These ligands possess a low lying π^* orbital that can function as an acceptor for π -backbonding.

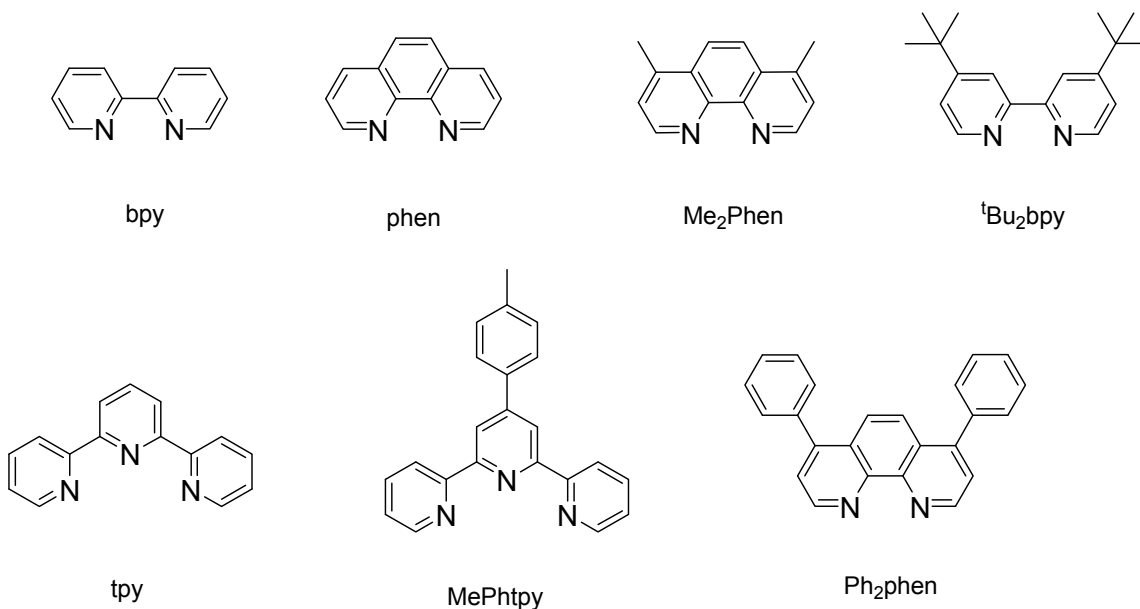


Figure 1.16. Representative terminal ligands ((bpy = 2,2'-bipyridine, phen = 1,10-phenanthroline, Me₂phen = 3,4-dimethylphenanthroline, ^tBu₂bpy = 4,4'-di-tert-butyl-2,2'-bipyridine, tpy = 2,2':6',2''-terpyridine, MePhtpy = 4'-(4-methylphenyl)-2,2':6',2''-terpyridine, Ph₂phen = 4,7-diphenyl-1,10-phenanthroline, and ^tBu₃tpy = 4,4',4''-tri-tert-butyl-2,2':6',2''-terpyridine).

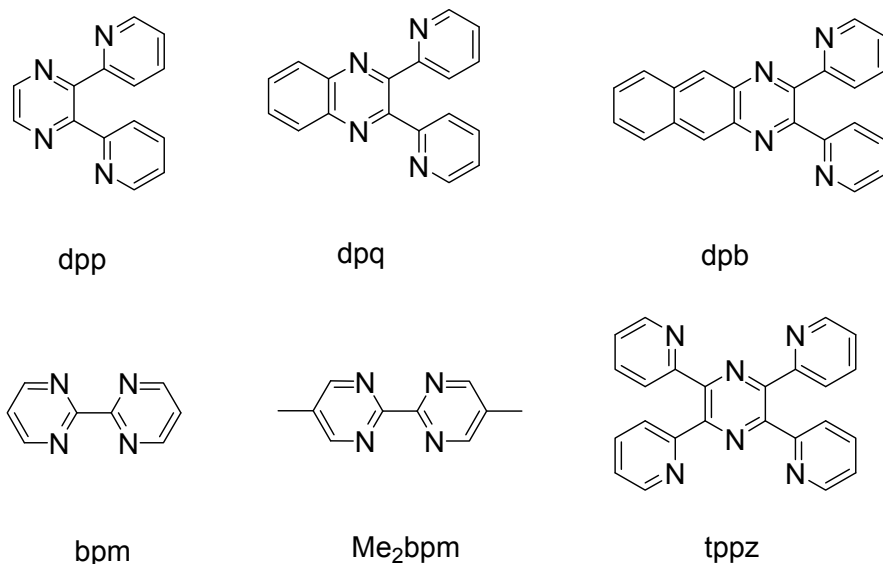


Figure 1.17. Representative polyazine bridging ligands (dpp = 2,3-bis(2-pyridyl)pyrazine, dpq = 2,3-bis(2-pyridyl)quinoxaline, dpb = 2,3-bis(2-pyridyl)benzoquinoxaline, bpm = 2,2'-bipyrimidine, Me₂bpm = 5,5'-dimethyl-2,2'-bipyrimidine, tppz = 2,3,5,6-tetrakis(2-pyridyl)pyrazine).

1.5.1.1. Coupling of Ruthenium Chromophores to a *cis*-PtCl₂ Moiety by a Non-Communicative Bridging Ligand

Coupling a polyazine LA to a reactive Pt(II) center via a non communicative BL do not allow for electronic communication between two subunits, thus the redox and photophysical properties of the individual units in a supramolecular assembly are maintained. The photophysical properties of Ru^{II}Pt^{II} bimetallic complexes coupled with the noncommunicative bridges are quite similar to the Ru light absorber, thus allowing for the design of metal complexes with the Ru LAs and reactive Pt subunits.

1.5.1.1.1. Spectroscopic and Electrochemical Properties

The non-communicative BLs allow for weak coupling of the metals. Rillema and coworkers have reported the redox and photophysical properties of Ru^{II}Pt^{II} and Ru^{II}Ru^{II} bimetallic complexes coupled via a noncommunicative Mebpy-CH₂-CH₂-Mebpy bridging ligand in [(bpy)₂Ru(Mebpy-CH₂-CH₂-Mebpy)PtCl₂]²⁺ and [(bpy)₂Ru(Mebpy-CH₂-CH₂-Mebpy)Ru(bpy)₂]⁴⁺.¹⁰⁵ The electronic absorption spectra of the Ru^{II}Pt^{II} and Ru^{II}Ru^{II} bimetallic complexes and their monometallic synthons are quite similar. The Ru^{II}Ru^{II} homobimetallic

complex shows twice the molar absorptivity of the heterobimetallic Ru^{II}Pt^{II} and the monometallic precursor, consistent with the presence of the two LA units. The redox properties of the Ru^{II}Pt^{II} and Ru^{II}Ru^{II} bimetallic complexes and their monometallic synthon resemble each other. The electrochemistry of the Ru^{II}Pt^{II} complex shows a Ru^{II/III} couple at 1.19 V and bpy^{0/-} couple at -1.38 V vs. Ag/AgCl. An additional couple is observed for the Ru^{II}Pt^{II} at -1.27 V and is attributed to the Mebpy^{0/-} reduction. The more positive ligand reduction potential for the Ru^{II}Pt^{II} compared to the Ru^{II}Ru^{II} and monometallic precursor is related to the π -backbonding properties of the ligand. The $d\pi$ orbitals of the Pt(II) do not overlap appreciably with π^* ligand orbitals as they are very different in energy. Thus, the π^* ligand orbitals remain stabilized in the presence of Pt(II), whereas they are destabilized when coordinated to the Ru(II) by π back-bonding to the $d\pi$ metal orbitals.

Sakai and coworkers have observed interesting luminescence behavior and DNA photocleavage upon coupling a ruthenium chromophore to a cisplatin moiety.¹⁰⁴ It has been known that the introduction of the *cis*-PtCl₂ moiety quenches the triplet excited state of the ruthenium chromophore. However, an increase in the luminescence intensity is observed upon coupling a ruthenium chromophore to a cisplatin moiety to form [(bpy)₂Ru(BL)PtCl₂](PF₆)₂ as compared to the monometallic synthon. The increase in the excited state lifetime of the Ru^{II}Pt^{II} bimetallic complex is attributed to the formation of a rigid metallocycle as compared to the flexible aminopropyl unit in the monometallic synthon. The formation of this rigid metallocycle promotes the nonradiative deactivation of the ³MLCT excited state.

1.5.1.1.2. DNA and Protein Interaction Properties

The Ru^{II}Pt^{II} bimetallic complexes act as DNA-DNA and DNA-protein cross-linking agents.^{106,107} Farrell and coworkers have reported the DNA-DNA and DNA-protein cross-linking properties of the [*cis, fac*-(RuCl₂(Me₂SO)₃)(μ -NH₂(CH₂)₄NH₂){*cis*-(Pt(NH₃)₂Cl₂)}] complex (Ru-Pt).¹⁰⁷ This complex interacts with DNA in two steps. First, one metal reacts with an adenine or guanine base of one strand of DNA. Depending upon the structure of the complex, the second metal can either react with DNA to form interstrand or intrastrand adducts and then cross-links with a protein or can directly cross-link with a protein. The Ru-Pt complex cross-links between

DNA and DNA repair proteins thus prevents the repair of damaged DNA. These DNA protein cross-links are therefore named “suicide DNA adducts”.^{106,107}

Reedijk and coworkers reported the X-ray crystal structure of the Ru^{II}Pt^{II} bimetallic complex, [(tpy)Ru(dtdeg)PtCl]Cl₃ (dtdeg = bis[4'-(2,2':6;2''-terpyridyl)]diethylenglycol).¹⁰⁸ They observed that the diethylene glycol ether linker folds to allow both the metal centers to interact with DNA. The crystal structures displayed the intermolecular stacking interaction between the platinum moieties. The presence of intermolecular stacking interactions between the Pt moieties suggested that the Pt moiety is able to both intercalate and coordinate with DNA without being hindered by the ruthenium unit. The ruthenium unit presumably helps pre-associate the complex with the DNA by providing an overall +2 charge.

1.5.1.2. Coupling of Ruthenium Chromophores to a cis-PtCl₂ Moiety by a Communicative Bridging Ligand

1.5.1.2.1. Spectroscopic and Electrochemical Properties

Coupling a polyazine LA to a reactive Pt(II) center via a communicative BL allows for electronic communication between the two subunits, thus the redox and photophysical properties of individual units are not maintained and as a result impart rich redox and photophysical properties to the heteronuclear bimetallic system. The electronic absorption spectra of these complexes are dominated by IL transitions in the UV region and Ru(dπ)→TL(π*) and Ru(dπ)→BL(π*) MLCT transition in the visible region of spectrum. Coordination of an electron deficient Pt(II) center to the monometallic synthon results in stabilization of the BL-based orbitals and shifts the BL-based MLCT transition to lower energies versus monometallic synthon.

The coupling of an electron-deficient Pt(II) center to a monometallic synthon vary the electrochemical properties of the molecule. The reduction of the bridging ligand shifts towards more positive potential compared to the monometallic synthon due to the electron withdrawing nature of the Pt(II) center. The Ru^{II}Pt^{II} bimetallic complexes exhibit two bridging ligand-based

one electron reductions typically assigned as BL/BL^- and BL^-/BL^{2-} . These electrochemical properties indicate that the change in the energy of the MLCT is due to the stabilization of the $BL(\pi^*)$ orbital by an electron deficient Pt(II) center. Table 1 summarizes the electrochemical and photophysical properties of $Ru^{II}Pt^{II}$ bimetallic complexes. The structures of $Ru^{II}Pt^{II}$ bimetallic complexes are shown in Figure 1.18.

Rillema and coworkers reported the photophysical and redox properties of $[(bpy)_2Ru(bpm)PtCl_2]^{2+}$ ($bpm = 2,2'$ -bipyrimidine) complex.¹⁰⁹ This complex displays the ligand-based $\pi \rightarrow \pi^*$ transitions in the UV region and $Ru(d\pi) \rightarrow bpy(\pi^*)$ and $Ru(d\pi) \rightarrow bpm(\pi^*)$ MLCT transition in the visible region (571 nm). The $Ru(d\pi) \rightarrow bpm(\pi^*)$ MLCT transition occurs at lower energy than the corresponding monometallic complex. This is consistent with the platinum coordination. The electrochemistry predicts a $Ru(d\pi)$ -based HOMO and $bpm(\pi^*)$ -based LUMO. The positive shift in the reduction potential of the bpm ligand is reported, suggesting the stabilization of the bpm ligand upon Pt(II) coordination. Similarly, Yam and coworkers have coupled a ruthenium-based light absorber, $[Ru(bpy)_2(dpp)]^{2+}$ to a *cis*- $PtCl_2$ moiety via 2,3-bis(2-pyridyl)pyrazine (dpp) BL.^{110,111} The $[Ru(bpy)_2dppPtCl_2]^{2+}$ displays intense $Ru(d\pi) \rightarrow dpp(\pi^*)$ MLCT transition in the visible region at ca 500-524 nm. The dpp-based MLCT transition shift to lower energies compared to the monometallic synthon $[Ru(bpy)_2(dpp)]^{2+}$ due to the stabilization of the $Ru(d\pi)$ orbitals with Pt(II) coordination. The electrochemistry of this molecule revealed the shift in $dpp^{0/-}$ reduction at a more positive potential compared to the monometallic synthon due to the stabilization of $dpp(\pi^*)$ orbital with coordination with an electron deficient Pt(II) center. Ruminski and coworkers have coupled the *cis*- $PtCl_2$ unit to a ruthenium chromophore by the dipyrido(2,3-a:3',2'-h)phenazine) (dpop) ligand to yield $[(bpy)_2Ru(dpop)PtCl_2]^{2+}$ complex.¹¹² This complex displays a $Ru(d\pi) \rightarrow dpop(\pi^*)$ MLCT transition in the visible region at a lower energy compared to the $Pt(d\pi) \rightarrow dpop(\pi^*)$ MLCT transition characteristic of $Ru^{II}Pt^{II}$ bimetallic complexes.

Table 1.1. Electrochemical and spectroscopic properties of Ru(II)/Os(II)-Pt(II) mixed metal bimetallic metal complexes.

Complex	$\lambda_{\max}^{\text{abs}}$ (nm)	$E_{1/2}^{\text{ox}}$ (V vs SCE)	$E_{1/2}^{\text{red}}$ (V vs SCE)			Ref.
			BL ^{0/-}	BL ⁻²⁻	TL ^{0/-}	
[(bpy) ₂ Ru(bpm)PtCl ₂] ^{2+ a}	571	1.35 (Ru ^{II/III})	-0.35	-1.02		113
[(bpy) ₂ Ru(dpp)PtCl ₂] ^{2+ b}	509	1.57 (Ru ^{II/III}) 1.47 (Pt ^{II/IV})	-0.54	-1.11	-1.49	111
[(bpy) ₂ Ru(AB)PtCl ₂] ^{2+ b}	455	1.35 (Ru ^{II/III})	-1.01		-1.52	114
			-1.35		-1.69	
[(bpy) ₂ Ru(BA)PtCl ₂] ^{2+ b}	452	1.48 (Ru ^{II/III})	-0.95		-1.52	114
			-1.30		-1.75	
[(bpy) ₂ Ru(dpq)PtCl ₂] ^{2+ c}	582	1.68 (Ru ^{II/III})	-0.33	-0.87		115
[(bpy) ₂ Ru(dpb)PtCl ₂] ^{2+ c}	630	1.57 (Ru ^{II/III})	-0.16	-0.80		115
[(bpy) ₂ Os(dpq)PtCl ₂] ^{2+ c}	589	1.07 (Os ^{II/III})	-0.35	-0.97		115
[(bpy) ₂ Os(dpb)PtCl ₂] ^{2+ c}	638	1.01 (Os ^{II/III})	-0.27	-0.85		115
[(tpy)RuCl(dpp)PtCl ₂] ^{+ c}	544	1.09 (Ru ^{II/III})	-0.55	-1.09	-1.48	116
[(tpy)RuCl(dpq)PtCl ₂] ^{+ c}	632	1.06 (Ru ^{II/III})	-0.37	-0.96	-1.55	116
[(tpy)RuCl(dpb)PtCl ₂] ^{+ c}	682	1.08 (Ru ^{II/III})	-0.25	-0.86	-1.56	116
[(tpy)Ru(PEt ₂ Ph)(bpm)PtCl ₂] ^{2+ c}	560	1.78 (Pt ^{II/IV}) 1.59 (Ru ^{II/III})	-0.39	-1.09	-1.50	117
[(tpy)Ru(PEt ₂ Ph)(dpp)PtCl ₂] ^{2+ c}	506	1.66 (Pt ^{II/IV}) 1.51 (Ru ^{II/III})	-0.55	-1.19	-1.45	117
[{(bpy) ₂ Ru(dpp)} ₂ Ru(dpp)PtCl ₂] ^{6+ c}	540	1.54 (2Ru ^{II/III})	-0.45	-1.17		103
			-0.65	-1.27		
			-0.76	-1.35		
[(bpy) ₂ Ru(dpop)PtCl ₂] ^{2+ c}	635	1.65 (Pt ^{II/IV}) 1.55 (Ru ^{II/III})	-0.04	-0.81		112
[(bpy) ₂ Ru(Mebpy-CH ₂ -CH ₂ -Mebpy)PtCl ₂] ^{2+ d}	457	1.19 (Ru ^{II/III})	-1.28		-1.39	109

^aIn propylene carbonate using Et_4NClO_4 as the supporting electrolyte.

^bIn acetonitrile.

^cIn acetonitrile with 0.1 M Bu_4NPF_6 as supporting electrolyte. Converted Ag/AgCl to SCE by adding -45 mV to the potential vs. Ag/AgCl.

^dIn propylene carbonate. Converted SSCE to SCE by adding -5 mV to the potential vs. SSCE.

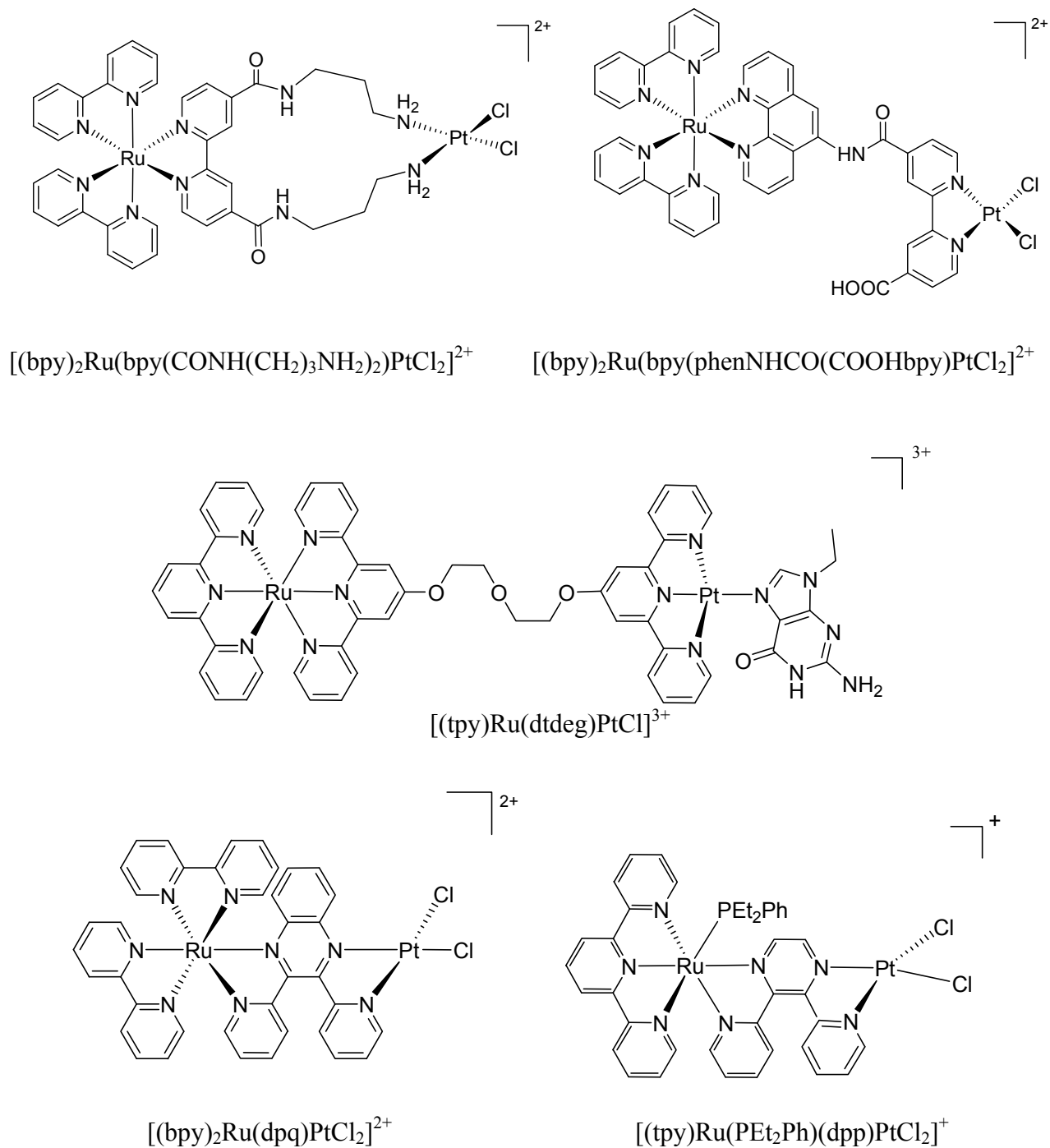


Figure 1.18. Structures of Ru^{II}Pt^{II} bimetallic complexes, $[(tpy)Ru(dtdeg)PtCl]^{3+}$, $[tpyRu(PEt_2Ph)(dpp)PtCl_2]^+$, $[(bpy)_2Ru(dpq)PtCl_2]^{2+}$, $[(bpy)_2Ru(bpy(CONH(CH_2)_3NH_2)_2)PtCl_2]^{2+}$, and $[(bpy)_2Ru(bpy(phenNHCO(COOHbpy))PtCl_2]^{2+}$ (bpy = 2, 2'-bipyridine, dpq = 2,3-bis(2-pyridyl)quinoxaline, dpp = 2,3-bis(2-pyridyl)pyrazine, dtdeg = bis[4'-(2,2':6',2''-terpyridyl)]diethyleneglycolether).

Bragelletti and coworkers have studied the effects of positional isomerization on the redox and spectroscopic properties of the $[(\text{bpy})_2\text{Ru}\{\text{AB}(\text{PtCl}_2)\}](\text{PF}_6)_2$ and $[(\text{PtCl}_2)\text{AB}\{(\text{bpy})_2\text{Ru}\}](\text{PF}_6)_2$ complexes.¹¹⁴ The BL, AB contains two bpy chelating sites: a less sterically hindered site, A, and a more sterically hindered site, B (Figure 1.19). The ruthenium center coordinated to site B is more difficult to oxidize, suggesting greater stability of the $\text{Ru}(d\pi)$ orbital coordinated to this site. A positive shift in the AB-based reduction is also observed, consistent with the $\text{Pt}(\text{II})$ coordination in $\text{Ru}^{\text{II}}\text{Pt}^{\text{II}}$ complex. The ruthenium to AB charge transfer transition energy ($\lambda_{\text{max}}^{\text{abs}} = 455 \text{ nm}$) is found to be lower than the ruthenium to BA charge transfer transition energy ($\lambda_{\text{max}}^{\text{abs}} = 452 \text{ nm}$).

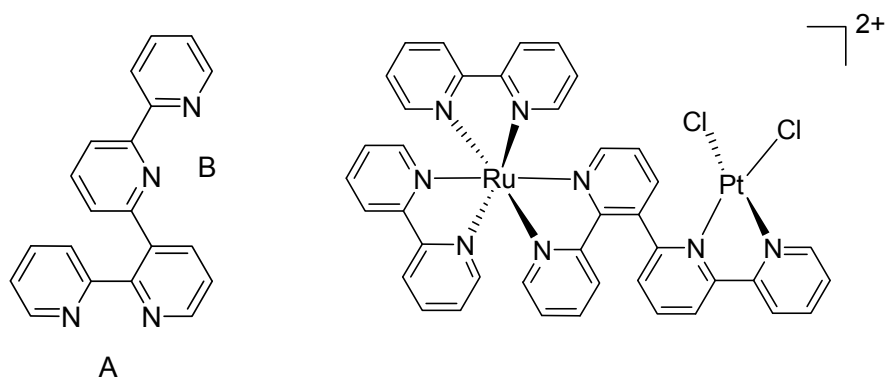


Figure 1.19. Structures of ligand 2,2':3',2'':6'',2'''-quaterpyridine (AB) and $[(\text{bpy})_2\text{Ru}(\text{AB})\text{PtCl}_2](\text{PF}_6)_2$ ($\text{bpy} = 2,2'$ -bipyridine).

Brewer and coworkers have done extensive studies on Ru polyazine-based chromophore coupled cisplatin analogs.¹¹⁵⁻¹²² They have designed a series of complexes of the form $[(\text{bpy})_2\text{M}(\text{BL})\text{PtCl}_2](\text{PF}_6)_2$ ($\text{M} = \text{Ru}$ or Os and $\text{BL} = \text{dpq}$ (2,3-bis(2-pyridyl)quinoxaline) and dpb (2,3-bis(2-pyridyl)benzoquinoxaline)). The spectroscopic properties of these complexes are dominated by the chromophoric metal but also experience the perturbation associated with the electronic influence of the remote Pt site.^{115,119} These complexes display IL $n \rightarrow \pi^*$ and $\pi \rightarrow \pi^*$ transitions in the UV region and $\text{M}(d\pi) \rightarrow \text{bpy}(\pi^*)$ and $\text{M}(d\pi) \rightarrow \text{dpp}(\pi^*)$ MLCT transitions in the visible region. The $\text{M}(d\pi) \rightarrow \text{dpp}(\pi^*)$ transition occur at 582 (dpq) and 630 nm (dpb) for the ruthenium systems and at 598 (dpq) and 638 nm (dpb) for the osmium systems. This slight shift to the lower energy of the $\text{Os}(d\pi) \rightarrow \text{BL}(\pi^*)$ CT compared to the ruthenium systems is the result of a higher energy $d\pi$ orbital on Os. The shift of the $\text{M} \rightarrow \text{dpb}$ CT to lower energy compared to the analogous $\text{M} \rightarrow \text{dpq}$ CT within each series results from the lower energy π^* acceptor orbitals

on the dpb ligand compared to dpq. The electrochemistry of the bimetallic complexes displays Ru^{II/III} or Os^{II/III} based HOMO with Os^{II/III} oxidations occurring at less positive potentials. In both the ruthenium and osmium-based systems, the dpb ligand was easier to oxidize than dpq ligand, suggesting that the dpb ligand acts as a π donor to the metal center thereby making the oxidation process more facile. The BL^{0/-} reduction in the Ru^{II}Pt^{II} bimetallic systems occur at a significantly more positive potential than their monometallic synthons, consistent with the platinum coordination.

The bidentate terminal ligand bpy is replaced by the tridentate ligand tpy in ruthenium polypyridyl complexes to allow for stereochemical control, eliminating the Δ and Λ isomeric mixtures, characteristic of tris-bidentate systems. The metal complexes containing tpy type ligands are less studied in the Ru chemistry as the Ru \rightarrow tpy MLCT excited state in the [Ru(tpy)₂]²⁺ is short lived. Polymetallic complexes incorporating the [Ru^{II}(tpy)(BL)X] (X = monodentate ligand) chromophore exhibit longer excited state lifetimes compare to [Ru(tpy)₂]²⁺ due to the lower energy of BL-based ³MLCT states, which limits thermal population of the deactivating ³LF state. The use of the tpy ligand in place of two bidentate ligands leaves the sixth coordination site which has been substituted to tune the properties of ruthenium chromophores.¹¹⁷ The visible region of the spectrum of the [(tpy)RuCl(BL)PtCl₂](PF₆) (BL = dpp, dpq, dpb), complexes is dominated by the Ru \rightarrow BL MLCT transition at $\lambda_{\text{max}}^{\text{abs}} = 544$ nm (dpp), 632 nm (dpq), and 682 nm (dpb).¹¹⁶ The Ru \rightarrow BL MLCT transitions in the [(tpy)RuCl(BL)PtCl₂](PF₆) complexes are red-shifted from those of their bpy analogues, [(bpy)₂Ru(BL)PtCl₂](PF₆)₂ (BL = dpp, dpq, dpb). This shift is due to the σ donating nature of the Cl compared to the bpy making the ruthenium center more electron rich. The Ru^{II/III} oxidations in the tpy-based systems, [(tpy)RuCl(BL)PtCl₂](PF₆) occur at a more negative potential relative to the bpy systems consistent with the more electron rich ruthenium center. The reductive electrochemistry displays reversible reductions with the BL^{0/-} and BL^{-2/-} followed by tpy-based reduction.

The chloride ligand in the [(tpy)RuCl(BL)PtCl₂](PF₆) is substituted with a ³¹P NMR tag to construct TAG-TL-LA-BL-RM.¹¹⁷ The complexes of the type [(tpy)Ru(PEt₂Ph)(BL)PtCl₂](PF₆)₂ (BL = dpp or bpm) have been synthesized and characterized.

The Ru($d\pi$) \rightarrow BL MLCT ($\lambda_{\max}^{\text{abs}} = 509 \text{ nm}$) transition in the [(tpy)Ru(PEt₂Ph)(BL)PtCl₂](PF₆)₂ is shifted towards higher energy relative to the Ru($d\pi$) \rightarrow BL MLCT ($\lambda_{\max}^{\text{abs}} = 544 \text{ nm}$) transition in [(tpy)RuCl(BL)PtCl₂](PF₆). The stabilization of the Ru($d\pi$) upon substitution of the weak field chloride by the strong field phosphine ligand is consistent with observed blue-shift in the Ru($d\pi$) \rightarrow BL MLCT transition in the [(tpy)Ru(PEt₂Ph)(BL)PtCl₂](PF₆) complex.

Recently, Brewer and coworkers have coupled three ruthenium chromophores to a *cis*-PtCl₂ moiety to form a tetrametallic complex, [{(bpy)₂Ru(dpp)}₂Ru(dpp)PtCl₂](PF₆)₆ (Figure 1.20).¹⁰³ This complex is an efficient light absorber throughout the UV and visible region of the spectrum. The lower energy absorption at ca. 520-540 nm with an extinction coefficient of 35,000 M⁻¹cm⁻¹ is attributed to the Ru($d\pi$) \rightarrow dpp(π^*) MLCT transition.

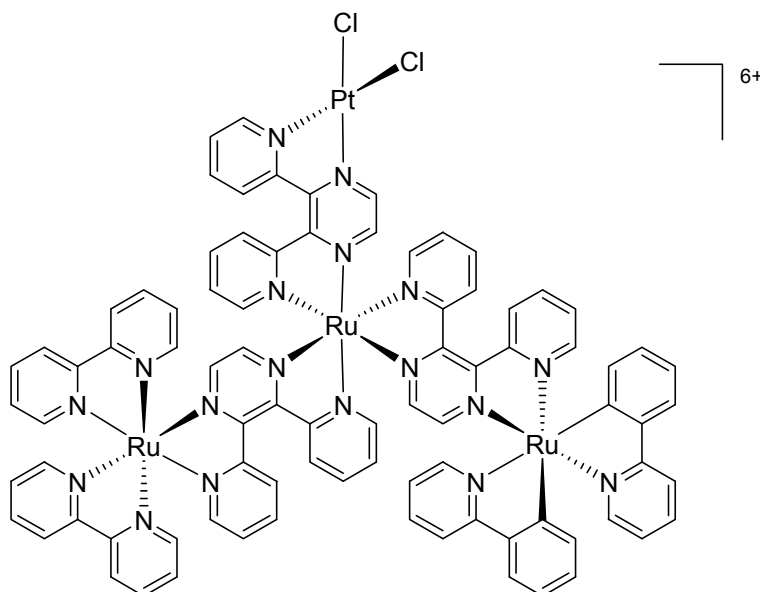


Figure 1.20. Structure of [(bpy)₂Ru(dpp)]₂Ru(dpp)PtCl₂(PF₆)₆ (bpy = 2,2-bipyridine, and dpp = 2,3-bis(2-pyridyl)pyrazine).

1.5.1.2.2. DNA Interaction Studies

Mixed metal supramolecular complexes consisting of ruthenium light absorbers and a cisplatin unit represent an emerging class of bioactive molecules of interest as anti-cancer agents. The enhanced covalent binding of mixed-metal supramolecular complexes compared to cisplatin has been reported.^{119,120} Coupling of the ruthenium-based light absorbers to a cisplatin moiety

not only provides light absorbing properties, but also modulates reactivity with DNA. The DNA cleaving agents can be localized at the site of action by coordinate covalent binding to the DNA through the *cis*-Pt^{II}Cl₂ moiety and may display enhanced photocleavage efficiency by prelocalization of the molecule at the target. Complexes of the general formula, [(bpy)₂M(dp_b)PtCl₂](PF₆) (M = Ru, Os), bind to DNA through a *cis*-Pt^{II}Cl₂ moiety and intercalate into DNA through the dp_b ligand.¹²⁰ The chlorides bound to the Pt(II) center are substitutionally labile, giving these complexes an ability to covalently bind to DNA. The positive charge imparted by the Ru(II) or Os(II) affords greater water solubility as well as increased electrostatic attraction towards DNA compared to cisplatin. For example, the complex, [(bpy)₂M(dp_q)PtCl₂](PF₆), has been shown to display enhanced DNA binding compared to cisplatin.¹²⁰

The DNA binding properties of the heteronuclear bimetallic complexes, [(tpy)RuCl(BL)PtCl₂](PF₆) (BL = dp_p, dp_q, dp_b), have been reported.¹¹⁶ The [(tpy)RuCl(dp_p)PtCl₂](PF₆) complex shows rapid binding to plasmid DNA with significant retardation of migration of the DNA through agarose gel as compared to cisplatin, though no photocleavage is reported. The metal complexes of the type [(tpy)RuCl(BL)PtCl₂](PF₆) (BL = dp_p, dp_q, dp_b) have been shown to avidly bind with DNA with a half time ($\tau_{1/2}$) of 1-2 min and occupy binding sites consistent with the covalent attachment of the *cis*-Pt^{II}Cl₂ to DNA. Brewer and coworkers have reported the Ru^{II}Pt^{II} tetrametallic complex displaying covalent binding by a *cis*-Pt^{II}Cl₂ unit and DNA photocleavage via ruthenium polypyridyl moiety.¹⁰³ The complex can both coordinate to DNA through the *cis*-dichloroplatinum(II) unit and photochemically sensitize molecular oxygen to cleave DNA through the three Ru chromophore units. Herman and coworkers have reported that the mixed metal supramolecular complex consisting of a cisplatin moiety and two imidazole (Im) analog of NAMI subunits, ([ImH][*trans*-RuCl₄(DMSO)-(Im)]), is capable of DNA binding and is potent against both neoplastic and metastatic cancer.¹²³

1.5.1.2.2.1. Gel Electrophoresis as an assay of the DNA-MC Interaction

Gel electrophoresis is a common method to study the structural effects of DNA-MC binding. It is an analytical technique used for the separation of biological macromolecules such

as DNA, RNA, and proteins by applying electric current to a gel matrix. The resulting molecular separation is based on the shape, size, charge, and molecular mass of the macromolecule as well as the pore size of the matrix. The larger molecules move faster compared to the smaller molecules. The most commonly-used gel media for electrophoresis are polyacrylamide and agarose.

A schematic of the use of agarose gel electrophoresis for the separation of nucleic acids is shown in Figure 1.21. In a typical experiment, negatively charged DNA molecules are loaded in the wells of an agarose gel. When voltage is applied, the negatively charged DNA molecules move towards the positively charged electrode. The migration of DNA in an agarose gel depends upon the molecular size and shape of the DNA. Compact forms of DNA migrate faster than relaxed forms.

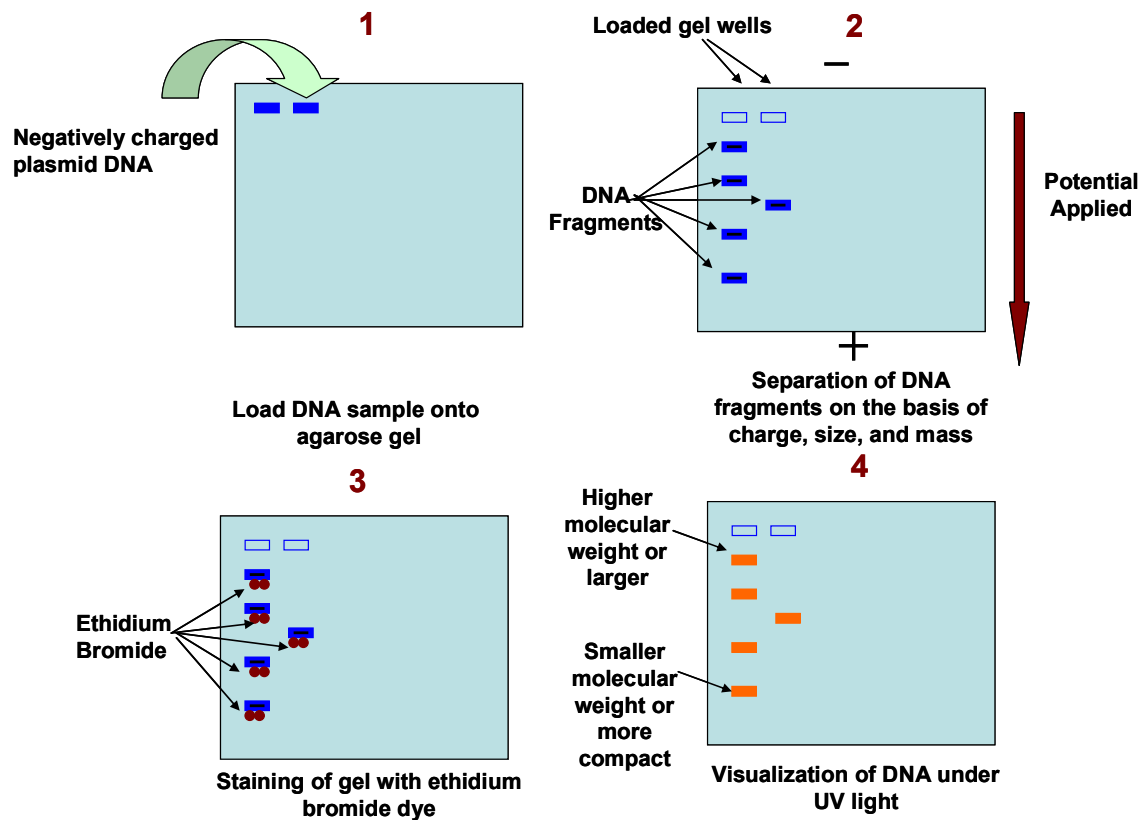


Figure 1.21. Schematic showing agarose gel electrophoresis.

The covalent binding of metal complexes to DNA increases the molecular weight and decreases the net negative charge, and as a result slows down the migration of DNA molecules on an agarose gel (Figure 1.22 gel B). Circular plasmid DNA is ideally suited to probe cleavage events as the plasmid DNA exists in a supercoiled state in its native form and converts to a relaxed form upon single strand cleavage (Figure 1.22 gel C). The supercoiled form being very compact migrates faster than the open circular or relaxed form. The change in supercoiled state of DNA to open circular or relaxed state is indicative of DNA cleavage, Figure 1.22 (gel C).

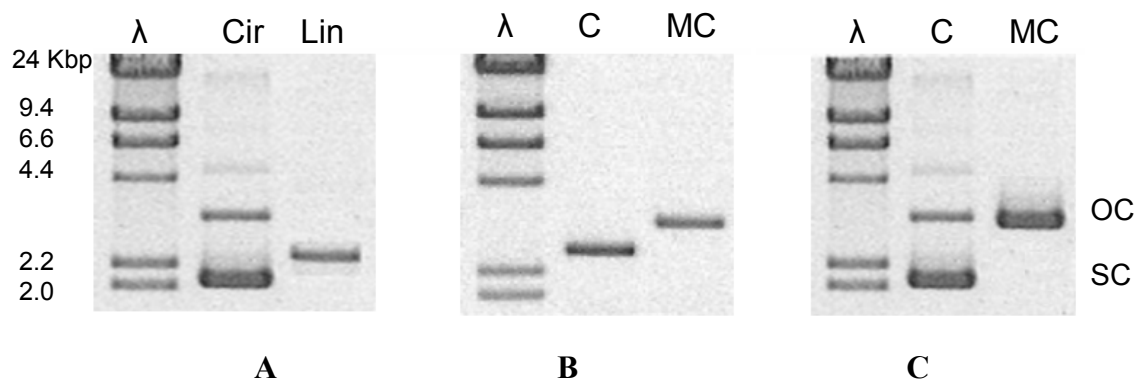


Figure 1.22. A typical 0.8% agarose gel illustrating the electrophoretic migration of three different forms of plasmid DNA (A), covalent binding using linear pUC18 DNA (B), and DNA photocleavage using circular pUC18 DNA (C). The lanes from left to right are as follows: λ is a Lambda DNA/*Hind*III digest molecular weight marker (kbp = 1,000 base-pairs), Cir is circular plasmid DNA containing native supercoiled (SC) and open-circular (OC) plasmid DNA, and Lin is linear plasmid DNA, C is DNA control, MC represent covalent binding of the metal complex to DNA in gel B and DNA photocleavage (conversion of supercoiled (SC) to open circular form (OC)) in gel C.

1.6. Project Description

The goal of this research was to design and develop a new class of supramolecular assemblies by coupling a ruthenium-based light absorber to a cisplatin moiety. The ruthenium chromophores possess interesting photophysical properties and have been shown to photocleave DNA.^{47,64} The cisplatin is a well known anticancer drug and known to covalently bind to DNA. The coupling of the two units together provides photoactivation along with the covalent binding and provides overall positive charge to the complex, thus increasing its water solubility. These supramolecular complexes consist of a terminal ligand (TL), a light absorber (LA), a bridging ligand (BL), and a bioactive site (BAS). The supramolecules were characterized by spectral and

analytical techniques and the redox properties of the complexes were studied by cyclic and square wave voltammetric methods. The impact of component modification on photophysical properties, DNA interaction, and antibacterial properties of chromophore coupled cisplatin analogs was studied. Specific goals of this project include:

1.6.1. Design of Ru^{II}-Pt^{II} Bimetallic Complexes

The coupling of a light absorbing unit to a bioactive site allows for the development of supramolecules with the potential of having multifunctional interactions with DNA and other biomolecules. A series of mixed metal supramolecular complexes that couple a DNA binding *cis*-Pt^{II}Cl₂ center to a ruthenium chromophore via polyazine bridging ligands have been synthesized. Metal complexes of the type TL-LA-BL-BAS (TL = terminal ligand, LA = light absorber, BL = bridging ligand, BAS = bioactive site) were prepared and their basic chemical properties as well as ground and excited state interactions with DNA were studied. These complexes are of the form [(TL)RuCl(dpp)PtCl₂](PF₆) with varying TL (tpy = 2,2':6',2''-terpyridine, MePhtpy = 4'-(4-methylphenyl)-2,2':6',2''-terpyridine, or ^tBu₃tpy = 4,4',4''-tri-tert-butyl-2,2':6',2''-terpyridine) and BL (dpp). The structure of the metal complexes was varied by the addition of different substituents on the terminal tpy ligand (Figure 1.23). The presence of the electron donating groups, MePh and t-butyl, on the terminal ligand enhance the lipophilicity of the molecules and offering potential applications as antibiotic agents. The photophysical, redox, and biological properties of MePhtpy and ^tBu₃tpy complexes were compared with the tpy containing complexes. Building block approach was used to synthesize the bimetallic complexes. The light absorbing unit contains chloride at its sixth coordination site which can be substituted to tune the properties of the ruthenium chromophores.

Understanding the spectroscopic and redox properties of the designed metal complexes can allow exploring their potential applications. Electronic absorption spectroscopy was used to assay the light absorbing properties of the designed molecules. Electrochemistry was used to understand the energetics associated with the frontier orbitals of the Ru^{II}Pt^{II} mixed metal complexes. Emission spectroscopy and excited state life time measurements were used to study the excited state properties of the designed metal complexes.

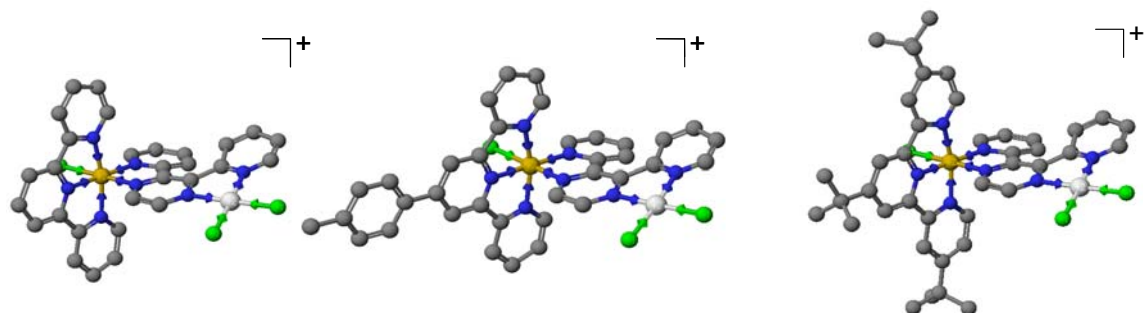


Figure 1.23. Mixed-metal Ru(II)-Pt(II) complexes of the form TL-LA-BL-BAS with hydrogens omitted for clarity (TL = terminal ligand, LA = light absorber, BL = bridging ligand, BAS = bioactive site, tpy = 2,2':6',2''-terpyridine, MePhtpy = 4'-(4-methylphenyl)-2,2':6',2''-terpyridine, tBu₃tpy = 4,4',4''-tri-tert-butyl-2,2':6',2''-terpyridine) and dpp = 2,3-bis(2-pyridyl)pyrazine, ● = carbon, ● = nitrogen, ● = chlorine, ● = ruthenium, ● = platinum)

1.6.2. Understanding the DNA-Metal Complex Interaction

The ability of designed metal complexes to bind and photocleave DNA was investigated. This was probed by agarose gel electrophoresis. The circular and linear forms of plasmid pUC18 DNA were used for these studies. Binding of the metal complexes to DNA changes the molecular mass, charge, and three dimensional shape of DNA, which was observed through gel electrophoresis. DNA photocleavage was observed through gel electrophoresis by conversion of the supercoiled form of DNA into the open circular form. The DNA metal complex binding constant was determined by dialysis of calf thymus DNA in the presence of metal complexes and selective precipitation of DNA using EtOH and NaCl. Coupling of a light absorber to a cisplatin moiety gives a spectroscopic handle to the metal complexes. Electronic absorption spectroscopy was used to determine the concentration of the bound and unbound metal complexes.

1.6.3. To Explore Antibacterial Properties

Development of metal containing antibiotics is an emerging area of research due to the demand for new antibacterial compounds. Bacterial resistance against antibiotics has become an important health issue in recent years. Bacteria replicate very rapidly and a mutation that helps a

microbe survive in the presence of an antibiotic drug quickly becomes predominant within the bacterial population. The metal containing complexes have shown promise as antibacterial agents. The antibacterial properties of the designed bimetallic complexes were investigated. In this project we varied the ligand structure to change the lipophilicity of the molecules in an effort to improve their membrane permeability. Bacterial cell culture studies of a group of complexes with varying molecular frameworks helped us elucidate the structure-activity relationships of this new class of supramolecules.

1.6.4. To Explore Photodynamic Antibacterial Properties

The antibacterial photodynamic activity of the designed molecules was also investigated. Bacteria and fungi are commonly used in preclinical studies for modeling cell growth. The impact of photoactivation on bacterial cell growth in the presence of $[(\text{MePhtpy})\text{RuCl}(\text{dpp})](\text{PF}_6)$ was studied by exposing the bacterial cell culture to 5W, 520 nm cutoff light-emitting diode (LED). The LED was used as an alternative light source in photodynamic therapy (PDT). The LED is an inexpensive light source and is readily available. The use of bacteria as a model system and LED as a light source allows for the development of an inexpensive method to assay the photobactericidal activity of the designed chromophores.

Chapter 2: Materials and Methods

2.1. Materials

2.1.1. Materials, Synthesis

All reagents were used as received unless otherwise noted. The ligands, 2,2':6',2''-terpyridine, 4'-(4-methylphenyl)2,2':6',2''-terpyridine, 4,4',4''-tri-tert-butyl-2,2':6',2''-terpyridine, and 2,3-bis(2-pyridyl)pyrazine were purchased from Aldrich Chemical Co. Ruthenium trichloride hydrate and potassium tetrachloroplatinate were obtained from Alfa Aesar. Adsorption alumina (80-200 mesh) was obtained from Fisher Scientific. The supporting electrolyte for electrochemical studies, tetrabutylammonium hexafluorophosphate (Bu₄NPF₆), was purchased from Fluka.

2.1.2. Materials, DNA Interaction Studies

Molecular biology grade chemicals used for DNA interaction studies were purchased from Fisher and used as received. *cis*-diamminedichloroplatinum(II) (cisplatin) was purchased from Aldrich. Lyophilized calf thymus DNA was obtained from Sigma. Bacteriophage Lambda DNA was obtained from Promega. pUC18 plasmid DNA was obtained from Bayou Biolabs. Electrophoresis grade agarose, tris(hydroxymethyl)-aminomethane (Tris), boric acid, ethidium bromide, and phenolhydroxyquinoline were obtained from Fisher. EcoRI and Hind III restriction endonuclease (including enzyme buffers) were purchased from Promega.

2.1.3. Materials, Cell Culture Studies

Ampicillin sodium salt and Luria Bertani (LB) broth were purchased from Fisher. pBluescript plasmid DNA was purchased from Stratagene. Ultra high-intensity light-emitting diodes (5W LED) were purchased through Future Electronics (Pointe-Claire, Quebec). Tris-HCl ethylene diamminetetraacetic acid, NaCl, and glacial acetic acid were purchased from Sigma.

RNAase, sucrose, sodium dodecylsulphate, and bromophenol blue were purchased from Promega.

2.2. Methods

2.2.1. Column Chromatography

The homoleptic and heteroleptic complexes were purified using alumina column chromatography. Pyrex chromatography columns measuring 180×2.5 cm with a coarse fritted bottom were used for this process. The solvent used was a 1:2 mixture of acetonitrile:toluene. The column was filled with the solvent mixture and 1 cm of washed sea sand. The alumina was filled slowly and continuously into the column while the solvent eluted from the bottom. Sample was dissolved in a minimum amount of the same solvent which was used to prepare the column. The sample was gently loaded into the column with a pipette. Since these complexes were colored, they were easily separated by visual inspection. The product band was collected and concentrated by rotary evaporation.

2.1.2. Mass Spectroscopy

FAB mass spectral analysis was performed by M-Scan Inc., West Chester, PA, on a VG analytical ZAB 2-SE high field mass spectrometer using *m*-nitrobenzylalcohol as a matrix. Electrospray ionization-MS was performed on a Waters (Millford, MA) Micromass quadrupole-time of flight (Q-TOF) mass spectrometer. Ion peak assignments were confirmed using Sheffield Chemputer isotopic peak distribution predictor.¹²⁴

2.1.3. Crystal Structure Determination

A slow evaporation method was used for crystal growth. The compound was dissolved in minimum amount of acetonitrile and the second solvent selected for slow evaporation was toluene. The chosen crystal was centered on the goniometer of an Oxford Diffraction diffractometer equipped with a Sapphire 3 CCD detector and operated with MoK α radiation. The

data collection routine, unit cell refinement, and data processing were carried out using the program, CrysAlisPro. The structure was solved by direct methods and refined using SHELXTL NT.

2.2.4. NMR Spectroscopy

^1H NMR spectra were obtained on a JOEL 500 MHz instrument. All spectra were obtained at room temperature using CD_3CN as the solvent and trimethylsilane as a ^1H chemical shift internal standard. The sample was prepared by dissolving 20 mg of the compound into 500 μL dry CD_3CN and the solution was then transferred to the NMR tube. The ^{195}Pt NMR spectra were obtained on an AVANCE 600 MHz instrument. ^{195}Pt NMR spectra were measured using an observation frequency 128 MHz and a spectra width of 2500 ppm. Typically 100,000 scans were accumulated over a period of about 70 minutes. All spectra were obtained at 37°C using DMSO as the solvent and K_2PtCl_4 as a ^{195}Pt chemical shift standard.

2.2.5. Electrochemistry

Cyclic and square wave voltammetric experiments were performed using a one compartment three-electrode cell, Epsilon potentiostat from Bioanalytical Systems (BAS). The three electrode system consisted of a platinum disc working electrode, platinum wire auxiliary electrode, and Ag/AgCl reference electrode (0.21 V vs. NHE). The reference electrode was calibrated using the $\text{Fe}(\text{C}_5\text{H}_5)_2/\text{Fe}(\text{C}_5\text{H}_5)_2^+$ couple (0.67 V vs. NHE).¹²⁵ The supporting electrolyte used was 0.1 M Bu_4NPF_6 , and measurements were carried out in Burdick and Jackson UV-grade acetonitrile. The platinum electrode was polished between each scan and the solutions were deoxygenated by bubbling with argon for 20 min.

2.2.6. Electronic Absorption Spectroscopy

Electronic absorption spectra were recorded at room temperature using a Hewlett-Packard 8452 diode array spectrophotometer with 2 nm resolution. Solutions were prepared gravimetrically in UV grade acetonitrile and data were collected at room temperature using 1 cm

quartz cuvettes. Extinction coefficient measurements were an average of three separate measurements of independently prepared solutions.

2.2.7. Emission Spectroscopy

Emission spectra were recorded at room temperature in UV-grade acetonitrile using a QuantaMaster Model QM-200-45E fluorimeter from Photon Technology Inc. The system was modified to use a 150 W cooled xenon lamp excitation source, with emission collected at a right angle by a thermoelectrically cooled Hamamatsu 1527 photomultiplier tube operating in photon counting mode. Spectrosil quartz cuvettes with four polished sides, a screw top fitted with a septum cap, and with a 1 cm path length, which were purchased from Starna, were used for all emission experiments. Room temperature measurements were performed in spectrograde acetonitrile and the 77 K measurements were done using 4:1 EtOH/MeOH glass. Solutions were deoxygenated by bubbling with high purity argon for 20 min and followed by sonicating for 20 min prior to the collection of emission spectra. As the response of photomultiplier tube was not equal for the whole detection region, a correction file was used to obtain an accurate signal. The correction file is shown in Figure 2.1.

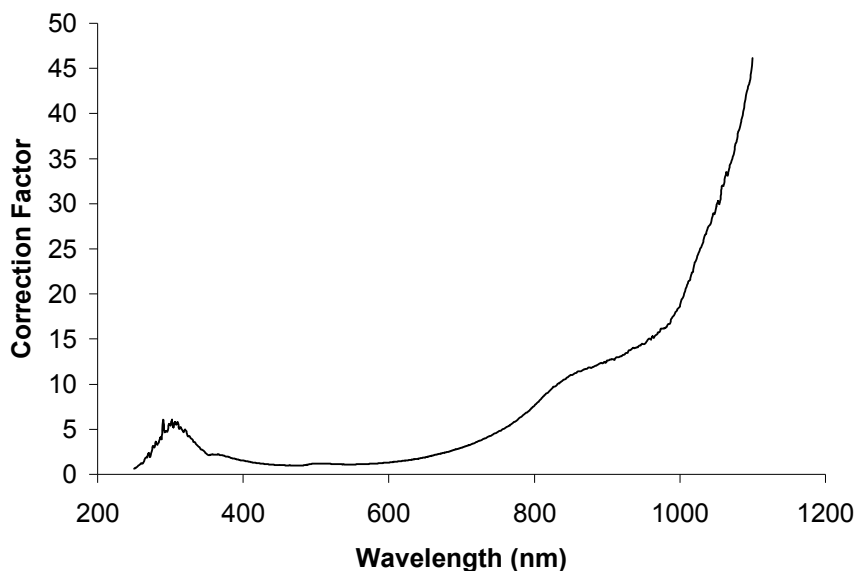


Figure 2.1. Hamamatsu 1527 photomultiplier response profile.

2.2.8. Quantum Yield Measurements

Quantum yield is defined as a ratio of the number of photons emitted to the number of photons absorbed. For quantum yield measurements, solutions were absorbance matched to the reference complex, [Os(bpy)₃](PF₆)₂ ($\Phi_{em} = 0.00462$; $\lambda_{max}^{em} = 746$ nm) in CH₃CN prepared by the method reported by Meyer.¹²⁶ The quantum yield was calculated from the peak area ratio using following equation:

$$\Phi = \Phi_0 \times (A/A_0)(Abs_0/Abs) \quad 2.1$$

where Φ is the quantum yield of the analyte, Φ_0 is the quantum yield of the standard, A is the area under the emission peak of the analyte, and A₀ is the area under the emission peak of the standard, Abs₀ is the absorbance of reference and Abs is the absorbance of analyte.

2.2.9. Excited State Life Time Measurements

Excited state lifetime measurements were performed on a Photon Technology Inc. (PTI), PL 2300 nitrogen laser equipped with a PTI PL 201 continuously tunable dye laser as an excitation source (360-900 nm). This excitation source has an energy output of 240 μ J per pulse and a pulse width of 500 ps. A Coumarin 480 laser dye (1×10^{-3} M in ethanol), purchased from PTI, was used for excitation wavelengths between 470 and 550 nm or a Stillbene 420 laser dye (1×10^{-3} M in ethanol), purchased from Exciton, Inc., for excitation wavelengths between 420 and 469 nm. The decay profile of the emission was collected at right angles to the excitation using Hamamatsu R928 red-sensitive photomultiplier tube. The signal was digitized and displayed on a LeCroy 9361 Dual 300 MHz oscilloscope (2.5 Gs/s) (Figure 2.2). The data were fitted to a single exponential function ($y = a+b[\exp(-kt)]$, where y is the PMT response; a and b are scaling factors, t is time, and k is the rate constant) after discarding the initial points that contain the laser pulse. Once the rate constant, k, was determined, emission lifetime was calculated using the equation: $\tau = 1/k$. Spectrosil quartz cuvettes with a septum screw top purchased from Starna were used for all excited state lifetime experiments. Solutions were

prepared in UV grade acetonitrile and deoxygenated by bubbling argon for 20 min or sonicating for 20 min.

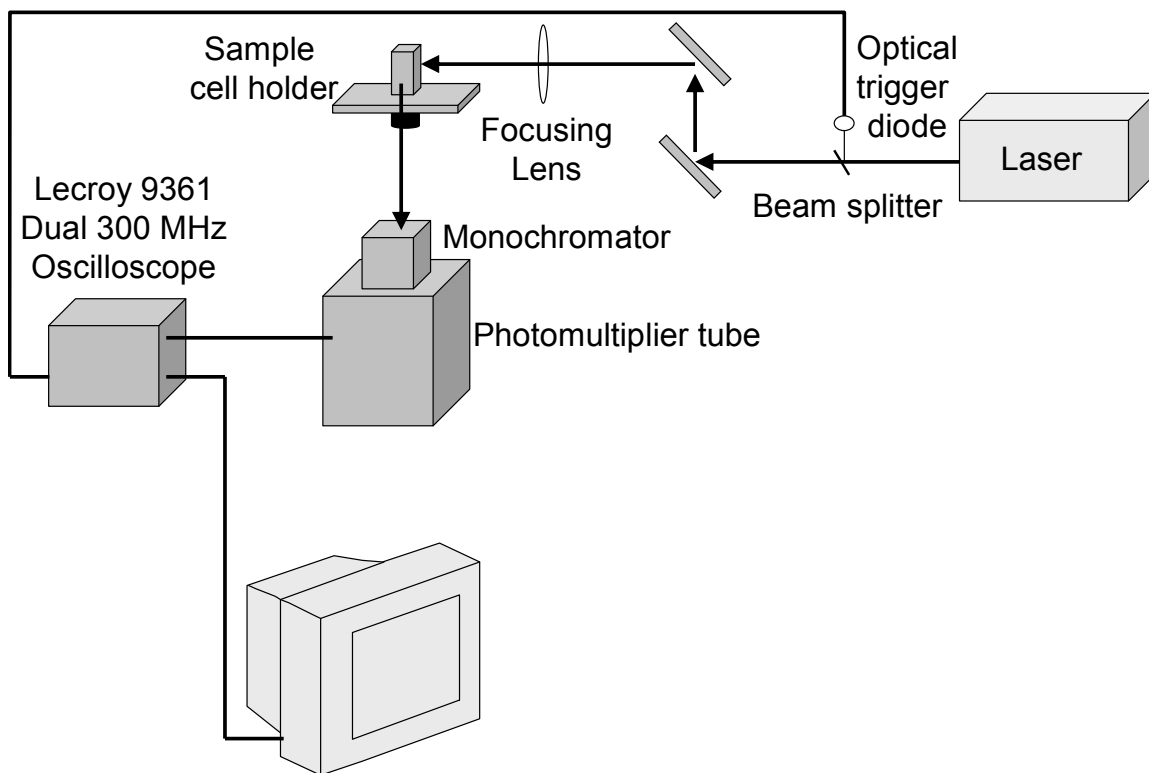


Figure 2.2. Schematic for emission lifetime measurements using a PTI PL 2300 nitrogen laser with a PL 201 dye chamber showing the excitation source, the beam path, beam stop, trigger, sample, emission monochromator, photomultiplier tube, and oscilloscope.

2.2.10. Partition Coefficient Determination

Partition coefficients were determined by a “shake flask” method using pH 7.4 phosphate buffer and *n*-octanol as solvents (Figure 2.3).¹²⁷ Prior to the experiment, the two solvents were mutually saturated with each other by shaking at room temperature. The two solvents were collected after 24 hrs to allow the phases to separate and to achieve saturation state. Each complex was dissolved in the solvent in which it was most soluble, at a concentration of 100 mM. Fifty rotations were performed by hand followed by 1 hr of phase separation time. After mixing and phase separation, each phase was analyzed by electronic absorption spectroscopy to determine the final concentration of the complex. The procedure was repeated to assure that the system had attained equilibrium

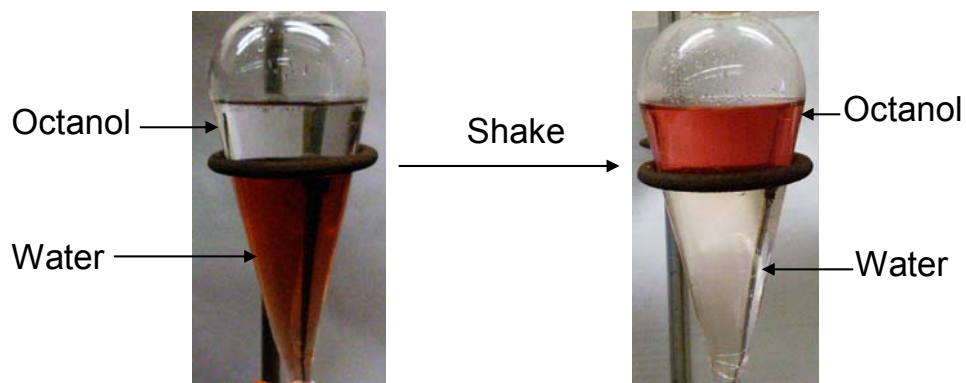


Figure 2.3. Representation of shake flask method to determine partition coefficient of $[(\text{MePhtpy})\text{RuCl}(\text{dpp})]\text{Cl}$ (MePhtpy = 4'-(4-methylphenyl)-2,2':6',2''-terpyridine, and dpp = 2,3-bis(2-pyridyl)pyrazine).

2.2.11. Photolysis with 1000 W Arc Lamp

The photolysis experiments were performed using a 1000 W xenon arc lamp purchased from Oriel. The system includes a water filter to remove radiation from the UV and IR regions of the spectrum. The light was passed through a 450 nm cutoff filter. Analyte solutions were deoxygenated by bubbling with argon for 20 min prior to photolysis. Figure 2.4 shows a schematic of the photolysis apparatus for filtered xenon arc lamp excitation. The temperature of the photolysis sample was regulated by water flow through a thermostated aluminum cell holder. Figure 2.5 shows the photon flux of light from a xenon arc lamp filtered with a 450 nm cutoff filter and Figure 2.6 shows the absorption profile of a 450 nm cutoff filter.

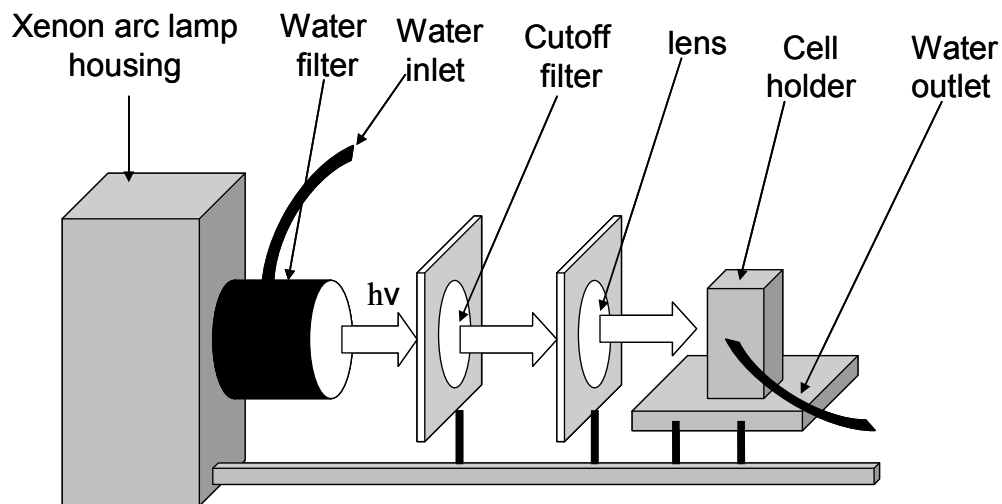


Figure 2.4. Schematic of experimental design for photolysis using 1000 W xenon arc lamp including H₂O UV and IR filter, and cutoff pass filter and focusing lens to focus the collimated light onto the cell and a thermostated cell holder.

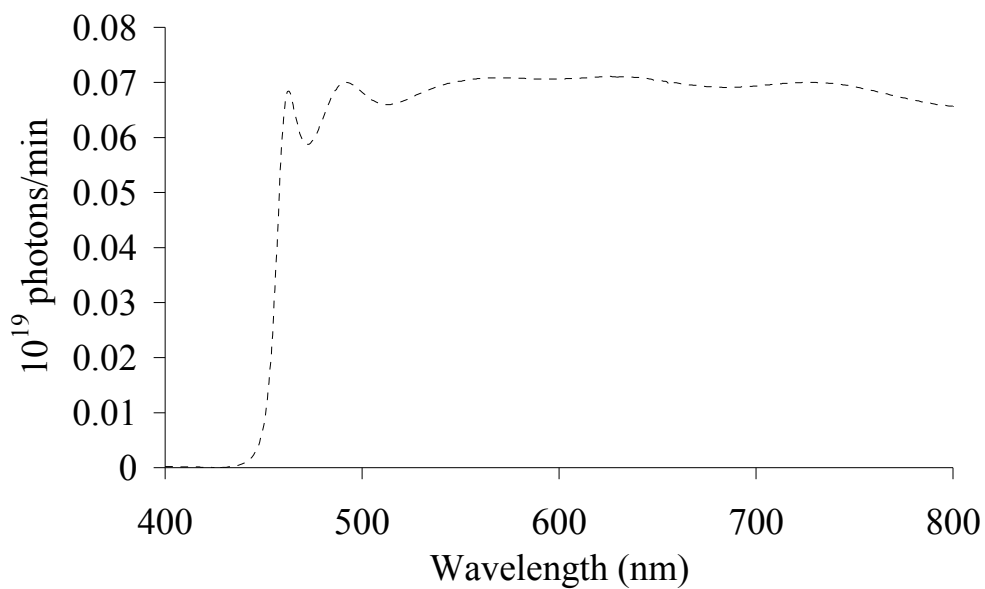


Figure 2.5. Graph showing the photon flux of light from a xenon arc lamp filtered with a 450 nm cutoff filter. Adapted from Ref 128.

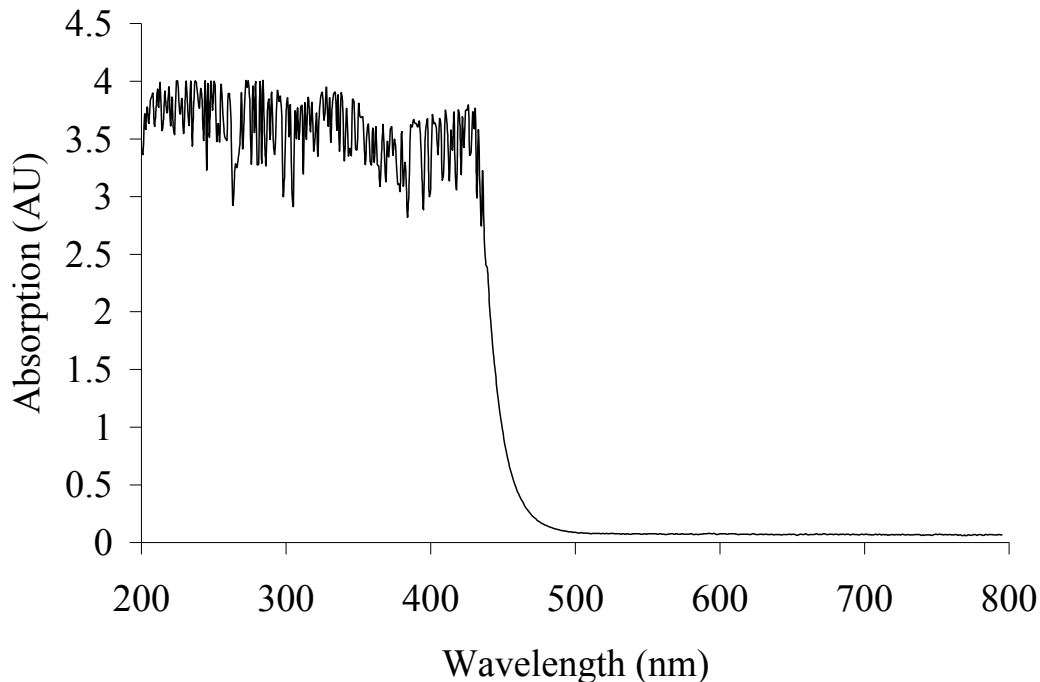


Figure 2.6. Graph showing the absorption profile of a 450 nm cutoff filter.

2.2.12. Agarose Gel Electrophoresis

Agarose gel electrophoresis was used to assay the DNA binding and DNA photocleavage activity of the metal complexes. Agarose gels (0.8% agarose) were prepared by combining 24 mg of electrophoresis grade agarose and 30 mL of H₂O in a 250 mL Erlenmeyer flask. The mixture was heated in a 1,100 W GE (Louisville, KY) microwave at a power setting of 10 for 90 min. While the solution was still hot, water was added into it to make the total mass 24 g. The 5X TB buffer, 6 mL was added in the mixture and the solution was swirled until the temperature reached about 60°C. The molten gel was then poured into the gel mold with 10 well comb in a minigel electrophoresis rig (Owl Separation Systems Inc. (Portsmouth, NH) and allowed to solidify for an hr.

Electrophoresis was performed using an Owl Separation Systems, Inc. (Portsmouth, NH) Model B1A electrophoresis stage at 104 V (~35 mA) for 1.5 hr. Gels were stained with 0.5 µg/mL ethidium bromide for 45 min followed by 45 min destaining in ddH₂O. Gels were

visualized on a Fisher Biotech UV transilluminator. Photographs were taken using an Olympus E-320 digital camera equipped with a Peca Products Inc. ethidium bromide filter.

2.2.12.1. DNA Photocleavage Studies

Photocleavage of pUC18 plasmid DNA was assayed using agarose gel electrophoresis. All samples were prepared according to a standard protocol.¹²⁹ Master solutions of metal complexes were prepared in 1% v/v aqueous DMSO:H₂O. Stock solutions (2 mL) were made to have ~1% DMSO, pUC18 DNA (0.7 μM in base pairs), and 0.14 μM metal complex (to achieve 5:1 BP to MC) in 10 mM NaH₂PO₄ buffer (pH 7). Prior to photolysis half of the stock solution was deoxygenated by bubbling with argon for 20 min. The samples were irradiated with light from a 1000 W xenon arc lamp equipped with a water IR filter and a 450 nm cutoff filter. Small aliquots of the solutions (10 μL containing 0.1 μg of DNA were mixed with 2 μL glycerol based gel loading buffer) and loaded into the wells of a gel.

2.2.12.2. DNA Binding Studies

Linear plasmid pUC18 DNA was used to study the DNA binding properties of the Ru^{II}Pt^{II} bimetallic metal complexes. The plasmid DNA was linearized by overnight incubation at 37°C with *Eco*R1 endonuclease. The concentration of linear plasmid DNA was determined spectrophotometrically. In this study, each metal complex was combined with linearized pUC18 DNA in a range of base pair to metal complex ratios. All reaction mixtures contain 1 μg of linearized plasmid DNA and 10 mM sodium phosphate, pH 7 in a total volume of 100 μL. The solution mixtures were incubated at 37°C for 2 hrs. Small aliquots of the solutions (10 μL containing 0.1 μg of DNA) were mixed with 2 μL glycerol based gel loading buffer and loaded into the wells of a gel.

2.2.12.3. R_f Value Determination

R_f values were determined by comparing the distance traveled by the 2.0 kb band of the molecular weight marker with the distance traveled by each band in the metal-DNA mixture

sample upon the completion of the gel electrophoresis experiment. Measurements were performed manually, measuring from the bottom of the electrophoresis well to the leading edge of the DNA band. The R_f value was calculated using formula

$$R_f = \frac{D_{mc}}{D_{mw}} \quad 2.2$$

where R_f is the retention factor, D_{MC} is the distance traveled by DNA-MC adduct after completion of gel electrophoresis and D_{MW} is the distance traveled by 2.0 kb band of molecular weight marker after completion of gel electrophoresis.

2.2.13. Equilibrium Dialysis

Binding constants for the association of the heteroleptic complexes with DNA were obtained by dialysis of calf thymus DNA in sodium phosphate buffer against metal complexes at room temperature in the dark. The DNA was dialyzed against the metal complexes with continuous agitation for at least 24 hrs. Each sample consisted of 20 mL of metal complex solution in buffer, varying in concentration between 50 and 100 μ M and within dialysis bag, 2 mL of 1 mM calf thymus DNA. Complex concentration was determined by absorbance measurement at the MLCT using electronic absorption spectrophotometer. The equilibrium dialysis data were analyzed using nonlinear least-squares fitting of the data to McGhee–von Hippel equation,¹³⁰

$$\left(\frac{r}{C_f} \right) = \left(\frac{K(0)}{2} \right) (1 - 2lr) \left(\frac{1 - 2lr}{1 - 2(l-1)r} \right)^{l-1} \quad 2.3$$

where r is the ratio of the bound concentration of ruthenium to the concentration of DNA phosphate, C_f is the concentration of free metal complex in solution, $K(0)$ is the intrinsic binding constant, and integer l is the size of a binding site in base pairs.

2.2.14. Electroporation

Electroporation technique was used to introduce the desired plasmid DNA into bacterial cells (*E. coli* JM109). Frozen *E. coli* JM109 cells were obtained from Prof. Brenda S. J. Winkel's lab. Frozen cells were thawed on ice and 20 μL of cells were mixed with 2 μL of pUC18 DNA (10^{-3} $\mu\text{g}/\mu\text{L}$). The gene pulser was set to 25 μF and 1.8 KV and the pulse controller was set to 200 units. The mixture of cells and DNA was transferred to a prechilled cuvette and was tapped on the bench several times to eliminate air bubbles. A pulse was applied at the above settings resulting in a pulse of 12.5 KV/cm with a time constant of 4-5 msec. This was followed by immediate addition of 1 mL of SOC (super optimal broth) medium and the mixture was transferred into a culture tube. The culture tube was incubated at 37°C, 100 rpm for 1 hr. About 100-200 μL of cells were then plated on a LB medium containing 100 $\mu\text{g}/\text{mL}$ ampicillin (LB-amp₁₀₀). Figure 2.7 shows the schematic of an electroporation apparatus.

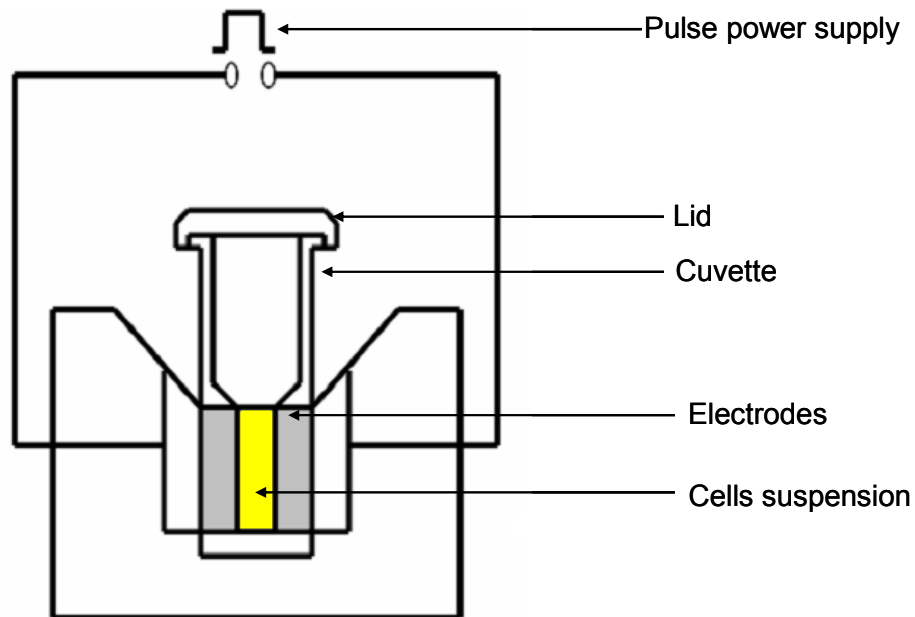


Figure 2.7. Schematic displaying major components of an electroporator.

2.2.15. Cell Culture Studies

Cell culture studies were done using previously published methods.¹³¹ An overnight culture was prepared by inoculating 10 mL LB-amp₁₀₀ broth with a small amount of a frozen stock of *E. coli* cells (stored in 50% glycerol at -80°C). The 2.5 mL of overnight culture was used to inoculate 50 mL LB medium. Fresh solutions of the metal complexes and cisplatin were made in 500 µL DMSO. Cultures (50 mL) were grown in 125 mL Erlenmeyer flasks at 37°C with shaking (180 rpm). Each culture was inoculated with a 500 µL solution of metal complex in DMSO to give desired final concentrations. One culture was inoculated with DMSO but no cisplatin or metal complex and served as a control. Every 30 min three 200 µL samples from each culture were diluted with 1800 µL of LB media and the optical density at 650 nm (OD₆₅₀) was recorded using a Beckman D U 7500 spectrophotometer, in order to monitor cell growth.

2.2.16. DNA Extraction

A Quagen plasmid miniprep kit was used to purify up to 20 µg high copy plasmid DNA from 1-5 mL overnight *E. coli* culture in LB medium. The cell pellet was collected by centrifugation of 5 mL bacterial cell culture for 10 min at 13,000 rpm using a table top microcentrifuge and discarding the supernatant. The bacterial cell pellets were resuspended in 250 µL of P1 buffer (50 mM tris-Cl, 10 mM EDTA, 100 µg/mL RNAase A) and transferred to a microcentrifuge tube. Then 250 µL of P2 buffer (200 mM NaOH, 1% SDS v/v) was added and the sample was mixed thoroughly. Next, 350 µL N-3 buffer (3.0 M KOAc, pH 5.5) was added and the sample was mixed immediately and thoroughly. The mixture was centrifuged for 10 min at 13,000 rpm using a table top microcentrifuge. The supernatant was applied to a QIAprep spin column by decanting. The column was spin for 30-60 sec and the flow-through was discarded. The column was washed by adding 0.75 mL PE buffer (75% NaOH, 25 mM NaCl, and 5 mM tris-Cl, pH 7.5) and spinning for 30-60 sec. The flow-through was discarded and the column was spin for 1 min to remove wash buffer. The plasmid was eluted from the QIAprep column into a clean 1.5 mL centrifuge tube by addition of 100 µL water and spinning for 1 min at a maximum speed using a microcentrifuge.

2.2.17. Cell Lysis in the Wells of Electrophoresis Gel

The cell lysis in the wells of electrophoresis gel was performed using a protocol from Epicenter Biotechnologies.¹³² This technique was used to understand the mechanism of cell growth inhibition by designed metal complexes. Cells (4 mL) were mixed with 5 μ L of protoplast buffer (Table 2.1) in a microcentrifuge tube and incubated for 15 min. A sample of lysis solution, 4-8 μ L, (Table 2.2) was added into the wells of a 0.8 % agarose gel in 5X TB buffer. The mixture was allowed to mix for 15 min. Gel electrophoresis was performed using an Owl Separation Systems, Inc. (Portsmouth, NH) Model B1A electrophoresis stage at 104 V (~35 mA) for 1.5 hrs. Gels were stained with 0.5 μ g/mL ethidium bromide for 45 min followed by 45 min destaining in ddH₂O. Gels were visualized and photographed as described in section 2.2.12.

Table 2.1. Protocol for Protoplast Buffer

Protoplast Buffer	Volume	Concentration
2.0 M Tris-HCl, pH 7.5	0.375 mL	30 mmol
0.5 M EDTA	0.25 mL	5 mmol
5.0 M NaCl	0.25 mL	50 mmol
Sucrose	6.25 g	25%
2 mg/mL RNAase A	0.31 mL	25 mg/mL
Ready-Lyse Lysozyme	-	2 x 10 ⁶ U
Water	to 25 mL	-

Table 2.2. Protocol for Lysis Solution

Lysis Solution	Volume
50X TAE Buffer	0.2 mL
10% SDS	2.0 mL
Sucrose	0.5 g
Bromophenol Blue	15 mg
Water to 10 mL	

2.2.18. Construction of LED Setup for Cell Culture Studies

A Luxeon 5 W LED with a maximum forward current rating of 700 mA was used as a light source to investigate the photodynamic antibacterial activity of the designed chromophores. The LED setup was constructed with the help of Mr. Jared Brown. The LED used has a maximum output at 520 nm with 35 nm FWHM (full width half maximum) and typical luminous flux, 4.18×10^{17} photons/sec. The LED was powered with a 700 mA constant current power supply. A schematic of the LED array used is shown in Figure 2.8. The LED was mounted on the heat sink using thermally conductive heat sink cement. The reflector was used to focus the light onto the sample. A polycarbonate sheet was mounted in front of the reflector to prevent any condensation from the growth media on the LED. The LED attached to the heat sink was mounted to the 1/8 inch thick aluminum base. The aluminum base was mounted to a 1 inch long polyethylene round tube with outer diameter 2.520" and inner diameter 1.440" using long screws. Holes were drilled on the polyethylene tube to allow for constant air supply. The whole assembly was then placed on a 250 mL Erlenmeyer flask containing LB medium (1.2 cm pathlength). The Erlenmeyer flask was placed in a shaker (180 rpm) to provide equal light flux to all the cells. At the beginning of an experiment, the optical density of the LB medium containing cells was 0.0002.

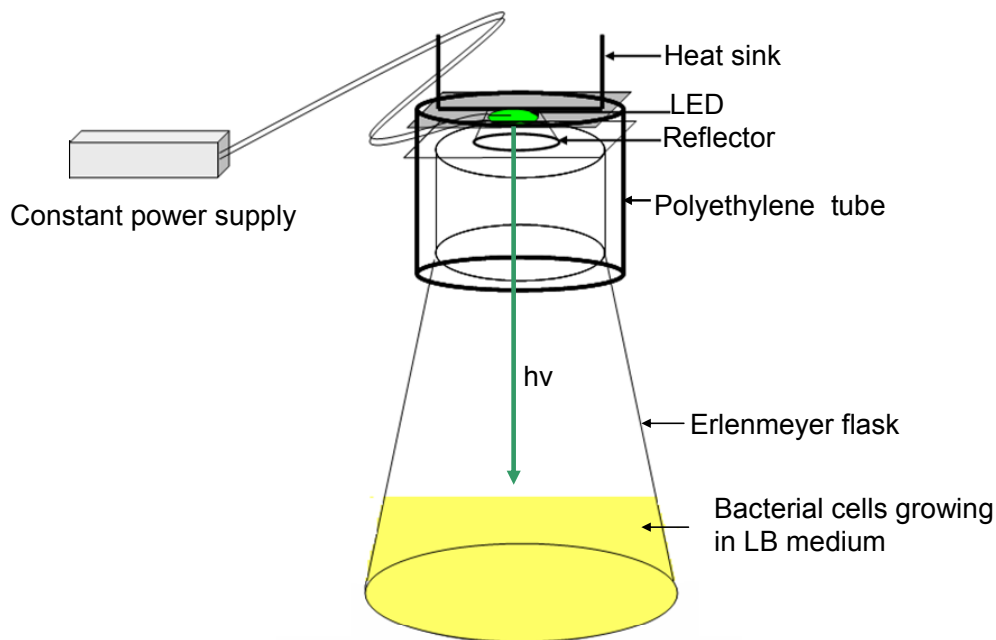


Figure 2.8. Schematic of LED setup used for photoantibacterial studies.

2.2.19. Determination of Spectral Output of Designed LED

The spectral output of the LED used in the present work was determined using irradiance measurements and physical actinometry. The relative irradiance of LED was measured using an Ocean Optics diode array spectrophotometer with 0.2 nm resolution and detection range from 178 to 890 nm. The LED was powered in a dark room and relative irradiance was measured by aligning the fiber optic probe of the spectrophotometer to the LED. The distance between the LED and the fiber optic probe was such that the relative peak irradiance was the maximum observable value. Figure 2.9 shows the instrument setup to determine spectral output of designed LED and The LED spectral output is shown in Figure 2.10.

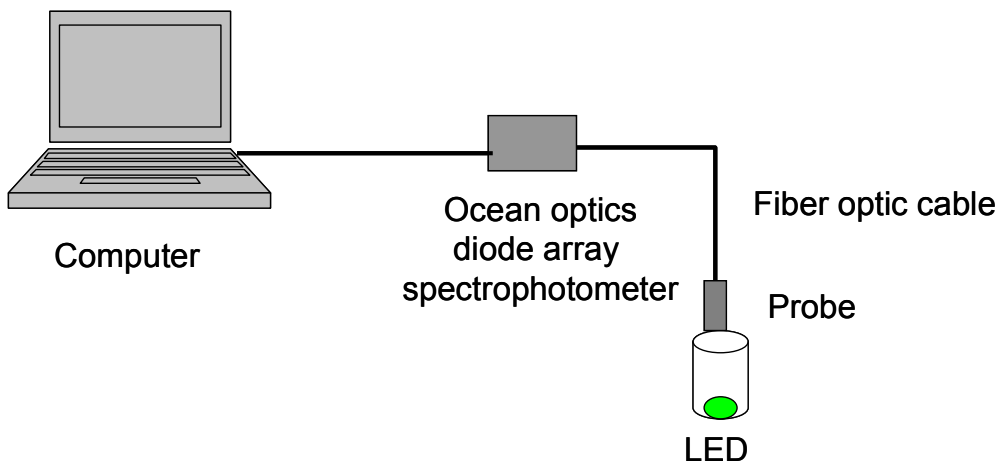


Figure 2.9. Spectral out measurement of designed LED. The fiber optic sensor from ocean optics diode array spectrophotometer oriented towards LED.

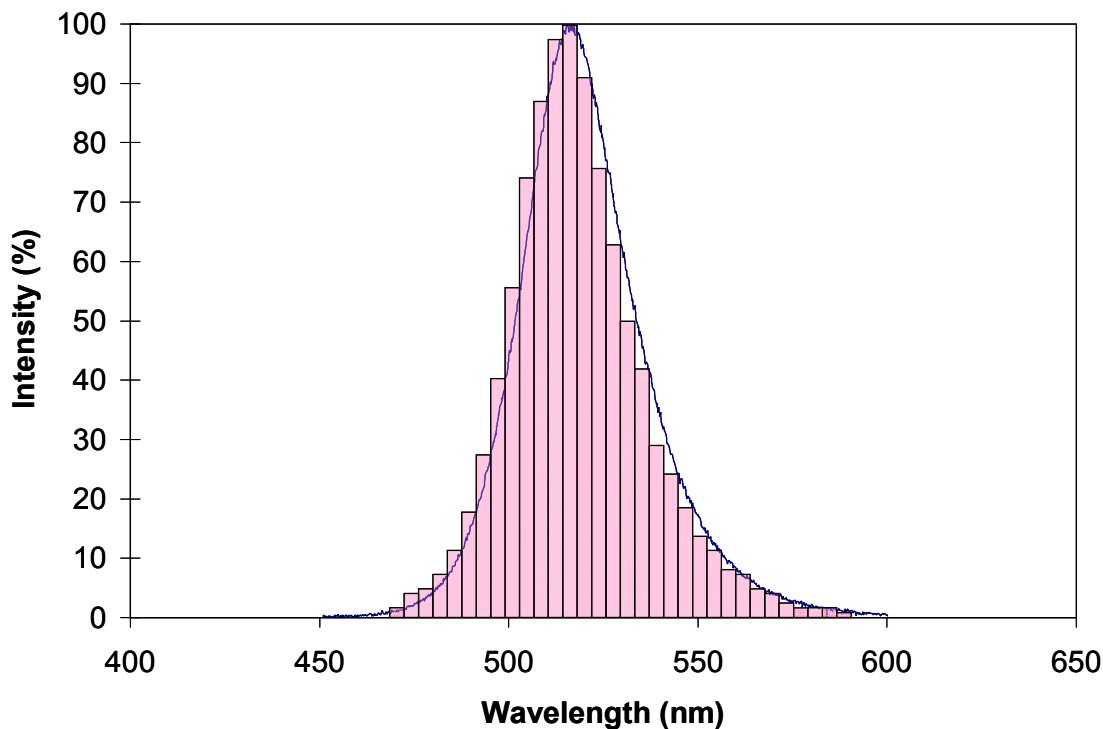


Figure 2.10. LED spectral output with rectangles overlaid representing the right endpoint approximation determining area. The step size used was 0.2 nm.

2.2.19.1. Physical Actinometry

A glossary of terms used in photochemistry defines an actinometer as a chemical system or a physical device by which the number of photons in a beam absorbed into the defined space of a chemical reactor can be determined integrally or per time.¹³³ In physical actinometry a physical device such as a photomultiplier tube converts the energy or number of the incident photons into quantifiable electrical signal. An electrical signal can then be calibrated to provide photon flux. In this study a calorimeter was used as a physical actinometer.

Calorimetric measurements were made using a Scientech, Inc. (Boulder, CO) mentor MA10 with a MC2501 calorimeter head unit. The measurement was done by aligning the calorimeter head unit over the LED. The calorimeter head consists of a black disk absorber coupled to a thermopile sensor. The black disk absorber absorbs radiant energy and transfers it to a thermopile. A thermopile is an electronic device that converts thermal energy into electrical

energy. Thermopile detectors consist of a series array of miniature thermocouple junctions connected in series as differential pairs. These differential pairs make up the cold junctions and the hot junctions. The cold and hot junctions are connected by alternating n-type and p-type semiconductors. A voltage is produced, proportional to the temperature gradient between the hot and cold junctions.

Since the LED used in the current studies is not monochromatic, integration of the energy of the total emitted light was used to determine photon flux from a calorimetric measurement. The total area of the spectral output was calculated first using the right end point approximation (Figure 2.10). In calculating total area, I is the intensity in counts, λ is the wavelength given in nm and n refers to the individual measurements

$$\text{Total Area} = \sum [I_{n+1}(\lambda_{n+1} - \lambda_n)] = 1.36 \times 10^4 \text{ counts}\cdot\text{nm} \quad 2.4$$

The spectral output was normalized to 1, allowing each rectangle to represent a normalized fraction per wavelength f_n , of the total area, equation 2.4. The fractional energy, J_n , was then calculated by multiplying the normalized fraction per wavelength, f_n , by the energy per wavelength using equation 2.5. The total energy contained in spectral output, J_{total} was then calculated using equation 2.6.

$$f_n = \left[\frac{I_{n+1}(\lambda_{n+1} - \lambda_n)}{\sum [I_{n+1}(\lambda_{n+1} - \lambda_n)]} \right] \quad 2.5$$

$$J_n = hc \frac{f_n}{\lambda_n} \quad 2.6$$

The photon flux, q_p , can be determined by dividing the measured light energy J_{meas} by the total energy from the LED emission profile, J_{total} , equation 2.7.

$$J_{total} = hc \sum \frac{f_n}{\lambda_n} = 3.82 \times 10^{-19} \text{ J} \quad 2.7$$

$$q_p = \frac{J_{meas}}{J_{total}} = \frac{0.097}{3.82 \times 10^{-19}} = 2.54 \times 10^{17} \text{ photons/sec} \quad 2.8$$

2.2.20. Synthesis and Purification of Metal Complexes

2.2.20.1. [(tpy)RuCl(dpp)](PF₆)

The complex, [(tpy)RuCl(dpp)](PF₆), was prepared by a modification of a previously published method.¹³⁴ The ligand 2,3-bis(2-pyridyl)pyrazine (0.35 g, 1.5 mmol), [(tpy)RuCl₃] (0.46 g, 1.0 mmol), and LiCl (0.064g, 1.5 mmol) were added in a 50 mL of 2:1 ethanol:water mixture and heated at reflux for 4 hrs under argon atmosphere. At the start of the reaction, triethylamine (4 mL) was added. The reaction mixture was allowed to cool at room temperature and precipitated by addition to an aqueous saturated solution of KPF₆ (50 mL). The maroon colored precipitate was collected by vacuum filtration and then purified by alumina column chromatography, using 2:1 toluene:acetonitrile as a solvent. The maroon colored crude complex separated into three major components. Colorless unreacted dpp ligand eluted first, followed by a purple band (the desired product) and then a brown band. The purple band was collected and the volatiles were removed under vacuum. The residue was dissolved in a minimum amount of acetonitrile and flash precipitated in diethyl ether. The product was separated by vacuum filtration and dried under vacuum. Typical yield: 88% (0.67 g, 0.88 mmol). FAB-MS (nitrobenzylalcohol matrix) (m/z; relative abundance): [M-PF₆]⁺ (620,100) (Figure A-10, Appendix).

2.2.20.2. [(MePhtpy)RuCl(dpp)](PF₆)

The complex, [(MePhtpy)RuCl(dpp)](PF₆), was prepared by a modification of the method used to prepare the tpy analog, [(tpy)RuCl(dpp)](PF₆).¹³⁴ The ligand 2,3-bis(2-pyridyl)pyrazine (0.35 g, 1.5 mmol), [(MePhtpy)RuCl₃] (0.54 g, 1.0 mmol), and LiCl (0.064g, 1.5 mmol) were added in 50 mL of 2:1 ethanol:water mixture and heated at reflux for 4 hrs under argon atmosphere. At the start of the reaction, triethylamine (4 mL) was added. The reaction

mixture was allowed to cool at room temperature and precipitated by addition to an aqueous saturated solution of KPF_6 (50 mL). The maroon colored precipitate was collected by vacuum filtration and then purified by alumina column chromatography, using 2:1 toluene:acetonitrile as a solvent. The maroon colored crude complex separated into three major components. Colorless unreacted dpp ligand eluted first, followed by a purple band (the desired product) and then a brown band. The purple band was collected and the volatiles were removed under vacuum. The residue was dissolved in a minimum amount of acetonitrile and flash precipitated in diethyl ether. The product was separated by vacuum filtration and dried under vacuum. Typical yield: 75% (0.63 g, 0.75 mmol). FAB-MS (nitrobenzylalcohol matrix) (m/z; relative abundance): $[\text{M-PF}_6]^+$ (694,100) (Figure A-6, Appendix). The ^1H NMR spectrum of the molecule in CD_3CN is shown in Figure A-5, Appendix.

2.2.20.3. [*t*-But₃tpy]RuCl(dpp)](PF₆)

The complex, [*t*-But₃tpy]RuCl(dpp)](PF₆), was prepared by a modification of the method used to prepare the tpy analog, [(tpy)RuCl(dpp)](PF₆).¹³⁴ The ligand 2,3-bis(2-pyridyl)pyrazine (0.35 g, 1.5 mmol [*t*-But₃tpy]RuCl₃) (0.62 g, 1.0 mmol), and LiCl (0.064g, 1.5 mmol) were added in 50 mL of 2:1 ethanol:water mixture and heated at reflux for 4 hrs under argon atmosphere. The reaction mixture was allowed to cool at room temperature and precipitated by addition to an aqueous saturated solution of KPF_6 (50 mL). The maroon colored precipitate was collected by vacuum filtration and then purified by alumina column chromatography, using 2:1 toluene:acetonitrile as a solvent. The maroon colored crude complex separated into three major components. Colorless unreacted dpp ligand eluted first, followed by a purple band (the desired product) and then a brown band. The purple band was collected and the volatiles were removed under vacuum. The residue was dissolved in a minimum amount of acetonitrile and flash precipitated in diethyl ether. The product was separated by vacuum filtration and dried under vacuum. Typical yield: 65% (0.60 g, 0.65 mmol). FAB-MS (nitrobenzylalcohol matrix) (m/z; relative abundance): $[\text{M-PF}_6]^+$ (788,100) (Figure A-8, Appendix). The ^1H NMR spectrum of the molecule in CD_3CN is shown in Figure A-4, Appendix.

2.2.20.4. $[Ru(tpy)_2](PF_6)_2$

The complex, $[Ru(tpy)_2](PF_6)_2$, was prepared by a modification of a previously published procedure.⁵⁸ The ligand tpy (0.668 g, 2.86 mmol) and $RuCl_3 \cdot xH_2O$ (0.250 g, 0.957 mmol) were added to 150 mL of 95% EtOH and heated at reflux for 4 hrs under argon atmosphere. The reaction mixture was then added to 150 mL of a saturated, aqueous solution of KPF_6 to induce precipitation and the product removed by vacuum filtration. Purification was achieved by column chromatography using adsorption alumina and a 3:2 toluene/ acetonitrile eluent. The desired orange product was the second band to elute after a pale colored band of excess tpy. This band was collected and evaporated to dryness under vacuum. The product was then chromatographed again to ensure high purity. Typical yield: 72% (0.589 g, 0.690 mmol). The 1H NMR spectrum of the molecule in CD_3CN is shown in Figure A-1, Appendix.

2.2.20.5. $[Ru(MePhtpy)_2](PF_6)_2$

The complex, $[Ru(MePhtpy)_2](PF_6)_2$, was prepared by a modification of a previously published procedure.⁵⁴ The ligand MePhtpy (0.923 g, 2.86 mmol) and $RuCl_3 \cdot xH_2O$ (0.250 g, 0.957 mmol) were added to 150 mL of 95% EtOH and heated at reflux for 4 hrs under argon atmosphere. The reaction mixture was then added to 150 mL of a saturated, aqueous solution of KPF_6 to induce precipitation and the product removed by vacuum filtration. Purification was achieved by column chromatography using adsorption alumina and a 3:2 toluene/ acetonitrile eluent. The desired orange product was the second band to elute after a pale colored band of excess tpy. This band was collected and evaporated to dryness under vacuum. The product was then chromatographed again to ensure high purity. Typical yield: 69% (0.685g, 0.660 mmol). The 1H NMR spectrum of the molecule in CD_3CN is shown in Figure A-2, Appendix.

2.2.20.6. $[Ru(^tBu_3tpy)_2](PF_6)_2$

This complex, $[Ru(^tBu_3tpy)_2](PF_6)_2$, was prepared by a modification of a previously published procedure.¹³⁵ The ligand tBu_3tpy (1.14 g, 2.86 mmol) and $RuCl_3 \cdot xH_2O$ (0.250 g, 0.957 mmol) were added to 150 mL of 95% EtOH and heated at reflux for 4 hrs under argon

atmosphere. The reaction mixture was added to 150 mL of a saturated, aqueous solution of KPF_6 to induce precipitation and the product removed by vacuum filtration. Purification was achieved by column chromatography using adsorption alumina and a 3:2 toluene/ acetonitrile eluent. The desired orange product was the second band to elute after a pale colored band of excess ${}^t\text{Bu}_3\text{tpy}$. This band was collected and evaporated to dryness under vacuum. The product was then chromatographed again to ensure high purity. Typical yield: 64% (0.731 g, 0.612 mmol). The ${}^1\text{H}$ NMR spectrum of the molecule in CD_3CN is shown in Figure A-3, Appendix.

2.2.20.7. $[\text{Pt}(\text{DMSO})_2\text{Cl}_2]$

The complex, $[\text{Pt}(\text{DMSO})_2\text{Cl}_2]$, was synthesized according to a modification of a previously published method.¹¹³ K_2PtCl_4 (2.23 g, 5.14 mmol) and DMSO (1.62 mL, 21.0 mmol) were dissolved in 25 mL of water. The mixture was allowed to incubate at room temperature overnight, after which yellow crystals formed. These crystals were collected by vacuum filtration, and washed three times with 90 mL portion of H_2O , ethanol, and diethylether. Typical yield: 93.5 % (2.038 g, 4.81 mmol).

Synthesis Ru-Pt Bimetallic Complexes

2.2.20.8. $[(\text{tpy})\text{RuCl}(\text{dpp})\text{PtCl}_2](\text{PF}_6)$

The complex, $[(\text{tpy})\text{RuCl}(\text{dpp})\text{PtCl}_2](\text{PF}_6)$, was prepared by heating at reflux in 10 mL of 95% ethanol $[(\text{tpy})\text{RuCl}(\text{dpp})](\text{PF}_6)$ (300 mg, 0.40 mmol) and $[\text{PtCl}_2(\text{DMSO})_2]$ (250 mg, 0.60 mmol). During the 1 hr reaction time, the solution changed from red to purple. After cooling to room temperature the reaction mixture was filtered through a fine porosity frit to remove unreacted $[\text{PtCl}_2(\text{DMSO})_2]$. The purple filtrate was then precipitated in KPF_6 and was separated by vacuum filtration on a fine-porosity fritted funnel. The product was washed with two 10 mL portions of ethanol and 10 mL of chloroform. The solid was redissolved in ca. 30 mL of CH_3CN and filtered, and the volume was reduced to 15 mL under vacuum. The product was then flash precipitated by addition to 60 mL of stirring diethyl ether. Typical yield: 90% (364 mg, 0.360 mmol). (m/z; relative abundance): $[\text{M}-\text{PF}_6]^+$ (870,100) (Figure A-12, Appendix).

2.2.20.9. [(MePhtpy)RuCl(dpp)PtCl₂](PF₆)

The complex, [(MePhtpy)RuCl(dpp)PtCl₂](PF₆), was prepared by heating at reflux in 10 mL of 95% ethanol [(MePhtpy)RuCl(dpp)](PF₆) (330 mg, 0.40 mmol) and [PtCl₂(DMSO)₂] (250 mg, 0.60 mmol). During the 1 hr reaction time, the solution changed from red to purple. After cooling to room temperature the reaction mixture was filtered through a fine porosity frit to remove unreacted [PtCl₂(DMSO)₂]. The purple filtrate was then precipitated in KPF₆ and was separated by vacuum filtration on a fine-porosity fritted funnel. The product was washed with two 10 mL portions of ethanol and 10 mL of chloroform. The solid was redissolved in ca. 30 mL of CH₃CN and filtered, and the volume was reduced to 15 mL under vacuum. The product was then flash precipitated by addition to 60 mL of stirring diethyl ether. Typical yield: 84% (397 mg, 0.3336 mmol). (m/z; relative abundance): [M-PF₆]⁺ (960,100) (Figure A-13, Appendix).

2.2.20.10. [(^tBu₃tpy)RuCl(dpp)PtCl₂](PF₆)

The complex, [(^tBu₃tpy)RuCl(dpp)PtCl₂](PF₆), was prepared by heating at reflux in 10 mL of 95% ethanol [(^tBu₃tpy)RuCl(dpp)](PF₆) (360mg, 0.40 mmol) and [PtCl₂(DMSO)₂] (250 mg, 0.60 mmol). During the 1 hr reaction time, the solution changed from red to purple. After cooling to room temperature the reaction mixture was filtered through a fine porosity frit to remove unreacted [PtCl₂(DMSO)₂]. The purple filtrate was then precipitated in KPF₆ and was separated by vacuum filtration on a fine-porosity fritted funnel. The product was washed with two 10 mL portions of ethanol and 10 mL of chloroform. The solid was redissolved in ca. 30 mL of CH₃CN and filtered, and the volume was reduced to 15 mL under vacuum. The product was then flash precipitated by addition to 60 mL of stirring diethyl ether. Typical yield: 72% (340 mg, 0.29 mmol). (m/z; relative abundance): [M-PF₆]⁺ (1038,100) (Figure A-15, Appendix).

Chapter 3: Results and Discussion

3.1. Synthesis

A series of Ru^{II}Pt^{II} bimetallic complexes was prepared using a building block approach. The building block method provides a means to understand the nature of each component and sequential reactions impart the desired molecular structure in high purity. This method allows for the construction of molecular architecture by first binding the terminal ligand, tpy, to the ruthenium metal center followed by the attachment of the bridging ligand, dpp. The Pt^{II} coordination is achieved in the final step. A building block approach for the synthesis of [(^tBu₃tpy)RuCl(dpp)PtCl₂](PF₆) is given in Figure 3.1.

The complex, [(TL)RuCl₃], was prepared with ~ 85% yield as described by Meyer by heating at reflux in ethanol, RuCl₃.xH₂O and TL ligand for 3 hrs.¹³⁶ Longer reaction times may lead to the formation of [Ru(TL)₂]Cl₂. The undesirable impurity, [Ru(TL)₂]Cl₂ can be removed by washing with copious amount of water. The homoleptic complexes, [Ru(TL)₂](PF₆)₂, (TL = tpy, MePhtpy, and ^tBu₃tpy) were synthesized by making slight modifications to previously published methods.¹³⁴ The ¹H NMR spectra of these complexes are shown in the Appendix, Figures A-1, A-2, and A-3.

The monometallic precursors, [(TL)RuCl(dpp)](PF₆) (TL = tpy, MePhtpy, and ^tBu₃tpy), were prepared by heating at reflux in EtOH:H₂O (2:1) mixture, [(TL)RuCl₃] and bridging ligand (dpp) for 5 hrs with 88, 75, and 65% yield for TL = tpy, MePhtpy, and ^tBu₃tpy, respectively. It was observed that addition of dpp dissolved in EtOH:H₂O (2:1) mixture to a solution of refluxing [(TL)RuCl₃] in EtOH:H₂O under argon atmosphere improves the overall product yield of the reaction. The monometallic precursors were purified using alumina chromatography. The ¹H NMR spectra of heteroleptic complexes, [(MePhtpy)RuCl(dpp)](PF₆) and [(^tBu₃tpy)RuCl(dpp)](PF₆) is shown in the Appendix, Figures A-4, and A-5, respectively.

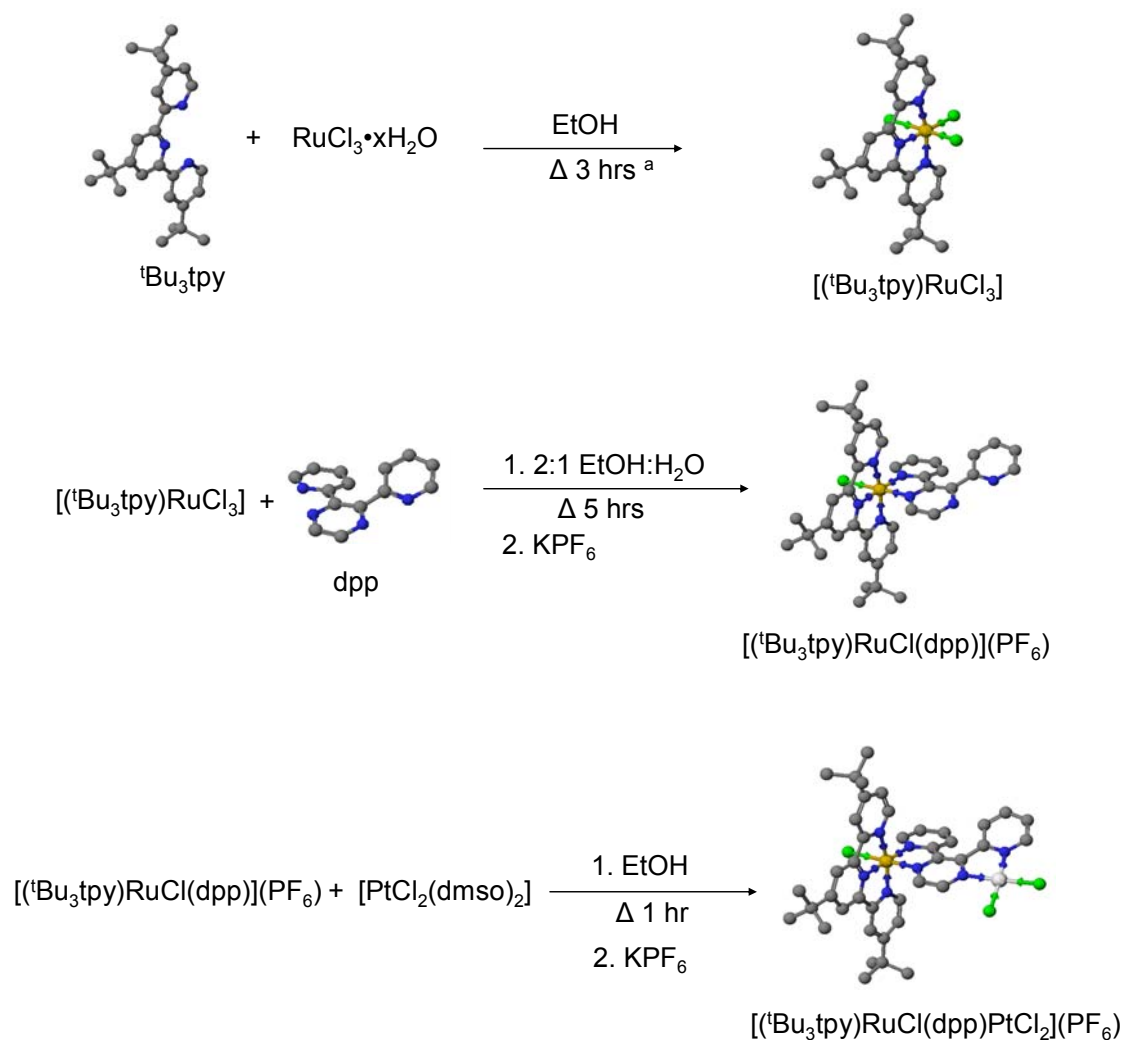


Figure 3.1. Building block method used to prepare mixed-metal supramolecular complex, $[(t\text{Bu}_3\text{tpy})\text{RuCl}(\text{dpp})\text{PtCl}_2](\text{PF}_6)$ ($t\text{Bu}_3\text{tpy}$ = 4,4',4''-tri-tert-butyl-2,2':6',2''-terpyridine) and dpp = 2,3-bis(2-pyridyl)pyrazine). ^a Synthetic procedure adapted from reference ¹³⁵.

The title bimetallic complexes, $[(\text{TL})\text{RuCl}(\text{dpp})\text{PtCl}_2](\text{PF}_6)$ (TL = tpy, MePhtpy, and $t\text{Bu}_3\text{tpy}$), were synthesized by heating, monometallic precursor, $[(\text{TL})\text{RuCl}(\text{dpp})](\text{PF}_6)$, and $[\text{Pt}(\text{DMSO})_2\text{Cl}_2]$ at reflux in ethanol under argon atmosphere for 1 hr. The stoichiometry of reactants plays a critical role in the synthesis the bimetallic complexes of high purity. The purification depends upon the differential solubility of the precursors and products of the reaction. The reaction time also plays an important role in the synthesis of $\text{Ru}^{\text{II}}\text{Pt}^{\text{II}}$ bimetallic

complexes. Increased reaction time leads to the formation of colloidal platinum Pt(s). Due to the labile nature of the Pt-Cl bond, the use of adsorption chromatography is undesirable to purify these complexes. The unreacted $[\text{Pt}(\text{DMSO})_2\text{Cl}_2]$ was removed by washing the complex with ethanol and chloroform. The high purity needed for spectroscopic analysis was achieved by hot ethanol recrystallization.

3.2. Crystal Structure Determination

X-ray crystallographic analysis of $[(\text{MePhtpy})\text{RuCl}(\text{dpp})](\text{PF}_6)$ confirmed the identity of the complex. The X-ray crystallographic structure determination was performed by Dr. Carla Slebodnick, Department of Chemistry, Virginia Polytechnic Institute and State University, Blacksburg, VA. The complex, $[(\text{MePhtpy})\text{RuCl}(\text{dpp})](\text{PF}_6)$, was crystallized from toluene/ CH_3CN by slow evaporation at room temperature. The thermal ellipsoid view of the metal complex, $[(\text{MePhtpy})\text{RuCl}(\text{dpp})]^+$, is shown in Figure 3.2 and the packing diagram is shown in Figure 3.3. The X-ray data is summarized in Table 3.1. The Ru-ligand environment was found to be distorted octahedral in geometry. The Ru-N bond lengths varied from 1.958(4)-2.080(4) Å, which is comparable to the related systems.^{137,138} The Ru-N(4) bond length to the dpp ring trans to the central terpyridine nitrogen was slightly longer than the Ru-N(5) bond length to the dpp ring trans to the chloride. The N-Ru-N bond angles of the chelating diimines were found to be in the range of 79.10(16) - 95.78°(15), much distorted from regular octahedral geometry, and typical of tpy systems.^{137,138}

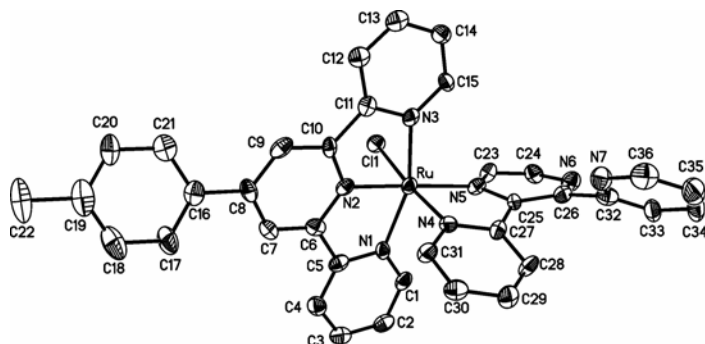


Figure 3.2. Perspective view of $[(\text{MePhtpy})\text{RuCl}(\text{dpp})]^+$ with atomic numbering (MePhtpy = 4'-(4-methylphenyl)-2,2':6',2''-terpyridine and dpp = 2,3-bis(2-pyridyl)pyrazine). The PF_6^- anion, toluene solvent molecules, and H-atoms have been omitted for clarity and thermal ellipsoids are shown at 50% probability level.

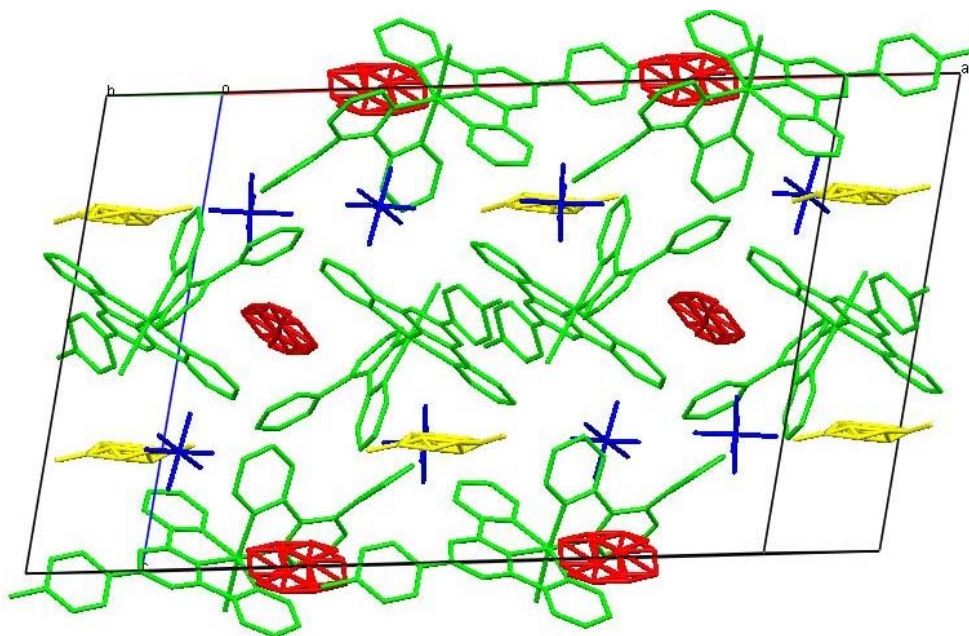


Figure 3.3. Packing diagram of $[(\text{MePhtpy})\text{RuCl}(\text{dpp})]^+$ (MePhtpy = 4'-(4-methylphenyl)-2,2':6',2''-terpyridine and dpp = 2,3-bis(2-pyridyl)pyrazine).

Table 3.1. Crystal data and summary of data collection and refinement for [(MePhtpy)RuCl(dpp)](PF₆).C₇H₈^a

[(MePhtpy)RuCl(dpp)](PF ₆).C ₇ H ₈	
Empirical formula	C ₄₃ H ₃₅ ClF ₆ N ₇ PRu
Formula weight	931.27
Temperature	100(2) K
Wavelength	0.71073 Å
Crystal system	Monoclinic
Space group	C 2/c
Unit cell dimensions	a = 30.5974(11) Å α = 90° B = 13.7173(4) β = 101.809(3)° C = 18.9723(5) γ = 90°
Volume	7794.4(4) Å ³
Z	8
Density (calculated)	1.587 Mg/m ³
Absorption coefficient	0.584 mm ⁻¹
F(000)	3776
Crystal size	0.53 × 0.11 × 0.02 mm ³
Theta range for data collection	3.67 to 25.14°.
Index ranges	-34 ≤ h ≤ 36, -16 ≤ k ≤ 16, -14 ≤ l ≤ 22
Reflections collected	20813
Independent reflections	6904 [R(int) = 0.0583]
Completeness to theta = 25.14°	99.1 %
Absorption correction	Gaussian
Max. and min. transmission	0.988 and 0.896
Refinement method	Full-matrix least-squares on F ²
Data / restraints / parameters	6904 / 5 / 495
Goodness-of-fit on F ²	0.931
Final R indices [I > 2σ(I)]	R1 = 0.0474, wR2 = 0.1066
R indices (all data)	R1 = 0.0932, wR2 = 0.1243

Largest diff. peak and hole

1.528 and -1.089 e.Å⁻³

^aMePhtpy = 4'-(4-methylphenyl)-2,2':6',2''-terpyridine and dpp = 2,3-bis(2-pyridyl)pyrazine.

3.3. Mass Spectrometry

The mass spectra for the complexes, [(TL)RuCl(dpp)PtCl₂](PF₆), and their monometallic precursors are included in the Appendix, Figures A6–A15. The fragmentation patterns observed were consistent with the formulations of the complexes.

The fragmentation pattern observed for the [(MePhtpy)RuCl(dpp)PtCl₂](PF₆) complex is summarized in Table 3.2. The mass spectrum of [(MePhtpy)RuCl(dpp)PtCl₂](PF₆) showed six ions. The molecular ion peak at *m/z* = 960 corresponds to [(MePhtpy)RuCl(dpp)PtCl₂]⁺. Loss of chloride leads to the peak at 924, corresponding to the [(MePhtpy)RuCl(dpp)PtCl]⁺. The peak at 694 corresponds to [(MePhtpy)RuCl(dpp)]⁺. The loss of chloride from the [(MePhtpy)RuCl(dpp)]⁺ leads to a peak at 460. The loss of dpp ligand and chloride give peaks at 460 and 424 corresponding to the [(MePhtpy)RuCl]⁺ and [(MePhtpy)Ru]⁺. The observed fragmentation patterns were consistent with the proposed identity of the [(MePhtpy)RuCl(dpp)PtCl₂](PF₆) metal complex.

Table 3.2. FAB MS spectral data for [(MePhtpy)RuCl(dpp)PtCl₂](PF₆)^a (MePhtpy = 4'-(4-methylphenyl)- 2,2':6',2''- terpyridine and dpp = 2,3-bis(2-pyridyl)pyrazine).

Fragment	<i>m/z</i>	%
[(MePhtpy)RuCl(dpp)PtCl ₂] ⁺	960	15
[(MePhtpy)RuCl(dpp)PtCl] ⁺	924	20
[(MePhtpy)RuCl(dpp)] ⁺	694	100
[(MePhtpy)Ru(dpp)] ⁺	658	10
[(MePhtpy)RuCl] ⁺	460	30
[(MePhtpy)Ru] ⁺	424	25

^aFAB mass spectral analysis was performed by M-Scan Inc., West Chester, PA, on a VG analytical ZAB 2–SE high field mass spectrometer using *m*-nitrobenzyl alcohol as a matrix.

The fragmentation pattern observed for the $[(\text{tpy})\text{RuCl}(\text{dpp})\text{PtCl}_2](\text{PF}_6)$ complex is summarized in Table 3.3. The peak at 870 corresponds to the molecular ion $[(\text{tpy})\text{RuCl}(\text{dpp})\text{PtCl}_2]^+$. The loss of chloride leads to the peak at 834 corresponding to $[(\text{tpy})\text{RuCl}(\text{dpp})\text{PtCl}]^+$. The loss of Pt leads to the peak at 604 corresponding to $[(\text{tpy})\text{RuCl}(\text{dpp})]^+$. The combination of molecular ion peaks and readily explained fragment peaks support the proposed identity of $[(\text{tpy})\text{RuCl}(\text{dpp})\text{PtCl}_2](\text{PF}_6)$.

Table 3.3. ESI-MS spectral data for $[(\text{tpy})\text{RuCl}(\text{dpp})\text{PtCl}_2](\text{PF}_6)^{\text{a}}$ (tpy = 2,2':6',2''-terpyridine and dpp = 2,3-bis(2-pyridyl)pyrazine).

Fragment	m/z	%
$[(\text{tpy})\text{RuCl}(\text{dpp})\text{PtCl}_2]^+$	870	100
$[(\text{tpy})\text{RuCl}(\text{dpp})\text{PtCl}]^+$	834	10
$[(\text{tpy})\text{RuCl}(\text{dpp})]^+$	604	≤ 10

^aElectrospray ionization-MS analysis was performed by M-Scan Inc., West Chester, PA using a VG Bio-Q (Quattro II upgrade) quadrupole mass spectrometer.

The fragmentation pattern for the $[(^t\text{Bu}_3\text{tpy})\text{RuCl}(\text{dpp})\text{PtCl}_2](\text{PF}_6)$ complex is summarized in Table 3.4. The peak at 1002 corresponds to the molecular ion, $[(^t\text{Bu}_3\text{tpy})\text{RuCl}(\text{dpp})\text{PtCl}]^+$. The loss of chloride ion leads to the peak at 965 corresponding to $[(^t\text{Bu}_3\text{tpy})\text{RuCl}(\text{dpp})\text{Pt}]^+$. The combination of molecular ion peaks and readily explained fragment peaks support the synthesis of $[(^t\text{Bu}_3\text{tpy})\text{RuCl}(\text{dpp})\text{PtCl}_2](\text{PF}_6)$.

Table 3.4. ESI MS spectral data for $[(^t\text{Bu}_3\text{tpy})\text{RuCl}(\text{dpp})\text{PtCl}_2](\text{PF}_6)^a$ ($^t\text{Bu}_3\text{tpy}$ = 4,4',4''-tri-tert-butyl-2,2':6',2''-terpyridine) and dpp = 2,3-bis(2-pyridyl)pyrazine).

Fragment	m/z	%
$[(^t\text{Bu}_3\text{tpy})\text{RuCl}(\text{dpp})\text{PtCl}_2]^+$	1038	100
$[(^t\text{Bu}_3\text{tpy})\text{RuCl}(\text{dpp})\text{PtCl}]^+$	1002	10
$[(^t\text{Bu}_3\text{tpy})\text{RuCl}(\text{dpp})\text{Pt}]^+$	965	≤ 10

^aElectrospray ionization-MS analysis was performed by M-Scan Inc., West Chester, PA using a VG Bio-Q (Quattro II upgrade) quadrupole mass spectrometer.

The fragmentation patterns for $[(\text{TL})\text{RuCl}(\text{dpp})](\text{PF}_6)$ are summarized in Table 3.5. All the spectra exhibit a molecular ion and a base peak of $[\text{M}-(\text{PF}_6)]^+$, at 604, 694, and 772 for $[(\text{tpy})\text{RuCl}(\text{dpp})]^+$, $[(\text{MePhtpy})\text{RuCl}(\text{dpp})]^+$, and $[(^t\text{Bu}_3\text{tpy})\text{RuCl}(\text{dpp})]^+$, respectively. All the spectra also exhibited fragmentation peaks corresponding to the loss of chloride ion and dpp ligand. The peak at 377 for $[(\text{MePhtpy})\text{RuCl}(\text{dpp})](\text{PF}_6)$ corresponds to the loss of dpp and MePh subunits from Mephtpy ligand to form $[(\text{MePhtpy})\text{RuCl}-(\text{MePh})]^+ + 4\text{H}^+$ fragment. Similarly, the loss of six primary CH_3 groups from $^t\text{Bu}_3\text{tpy}$ was observed for $[(^t\text{Bu}_3\text{tpy})\text{RuCl}(\text{dpp})](\text{PF}_6)$ complex. The peak at 655 corresponds to $[(^t\text{Bu}_3\text{tpy})\text{RuCl}(\text{dpp})-(6\text{CH}_3)]^+$ ion. Subsequent loss of dpp leads to the peak at 453. The fragmentation patterns for the monometallic precursors were also consistent with the proposed identities of these complexes.

Table 3.5. ESI MS spectral data for [(TL)RuCl(dpp)](PF₆)^a (tpy = 2,2':6',2''-terpyridine, MePhtpy = 4'-(4-methylphenyl)-2,2':6',2''-terpyridine, ^tBu₃tpy = 4,4',4''-tri-tert-butyl-2,2':6',2''-terpyridine), and dpp = 2,3-bis(2-pyridyl)pyrazine).

Fragments	m/z	%
[(tpy)RuCl(dpp)] ⁺	604	100
[(tpy)Ru(dpp)] ⁺	568	12
[(tpy)RuCl] ⁺	370	15
[(tpy)Ru] ⁺	334	15
[(MePhtpy)RuCl(dpp)] ⁺	694	100
[(MePhtpy)RuCl] - (MePh) ⁺ + 4H] ⁺	374	40
[(^t Bu ₃ tpy)RuCl(dpp)] ⁺	772	100
[(^t Bu ₃ tpy)Ru(dpp) - (6CH ₃)] ⁺	655	≤10
[(^t Bu ₃ tpy)Ru] - (6CH ₃)] ⁺	453	≤10

^aElectrospray ionization-MS analysis was performed by M-Scan Inc., West Chester, PA using a VG Bio-Q (Quattro II upgrade) quadrupole mass spectrometer.

3.4. NMR Spectroscopy

¹⁹⁵Pt NMR spectroscopy was used to confirm the coordination of Pt in the supramolecular complexes and establish the absence of detectable amounts of unreacted Pt impurities. The chemical shift of ¹⁹⁵Pt is usually influenced by various factors including the nature of the ligands present in the coordination sphere, their spatial arrangement, the nature of the bound donor atoms, concentration, pH, temperature, and solvent. Figure 3.5 shows ¹⁹⁵Pt NMR spectra of the [(TL)RuCl(dpp)PtCl₂](PF₆) complexes in d₆-DMSO. Single isolated ¹⁹⁵Pt NMR resonances at -2199.5, -2201.0, and -2220.5 ppm was observed for the complexes, [(tpy)RuCl(dpp)PtCl₂]⁺, [(MePhtpy)RuCl(dpp)PtCl₂]⁺, and [(^tBu₃tpy)RuCl(dpp)PtCl₂]⁺, respectively. The presence of single ¹⁹⁵Pt NMR resonances confirmed the purity of these supramolecular complexes. The ¹⁹⁵Pt NMR spectrum of [Pt(DMSO)₂Cl₂] reveals a resonance at -2970 ppm.¹³⁹ Absence of a resonance at -2970 confirmed that the unreacted [Pt(DMSO)₂Cl₂] impurity was not present in the sample.

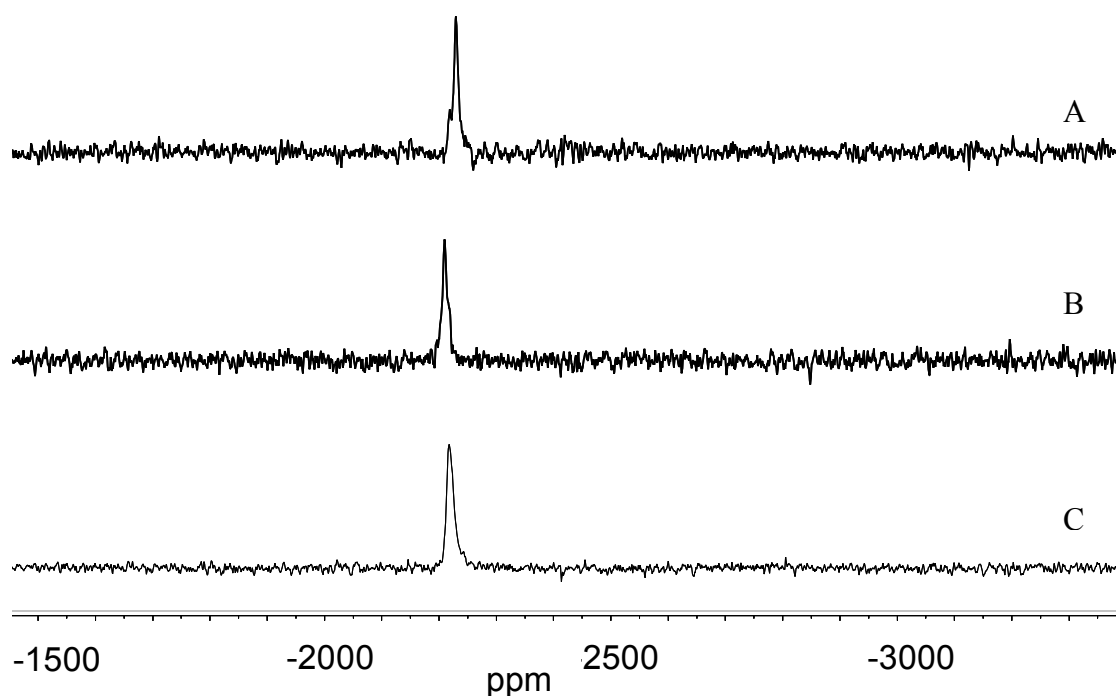


Figure 3.4. ^{195}Pt NMR of $[(\text{TL})\text{RuCl}(\text{dpp})\text{PtCl}_2](\text{PF}_6)$ in $\text{d}_6\text{-DMSO}$ (TL = ${}^t\text{Bu}_3\text{tpy}$ (A), tpy (B), and MePhtpy (C) (tpy = 2,2':6',2''- terpyridine, MePhtpy = 4'-(4-methylphenyl)- 2,2':6',2''- terpyridine, ${}^t\text{Bu}_3\text{tpy}$ = 4,4',4''-tri-tert-butyl-2,2':6',2''- terpyridine), and dpp = 2,3-bis(2-pyridyl)pyrazine). Spectra were taken at 600 MHz and chemical shifts are reported relative to K_2PtCl_6 .

3.5. Electrochemical Properties

Electrochemistry was used to understand the energetics associated with the frontier orbitals of the $\text{Ru}^{\text{II}}\text{Pt}^{\text{II}}$ mixed metal complexes. Ruthenium polypyridyl complexes typically display reversible Ru-based oxidations and a series of reversible ligand-based reductions. The heteronuclear bimetallic complexes and the monometallic precursors have been studied by cyclic voltammetry, and the data is summarized in Table 3.6.

Table 3.6. Cyclic voltammetric data for [(TL)RuCl(dpp)PtCl₂](PF₆) and monometallic synthons (TL = terminal ligand (tpy = 2,2':6',2''-terpyridine, MePhtpy = 4'-(4-methylphenyl)-2,2':6',2''-terpyridine, ^tBu₃tpy = 4,4',4''-tri-tert-butyl-2,2':6',2''-terpyridine), dpp = 2,3-bis(2-pyridyl)pyrazine).

Metal Complex	E _{1/2} ^{ox} (V)	E _{1/2} ^{red} (V)
[(tpy)RuCl(dpp)PtCl ₂](PF ₆)	+1.10 Ru ^{II/III}	-0.50 dpp ^{0/-} -1.15 dpp ⁻²⁻ -1.43 tpy ^{0/-}
[(MePhtpy)RuCl(dpp)PtCl ₂](PF ₆)	+1.10 Ru ^{II/III}	-0.55 dpp ^{0/-} -1.20 dpp ⁻²⁻ -1.44 MePhtpy ^{0/-}
[(^t Bu ₃ tpy)RuCl(dpp)PtCl ₂](PF ₆)	+1.01 Ru ^{II/III}	-0.59 dpp ^{0/-} -1.15 dpp ⁻²⁻ -1.59 ^t Bu ₃ tpy ^{0/-}
[(tpy)RuCl(dpp)](PF ₆)	+1.02 Ru ^{II/III}	-1.15 dpp ^{0/-} -1.41 tpy ^{0/-}
[(MePhtpy)RuCl(dpp)](PF ₆)	+1.01 Ru ^{II/III}	-1.16 dpp ^{0/-} -1.40 MePhtpy ^{0/-}
[(^t Bu ₃ tpy)RuCl(dpp)](PF ₆)	+0.88 Ru ^{II/III}	-1.22 dpp ^{0/-} -1.59 ^t Bu ₃ tpy ^{0/-}
[Ru(tpy) ₂](PF ₆) ₂	+1.30 Ru ^{II/III}	-1.24 tpy ^{0/-}
[Ru(MePhtpy) ₂](PF ₆) ₂	+1.25 Ru ^{II/III}	-1.24 MePhtpy ^{0/-}
[Ru(^t Bu ₃ tpy) ₂](PF ₆) ₂	+1.12 Ru ^{I/III}	-1.37 ^t Bu ₃ tpy ^{0/-}

^a Potential reported in CH₃CN with 0.1 M Bu₄NPF₆ and reported vs. Ag/AgCl (0.21 V vs. NHE) reference electrode.

3.5.1. Electrochemical Properties: Heteroleptic and Homoleptic Complexes

The heteroleptic complexes displayed electrochemistry consistent with their formulation. These complexes displayed a reversible Ru^{II/III} oxidation, establishing the Ru metal center as a site for the localization of the highest occupied molecular orbital (HOMO). The heteroleptic complexes displayed a Ru^{II/III} oxidation at +1.02, +1.01, and +0.98 V vs. Ag/AgCl for TL = tpy, MePhtpy, and ^tBu₃tpy, respectively. Two well-resolved reductive waves were observed for these complexes representing the one electron reduction of the dpp and tpy ligand, respectively. The first reduction observed at -1.15 V, -1.16 V, and -1.22 V vs. Ag/AgCl was assigned to dpp^{0/-} reduction for the tpy, MePhtpy, and ^tBu₃tpy containing complexes, respectively. The bridging ligand-based first reduction was confirmed by varying the bridging ligands in similar types of complexes by Brewer and coworkers.¹³⁴ The second reduction observed at -1.41, -1.40, and -1.59 V was assigned to tpy^{0/-}, MePhtpy^{0/-}, and ^tBu₃tpy^{0/-} reductions, respectively. The less positive potential observed for ^tBu₃tpy reduction compared to other two tpy analogs is due to the electron donating character of t-butyl groups. A similar effect was reported by Hadda and LeBoez with decrease in potential when the ^tBu₃tpy and ^tBu₃bpy were substituted for tpy and bpy, respectively in [^tBu₃tpy)RuCl(bpy)]⁺ and [^tBu₃bpy)RuCl(tpy)]⁺.^{135,140-142} The electrochemical properties of the heteroleptic complexes are in agreement with those of the previously reported [(MePhtpy)RuCl(bpy)](PF₆) complex.¹⁴³ The first reduction at -1.32 V for [(MePhtpy)RuCl(bpy)](PF₆) complex was reported to be MePhtpy-based and the second reduction at -1.58 V was bpy-based. This is because the bpy ligand is more difficult to reduce as compared to the dpp ligand. The electrochemical properties of [(tpy)RuCl(dpp)](PF₆) are consistent with already reported values.¹¹⁶ The cyclic voltammograms of [(TL)RuCl(dpp)](PF₆) are shown in Figure 3.5. An electrochemical mechanism illustrating the redox behavior of these complexes is shown in Scheme 3.1.

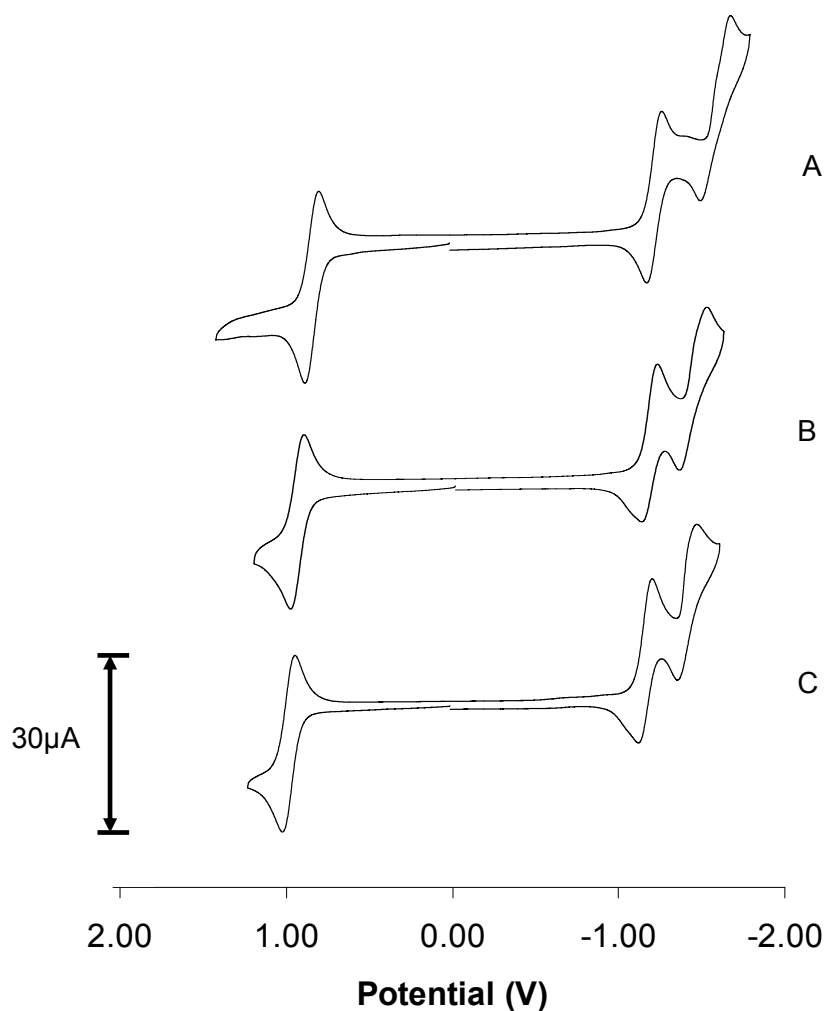
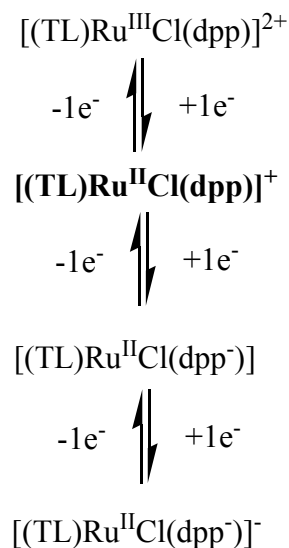


Figure 3.5. Cyclic voltammograms of $[(^t\text{Bu}_3\text{tpy})\text{RuCl}(\text{dpp})](\text{PF}_6)$ (A), $[(\text{MePhtpy})\text{RuCl}(\text{dpp})](\text{PF}_6)$ (B), and $[(\text{tpy})\text{RuCl}(\text{dpp})](\text{PF}_6)$ (C) in 0.1 M Bu_4NPF_6 in CH_3CN and reported vs. Ag/AgCl (tpy = 2,2':6',2''-terpyridine, MePhtpy = 4'-(4-methylphenyl)-2,2':6',2''-terpyridine, $^t\text{Bu}_3\text{tpy}$ = 4,4',4''-tri-tert-butyl-2,2':6',2''-terpyridine), and dpp = 2,3-bis(2-pyridyl)pyrazine).



Scheme 3.1. Electrochemical mechanism for $[(\text{TL})\text{RuCl}(\text{dpp})](\text{PF}_6)$ with synthesized oxidation state in bold (TL = terminal ligand (tpy = 2,2':6',2''-terpyridine, MePhpty = 4'-(4-methylphenyl)-2,2':6',2''-terpyridine, ^tBu₃tpy = 4,4',4''-tri-tert-butyl-2,2':6',2''-terpyridine), and dpp = 2,3-bis(2-pyridyl)pyrazine).

The electrochemical properties of the heteroleptic complexes were compared with those of the homoleptic complexes containing tpy terminal ligands. The electrochemical properties of these complexes provide an insight into the relative orbital energies of the HOMO and LUMO. Consistent with previous reports, the homoleptic complexes, $[\text{Ru}(\text{tpy})_2]^{2+}$, $[\text{Ru}(\text{MePhpty})_2]^{2+}$, and $[\text{Ru}(\text{}^t\text{Bu}_3\text{tpy})_2]^{2+}$ displayed a reversible $\text{Ru}^{\text{II/III}}$ wave couple at 1.35, 1.30, and 1.12 V, with first reduction at -1.23, -1.20, and -1.37 V, respectively, vs. Ag/AgCl in CH₃CN (Table 3.6) (Figure 3.6).^{48,58,135,141,144} The HOMO in both homoleptic and heteroleptic complexes is Ru-based. The metal-based oxidations for the heteroleptic complexes occurred at a significantly less positive potential than the corresponding oxidation for the homoleptic complexes. The shift in the oxidation potential resulted from the decreased σ donating and increased π accepting ability of the pyridine nitrogen relative to the chloride. The LUMO in the heteroleptic complexes is dpp-based compared to the tpy-based LUMO in the homoleptic complexes. The dpp-based reduction occurred at a more positive potential than the tpy-based reduction due to the lower energy π^* orbital of dpp relative to tpy. The nature of the HOMO and LUMO in these complexes predicts a lowest lying excited state that is MLCT in nature. The lower HOMO-LUMO energy gap in the

heteroleptic complexes, compared to the homoleptic complexes, predicts a lower energy MLCT transitions in these complexes.

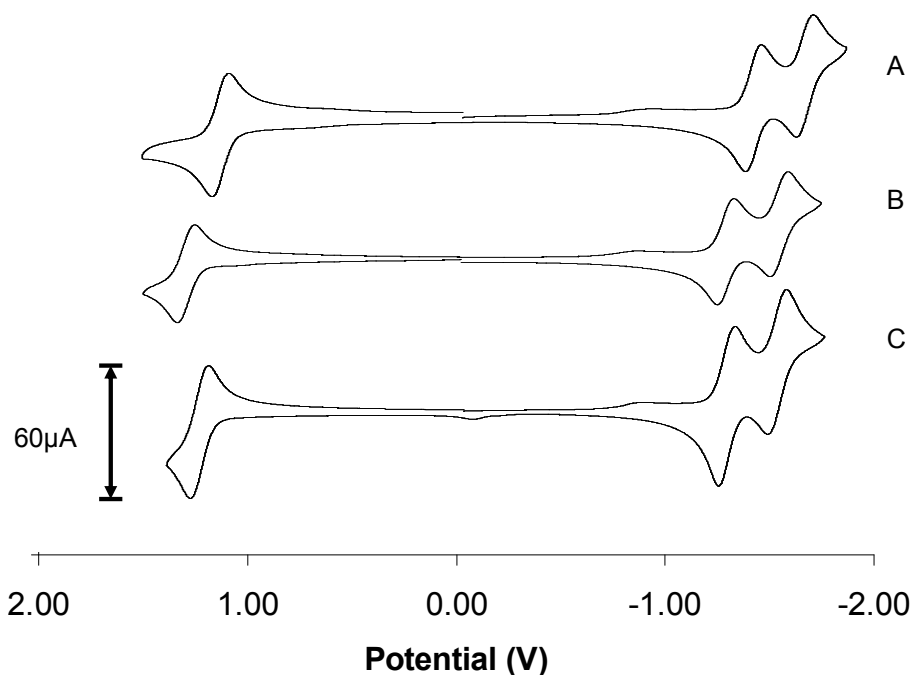


Figure 3.6. Cyclic voltammograms of $[(t\text{Bu}_3\text{tpy})_2\text{Ru}](\text{PF}_6)$ (A), $[(\text{MePhtpy})_2\text{Ru}](\text{PF}_6)$ (B), and $[(\text{tpy})_2\text{Ru}](\text{PF}_6)$ (C) in 0.1 M Bu_4NPF_6 in CH_3CN and reported vs. Ag/AgCl (tpy = 2,2':6',2''-terpyridine, MePhtpy = 4'-(4-methylphenyl)-2,2':6',2''-terpyridine, $t\text{Bu}_3\text{tpy}$ = 4,4',4''-tri-tert-butyl-2,2':6',2''-terpyridine).

3.5.2. Electrochemical Properties: $\text{Ru}^{\text{II}}\text{Pt}^{\text{II}}$ Heterobimetallic Complexes

The heterobimetallic complexes displayed electrochemistry consistent with their formulation. These complexes displayed a reversible $\text{Ru}^{\text{II/III}}$ oxidation, establishing the Ru metal center as a site for the localization of the highest occupied molecular orbital (HOMO). Each $[(\text{TL})\text{RuCl}(\text{dpp})\text{PtCl}_2](\text{PF}_6)$ complex displayed a reversible $\text{dpp}^{0/-}$ based first reduction, establishing the BL as the site of localization of LUMO for these heterobimetallic complexes. The $\text{Ru}^{\text{II/III}}$ oxidation in $[(\text{tpy})\text{RuCl}(\text{dpp})\text{PtCl}_2](\text{PF}_6)$ and $[(\text{MePhtpy})\text{RuCl}(\text{dpp})\text{PtCl}_2](\text{PF}_6)$ complexes occurred at 1.10 V vs. Ag/AgCl , which is shifted to a more positive potential relative to the monometallic synthons. The positive shift in Ru-based oxidation upon platination is consistent with previous reports on $\text{Ru}^{\text{II}}\text{Pt}^{\text{II}}$ bimetallic complexes.^{110,115,116} The $\text{Ru}^{\text{II/III}}$ oxidation

couple occurred at a less positive potential in $[(^t\text{Bu}_3\text{tpy})\text{RuCl}(\text{dpp})\text{PtCl}_2](\text{PF}_6)$ compared to the other two heterobimetallic complexes, $[(\text{MePhtpy})\text{RuCl}(\text{dpp})\text{PtCl}_2](\text{PF}_6)$, and $[(\text{tpy})\text{RuCl}(\text{dpp})\text{PtCl}_2](\text{PF}_6)$. This negative shift in the oxidation potential of $[(^t\text{Bu}_3\text{tpy})\text{RuCl}(\text{dpp})\text{PtCl}_2](\text{PF}_6)$ resulted from the electron donating character of the t-butyl groups, making the Ru center more electron rich, and therefore easy to oxidize. A similar effect was reported by Hadda and LeBoez with a 75 mV decrease in potential when the $^t\text{Bu}_3\text{tpy}$ and $^t\text{Bu}_3\text{bpy}$ were substituted for tpy and bpy, respectively in $[(^t\text{Bu}_3\text{tpy})\text{RuCl}(\text{bpy})]^+$ and $[(^t\text{Bu}_3\text{bpy})\text{RuCl}(\text{tpy})]^+$.^{135,140-142} According to them, the replacement of hydrogens by t-butyl groups plays a significant role in stabilizing Ru oxidation. They observed ~ 25 mV decrease in $\text{Ru}^{\text{II/III}}$ oxidation potential per t-butyl substituent.¹³⁵ Each $[(\text{TL})\text{RuCl}(\text{dpp})\text{PtCl}_2](\text{PF}_6)$ complex displayed a reversible $\text{dpp}^{0/-}$ based first reduction. The second reduction in the bimetallic complexes is $\text{dpp}^{-2/-}$ in nature. Stabilization of the $\text{dpp}(\pi^*)$ acceptor orbital as a result of the coordination to the *cis*- $\text{Pt}^{\text{II}}\text{Cl}_2$ moiety shifts this $\text{dpp}^{-2/-}$ couple more positive than the $\text{TL}^{0/-}$ couple. This positive shift in $\text{dpp}^{-2/-}$ reductions in bimetallic complexes is consistent with previously published reports.^{115,116} The third reduction in these metal complexes is $\text{TL}^{0/-}$ in nature. The reduction of tpy and MePhtpy in these heterobimetallic complexes occurred at -1.40 and -1.46 V. The reduction of the $^t\text{Bu}_3\text{tpy}$ occurred at a more negative potential, -1.59 V, due to the electron donating character of t-butyl groups. This confirmed the terminal ligand-based third reduction in the designed $\text{Ru}^{\text{II}}\text{Pt}^{\text{II}}$ bimetallic complexes.

The cyclic voltammograms of $[(\text{TL})\text{RuCl}(\text{dpp})\text{PtCl}_2](\text{PF}_6)$ is shown in Figure 3.7. The reversible oxidation at +1.10 V for $[(\text{tpy})\text{RuCl}(\text{dpp})\text{PtCl}_2](\text{PF}_6)$ is assigned to the $\text{Ru}^{\text{II/III}}$ couple. The first and second reductions at -0.50 and -1.15 V were assigned to the $\text{dpp}^{0/-}$ and $\text{dpp}^{-2/-}$ couples, respectively. The third reduction at -1.43 V was assigned to the $\text{tpy}^{0/-}$ couple. The cyclic voltammogram of $[(\text{MePhtpy})\text{RuCl}(\text{dpp})\text{PtCl}_2](\text{PF}_6)$ also displayed $\text{Ru}^{\text{II/III}}$ oxidation at 1.10 V (Figure 3.7). The first two reduction couples at -0.55 and -1.20 V were assigned to $\text{dpp}^{0/-}$ and $\text{dpp}^{-2/-}$ reductions and the third reduction couple at -1.44 V was assigned to $\text{MePhtpy}^{0/-}$. The cyclic voltammogram of $[(^t\text{Bu}_3\text{tpy})\text{RuCl}(\text{dpp})\text{PtCl}_2](\text{PF}_6)$, exhibited a dramatic shift in the tpy-based reduction (Figure 3.7). The $^t\text{Bu}_3\text{tpy}$ reduction occurred at a more negative potential, -1.59 V, due to the electron donating character of t-butyl groups. The first two reduction couples at -0.59 and -1.15 V were assigned as $\text{dpp}^{0/-}$ and $\text{dpp}^{-2/-}$ based reductions. The $\text{Ru}^{\text{II/III}}$ couple

occurred at 1.01 V, less positive potential than other analogs due to the electron donating character of the t-butyl groups.

The electrochemical properties of the Ru^{II}Pt^{II} bimetallic complexes were compared. The dpp-based reduction occurred at almost the same potential in all the three bimetallic complexes. However a change in the third reduction potential was observed with the variation in tpy ligand. This supports the assignment of the first two reduction couples as dpp-based reductions and the third as a tpy-based reduction.

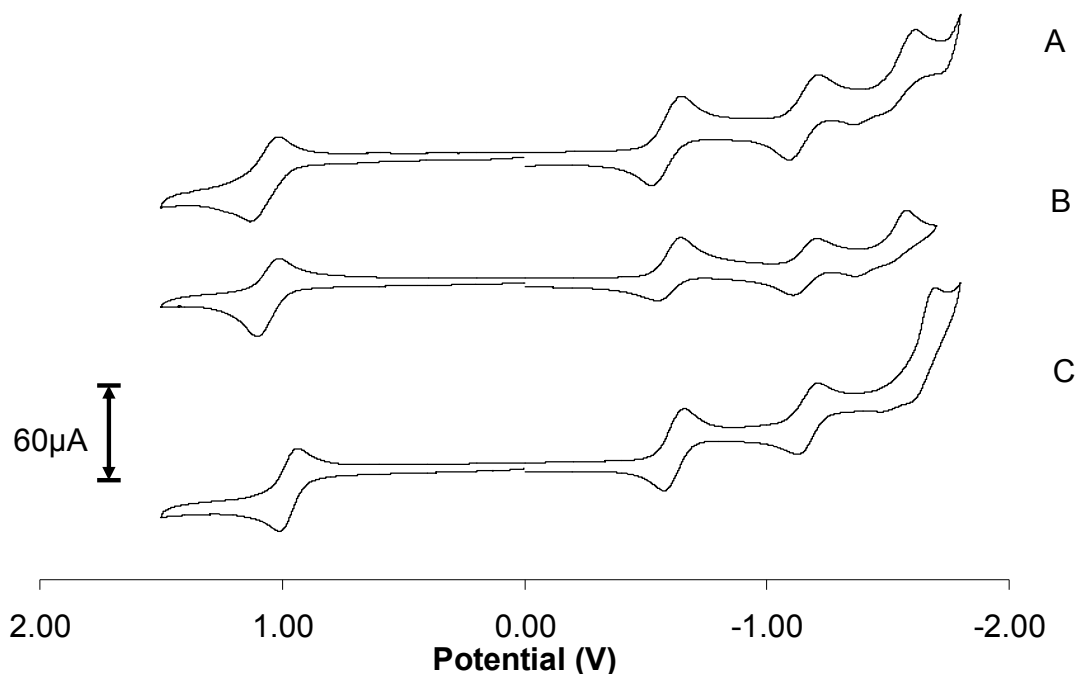
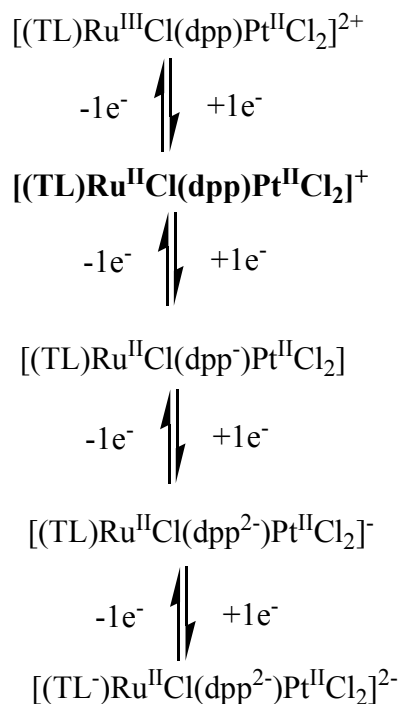


Figure 3.7. Cyclic voltammograms of [(tpy)RuCl(dpp)PtCl₂](PF₆) (A), [(MePhtpy)RuCl(dpp)PtCl₂](PF₆) (B), and [(^tBu₃tpy)RuCl(dpp)PtCl₂](PF₆) (C) in 0.1 M Bu₄NPF₆ in CH₃CN and reported vs. Ag/AgCl (tpy = 2,2':6',2''-terpyridine, MePhtpy = 4'-(4-methylphenyl)-2,2':6',2''-terpyridine, ^tBu₃tpy = 4,4',4''-tri-tert-butyl-2,2':6',2''-terpyridine), dpp = 2,3-bis(2-pyridyl)pyrazine).

Scheme 3.1. Electrochemical mechanism for $[(\text{TL})\text{RuCl}(\text{dpp})\text{PtCl}_2](\text{PF}_6)$ with synthesized oxidation state in bold (TL = terminal ligand (tpy = 2,2':6',2''-terpyridine, MePhtpy = 4'-(4-methylphenyl)-2,2':6',2''-terpyridine, ${}^t\text{Bu}_3\text{tpy}$ = 4,4',4''-tri-tert-butyl-2,2':6',2''-terpyridine) and dpp = 2,3-bis(2-pyridyl)pyrazine).



3.5.3. Comparison of Electrochemical Properties of $\text{Ru}^{\text{II}}\text{Pt}^{\text{II}}$ Bimetallic Complexes with their Monometallic Precursors

The redox properties of the $\text{Ru}^{\text{II}}\text{Pt}^{\text{II}}$ bimetallic complexes were compared with that of their respective monometallic synthons. In the title bimetallic complexes the chromophore unit is coupled to a *cis*- PtCl_2 unit by a communicative bridging ligand, dpp. Coupling a polyazine LA to a reactive $\text{Pt}(\text{II})$ center through a communicative bridging ligand allows for electronic communication between two subunits, thus the redox and photophysical properties of individual units are not maintained and as a result imparts rich redox and photophysical properties to these heteronuclear bimetallic system. The $\text{Ru}^{\text{II/III}}$ oxidation occurred at a more positive potential in the mixed-metal $\text{Ru}^{\text{II}}\text{Pt}^{\text{II}}$ complexes relative to the Ru monometallic synthons. This is indicative of a less electron-rich Ru metal center in the bimetallic, $\text{Ru}^{\text{II}}\text{Pt}^{\text{II}}$ complexes. This is due to the

coupling of the electron deficient Pt^{II} center. Both monometallic and bimetallic complexes displayed BL-based first reduction. However the BL-based first reduction occurred at a more positive potential in the bimetallic complexes compared to the monometallic complexes. This results from the stabilization of BL(π^*) orbital on coordination with electropositive Pt^{II} center. The second reduction in the bimetallic complexes is the BL^{-/2-} couple compared to the TL^{0/-} couple in the monometallic complexes. The occurrence of a BL^{-/2-} couple prior to the reduction of the tpy terminal ligands is indicative of bimetallic formation in which the BLs are bound to two electropositive metal centers, consistent with previous reports for Ru^{II}Pt^{II} complexes.^{110,115,116}

3.6. Electronic Absorption Spectroscopy

3.6.1. Electronic Absorption Properties: Heteroleptic Complexes

Electronic absorption spectroscopy was used to understand the light absorbing properties of the designed molecules. The electronic absorption spectra of the heteroleptic complexes in acetonitrile at room temperature are shown in Figure 3.8. The electronic absorption spectra of all the three complexes are found to be very similar. A summary of electronic absorption spectroscopy data for the monometallic precursors and bimetallic complexes is reported in Table 3.7. The spectra of all the complexes displayed intense TL-based $\pi \rightarrow \pi^*$ transitions in the UV region at ca. 230, 275, and 315 nm. The dpp-based $\pi \rightarrow \pi^*$ transitions occurred at lower energy as a shoulder at ca. 360 nm. These complexes displayed MLCT transitions in the visible region to both the acceptor ligands, with the Ru \rightarrow dpp charge transfer being lower in energy than the Ru \rightarrow tpy charge transfer transitions. The MLCT transitions of metal complexes containing MePhtpy and ^tBu₃tpy as a terminal ligand were slightly red-shifted ($\lambda_{\text{max}}^{\text{abs}} = 521$ nm) as compared to the tpy terminal ligands ($\lambda_{\text{max}}^{\text{abs}} = 518$ nm). This is due to the stabilization of MLCT state as a result of electron donating character of ^tBu₃tpy substituent. This is consistent with previous reports for substituted tpy type complexes.^{58,144}

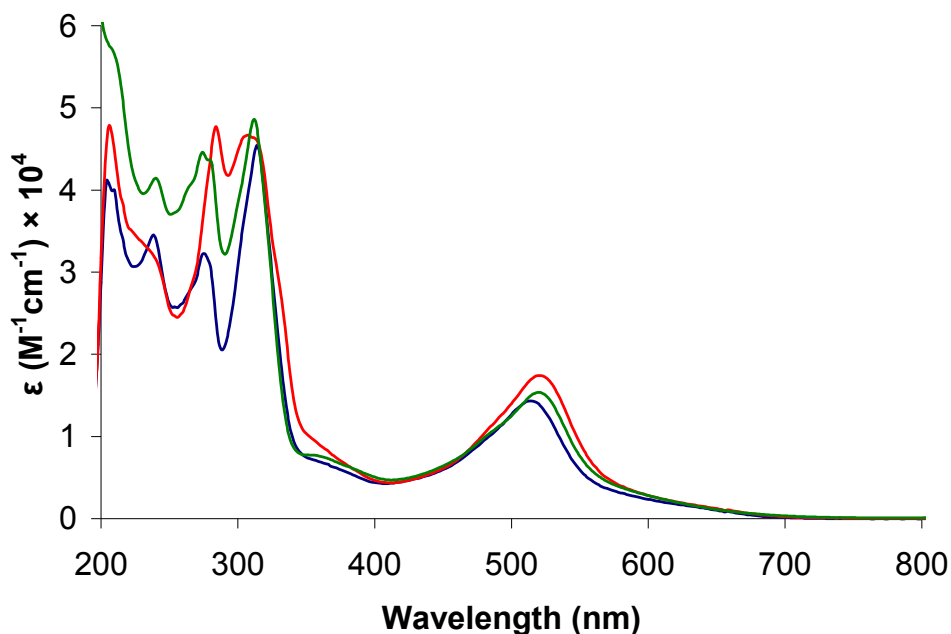


Figure 3.8. Electronic absorption spectroscopy of $[(^t\text{Bu}_3\text{tpy})\text{RuCl}(\text{dpp})](\text{PF}_6)$ (—), $[(\text{MePhpty})\text{RuCl}(\text{dpp})](\text{PF}_6)$ (—), and $[(\text{tpy})\text{RuCl}(\text{dpp})](\text{PF}_6)$ (—) in CH_3CN at room temperature (tpy = 2,2':6',2''- terpyridine, MePhpty = 4'-4-methylphenyl-2,2':6',2''-terpyridine, $^t\text{Bu}_3\text{tpy}$ = 4,4',4''-tri-tert-butyl-2,2':6',2''- terpyridine), and dpp = 2,3-bis(2-pyridyl)pyrazine).

3.6.2. Comparison of Electronic Absorption Properties of Homoleptic and Heteroleptic Complexes

The electronic absorption spectra of the heteroleptic and homoleptic complexes in acetonitrile at room temperature are shown in Figure 3.17 and summarized in Table 3.7. The spectra of all the complexes displayed intense $\pi \rightarrow \pi^*$ transitions in the UV region and MLCT transitions in the visible region. The heteroleptic complexes displayed MLCT transitions in the visible region to both the acceptor ligands, with the $\text{Ru} \rightarrow \text{dpp}$ charge transfer being lower in energy than the $\text{Ru} \rightarrow \text{tpy}$ charge transfer transitions. The MLCT transition of the heteroleptic complexes occurred at lower energy as compared to the homoleptic complexes, reflective of the higher energy $\text{Ru}(d\pi)$ orbital as well as lower energy dpp based π^* orbital relative to the energy of the tpy or MePhpty-based π^* orbital.¹³⁴

Table 3.7. Electronic absorption spectroscopy for [(TL)RuCl(dpp)PtCl₂](PF₆) and related monometallic synthons in CH₃CN at RT (TL = terminal ligand (tpy = 2,2':6',2''-terpyridine, MePhtpy = 4'-(4-methylphenyl)-2,2':6',2''-terpyridine, ^tBu₃tpy = 4,4',4''-tri-tert-butyl-2,2':6',2''-terpyridine), and dpp = 2,3-bis(2-pyridyl)pyrazine).

Complex	$\lambda_{\max}^{\text{abs}}$ (nm)	$\epsilon \times 10^{-4}$ (M ⁻¹ cm ⁻¹)	Assignment
[(tpy)RuCl(dpp)PtCl ₂](PF ₆) ^a	236	2.87	$\pi \rightarrow \pi^*$ tpy
	274	2.20	$\pi \rightarrow \pi^*$ tpy
	317	3.22	$\pi \rightarrow \pi^*$ tpy
	354(sh)	1.40	$\pi \rightarrow \pi^*$ dpp
	462(sh)	0.490	Ru \rightarrow tpy CT
	544	1.53	Ru \rightarrow dpp CT
[(MePhtpy)RuCl(dpp)PtCl ₂](PF ₆)	227	4.67	$\pi \rightarrow \pi^*$ MePhtpy
	284	4.49	$\pi \rightarrow \pi^*$ MePh tpy
	318	4.82	$\pi \rightarrow \pi^*$ MePhtpy
	354(sh)	1.90	$\pi \rightarrow \pi^*$ dpp
	464(sh)	0.670	Ru \rightarrow MePhtpy CT
	548	2.09	Ru \rightarrow dpp CT
[(^t Bu ₃ tpy)RuCl(dpp)PtCl ₂](PF ₆)	230	3.92	$\pi \rightarrow \pi^*$ ^t Bu ₃ tpy
	271	3.38	$\pi \rightarrow \pi^*$ ^t Bu ₃ tpy
	314	3.53	$\pi \rightarrow \pi^*$ ^t Bu ₃ tpy
	354(sh)	1.42	$\pi \rightarrow \pi^*$ dpp
	462(sh)	0.490	Ru \rightarrow ^t Bu ₃ tpy CT
	545	1.54	Ru \rightarrow dpp CT
[(tpy)RuCl(dpp)](PF ₆) ^b	237	3.40	$\pi \rightarrow \pi^*$ tpy
	274	3.10	$\pi \rightarrow \pi^*$ tpy
	315	4.60	$\pi \rightarrow \pi^*$ tpy
	364(sh)	0.680	$\pi \rightarrow \pi^*$ dpp
	516	1.43	Ru \rightarrow dpp CT Ru \rightarrow tpy CT
[(MePhtpy)RuCl(dpp)](PF ₆)	228	3.32	$\pi \rightarrow \pi^*$ MePhtpy
	286	4.25	$\pi \rightarrow \pi^*$ MePhtpy
	312	4.32	$\pi \rightarrow \pi^*$ MePhtpy
	356(sh)	0.610	$\pi \rightarrow \pi^*$ dpp
	522	1.72	Ru \rightarrow dpp CT Ru \rightarrow MePhtpy CT

[(^t Bu ₃ tpy)RuCl(dpp)](PF ₆)	240	4.20	$\pi \rightarrow \pi^*$ ^t Bu ₃ tpy
	275	4.28	$\pi \rightarrow \pi^*$ ^t Bu ₃ tpy
	314	5.02	$\pi \rightarrow \pi^*$ ^t Bu ₃ tpy
	360(sh)	0.801	$\pi \rightarrow \pi^*$ dpp
	521	1.53	Ru \rightarrow dpp CT
			Ru \rightarrow ^t Bu ₃ tpy CT

^aExtinction coefficients recorded under our conditions, consistent with the previous report.[117]

^bExtinction coefficients recorded under our conditions, consistent with the previous report.[135]

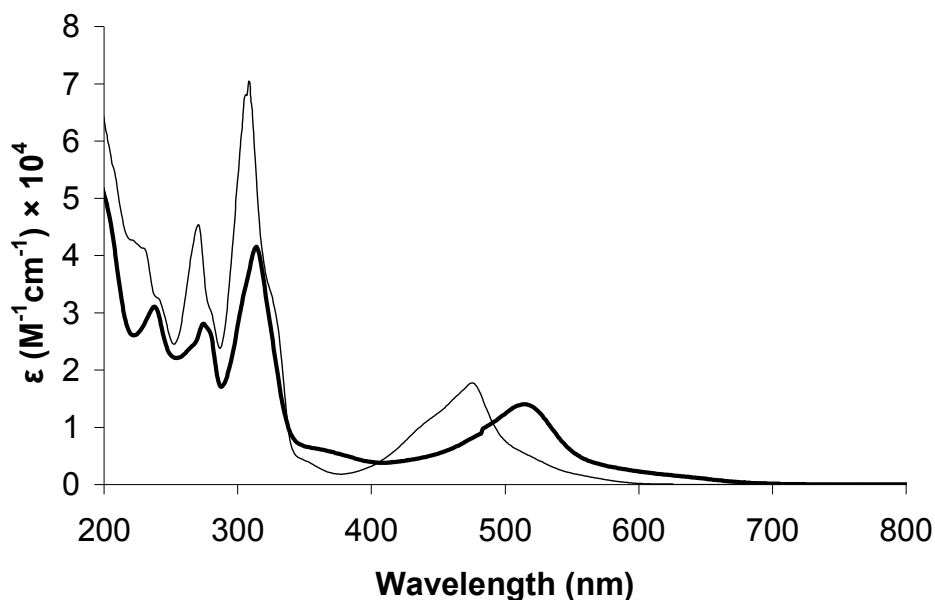


Figure 3.9. Electronic absorption spectroscopy of heteroleptic complex, [(tpy)RuCl(dpp)](PF₆), (—) and homoleptic complex, [(tpy)₂Ru](PF₆)₂ (---) in CH₃CN at RT (tpy = 2,2':6',2''-terpyridine and dpp = 2,3-bis(2-pyridyl)pyrazine).

3.6.3. Electronic Absorption Spectroscopy: Ru^{II}Pt^{II} Heterobimetallic Complexes

All the heterobimetallic complexes are efficient light absorbers with the spectrum dominated by the TL-LA-BL subunit. These complexes displayed ligand-based $\pi \rightarrow \pi^*$ transition in the UV region and MLCT transition in the visible region, terminating in each acceptor ligand. The spectra of all the complexes displayed intense TL-based $\pi \rightarrow \pi^*$ transitions in the UV region with the two major peaks at 272 and 316 nm attributed to the tpy ligand. The dpp-based $\pi \rightarrow \pi^*$

transition occurred at lower energy as a shoulder at ca. 354 nm. These complexes displayed intense MLCT bands in the visible region of the spectrum. The Ru→BL charge transfer bands occurred at lower energy than the Ru→TL charge transfer bands and were centered at ca. 460 nm for all the three complexes. The electronic absorption spectra of heterobimetallic complexes of the form [(TL)RuCl(dpp)PtCl₂](PF₆) in acetonitrile are shown in Figure 3.10.

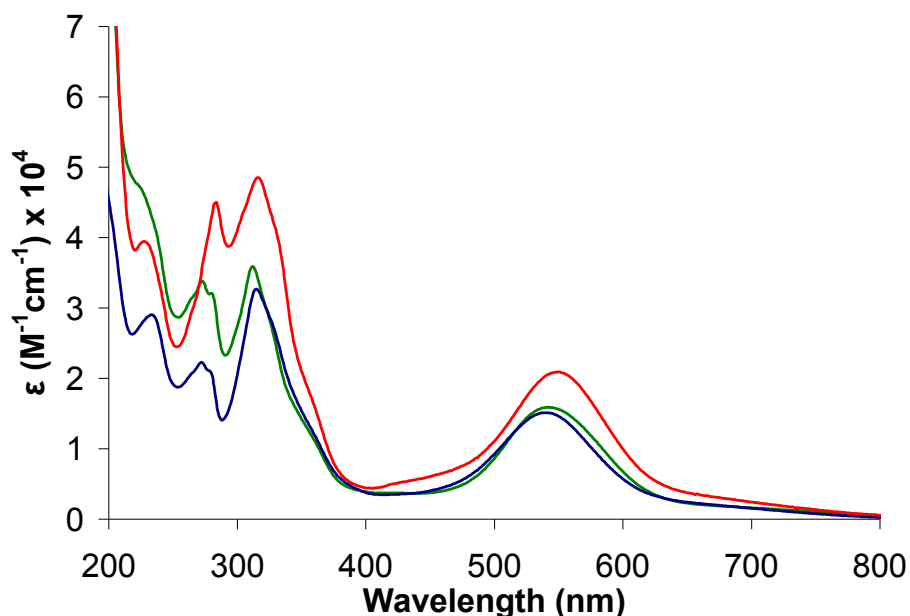


Figure 3.10. Electronic absorption spectroscopy of [(^tBu₃tpy)RuCl(dpp)PtCl₂](PF₆) (—), [(MePhtpy)RuCl(dpp)PtCl₂](PF₆) (—), and [(tpy)RuCl(dpp)PtCl₂](PF₆) (—) in CH₃CN at room temperature (tpy = 2,2':6',2''-terpyridine, MePhtpy = 4'-4-methylphenyl)-2,2':6',2''-terpyridine, ^tBu₃tpy = 4,4',4''-tri-tert-butyl-2,2':6',2''-terpyridine), and dpp = 2,3-bis(2-pyridyl)pyrazine).

3.6.4. Comparison of Electronic Absorption Properties of Monometallic and Bimetallic Complexes

The electronic properties of the bimetallic complexes were compared with their monometallic synthons. Figure 3.11 shows the electronic absorption spectra of bimetallic complex, [(tpy)RuCl(dpp)PtCl₂](PF₆), and its monometallic precursor, [(tpy)RuCl(dpp)](PF₆). The Ru→dpp CT band centered at 540 nm was red-shifted ca. 20 nm in the bimetallic complexes relative to the corresponding [(TL)RuCl(dpp)](PF₆) monometallic synthons. This red-shift is due to the stabilization of the dpp π* orbitals due to the coordination to the electropositive Pt(II)

metal center. Brewer and Yam have separately reported a similar red-shift in absorption upon platination of ruthenium-based chromophores.^{110,115,116}

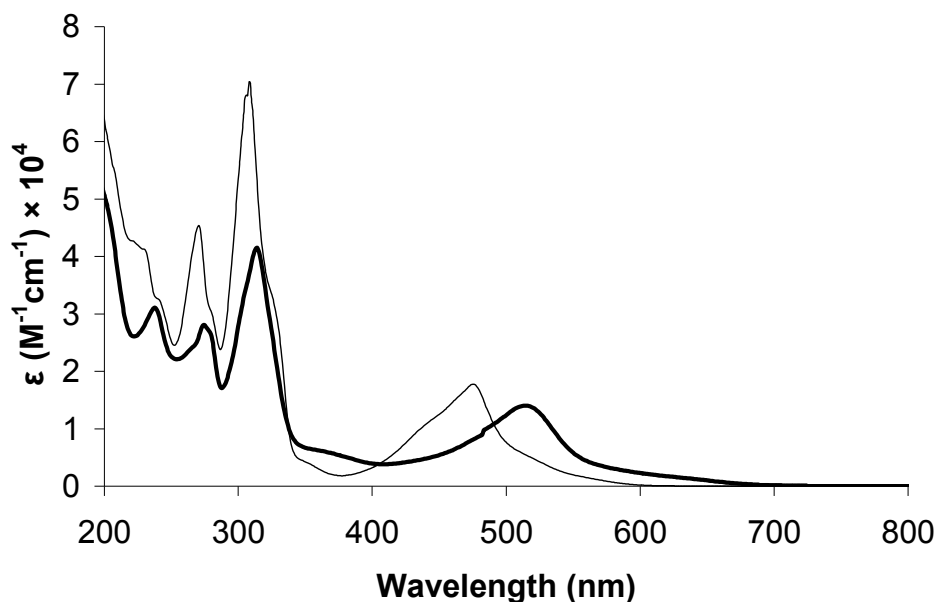


Figure 3.11. Electronic absorption spectroscopy of $[(\text{tpy})\text{RuCl}(\text{dpp})\text{PtCl}_2](\text{PF}_6)$ (—) and its monometallic precursor $[(\text{tpy})\text{RuCl}(\text{dpp})](\text{PF}_6)$ (---) in CH_3CN at room temperature (tpy = 2,2':6',2''-terpyridine and dpp = 2,3-bis(2-pyridyl)pyrazine).

3.7. Comparison of Electrochemical and Spectroscopic Properties

It has been shown that the oxidation and reduction potentials can be related to the CT energies, if both processes involve the same orbitals.¹⁴⁵⁻¹⁴⁹ The energy gap between HOMO and LUMO can be calculated from both electrochemical and spectroscopic studies. In ruthenium polypyridyl complexes the HOMO is metal-based and LUMO is ligand-based. For the lowest energy spin allowed MLCT transition the relationship between the spectroscopic energy gap between HOMO and LUMO and the first oxidation potential (E_{ox}) and first reduction potential (E_{red}) can be written as:¹⁴⁵

$$E_{\text{MLCT}} = E_{\text{ox}} - E_{\text{red}} + Q + \Delta\Delta G_s + \Delta(\text{sol}) + \chi_o + \chi_i \quad 3.1$$

where χ_o is the solvent reorganization energy and χ_i is the vibrational reorganizational energy associated with electronic transition. Q is the energy involved in transferring an electron from the reduced species to oxidized species, creating a ground state and excited state molecule. The term $\Delta\Delta G_s$ is $(2\Delta G_s^o - \Delta G_s^{o+} - \Delta G_s^{o-})$ and $\Delta(\text{sol})$ is $(\Delta G_s^{o*} - \Delta G_s^o)$ where G_s^o is the standard free energies of solvation of parent species, its oxidized form (ΔG_s^{o+}), reduced form (ΔG_s^{o-}), and excited form ΔG_s^{o*} . The ΔE_{redox} and $\lambda_{\text{max}}^{\text{abs}}$ of a series of ruthenium comphores containing tridentate terminal ligand and Ru^{II}Pt^{II} bimetallic complexes were compared, the values are reported in Tables 3.8 and 3.9). Plots of ΔE_{redox} versus ΔE_{MLCT} for the heteroleptic complexes containing tpy as a terminal ligand and Ru^{II}Pt^{II} bimetallic complexes are shown in Figure 3.12. A fit of the data for the heteroleptic complexes to a straight line resulted in a correlation coefficient of 0.91 with a slope of 0.71 and a y-intercept of 0.85. A fit of the data for the Ru^{II}Pt^{II} bimetallic to a straight line resulted in a correlation coefficient of 0.77 with a slope of 0.67 and a y-intercept of 1.07. A plot of ΔE_{redox} versus ΔE_{MLCT} of the tpy-containing chromophores and Ru^{II}Pt^{II} bimetallic complexes is shown in Figure 3.13. A fit of this data to a straight line resulted in a correlation coefficient of 0.87 with a slope of 0.57 and a y-intercept of 0.87. The scatter in these plots represents the variation in the solvation and reorganization energies as described by Lever and Bosworth.^{145,149}

The two plots (Figure 3.12 and 3.13) indicate that a linear correlation exists between the redox and spectroscopic properties to calculate the energy gap between HOMO and LUMO. The slopes of the two plots were found to be non unity, indicating the variation in solvation and reorganization energies.

Table 3.8. Electrochemical and spectroscopic properties of a series of ruthenium complexes incorporating tridentate, 2,2',6',2''-terpyridine (tpy) terminal ligand (bpy = 2,2'-bipyridine, tpp = 2,3,5,6-tetrakis (2-pyridyl)pyrazine, dpp = 2,3-bis(2-pyridyl)pyrazine, dpq = 2,3-bis(2-pyridyl)quinoxaline, dpb = 2,3-bis(2-pyridyl)benzoquinoxaline, MePhtpy = 4'-4-methylphenyl)-2,2':6',2''-terpyridine, ^tBu₃tpy = 4,4',4''-tri-tert-butyl-2,2':6',2''- terpyridine, and $\Delta E_{\text{redox}} = E_{\text{ox}} - E_{\text{red}}$).

Complex	ΔE_{redox}	$\lambda_{\text{max}}^{\text{abs}}$	Ref.
[Ru(tpp)(bpy)Cl] ⁺	2.03	504	134
[Ru(tpy)(tpp)] ²⁺	2.37	474	150
[Ru(tpp)(bpy)(CH ₃ CN)] ²⁺	2.33	456	151
[Ru(tpy)(dpq)Cl] ⁺	1.83	568	152
[Ru(tpy)(dpb)Cl] ⁺	1.63	598	152
[Ru(tpy)(dpp)(py)] ²⁺	2.46	482	152
[Ru(tpy)(dpq)(py)] ²⁺	2.16	522	152
[Ru(tpy)(dpb)(py)] ²⁺	2.03	558	152
[(MePhtpy)RuCl(bpy)] ⁺	2.14	510	143
[Ru(tpy)(dpp)Cl] ⁺	2.11	518	152
[(MePhtpy)RuCl(dpp)] ⁺	2.17	522	
[(^t Bu ₃ tpy)RuCl(dpp)] ⁺	2.20	521	

Table 3.9. Electrochemical and spectroscopic properties of a series of Ru^{II}Pt^{II} bimetallic complexes incorporating tridentate, 2,2',6',2''-terpyridine (tpy) terminal ligand (tpp = 2,3,5,6-tetrakis-(2-pyridyl)pyrazine, dpp = 2,3-bis(2-pyridyl)pyrazine, dpq = 2,3-bis(2-pyridyl)quinoxaline, dpb = 2,3-bis(2-pyridyl)benzoquinoxaline, MePhtpy = 4'-4-methylphenyl)-2,2':6',2''-terpyridine, ^tBu₃tpy = 4,4',4''-tri-tert-butyl-2,2':6',2''-terpyridine, and $\Delta E_{\text{redox}} = E_{\text{ox}} - E_{\text{red}}$).

Complex	ΔE_{redox}	$\lambda_{\text{max}}^{\text{abs}}$	Ref.
[(tpy)RuCl(dpp)PtCl ₂] ⁺	1.64	544	116
[(tpy)RuCl(dpq)PtCl ₂] ⁺	1.42	632	116
[(tpy)RuCl(dpb)PtCl ₂] ⁺	1.32	682	116
[(MePhtpy)RuCl(dpp)PtCl ₂] ⁺	1.65	540	
[(^t Bu ₃ tpy)RuCl(dpp)PtCl ₂] ⁺	1.60	542	
[(tpy)Ru(tpp)PtCl] ³⁺	1.79	530	153
[(tpy)RuCl(PEt ₂ Ph)(bpm)PtCl ₂] ⁺	1.97	560	117
[ClPt(tpp)Ru(tpp)PtCl] ⁴⁺	1.86	538	153

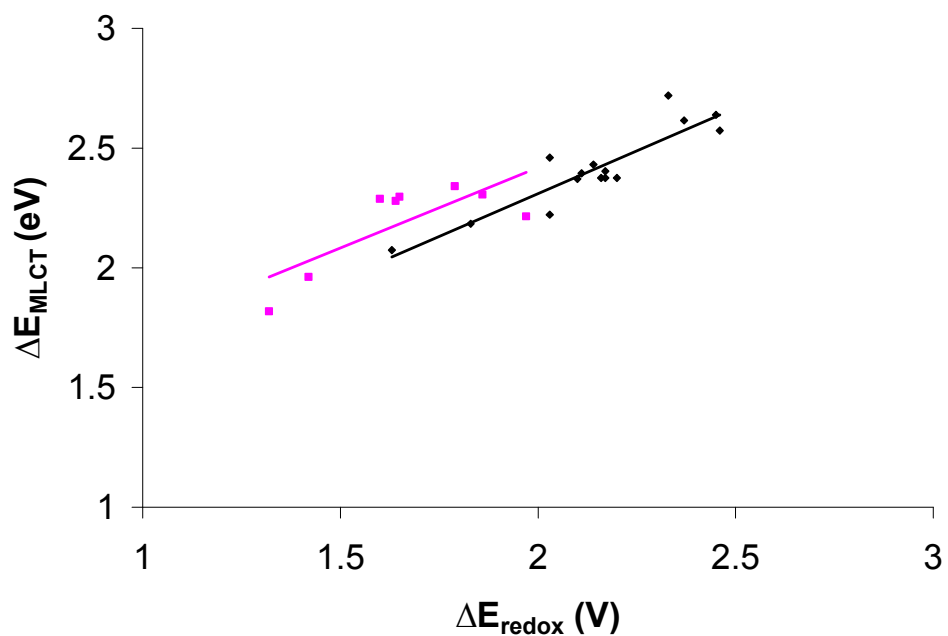


Figure 3.12 . The ΔE_{redox} versus ΔE_{MLCT} plot for a series of tpy-containing ruthenium chromophores (■) and $\text{Ru}^{\text{II}}\text{Pt}^{\text{II}}$ bimetallic complexes (■) in CH_3CN at RT.

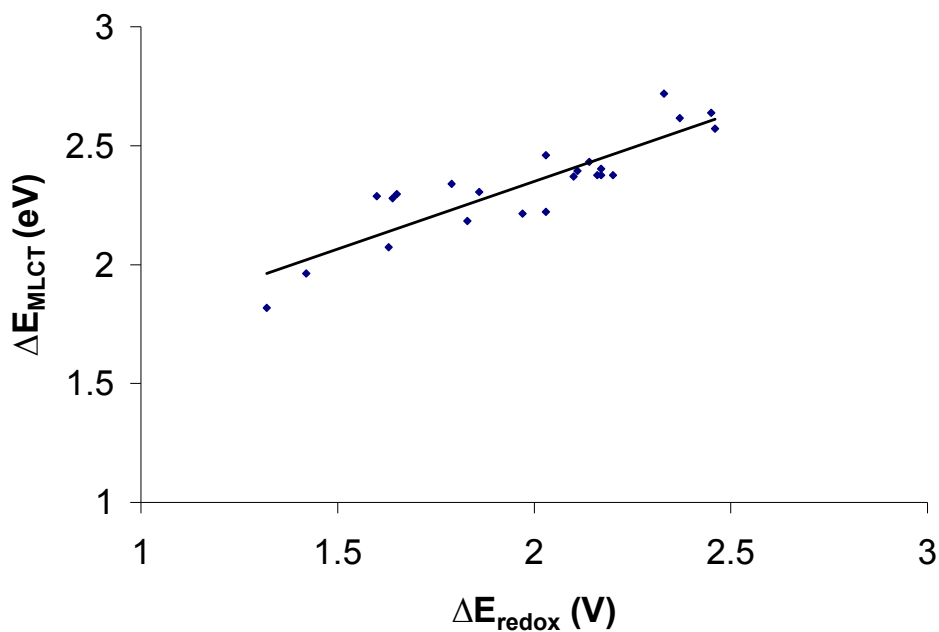


Figure 3.13. The ΔE_{redox} versus ΔE_{MLCT} plot for a series of tpy-containing ruthenium chromophores and $\text{Ru}^{\text{II}}\text{Pt}^{\text{II}}$ bimetallic complexes in CH_3CN at RT.

3.8. Emission Spectroscopy

3.8.1. Emission Spectroscopy: Heteroleptic Complexes

Emission spectroscopy was used to probe the excited state properties of the complexes. The heteroleptic complexes displayed weak emissions at room temperature in spectral grade acetonitrile solutions from the $^3\text{MLCT}$ state (Figure 3.14). The emission spectra for the heteroleptic complexes, $[(\text{TL})\text{RuCl}(\text{dpp})](\text{PF}_6)$, showed phosphorescence from the $\text{Ru} \rightarrow \text{dpp}$ based $^3\text{MLCT}$ state. The emission quantum yields were obtained with reference to the model complex, $[\text{Os}(\text{bpy})_3](\text{PF}_6)_2$ ($\Phi^{\text{em}} = 0.00462$; $\lambda_{\text{max}}^{\text{em}} = 746 \text{ nm}$) in CH_3CN .¹²⁶ The emission maxima occurred at 750 and 748 nm with emission quantum yields of $\Phi^{\text{em}} = 1.4 \times 10^{-4}$ and 9.8×10^{-5} , for $[(\text{tpy})\text{RuCl}(\text{dpp})](\text{PF}_6)$ and $[(\text{MePhtpy})\text{RuCl}(\text{dpp})](\text{PF}_6)$, respectively. Both the complex displayed almost equal emission quantum yields. The variation the terminal ligand had no impact on the quantum yield of the molecule.

The emission quantum yields obtained for these two complexes were higher than those reported for the homoleptic complexes (Table 3.10).^{56,58} The $^3\text{MLCT}$ states for the heteroleptic complexes are $\text{Ru} \rightarrow \text{dpp}$ charge transfer in nature and are stabilized due to the higher energy $\text{Ru}(d\pi)$ and lower energy $\text{dpp}(\pi^*)$ acceptor orbital. This stabilized MLCT state limits the thermal population of ^3LF state at room temperature, extending the $^3\text{MLCT}$ lifetime and quantum yield. However, the effect is not strong enough to completely prevent the thermal population of the ligand field state.

Table 3.10. Photophysical data for series of Ru(II) complexes containing tridentate terminal ligands.

Complex ^a	$\lambda_{\max}^{\text{abs}} \text{ RT}$ (nm)	$\lambda_{\max}^{\text{em}} \text{ RT}$ (nm)	τ_{RT} (ns)	Φ^{em} (RT)	$\lambda_{\max}^{\text{em}} 77 \text{ K}$ (nm)	$\tau_{77 \text{ K}}$ (μs)
$[(\text{MePhtpy})\text{RuCl}(\text{dpp})](\text{PF}_6)$	522	750	16	1.4×10^{-4}	705	3.3
$[(\text{tpy})\text{RuCl}(\text{dpp})](\text{PF}_6)$	516	748	17	9.8×10^{-5}	700	1.0
$[\text{Ru}(\text{MePhtpy})_2](\text{PF}_6)_2$	490	640 ^b	0.95 ^b	$3.2 \times 10^{-5 \text{ b}}$	628 ^b	9.1 ^b
$[\text{Ru}(\text{tpy})_2](\text{PF}_6)_2$	476	629 ^c	0.25 ^c	$5.0 \times 10^{-6 \text{ c}}$	598 ^c	11 ^c

$\lambda_{\max}^{\text{abs}}$ is absorption maximum, $\lambda_{\max}^{\text{em}}$ is emission maximum, τ_{RT} is lifetime at 298 K, $\tau_{77 \text{ K}}$ is lifetime at 77 K, Φ^{em} is quantum yield at room temperature measured relative to $[\text{Os}(\text{bpy})_3](\text{PF}_6)_2$. All experiments were performed in spectrograde CH_3CN .

^aMePhtpy = 4'-(4-methylphenyl)-2,2':6',2''-terpyridine, tpy = 2,2':6',2''-terpyridine, and dpp = 2,3-bis(2-pyridyl)pyrazine.

^bPhotophysical data previously reported Ref. 57.

^cPhotophysical data previously reported Ref. 59.

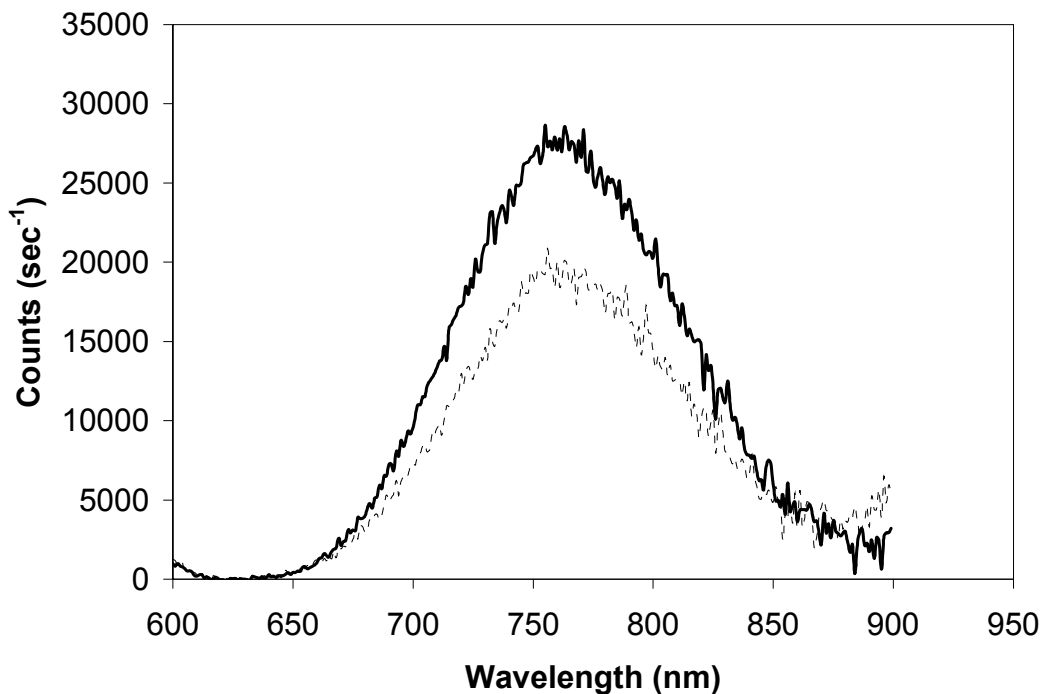


Figure 3.14. The emission spectra of the complexes, $[(\text{tpy})\text{RuCl}(\text{dpp})](\text{PF}_6)$ (.....) $[(\text{MePhpty})\text{RuCl}(\text{dpp})](\text{PF}_6)$ (—), in degassed CH_3CN at RT, where each emission data corrected for instrument response ($\lambda^{\text{ex}} = 520 \text{ nm}$, PMT = Hamamatsu 1527 red sensitive photomultiplier tube) (tpy = 2,2':6',2''-terpyridine, MePhpty = 4'-(4-methylphenyl)-2,2':6',2''-terpyridine, and dpp = 2,3-bis(2-pyridyl)pyrazine).

3.8.2. Emission Spectroscopy: Homoleptic Complexes

The tpy containing homoleptic complexes lack room temperature luminescence due to the low lying ^3LF state. At lower temperatures, thermal population of ligand field state is not possible and therefore luminescence is observed. The emission spectra of homoleptic complexes containing tpy, MePhpty, and $^t\text{Bu}_3\text{tpy}$ ligands in 4:1 ethanol/methanol glass at 77 K are shown in Figure 3.15. The emission spectra for these complexes showed phosphorescence from Ru \rightarrow tpy based $^3\text{MLCT}$ state. The emission maxima at 77 K occurred at 594, 595, and 621 nm for $[\text{Ru}(\text{tpy})_2](\text{PF}_6)_2$, $[\text{Ru}(^t\text{Bu}_3\text{tpy})_2](\text{PF}_6)_2$, and $[\text{Ru}(\text{MePhpty})_2](\text{PF}_6)_2$, respectively. The $[\text{Ru}(\text{MePhpty})_2](\text{PF}_6)_2$ complex exhibited red-shifted emission maxima compare to tpy and $^t\text{Bu}_3\text{tpy}$ containing complexes. This is due to the coplanarity of the phenyl ring with the pyridine ring upon excitation, which leads to extended electron delocalization of the π^* electron in the MLCT excited state of $[\text{Ru}(\text{MePhpty})_2](\text{PF}_6)_2$.¹⁵⁴ This prevents the degree of geometric distortion

upon formation of excited state and thereby increases the emission quantum yield. This is consistent with previous reports on tpy containing homoleptic complexes.¹⁵⁵⁻¹⁵⁷ The quantum yield of radiative decay of the luminescing state can be expressed by:¹⁵⁸

$$Q_r = \tau_0^{-1} / (\tau_0^{-1} + k_q) \quad 3.2$$

where k_q is the rate constant of the radiationless decay and τ_0 is radiative lifetime. The MePh substituent decreases K_q and therefore increases the emission quantum yield. Crosby and coworkers have observed similar increase in emission quantum yield for the metal complexes containing phenyl substituents.¹⁵⁸

The $[\text{Ru}(\text{}^t\text{Bu}_3\text{tpy})_2](\text{PF}_6)_2$ complex exhibited the lowest emission intensity compared to the other two homoleptic complexes. This is due to the presence of strong electron donating *t*-butyl groups on tpy ligand. In the ground state the electron donating groups on the ligand destabilize the π^* ligand centered orbital more than the metal centered orbitals. However in the excited state, the metal-based orbitals are strongly destabilized due to the presence of electron donating groups. This decreases the emission quantum yield. A similar trend was observed by Balzani and Sauvage for substituted tpy containing homoleptic complexes.^{58,144}

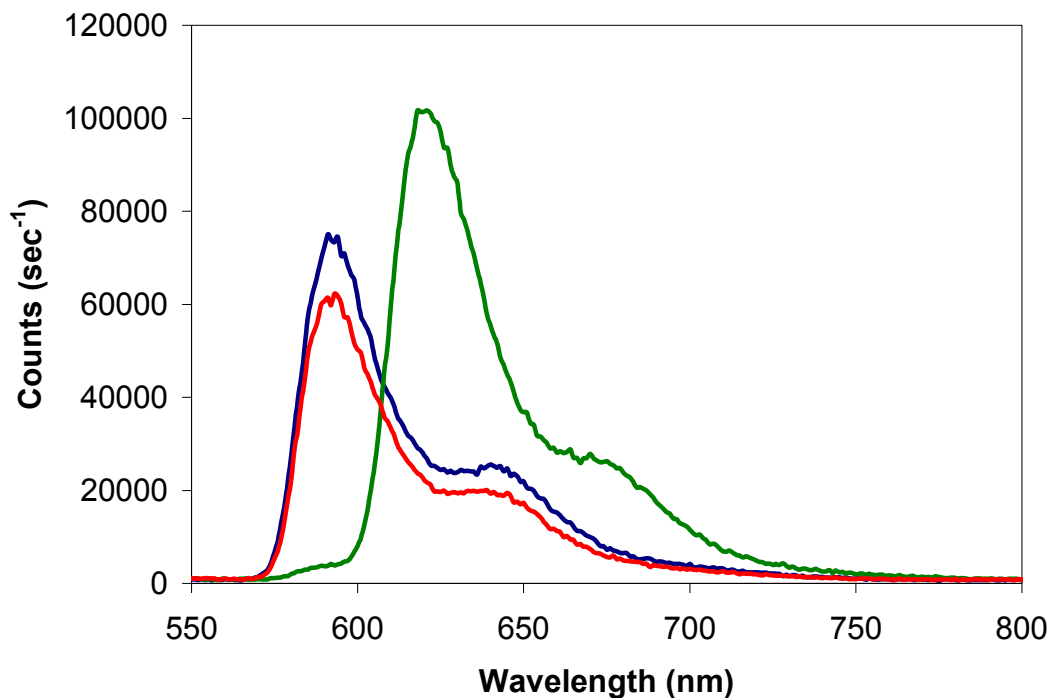


Figure 3.15. The 77 K emission spectrum for homoleptic complexes $[\text{Ru}(\text{MePhtpy})_2](\text{PF}_6)_2$ (—) $[\text{Ru}(\text{}^t\text{Bu}_3\text{tpy})_2](\text{PF}_6)_2$ (—), and $[\text{Ru}(\text{tpy})_2](\text{PF}_6)_2$ (—) (tpy = 2,2':6',2''-terpyridine, MePhtpy = 4'-(4-methylphenyl)-2,2':6',2''-terpyridine ${}^t\text{Bu}_3\text{tpy}$ = 4,4',4''-tri-tert-butyl-2,2':6',2''-terpyridine; and dpp = 2,3-bis(2-pyridyl)pyrazine) in 4:1 Ethanol:methanol mixture (λ^{ex} = 480 nm, PMT = Hamamatsu 1527 red sensitive photomultiplier tube).

3.9. Excited State Lifetime

3.9.1. Excited State Lifetime: Heteroleptic Complexes

The excited state lifetime of the ${}^3\text{MLCT}$ excited state was determined on a nanosecond timescale by monitoring the emission decay profile after excitation with a nitrogen dye laser. The excited state lifetimes of $[(\text{tpy})\text{RuCl}(\text{dpp})](\text{PF}_6)$ and $[(\text{MePhtpy})\text{RuCl}(\text{dpp})](\text{PF}_6)$ were found to be 17 and 16 nsec, respectively. These lifetimes are in agreement with the excited state lifetime of the previously reported $[(\text{MePhtpy})\text{RuCl}(\text{bpy})](\text{PF}_6)$ complex (13 nsec).¹⁴³ The ${}^3\text{MLCT}$ states for the heteroleptic complexes are Ru \rightarrow dpp charge transfer in nature and are stabilized due to the higher energy Ru($d\pi$) and lower energy dpp (π^*) acceptor orbital. This stabilized ${}^3\text{MLCT}$ state

limits the thermal population of ^3LF state at room temperature, extending the $^3\text{MLCT}$ lifetime. However, the effect is not strong enough to completely prevent the thermal population of the ^3LF state. This effect is consistent with prior reports on the properties of substituted bis-terpyridine complexes.⁴⁸ This extension of the $^3\text{MLCT}$ lifetime at room temperature for the heteroleptic complexes relative to the homoleptic complexes makes them chromophores of interest for applications in DNA-MC photochemistry. The coupling of an electron deficient Pt(II) center to the ruthenium chromophore stabilizes the dpp-based (π^*) orbital, stabilizing the $^3\text{MLCT}$ state which via energy gap law has a shorter lifetime.

3.9.2. Comparison of Photophysical Properties of Homoleptic and Heteroleptic Complexes

Incorporation of a polyazine bridging ligand into the molecular architecture leads to the modification in the photophysical properties of these complexes. The heteroleptic complexes displayed red shifted absorption and emission maxima compared to the homoleptic complexes. The LUMO in the heteroleptic complexes is dpp-based compared to the tpy-based LUMO in the homoleptic complexes. The dpp-based π^* orbital is more stabilized than the tpy-based π^* orbital. This reduces the energy gap between the HOMO and LUMO leading to the red shift in the absorption and emission maxima. The differences in photophysical properties of the designed molecules can be explained by the energy state diagrams, shown in Figure 3.16 and 3.17. The heteroleptic complexes possess longer excited state lifetime and higher emission quantum yield compared to the homoleptic complexes. This can be attributed to stabilization of the π^* orbital, on the dpp ligand leading to a stabilized $^3\text{MLCT}$ state. This stabilization of the $^3\text{MLCT}$ state limits thermal population of the ^3LF state. The thermal accessibility of the ^3LF state in tpy type complexes is due to the unfavorable bite angle for octahedral coordination associated with tpy type ligands, lowering the energy of the ligand field state.⁵³ The low lying ^3LF state quenches the emission of the normally emissive $^3\text{MLCT}$ state. The increase in energy difference between $^3\text{MLCT}$ state and ^3LF state extends the $^3\text{MLCT}$ excited state lifetimes of these chromophores.

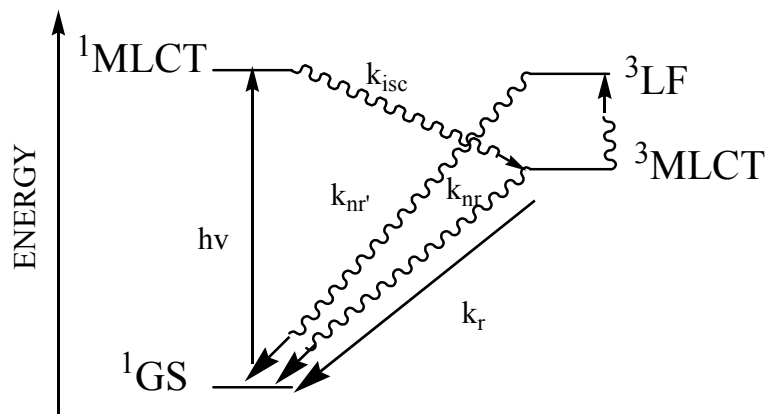


Figure 3.16. Jablonski diagram for $[\text{Ru}(\text{TL})_2]^{2+}$ (tpy = 2,2':6',2''-terpyridine; GS = ground state; MLCT = metal-to-ligand charge-transfer; k_{r} = rate constant for radiative decay; k_{nr} = rate constant for non-radiative decay; k_{isc} = rate constant for intersystem crossing).

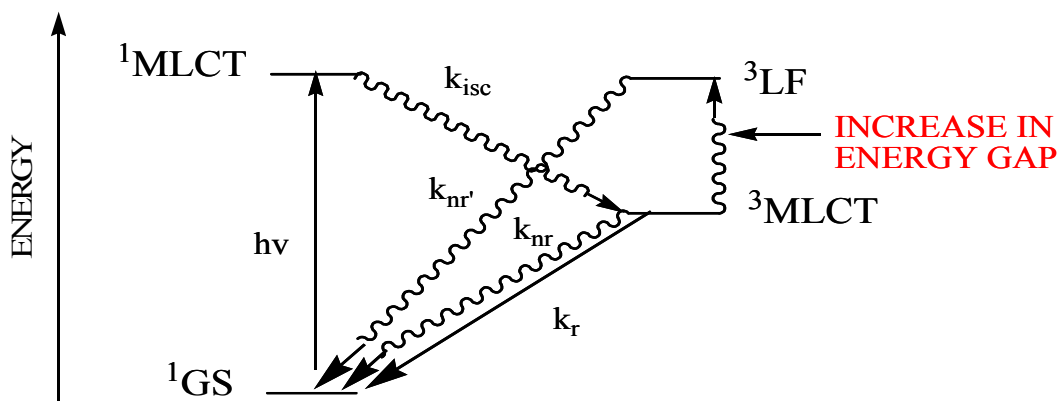


Figure 3.17. Jablonski diagram for $[(\text{tpy})\text{RuCl}(\text{dpp})]^+$ (tpy = 2,2':6',2''-terpyridine; GS = ground state; MLCT = metal to ligand charge-transfer; k_{r} = rate constant for radiative decay; k_{nr} = rate constant for non-radiative decay; k_{isc} = rate constant for intersystem crossing).

3.10. Partition Coefficient Determination

The partition coefficient of a molecule gives an indication of its potential to diffuse across the plasma membrane of a cell.^{159,160} If a molecule is added in a small quantity to two immiscible liquids like water and octanol, it distributes itself between the two solvents until the equilibrium is attained, and the ratio of the concentrations in each phase leads to a constant known as partition coefficient.

The partition coefficients of the designed molecules were determined using the “shake flask” method, with *n*-octanol and water as solvents, which was applied to the molecules with log P values that range from -2 (most hydrophilic) to +4 (most hydrophobic).¹⁶¹ The log P value in the range of 1 to 3 has good passive absorption across lipid membranes, and greater or less than 3 have poor transport properties.¹²⁷ The values of log P for the homoleptic and heteroleptic complexes are summarized in Table 3.11.

The unmodified tpy containing complexes displayed negative log P values in contrast to MePhtpy and ^tBu₃tpy type complexes, which showed positive log P values. The negative partition coefficients of the tpy type complexes illustrate the hydrophilic nature of these complexes. In contrast, the positive partition coefficients observed for complexes containing the MePhtpy and ^tBu₃tpy ligands, indicate that these molecule are lipophilic in nature. The log P value of +0.38 for [Ru(MePhtpy)₂]Cl₂ complex as compared to -0.49 for heteroleptic complex, [(MePhtpy)RuCl(dpp)]Cl is consistent with the presence of two hydrophobic MePh ligand in [Ru(MePhtpy)₂]Cl₂ and only one MePh ligand in [(MePhtpy)RuCl(dpp)]Cl.

The partition coefficients of homoleptic and heterobimetallic complexes are reported for the chloride salts because of the limited solubility of hexafluorophosphate salts in water and *n*-octanol. The negative values of the MePhtpy and ^tBu₃tpy containing complexes show their potential to cross the cell membrane and act as potential anticancer and/or antimicrobial agents.⁷¹

Table 3.11. Log P values for homoleptic and heteroleptic complexes.

Complex	log P
$[(^t\text{Bu}_3\text{tpy})\text{RuCl}(\text{dpp})]\text{Cl}$	+4.00
$[\text{Ru}(^t\text{Bu}_3\text{tpy})_2]\text{Cl}_2$	+4.00
$[(^t\text{Bu}_3\text{tpy})\text{RuCl}(\text{dpp})\text{PtCl}_2]\text{Cl}$	+4.00
$[\text{Ru}(\text{MePhtpy})_2]\text{Cl}_2$	+0.38
$[(\text{MePhtpy})\text{RuCl}(\text{dpp})]\text{Cl}$	-0.49
$[(\text{MePhtpy})\text{RuCl}(\text{dpp})\text{PtCl}_2]\text{Cl}$	-0.39
$[\text{Ru}(\text{tpy})_2]\text{Cl}_2$	-2.00
$[(\text{tpy})\text{RuCl}(\text{dpp})\text{PtCl}_2]\text{Cl}$	-2.00

Partition coefficient $P = C_i^o/C_i^w$ (C_i^o and C_i^w are the concentrations (moles/L) of the solute in the octanol and water respectively). (MePhtpy = 4'-(4-methylphenyl)-2,2':6',2''-terpyridine, dpp = 2,3-bis(2-pyridyl)pyrazine, tpy = 2,2':6',2''-terpyridine, and $^t\text{Bu}_3\text{tpy}$ = 4,4',4''-tri-tert-butyl-2,2':6',2''-terpyridine).

3.11. DNA-MC Binding Constant Determination

DNA binding constants were determined for the metal complexes by dialysis of calf thymus DNA in sodium phosphate buffer against metal complexes at room temperature. The results are shown in Figures 3.18 and 3.19 in the form of Scatchard plots. The data was fit by nonlinear least-squares analysis using the McGhee and von Hippel equation.¹³⁰

$$\left(\frac{r}{C_f}\right) = \left(\frac{K(0)}{2}\right)(1 - 2lr) \left(\frac{1 - 2lr}{1 - 2(l-1)r}\right)^{l-1} \quad 3.3$$

where r is the ratio of the bound concentration of metal complex to the DNA concentration, C_f is the concentration of free metal complex in solution, $K(0)$ is the intrinsic binding constant, and the integer l , which measures the size of a binding site in base pairs. In fitting the data, the binding parameter $K(0)$ was varied for several integer values of l . The best fit is shown as the solid curves in Figure 3.18 and 3.19.

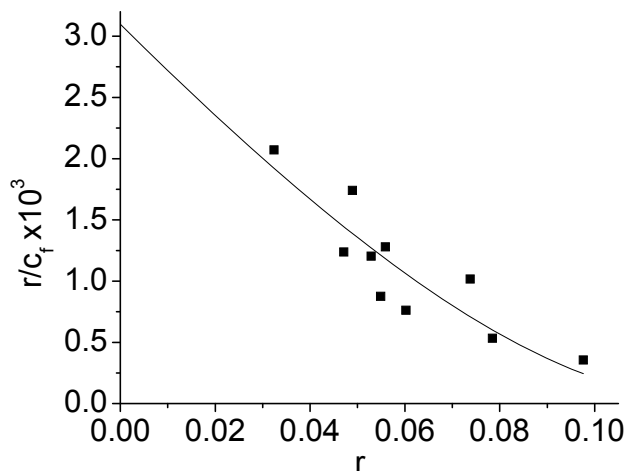


Figure 3.18. Representative Scatchard plot of binding isotherm for [(MePhtpy)RuCl(dpp)]Cl with calf thymus DNA in buffer at room temperature, where r is the ratio of bound metal complex to nucleotide concentrations and c is the concentration of the free metal complex. The solid line is the best fit to the McGhee and von Hippel equation.¹³⁰

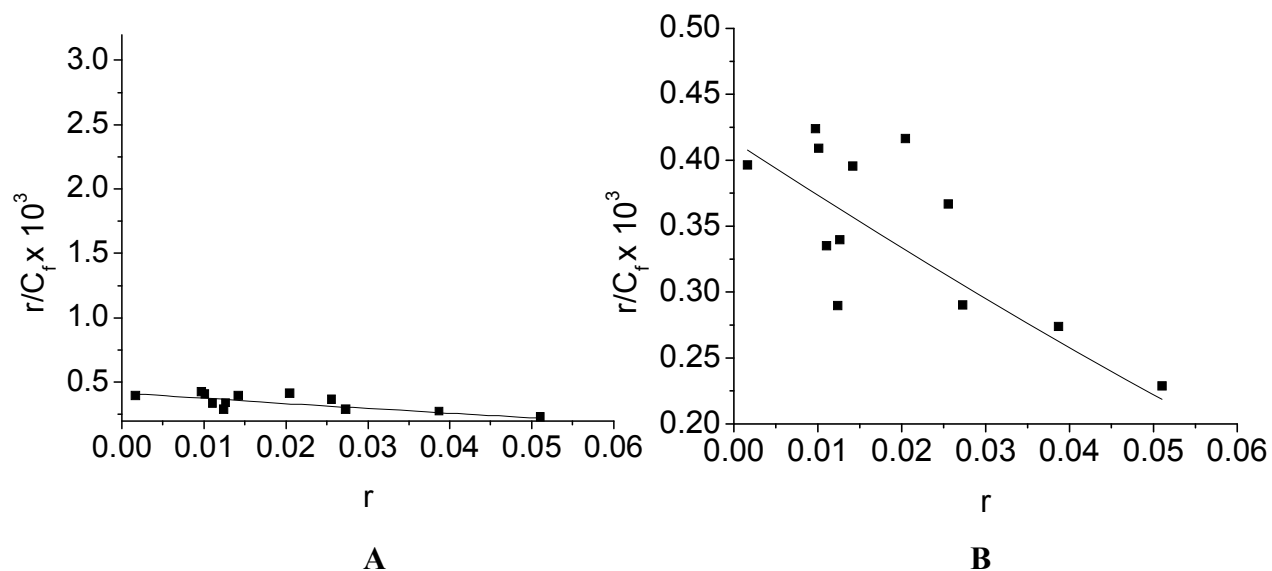


Figure 3.19. Representative Scatchard plot of binding isotherm for [(tpy)RuCl(dpp)]Cl with calf thymus DNA in buffer at room temperature (A). Plot B represents the Scatchard plot of binding isotherm for [(tpy)RuCl(dpp)]Cl with calf thymus DNA in buffer at room temperature with lower values of r/C_f (r is the ratio of bound metal complex to nucleotide concentrations and c is the concentration of the free metal complex). The solid lines are the best fits to the McGhee and von Hippel equation.¹³⁰

The DNA binding constants obtained for [(MePhtpy)RuCl(dpp)]Cl and [(tpy)RuCl(dpp)]Cl via the dialysis experiments were found to be $6.2 \times 10^3 \text{ M}^{-1}$ and $8.8 \times 10^2 \text{ M}^{-1}$, respectively with binding size in base pair, (l) = 4. The binding constant for the [(MePhtpy)RuCl(dpp)]Cl complex was found to be 10 times higher in magnitude than that determined for [(tpy)RuCl(dpp)]Cl. The latter is comparable to the binding constant of [(tpy)Ru(bpy)OH]²⁺ with DNA (6.6×10^2).¹⁶² Similarly, the binding constant obtained for [(MePhtpy)RuCl(dpp)]Cl is comparable to that of a well studied DNA minor groove binding complex, [Ru(phen)₃]²⁺ (6.2×10^3).¹⁶³ Due to the precipitation of the [(^tBu₃tpy)RuCl(dpp)]Cl inside the dialysis bag as a result of its hydrophobic nature, we were unable to determine the binding constant for this molecule.

3.12. DNA Interaction Studies

Agarose gel electrophoresis was used to assay the DNA binding and photocleavage properties of the metal complexes. The mobility of DNA on an agarose gel depends upon the molecular weight, molecular shape, charge, and the applied voltage. The DNA photocleavage activity of the complexes was probed using circular pUC18 plasmid DNA while DNA binding properties were assayed using linearized pUC18 DNA over a range of DNA base pair (BP) to metal complex (MC) ratios.

3.12.1. DNA Photocleavage Properties: Homoleptic Complexes

The ability of the homoleptic complexes, [Ru(tpy)₂](PF₆)₂, [Ru(MePhtpy)₂](PF₆)₂, and [Ru(^tBu₃tpy)₂](PF₆)₂, to photocleave DNA was examined using agarose gel electrophoresis of circular pUC18 plasmid DNA. Circular plasmid DNA is ideally suited to probe cleavage events as the plasmid DNA exists in a supercoiled state in its native form and converts to a relaxed form upon single strand cleavage. The supercoiled form being very compact migrates faster than the open circular or relaxed form. The change in the supercoiled state of DNA to an open circular or relaxed state is indicative of DNA cleavage.

In DNA photocleavage studies metal complexes were combined with pUC18 DNA at a 5:1 basepair (BP): metal complex (MC) ratio in an aqueous 10 mM sodium phosphate buffer, pH 7.0. The solutions were photolyzed with a wavelength-filtered 1000 W Xe arc lamp $k_{\text{irr}} = 450\text{--}1000$ nm for 2 hrs and assayed immediately after photolysis using agarose gel electrophoresis. Representative results of the DNA photocleavage studies are shown in Figure 3.20. In each panel, λ is the molecular weight standard (24, 9.4, 6.6, 4.4, 2.2, 2.0, 0.56 kb); C is the DNA control, showing that pUC18 DNA exists mostly in the supercoiled state together with a small amount of nicked circular DNA; MC is DNA incubated with the metal complex in the dark at room temperature showing the lack of covalent binding of this MC to DNA; O₂ is DNA and metal complex irradiated with 450–1000 nm light for 2 hrs under atmospheric conditions; Ar is DNA and metal complex irradiated with 450–1000 nm light for 2 hrs under argon. The gel (Figure 3.20) illustrates that no photocleavage was observed when pUC18 DNA was irradiated ($\lambda_{\text{irr}} \geq 450$ nm) for 2 hrs in the presence of the complex, [Ru(tpy)₂](PF₆)₂, under atmospheric conditions, consistent with the literature.⁶⁹ The very short ³MLCT lifetime of this complex prohibits significant oxygen quenching, leading to the observed lack of DNA photodamage.

The [Ru(MePhtpy)₂](PF₆)₂ complex displayed photocleavage activity upon irradiation with xenon arc lamp (450-1000 nm) under atmospheric conditions (second gel in Figure 3.20). In the absence of oxygen (lane Ar), no photocleavage was observed. Thus, the [Ru(MePhtpy)₂](PF₆)₂ complex appears to cleave DNA via an oxygen mediated pathway, likely through ¹O₂ generation, typical of ruthenium(II) polypyridyl complexes.⁶⁴⁻⁶⁶ The enhanced photocleavage activity shown by the [Ru(MePhtpy)₂](PF₆)₂ complex likely results from the higher ³MLCT lifetime and enhanced DNA binding. The aryl substituted ruthenium bis-terpyridine complexes have been shown to intercalate and/or groove bind DNA.⁷⁰ Ding and coworkers have demonstrated the effects of substituted aryl groups on ¹O₂ generation and DNA photocleavage properties.⁷⁰ The ruthenium bis-terpyridine complex possessing a 4' biphenyl tail has been shown to exhibit groove binding.¹⁶⁴ The enhanced DNA binding of metal complexes possessing a MePhtpy group could thus be due to the groove binding of the aryl group.

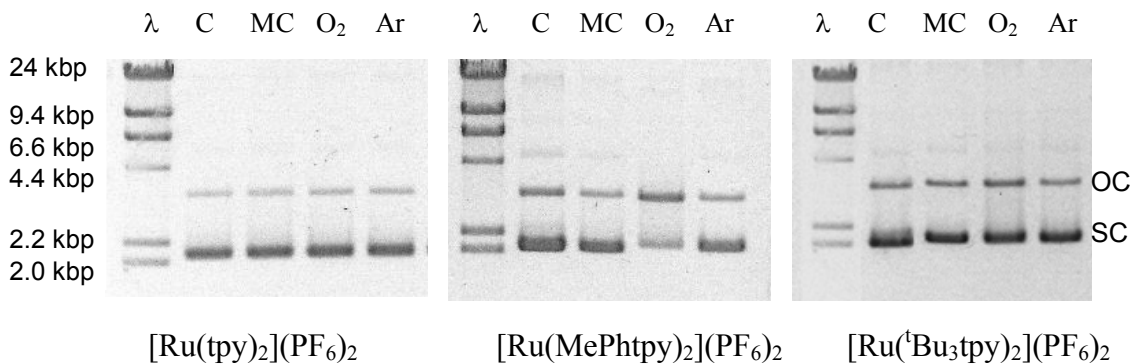


Figure 3.20. DNA photocleavage by Ru(II) terpyridine complexes assayed with 0.8% agarose gel electrophoresis using circular plasmid pUC18 DNA (MePhtpy = 4'-(4-methylphenyl)-2,2':6',2''-terpyridine, dpp = 2,3-bis(2-pyridyl)pyrazine, tpy = 2,2':6',2''-terpyridine, ^tBu₃tpy = 4,4',4''-tri-tert-butyl-2,2':6',2''-terpyridine). λ is the molecular weight standard (24, 9.4, 6.6, 4.4, 2.2, 2.0 kb), C is the DNA control, MC is 5:1 base pair (BP):metal complex (MC) kept in the dark at room temperature, O₂ is 5:1 BP/MC photolyzed with 450 nm –1000 nm light for 2 hrs under atmospheric conditions, Ar is 5:1 BP/MC photolyzed with 450 nm –1000 nm light for 2 hrs (OC = open circular DNA, SC = supercoiled DNA).

The [Ru(^tBu₃tpy)₂](PF₆)₂ complex displayed minimal photocleavage activity upon irradiation with a xenon arc lamp (450-1000 nm) under atmospheric conditions (third gel in Figure 3.20). The bulkiness of ^tBu₃tpy ligand could restrict the proximity of this complex to DNA.

The results of DNA photocleavage studies of the homoleptic complexes are in accord with the DNA interaction and photophysical properties of these molecules. The MePhtpy containing complex exhibits longer excited state lifetime, higher emission quantum yield, and improved DNA interaction compared to other two complexes and also displays enhanced DNA photocleavage as compared to the [Ru(tpy)₂](PF₆)₂ and [Ru(^tBu₃tpy)₂](PF₆)₂ complexes which appear to have no such activity. The DNA photocleavage exhibited by the MePhtpy containing chromophore displays the potential of this class of generally unexplored light absorbers for DNA-MC photochemistry.

3.12.2. DNA Photocleavage Properties: Heteroleptic Complexes

The DNA photocleavage properties of the heteroleptic complexes were also assessed by agarose gel electrophoresis of circular pUC18 plasmid DNA. The results of the DNA

minimal photocleavage was observed for $[(^t\text{Bu}_3\text{tpy})\text{RuCl}(\text{dpp})](\text{PF}_6)$ under same conditions. The more pronounced effect of the $[(\text{MePhtpy})\text{RuCl}(\text{dpp})](\text{PF}_6)$ complex could result from a higher degree of DNA interaction relative to the other two complexes. The Ar lane in the $[(\text{MePhtpy})\text{RuCl}(\text{dpp})](\text{PF}_6)$ gel suggests that the $[(\text{MePhtpy})\text{RuCl}(\text{dpp})](\text{PF}_6)$ photobinds DNA. This is most evident in the Ar lane which removes photocleavage effects (second gel in Figure 3.21). However the lifetime of $^3\text{MLCT}$ state is longer and can lead to higher yields on photoreactions that are oxygen independent. The stronger association of the $[(\text{MePhtpy})\text{RuCl}(\text{dpp})](\text{PF}_6)$ with DNA relative to $[(\text{tpy})\text{RuCl}(\text{dpp})](\text{PF}_6)$ likely results in higher yields of DNA-metal complex photobinding. The binding constant obtained for $[(\text{MePhtpy})\text{RuCl}(\text{dpp})]\text{Cl}$ ($6.2 \times 10^3 \text{ M}^{-1}$) was found to be almost 10 times higher than that determined for $[(\text{tpy})\text{RuCl}(\text{dpp})]\text{Cl}$ ($8.8 \times 10^2 \text{ M}^{-1}$). Due to the hydrophobic nature of $[(^t\text{Bu}_3\text{tpy})\text{RuCl}(\text{dpp})](\text{PF}_6)$, we could not perform dialysis experiments and therefore were unable to determine its binding constant with DNA. The enhanced DNA reactivity associated with the presence of a MePhtpy ligand in $[(\text{MePhtpy})\text{RuCl}(\text{dpp})]\text{Cl}$ makes this a complex of interest as a light absorbing unit in more extended supramolecular assemblies.

3.12.3. DNA Photo Binding Properties: $[(\text{MePhtpy})\text{RuCl}(\text{dpp})]\text{Cl}$

The observed photobinding of metal complex, $[(\text{MePhtpy})\text{RuCl}(\text{dpp})]\text{Cl}$, through gel electrophoresis was confirmed via DNA precipitation studies. The DNA precipitation experiments were adapted from previously reported procedures.¹¹⁶ Solutions of calf thymus DNA and $[(\text{MePhtpy})\text{RuCl}(\text{dpp})]\text{Cl}$ at 5:1 BP:MC ratio were photolyzed using a 5 W, 455 nm light emitting diode (LED). DNA was selectively precipitated by addition of 5 M NaCl and 95% ethanol to an aliquot of photolysis solution. The supernatant was collected followed by vortexing for 5 minutes and the absorbance at 520 nm was measured. A plot of absorbance of supernatant versus photolysis time is shown in Figure 3.22.

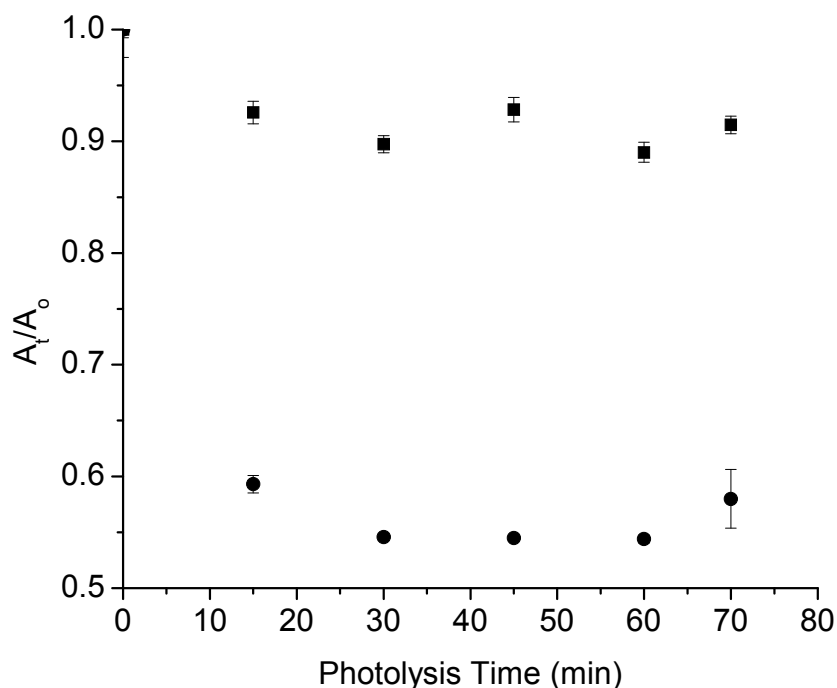


Figure 3.22. DNA photobinding assay of $[(\text{MePhtpy})\text{RuCl}(\text{dpp})]\text{Cl}$ complex using calf thymus DNA at 5:1 BP:MC ratio DNA (MePhtpy = 4'-(4-methylphenyl)-2,2':6',2''-terpyridine, dpp = 2,3-bis(2-pyridyl)pyrazine). Plot displays the absorbance at 520 nm of remaining $[(\text{MePhtpy})\text{RuCl}(\text{dpp})]\text{Cl}$ in the solution followed by photolysis and selective precipitation of DNA versus time. A 5 W, 455 nm LED was used for photolysis. Sample points (●) were compared with that of dark control (■).

Figure 3.22 displays the DNA photobinding assay of the $[(\text{MePhtpy})\text{RuCl}(\text{dpp})]\text{Cl}$ complex. Decrease in the concentration of the metal complex remaining in the solution was observed with increased photolysis. This is due to the selective precipitation of DNA-bound metal complex. At longer photolysis time no change in absorbance was observed. The absorbance of dark control did not change with time. This result gives the binding site size of 12.5 BP/MC, consistent with the molecular size of the complex. This assay confirms that the $[(\text{MePhtpy})\text{RuCl}(\text{dpp})]\text{Cl}$ complex binds with DNA under photolysis conditions.

3.12.5. DNA Binding Properties: Bimetallic Complexes

The DNA binding ability of the heterobimetallic complexes, $[(TL)RuCl(dpp)PtCl_2](PF_6)$, was explored using agarose gel electrophoresis. These metal complexes contain a *cis*- $Pt^{II}Cl_2$ moiety, which is known to covalently bind to DNA and is the basis of a class of anticancer agents. The covalent binding of the metal complexes to DNA increases the molecular weight and decreases the net negative charge, and as a result slows down the migration of DNA in an agarose gels. Figure 3.23 shows the gel electrophoresis studies of the interactions of these complexes with linearized pUC18 plasmid DNA as compared to the standard, cisplatin. In this study, each metal complex was combined with linearized pUC18 plasmid DNA at a range of BP to MC ratios. These mixtures were incubated for 2 hrs at 37°C and analyzed by agarose gel electrophoresis as shown in Figure 3.23. Lane λ is the molecular weight standard (24, 9.4, 6.6, 4.4, 2.2, 2.0, 0.56 kb), lane C is the pUC18 DNA control without any metal complex present, lane 5:1 is the pUC18 DNA incubated with 5:1 BP:MC, lane 10:1 is the pUC18 DNA incubated with 10:1 BP:MC, and lane 20:1 is the pUC18 DNA incubated with 20:1 BP:MC.

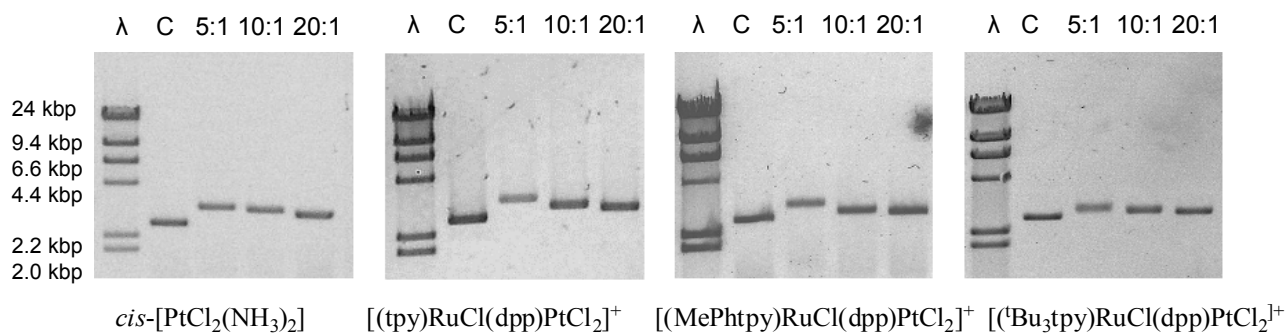


Figure 3.23. DNA binding study for $[(TL)RuCl(dpp)PtCl_2](PF_6)$ by agarose gel electrophoresis using linearized pUC18 DNA (dpp = 2,3-bis(2-pyridyl)pyrazine, TL = terminal ligand (tpy = 2,2':6',2''-terpyridine, MePhtpy = 4'-(4-methylphenyl)-2,2':6',2''-terpyridine, tBu_3tpy = 4,4',4''-tri-tert-butyl-2,2':6',2''-terpyridine). Lane 1 is the molecular weight standard (9.4, 6.6, 4.4, 2.3, and 2.0 kbp), lane 2 is the DNA control, lane 3 is the 5:1 base pairs (BP):metal complex (MC) ratio, lane 4 is the 10:1 BP:MC ratio, and lane 5 is the 20:1 BP:MC ratio.

Cisplatin is known to form coordinate covalent bonds with DNA and this can be visualized as a decrease in DNA migration through the gel with the increase of MC

concentration moving from lane 20:1 to 10:1 to 5:1. This results from both a decrease in the negative charge of DNA upon covalent binding of a Pt^{II} center as well as changes in the size and molecular weight of the DNA upon metal complex binding. The [(tpy)RuCl(dpp)PtCl₂](PF₆) and [(MePhtpy)RuCl(dpp)PtCl₂](PF₆) complexes exhibited coordinate covalent binding to DNA with significant retardation of pUC18 plasmid DNA migration through the gel and with a greater effect at lower BP:MC ratios or higher metal complex concentrations. The reduction of the DNA migration through the gel was found to be greater for these two complexes as compared to cisplatin. These types of metal complexes and cisplatin have been shown to bind to the guanine (G-7) base of DNA.¹²⁰ The [(^tBu₃tpy)RuCl(dpp)PtCl₂](PF₆) complex displayed a somewhat smaller effect on DNA migration through the agarose gel. The introduction of the t-butyl groups on the terpyridine ligand makes the molecule sterically hindered relative to the unsubstituted tpy containing complex and provides a lipophilic site remote from *cis*-Pt^{II}Cl₂ site. Due to the steric hindrance, it may be difficult for *cis*-Pt^{II}Cl₂ subunits of this metal complex to reach the G-7 of DNA or the molecule may orient itself where the ^tBu₃tpy ligand directed towards the DNA. Baguely and coworkers have also shown that the presence of bulky groups lowers the DNA binding and cytotoxicity of an organic DNA intercalator, amsacrine (N-(4-(acridin-9-ylamino)-3-methoxyphenyl)methanesulfonamide).¹⁶⁵

3.12.5. *R_f* value Determination

The agarose gel electrophoresis displayed DNA-MC binding for the Ru^{II}Pt^{II} bimetallic complexes. However, these observations were made purely by visual inspection. To quantitate the migration of the DNA-MC adducts the *R_f* values were determined as shown in Table 3.12.

Table 3.12. R_f values of Ru^{II}Pt^{II} bimetallic complexes and standard cisplatin. The R_f values were calculated by dividing the distance traveled by the DNA-MC adduct by the distance traveled by the 2.0 kb band of the molecular weight standards (dpp = 2,3-bis(2-pyridyl)pyrazine, tpy = 2,2':6',2''-terpyridine, MePhtpy = 4'-(4-methylphenyl)-2,2':6',2''-terpyridine, ^tBu₃tpy = 4,4',4''-tri-tert-butyl-2,2':6',2''-terpyridine).

Metal complex	Control	5:1 BP:MC	10:1 BP:MC	20:1 BP:MC
Cisplatin	0.80	0.68	0.71	0.75
[(tpy)RuCl(dpp)PtCl ₂](PF ₆)	0.78	0.62	0.66	0.74
[(MePhtpy)RuCl(dpp)PtCl ₂](PF ₆)	0.79	0.64	0.70	0.73
[(^t Bu ₃ tpy)RuCl(dpp)PtCl ₂](PF ₆)	0.80	0.74	0.75	0.77

The R_f values of the designed metal complexes, [(tpy)RuCl(dpp)PtCl₂](PF₆) and [(MePhtpy)RuCl(dpp)PtCl₂](PF₆) were found to be lower than the R_f value of cisplatin at BP:MC ratio of 5:1. This suggests that these complexes reduce the migration of DNA on an agarose more efficiently than cisplatin. However the R_f value of [(^tBu₃tpy)RuCl(dpp)PtCl₂](PF₆) was found to be higher than that of cisplatin at 5:1 BP:MC ratio. Increase in R_f values was observed with increased in BP:MC ratios or decreased MC or cisplatin concentrations. Higher R_f factor values of [(^tBu₃tpy)RuCl(dpp)PtCl₂](PF₆) compared to [(tpy)RuCl(dpp)PtCl₂](PF₆) and [(MePhtpy)RuCl(dpp)PtCl₂](PF₆) suggest that this complex binds to DNA less efficiently than the other two homoleptic complexes. This could be due to the steric hindrance, it may be difficult for the *cis*-Pt^{II}Cl₂ subunits of this metal complex to reach the G-7 of DNA or the molecule may orient itself with the ^tBu₃tpy ligand directed towards the DNA. Figure 3.24 displays the interaction of [(^tBu₃tpy)RuCl(dpp)PtCl₂](PF₆) complex with DNA. The cisplatin bound DNA fragment was taken from the Protein data bank.²² The bound cisplatin was replaced by the [(^tBu₃tpy)RuCl(dpp)PtCl₂](PF₆) complex. The [(^tBu₃tpy)RuCl(dpp)PtCl₂](PF₆) was oriented to make a coordinate bond between Pt and DNA bases. The CAChe structure displaying DNA-[(^tBu₃tpy)RuCl(dpp)PtCl₂](PF₆) complex interaction is shown in Figure 3.24.

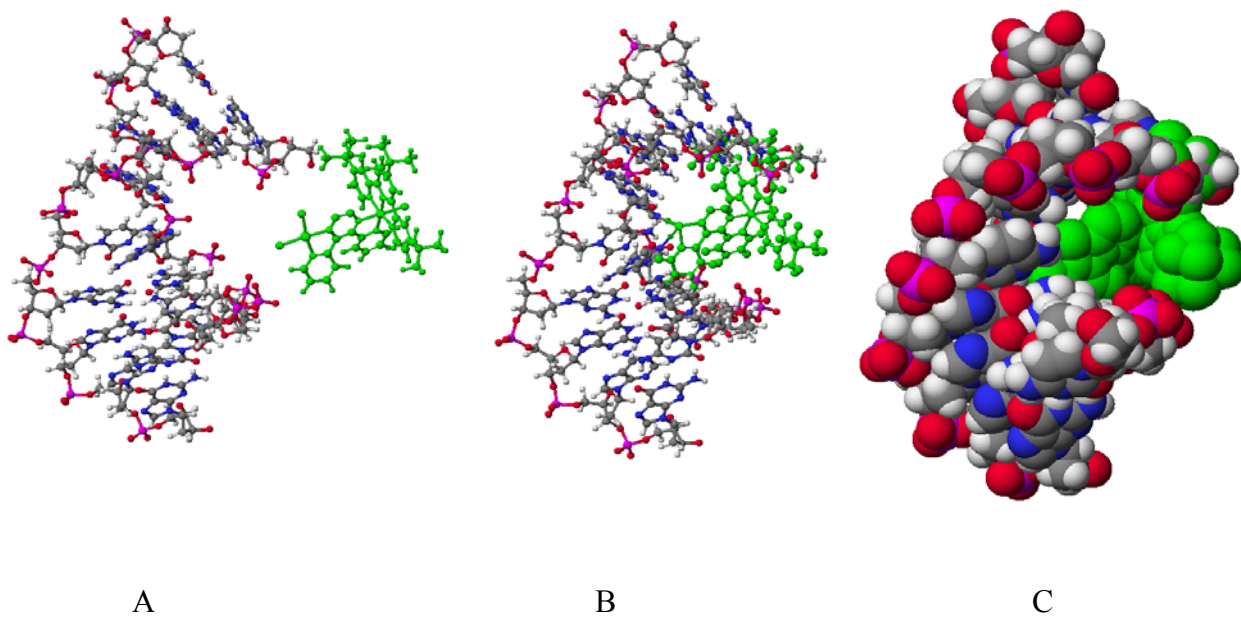


Figure 3.24. CAChe figure displaying DNA interaction of $[(^t\text{Bu}_3\text{tpy})\text{RuCl}(\text{dpp})\text{PtCl}_2](\text{PF}_6)$ ($\text{dpp} = 2,3\text{-bis}(2\text{-pyridyl})\text{pyrazine}$, $^t\text{Bu}_3\text{tpy} = 4,4',4''\text{-tri-tert-butyl-}2,2':6',2''\text{-terpyridine}$). A = ball and cylinder model showing proximity of DNA and metal complex. B = ball and cylinder model displaying the sterics associated with the interaction of $[(^t\text{Bu}_3\text{tpy})\text{RuCl}(\text{dpp})\text{PtCl}_2](\text{PF}_6)$ with DNA and C = space filling model displaying the sterics associated with the interaction of $[(^t\text{Bu}_3\text{tpy})\text{RuCl}(\text{dpp})\text{PtCl}_2](\text{PF}_6)$ with DNA. All the atoms of $[(^t\text{Bu}_3\text{tpy})\text{RuCl}(\text{dpp})\text{PtCl}_2](\text{PF}_6)$ are shown as green spheres in order to achieve a better picture of DNA-MC interaction. In DNA molecule, $\text{Pt} = \text{grey}$, $\text{C} = \text{black}$, $\text{N} = \text{blue}$, $\text{P} = \text{red}$, $\text{H} = \text{white}$.

3.12.5. DNA Photocleavage Properties: $\text{Ru}^{\text{II}}\text{Pt}^{\text{II}}$ Bimetallic Complexes

The stabilization of the $^3\text{MLCT}$ due to the coordination of Pt and enhanced association with DNA should make the bimetallic complexes even better photocleaving agents than corresponding monometallic precursors. The ability of the heterobimetallic complexes to photocleave DNA was studied by agarose gel electrophoresis using circular pUC18 plasmid DNA (Figure 3.25). In this study metal complexes were combined with pUC18 DNA at a 20:1 BP:MC ratio. The mixtures were irradiated with visible light ($\lambda_{\text{irr}} \geq 450\text{-}1000\text{ nm}$) for 2 hrs and the ability to photocleave DNA was analyzed by gel electrophoresis. In each panel, λ is the molecular weight standard, C is the DNA control showing that untreated pUC18 exists mostly in the supercoiled state together with a small amount of nicked circular DNA, RT is DNA

incubated with the metal complex in the dark at room temperature, 37 is DNA incubated with the metal complex in the dark at 37°C, O₂ is DNA and metal complex irradiated with 450–1000 nm light for 2 hrs under atmospheric conditions, and Ar is DNA and metal complex irradiated with 450–1000 nm light for 2 hrs under argon.

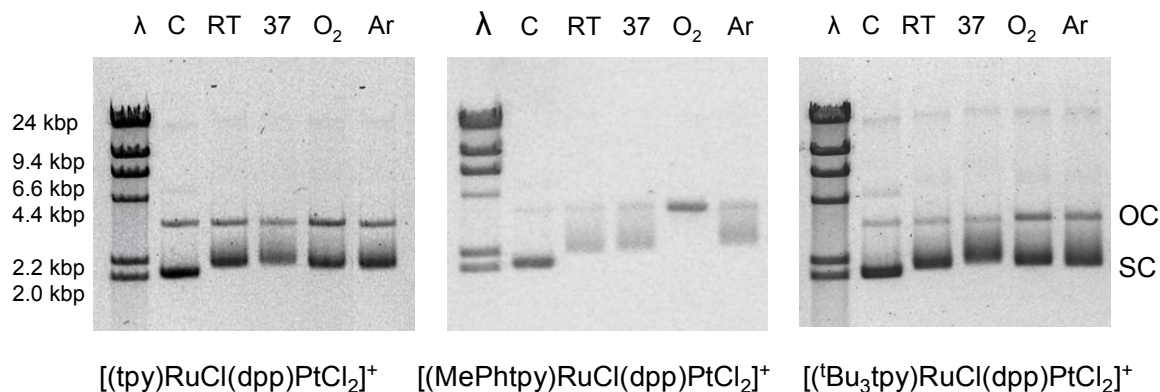


Figure 3.25. DNA binding and photocleavage study for [(TL)RuCl(dpp)PtCl₂](PF₆) by agarose gel electrophoresis using circular pUC18 DNA (dpp = 2,3-bis(2-pyridyl)pyrazine, TL = terminal ligand (tpy = 2,2':6',2''-terpyridine, MePhtpy = 4'-(4-methylphenyl)-2,2':6',2''-terpyridine, ^tBu₃tpy = 4,4',4''-tri-tert-butyl-2,2':6',2''-terpyridine). λ is the molecular weight standard (9.4, 6.6, 4.4, 2.3, and 2.0 kbp), C is the DNA control, RT is the 20:1 BP:MC incubated at room temperature for 2 hrs, 37 is the 20:1 BP:MC incubated at 37°C for 2 hrs, O₂ is 20:1 base pair (BP): metal complex (MC) photolyzed with 450 nm–1000 nm light for 2 hrs under atmospheric conditions, and Ar is 20:1 BP:MC photolyzed with 450 nm–1000 nm light for 2 hrs in the absence of oxygen (OC = open circular DNA, SC = supercoiled DNA).

The gel electrophoresis studies using circular pUC18 plasmid DNA show that the three metal complexes bind to DNA at room temperature or upon 37°C incubation (RT and 37 lanes in the first two gels in Figure 3.25) and photocleave DNA upon visible light irradiation (Lanes O₂ in Figure 3.25). The slowing down of DNA migration through the agarose gel in lanes RT and 37 displays DNA-MC binding. The observed DNA binding in lanes RT and 37 are consistent with the DNA binding studies using linear pUC18 DNA (Figure 3.25). All the complexes bind more avidly at 37°C. Photolysis under atmospheric conditions yielded DNA photocleavage in the presence of [(tpy)RuCl(dpp)PtCl₂](PF₆) and [(MePhtpy)RuCl(dpp)PtCl₂](PF₆), with the most efficient conversion of the supercoiled form into the open circular form in the presence of the latter complex upon 2 hrs of photolysis. Minimal photocleavage was observed in the presence of the [(^tBu₃tpy)RuCl(dpp)PtCl₂](PF₆) metal complex. The lipophilic nature of the ^tBu₃tpy ligand

and/or the steric hindrance in the molecule may prevent Pt complexation to the DNA, which would inhibit DNA photocleavage. Similarly, Baguey and coworkers have demonstrated that by increasing the bulk of the group on the acridine moiety of amsacrine from methyl to ethyl and isopropyl, the intercalative binding to DNA was retained but the apparent unwinding angle was lowered to about 30% by isopropyl.¹⁶⁵ In the presence of the t-butyl group they observed abrupt change to non-intercalative binding from the intercalative binding mode.¹⁶⁵ These results show that the DNA reactivity can be modulated by enhancing photocleavage with a MePhtpy ligand while impairing photocleavage with a ^tBu₃tpy ligand within a bimetallic framework. The ability of the Pt coordination to provide for efficient DNA photocleavage to a Ru^{II}tpy containing chromophores provides for the application of this class of generally unexplored light absorbers for DNA photochemistry.

3.13. Antibacterial Properties

Antibacterial drug resistance is recognized as a rising and threatening public health problem. Although most antibiotics do not need metal ions for their biological activities, there are several families of antibiotics (bacitracin, bleomycin (BLM), streptonigrin (SN), and albomycin) that require metal ions to function properly.^{166,84}

The biological effects of cisplatin were discovered in 1965 when Rosenberg observed a filamentous growth in *an E. coli* culture due to the presence of cisplatin.^{14,15} Cisplatin has been shown to have a number of effects on bacterial systems, such as induction of filamentous growth in *E. coli* and inhibition of DNA replication.¹⁶⁷⁻¹⁷⁰ Recently, Brabec and coworkers reported the lower toxicity of the anti-tumor complex *trans*-[PtCl₂(E-iminoether)₂] against bacterial cells relative to cisplatin due to the difference in the DNA binding mode of the *trans*-platinum complex.¹⁷¹ The Pt(II) complex, [PtCl₂(C₂₂H₂₄N₂O₈)], has been reported to be six times more effective against *E. coli* HB101 (carrying a tetracycline-resistant marker on the plasmid pBR322).¹⁷² The antibacterial activity of the complex, [Pt(NH₃)(achsh)Cl₂] (achsh = 3-aminocyclohexanespiro-5-hydantoin), has also recently been reported.¹⁷³ The minimum inhibitory concentration of [Pt(NH₃)(achsh)Cl₂] was found to be 0.2 mM as compared to 0.1 mM for cisplatin against the *E. coli* 600 strain.

The bacterial cell culture study of Ru^{II}Pt^{II} heterodinuclear complexes and their monometallic precursors were performed. *E. coli* strain JM109 carrying the plasmid pBluescript or pUC18 was used in the current study. Antibacterial properties of Ru^{II}Pt^{II} bimetallic metal complexes have not been explored until now. However antibacterial properties of the platinum containing complexes have been briefly explored.^{171,173} In this study, the impact of different concentrations of [(TL)RuCl(dpp)PtCl₂](PF₆) and their monometallic precursors on the growth of *E. coli* was investigated. The impact of Ru^{II}Pt^{II} bimetallic complexes on bacterial cell growth was compared with that of cisplatin.

The plasmid DNA pBluescript (Stratagene) or pUC18 (Bayou Biolabs) were introduced into the bacterial cells, *E. coli* JM109, by electroporation process. Electroporation is a significant increase in the electrical conductivity or permeability of the cell membrane caused by an externally applied electrical field. When voltage across a plasma membrane exceeds its dielectric strength, the pores are formed and desired plasmid DNA can be introduced. The pore size depends upon electrical field and duration of exposure. The electroporation process is described in detail in Chapter 2.

Due to the limited solubility of the designed metal complexes in LB (Luria-Bertani) medium, they were first dissolved in DMSO. Therefore, the first aim of this study was to investigate the effect of DMSO on bacterial cell growth. This was determined by growing bacterial cell culture in the presence of different concentrations of DMSO. An overnight culture was prepared by inoculating 10 mL LB_{amp100} broth with a small amount of a frozen stock of *E. coli* cells (stored in 50% glycerol at -80 °C). The 2.5 mL of overnight culture was used to inoculate 50 mL LB medium containing 1, 2, 3, and 4 % DMSO. Figure 3.26 shows the resulting bacterial growth curves. Every 30 min three 200 µL samples from each culture were diluted with 1800 µL of LB media and the optical density at 650 nm (OD₆₅₀) was recorded. The average values with standard deviations were plotted.

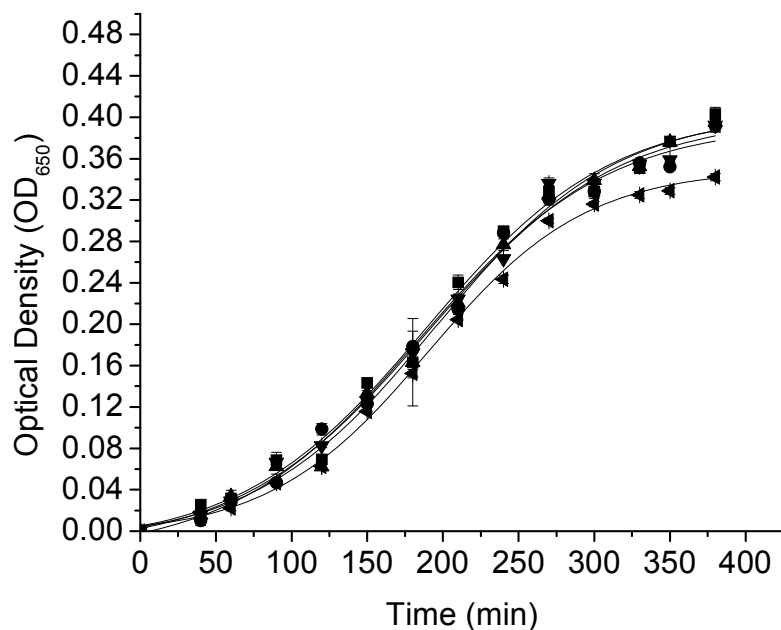


Figure 3.26. Growth curves of *E. coli* JM109 (pBluescript) at different concentrations of DMSO (DMSO = dimethylsulphoxide). Cells were grown in the presence of 1% (■), 2% (▲), 3% (▼), 4% DMSO (◄), and Control (●).

No cell growth inhibition was observed in the presence of 1, 2, or 3% DMSO; at 4%, a slight cell growth inhibition was observed. This implies that DMSO in concentrations $\leq 3\%$ does not have detrimental effects on the growth of bacterial culture. Therefore these studies were performed in the presence of either 1 or 3% DMSO.

3.13.1. Antibacterial Properties: Cisplatin

The antibacterial properties of cisplatin have been known for a long time. The antibacterial properties of cisplatin against *E. coli* JM109 carrying the ampicillin resistance plasmids, pBluescript or pUC18 were explored in our experimental conditions. Fresh solutions of cisplatin were made in DMSO. Cultures (50 mL) were grown in 125 mL Erlenmeyer flasks at 37°C with shaking (180 rpm). Each culture was inoculated with 500 μ L solutions of cisplatin in 1% DMSO to give 0.1 mM, 0.2 mM, and 0.4 mM final concentrations. One culture was inoculated only with DMSO but no cisplatin and served as a control. Every 30 min, a 200 μ L sample from each culture was diluted with 1800 μ L of LB medium and the optical density at 650

nm (OD_{650}) was recorded in order to monitor cell growth. Figure 3.27 shows the bacterial cell growth curves grown in the presence of 0.1, 0.2, and 0.4 mM cisplatin. Complete cell growth inhibition was observed at these concentrations of cisplatin. The concentration at which cisplatin inhibits bacterial cell growth in our conditions was determined by Ms. Lilit Stephyan, undergraduate student, Virginia Polytechnic Institute and State University. Cisplatin was found to inhibit bacterial cell growth at 0.005 mM under our experimental conditions.

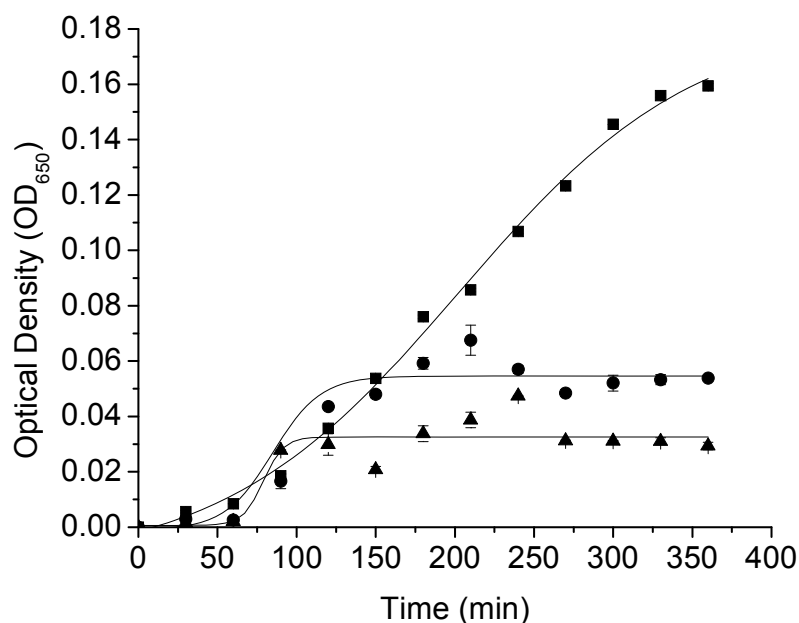


Figure 3.27. Growth curves of *E. coli* JM109 (pBluescript) at different concentrations of cisplatin. Cells were grown in the presence of 0.2 mM cisplatin (▲), 0.4 mM cisplatin (■), and Control (●).

3.13.2. Antibacterial Properties: $[(\text{tpy})\text{RuCl}(\text{dpp})\text{PtCl}_2](\text{PF}_6)$ and its Monometallic Precursor

Cell culture studies were performed in the presence of the heterobimetallic complex, $[(\text{tpy})\text{RuCl}(\text{dpp})\text{PtCl}_2](\text{PF}_6)$. Figure 3.28 displays bacterial growth curves for cultures containing 0.2, 0.4, and 0.6 mM $[(\text{tpy})\text{RuCl}(\text{dpp})\text{PtCl}_2](\text{PF}_6)$. No effect on bacterial cell growth was observed with 0.2 mM concentration of $[(\text{tpy})\text{RuCl}(\text{dpp})\text{PtCl}_2](\text{PF}_6)$. However, cell growth

inhibition was observed at 0.4 mM and 0.6 mM concentrations. Higher concentrations of this complex are required to impede cell growth than for cisplatin.

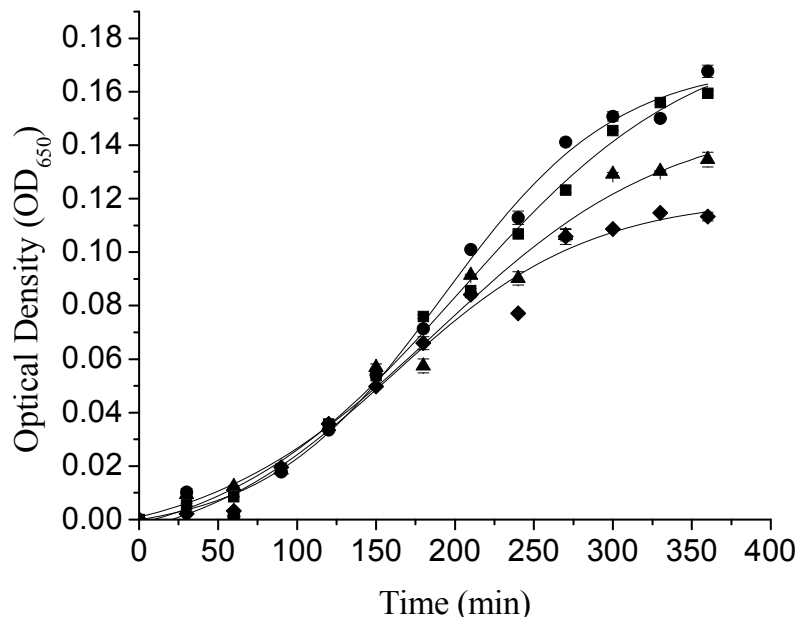


Figure 3.28. Growth curves of *E. coli* JM109 (pBluescript) at different concentrations of $[(\text{tpy})\text{RuCl}(\text{dpp})\text{PtCl}_2](\text{PF}_6)$ (dpp = 2,3-bis(2-pyridyl)pyrazine and tpy = 2,2':6',2''-terpyridine). Cells were grown in the presence of 0.2 mM $[(\text{tpy})\text{RuCl}(\text{dpp})\text{PtCl}_2](\text{PF}_6)$ (◆), 0.4 mM $[(\text{tpy})\text{RuCl}(\text{dpp})\text{PtCl}_2](\text{PF}_6)$ (■), 0.6 mM $[(\text{tpy})\text{RuCl}(\text{dpp})\text{PtCl}_2](\text{PF}_6)$ (▲), and Control (●).

To learn more about the possible means by which this metal complex inhibits cell growth inhibition, the impact of exposure to different concentrations of the monometallic precursor, $[(\text{tpy})\text{RuCl}(\text{dpp})](\text{PF}_6)$, was examined. Figure 3.29 illustrates the bacterial growth curves for cells exposed to 0.4 mM and 0.6 mM $[(\text{tpy})\text{RuCl}(\text{dpp})](\text{PF}_6)$. This complex displayed no measurable effect on cell growth at either concentration.

Coupling of the *cis*-PtCl₂ moiety to a monometallic precursor was shown in independent experiments to confer the ability to bind with DNA and to inhibit cell growth. The cell growth inhibition could be attributed to the inhibition of DNA replication and/or transcription by the *cis*-PtCl₂ moiety. However, the $[(\text{tpy})\text{RuCl}(\text{dpp})\text{PtCl}_2](\text{PF}_6)$ complex was found to inhibit cell

growth at much higher concentrations than cisplatin, even though gel electrophoresis studies indicated more efficient binding of the complex to DNA. There are various possible explanations for this phenomenon, including differential rate of cellular uptake of the two complexes. Another possibility is that the adduct formed on DNA by $[(\text{tpy})\text{RuCl}(\text{dpp})\text{PtCl}_2](\text{PF}_6)$ complex is less effective in inhibiting replication or transcription than those formed by cisplatin. We also cannot rule out the possibility of reaction of the *cis*- PtCl_2 moiety with other biomolecules like RNA and sulfur containing enzymes (e.g. metallothionine and glutathione). The results of our work show that *in vitro* studies do not always translate to *in vivo* studies using the same molecule.

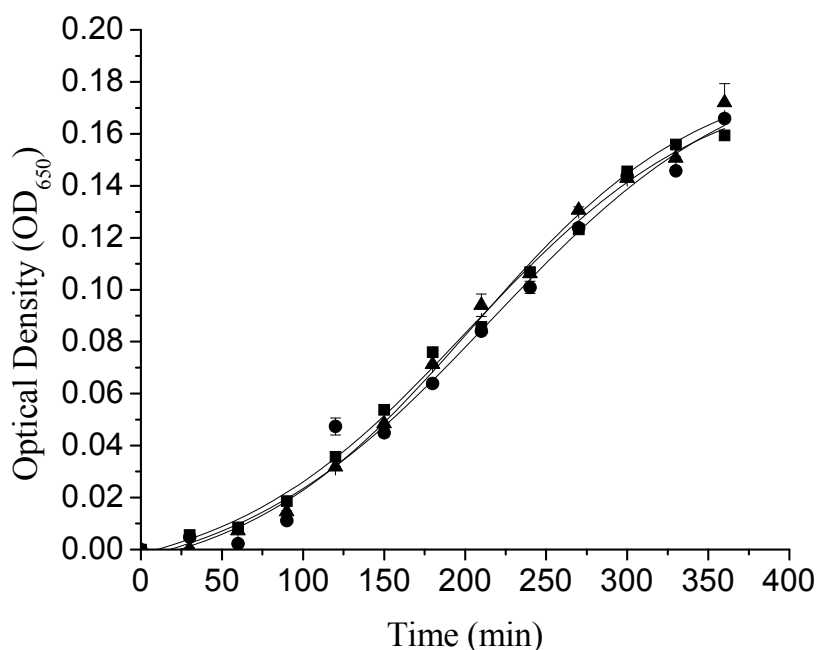


Figure 3.29. Growth curves of *E. coli* JM109 (pBluescript) at different concentrations of $[(\text{tpy})\text{RuCl}(\text{dpp})](\text{PF}_6)$ ($\text{dpp} = 2,3\text{-bis}(2\text{-pyridyl})\text{pyrazine}$ and $\text{tpy} = 2,2':6',2''\text{-terpyridine}$). Cells grown in the presence of 0.4 mM $[(\text{tpy})\text{RuCl}(\text{dpp})](\text{PF}_6)$ (\blacktriangle), 0.6 mM $[(\text{tpy})\text{RuCl}(\text{dpp})](\text{PF}_6)$ (\blacksquare), and Control (\bullet).

3.13.3. Antibacterial Properties: $[(\text{MePhtpy})\text{RuCl}(\text{dpp})\text{PtCl}_2](\text{PF}_6)$ and its Monometallic Precursor

Bacterial cell culture studies were performed in the presence of the lipophilic complex, $[(\text{MePhtpy})\text{RuCl}(\text{dpp})\text{PtCl}_2](\text{PF}_6)$. It has been shown that lipophilic compounds inhibit bacterial

cell growth at lower concentrations than hydrophilic compounds.⁷¹ Figure 3.30 displays the growth curves for cultures containing 0.0 mM, 0.05 mM, and 0.1 mM [(MePhtpy)RuCl(dpp)PtCl₂](PF₆). At 0.05 mM, this complex had no measurable effect on cell growth. However, cell growth inhibition was observed at 0.1 mM concentration, which is lower than the concentration needed to inhibit bacterial cell growth with [(tpy)RuCl(dpp)PtCl₂](PF₆). This lowering of concentration to impede bacterial cell growth could be due to the higher lipophilicity of the MePhtpy containing complex compared to the tpy containing complex. The partition coefficient of MePhtpy containing complex measured using octanol water system was found to be -0.39 compared to -2.00 for the tpy complex. The higher lipophilicity of this molecule may enable it to cross the cell wall more easily or interact more readily with proteins present on the cell wall. Interaction of cisplatin analogs with cell wall proteins have previously been reported to cause cell death.¹⁷⁴

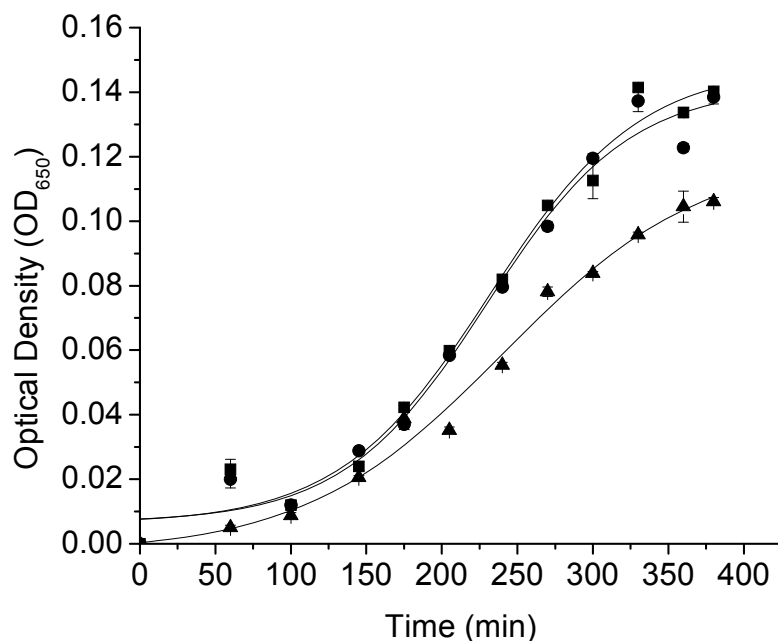


Figure 3.30. Growth curves of *E. coli* JM109 (pUC18) at different concentrations of [(MePhtpy)RuCl(dpp)PtCl₂](PF₆) (dpp = 2,3-bis(2-pyridyl)pyrazine and MePhtpy = 4'-(4-methylphenyl)-2,2':6',2''-terpyridine). Cells grown in the presence of 0.05 mM [(MePhtpy)RuCl(dpp)PtCl₂](PF₆) (●), 0.1 mM [(MePhtpy)RuCl(dpp)PtCl₂](PF₆) (▲), and Control (■).

To further explore the mechanism of cell growth inhibition, the impact of exposure to different concentrations of the monometallic precursor, [(MePhtpy)RuCl(dpp)](PF₆), on bacterial cell growth was examined. Figure 3.31 shows the growth curves for bacterial cells exposed to 0.05 and 0.025 mM concentrations of [(MePhtpy)RuCl(dpp)](PF₆). At 0.025 mM concentration, this complex had no measurable effect on bacterial cell growth. Cell growth inhibition was observed at 0.05 mM concentration. At higher concentrations, precipitation of the metal complex in LB medium was observed. The cell growth inhibition at 0.05 mM could be attributed to its closer interaction with DNA. Although the pharmaceutical target for ruthenium complexes has not been identified, there are evidences indicating that the cytotoxicity of many ruthenium complexes correlates with their ability to bind with DNA.⁸³ The cytotoxic nature of the ruthenium polypyridyl complex, *mer*-[Ru(tpy)Cl₃], has been attributed to interstrand DNA cross-linking.⁸³ Ruthenium complexes containing 1,10-phenanthroline ligands have also been reported to show antibacterial properties due to the interaction with DNA.¹⁷⁵ The MePhtpy ligand improves the lipophilicity of the molecule and may thereby enhance its interaction with biomolecules. The [(MePhtpy)RuCl(dpp)](PF₆) complex displayed strong interaction with DNA, with a DNA binding constant of $6.2 \times 10^3 \text{ M}^{-1}$ (section 3.11). The antibacterial property could result from the strong mode of interaction of the metal complex with DNA. The analogous hydrophilic complex, [(tpy)RuCl(dpp)](PF₆), showed no antibacterial activity. This may be due to its inability to cross the cell wall and poor interaction with DNA

The concentration at which the monometallic precursor, [(MePhtpy)RuCl(dpp)](PF₆), inhibits cell growth was found to be lower than the concentration of [(MePhtpy)RuCl(dpp)PtCl₂](PF₆) required to achieve the similar effect. The gel electrophoresis experiments have shown enhanced binding with bimetallic complex compared to monometallic precursor (section 3.12.3.). However the dialysis experiments have shown that monometallic precursor, [(MePhtpy)RuCl(dpp)](PF₆), also interacts with DNA with a binding constant of $6.2 \times 10^3 \text{ M}^{-1}$. The lipophilicity of the complex, [(MePhtpy)RuCl(dpp)], is higher than the bimetallic complex, [(MePhtpy)RuCl(dpp)PtCl₂](PF₆). This means that it may cross the cell wall more easily than the bimetallic complex. Higher lipophilicity and DNA interaction properties may be responsible for the inhibition of cell growth at lower concentrations by [(MePhtpy)RuCl(dpp)](PF₆) compare to the bimetallic complex.

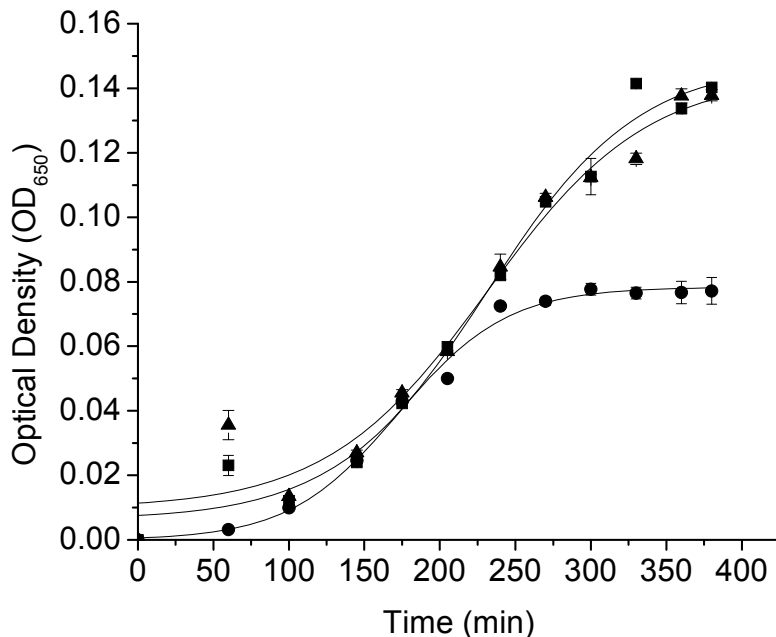


Figure 3.31. Growth curves of *E. coli* JM109 (pBluescript) at different concentrations of $[(\text{MePhtpy})\text{RuCl}(\text{dpp})](\text{PF}_6)$ (dpp = 2,3-bis(2-pyridyl)pyrazine and MePhtpy = 4'-(4-methylphenyl)-2,2':6',2''-terpyridine). Cells grown in the presence of 0.025 mM $[(\text{MePhtpy})\text{RuCl}(\text{dpp})](\text{PF}_6)$ (▲), 0.05 mM $[(\text{MePhtpy})\text{RuCl}(\text{dpp})](\text{PF}_6)$ (●), and Control (■).

3.13.4. Antibacterial Properties: $[(^t\text{Bu}_3\text{tpy})\text{RuCl}(\text{dpp})\text{PtCl}_2](\text{PF}_6)$ and its Monometallic Precursor

To further investigate the effect of lipophilicity on bacterial cell growth inhibition, the cell culture experiment was performed in the presence of $[(^t\text{Bu}_3\text{tpy})\text{RuCl}(\text{dpp})\text{PtCl}_2](\text{PF}_6)$ complex. The reason we have selected this complex is because it displayed minimum interaction with DNA while exhibiting maximum lipophilicity compared to other two bimetallic complexes. Figure 3.32 shows the growth curves for cell cultures grown in the presence of $[(^t\text{Bu}_3\text{tpy})\text{RuCl}(\text{dpp})\text{PtCl}_2](\text{PF}_6)$. Due to the lower solubility of this complex in LB medium, 3% DMSO was used for these studies. No effect on cell growth was observed in the presence of 0.05 mM concentration of $[(^t\text{Bu}_3\text{tpy})\text{RuCl}(\text{dpp})\text{PtCl}_2](\text{PF}_6)$. However cell growth inhibition was observed at 0.1 mM. This concentration is similar to the concentration of $[(\text{MePhtpy})\text{RuCl}(\text{dpp})\text{PtCl}_2](\text{PF}_6)$ and lower than the concentration of

$[(\text{tpy})\text{RuCl}(\text{dpp})\text{PtCl}_2](\text{PF}_6)$ required to inhibit bacterial cell growth. We expected to see a decrease in inhibitory concentration with the increase in lipophilicity, however, this was not the case. This may be explained by the DNA interaction properties of the two complexes. The $[(\text{MePhtpy})\text{RuCl}(\text{dpp})\text{PtCl}_2](\text{PF}_6)$ complex exhibited a higher degree of DNA binding compared to $[(^t\text{Bu}_3\text{tpy})\text{RuCl}(\text{dpp})\text{PtCl}_2](\text{PF}_6)$ in gel electrophoresis studies of the $\text{Ru}^{\text{II}}\text{Pt}^{\text{II}}$ bimetallic complexes (section 3.12.3). Decreased DNA interaction of $[(^t\text{Bu}_3\text{tpy})\text{RuCl}(\text{dpp})\text{PtCl}_2](\text{PF}_6)$ compared to $[(\text{MePhtpy})\text{RuCl}(\text{dpp})\text{PtCl}_2](\text{PF}_6)$ could be responsible for higher inhibitory concentration.

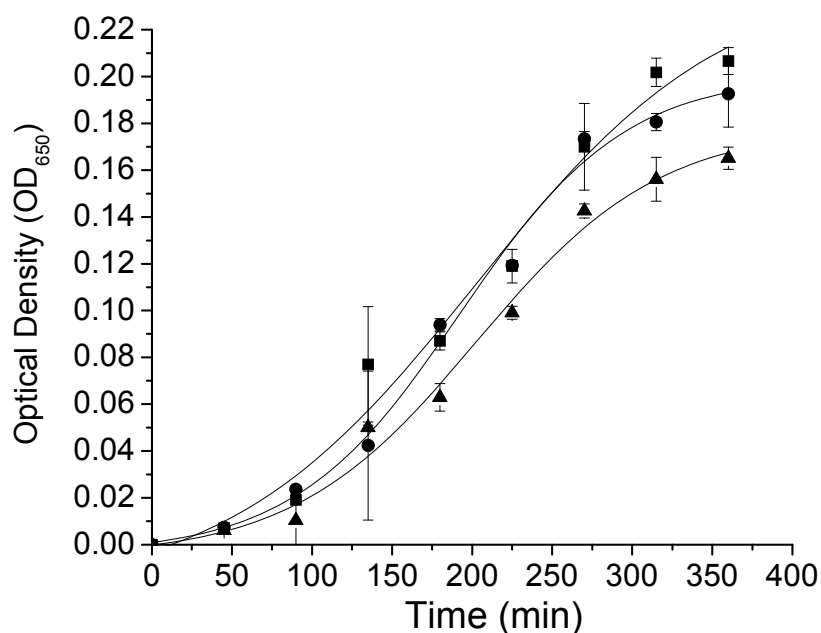


Figure 3.32. Growth curves of *E. coli* JM109 (pUC18) at different concentrations of $[(^t\text{Bu}_3\text{tpy})\text{RuCl}(\text{dpp})](\text{PF}_6)$ (dpp = 2,3-bis(2-pyridyl)pyrazine and $^t\text{Bu}_3\text{tpy}$ = 4,4',4''-tri-tert-butyl-2,2':6',2''-terpyridine). Cells grown in the presence of 0.05 mM $[(^t\text{Bu}_3\text{tpy})\text{RuCl}(\text{dpp})](\text{PF}_6)$ (●), 0.1 mM $[(^t\text{Bu}_3\text{tpy})\text{RuCl}(\text{dpp})](\text{PF}_6)$ (▲), and Control (■).

To explore the effect of *cis*-PtCl₂ subunit on cell growth, cell culture studies were performed with $[(^t\text{Bu}_3\text{tpy})\text{RuCl}(\text{dpp})](\text{PF}_6)$ complex. Figure 3.33 displays bacterial cell growth curves when cells were grown in the presence of 0.1 and 0.2 mM $[(^t\text{Bu}_3\text{tpy})\text{RuCl}(\text{dpp})](\text{PF}_6)$. Cell growth inhibition was observed at 0.1 and 0.2 mM $[(^t\text{Bu}_3\text{tpy})\text{RuCl}(\text{dpp})](\text{PF}_6)$. The bimetallic and monometallic precursor containing $^t\text{Bu}_3\text{tpy}$ ligand displayed cell growth inhibition

at similar concentrations. Coupling of a cisplatin moiety to the monometallic precursor had no measurable effect on cell growth inhibition. These results are consistent with the DNA binding studies of these complexes (section 3.12.3).

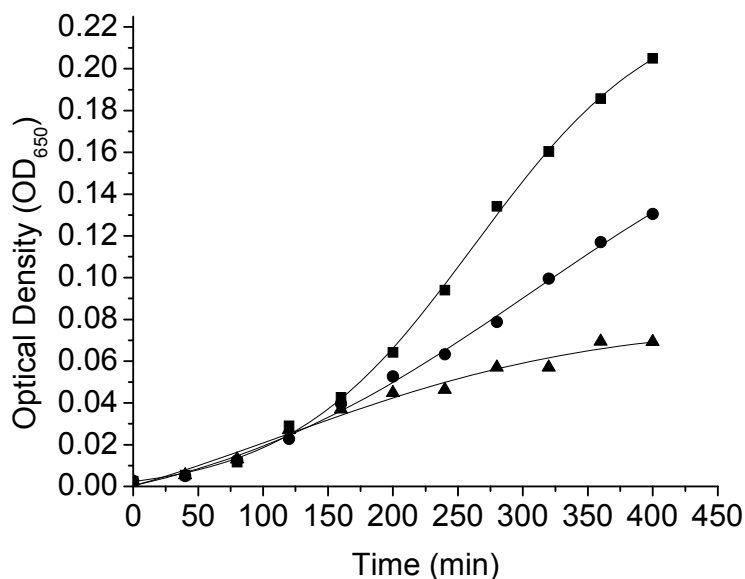


Figure 3.33. Growth curves of *E. coli* JM109 (pUC18) at different concentrations of $[(^t\text{Bu}_3\text{tpy})\text{RuCl}(\text{dpp})\text{PtCl}_2](\text{PF}_6)$ (dpp = 2,3-bis(2-pyridyl)pyrazine and $^t\text{Bu}_3\text{tpy}$ = 4,4',4''-tri-tert-butyl-2,2':6',2''-terpyridine). Cells grown in the presence of 0.1 mM $[(^t\text{Bu}_3\text{tpy})\text{RuCl}(\text{dpp})\text{PtCl}_2](\text{PF}_6)$ (●), 0.2 mM $[(^t\text{Bu}_3\text{tpy})\text{RuCl}(\text{dpp})\text{PtCl}_2](\text{PF}_6)$ (▲), and Control (■).

3.13.4. Comparison of Antibacterial Properties of $\text{Ru}^{\text{II}}\text{Pt}^{\text{II}}$ Complexes

A direct correlation was observed between the DNA binding and antibacterial properties of $\text{Ru}^{\text{II}}\text{Pt}^{\text{II}}$ bimetallic complexes and their monometallic precursors. The MePhtpy containing complexes inhibited bacterial cell growth at a lowest concentration compared to the tpy and $^t\text{Bu}_3\text{tpy}$ containing complexes. Table 3.13 summarizes the DNA interaction properties, lipophilicity and antibacterial properties of the designed molecules.

Table 3.13. Comparison of antibacterial, DNA interaction properties, and lipophilicity shown by complexes, [(TL)RuCl(dpp)PtCl₂](PF₆) (TL = tpy, MePhtpy, and ^tBu₃tpy).

Metal Complex ^a	log P ^b	DNA ^c Covalent Binding	DNA ^c Photocleavage Efficiency	Concentration at which cell growth inhibition was observed ^d
[(^t Bu ₃ tpy)RuCl(dpp)] ⁺	+4.00	No	Low	0.1 mM
[(MePhtpy)RuCl(dpp)] ⁺	+1.16	No	High	0.05 mM
[(tpy)RuCl(dpp)] ⁺	-2.00	No	Moderate	≥0.6 mM
[(^t Bu ₃ tpy)RuCl(dpp)PtCl ₂] ⁺	+4.00	Low	Low	0.1 mM
[(MePhtpy)RuCl(dpp)PtCl ₂] ⁺	-0.39	High	High	0.1 mM
[(tpy)RuCl(dpp)PtCl ₂] ⁺	-1.27	High	Moderate	0.4 mM

^aMePhtpy = 4'-(4-methylphenyl)-2,2':6',2''-terpyridine, dpp = 2,3-bis(2-pyridyl)pyrazine, tpy = 2,2':6',2''-terpyridine, ^tBu₃tpy = 4,4',4''-tri-tert-butyl-2,2':6',2''-terpyridine.

^blog P = log(C_i^o/C_i^w) (C_i^o and C_i^w are the concentrations (moles/L) of the solute in the octanol and water respectively).

^cDNA interaction studies were assayed via agarose gel electrophoresis experiments.

^dConcentration at which inhibition was observed was determined using bacterial cell culture studies.

The antibacterial properties of ruthenium complexes have been previously reported.^{89-92,175} It has previously been shown that the antibacterial action of the molecules increases with the increase in lipophilicity.⁹⁰ We have observed the similar effects with MePhtpy containing complexes in contrast to the ^tBu₃tpy containing complexes. The monometallic complex, [(MePhtpy)RuCl(dpp)](PF₆), displayed cell growth inhibition at the lowest concentration (0.05 mM). This complex displayed higher DNA binding and higher lipophilicity compare to [(tpy)RuCl(dpp)](PF₆). In contrast, the [(tpy)RuCl(dpp)](PF₆) complex displayed no antibacterial properties. The increased antibacterial property of [(MePhtpy)RuCl(dpp)](PF₆) could be due to the increased lipophilicity and DNA interaction. The [(^tBu₃tpy)RuCl(dpp)](PF₆) complex displayed cell growth inhibition at 0.1 mM concentration which is higher than the concentration of [(MePhtpy)RuCl(dpp)](PF₆) and lower than the concentration of [(tpy)RuCl(dpp)](PF₆) needed to inhibit cell growth.

The ruthenium chromophore coupled cisplatin analogs display antibacterial properties. The complex, [(tpy)RuCl(dpp)PtCl₂](PF₆), displayed cell growth inhibition at 0.4 mM concentration. The bioactivity of this complex appears to be due to the presence of the cis-PtCl₂ moiety, as the monometallic synthon, [(tpy)RuCl(dpp)](PF₆), did not inhibit bacterial cell growth. On the other hand, coupling of the cisplatin moiety to [(^tBu₃tpy)RuCl(dpp)](PF₆) did not influence the minimum concentration needed to provide antibacterial action. The [(MePhpty)RuCl(dpp)PtCl₂](PF₆) complex displayed cell growth inhibition at higher concentration than the monometallic synthon, [(MePhpty)RuCl(dpp)](PF₆). This could be due to the higher lipophilicity of [(MePhpty)RuCl(dpp)](PF₆) compared to the bimetallic [(MePhpty)RuCl(dpp)PtCl₂](PF₆) complex.

3.14. Photodynamic Antibacterial Chemotherapy

Most of the antibiotics currently in use display a site directed mode of action.⁸⁴ For example, penicillin works by inhibiting the formation of peptidoglycan cross-links in cell wall. With sufficient exposure, microbes can develop resistance against these antibiotics. On the other hand, photodynamic antibacterial chemotherapy is not site directed. Photodynamic viral disinfection using methylene blue and phenothiazene derivatives is known.^{176,177} The singlet oxygen produced upon photoexcitation of a sensitizer can damage many different biomolecules. According to Wanbright and coworkers there is also a possibility of a redox reaction of the photosensitizer with water in the cell cytoplasm to create more reactive oxygen species.⁷⁴

The photodynamic antibacterial action of [(MePhpty)RuCl(dpp)](PF₆) was determined as it displayed enhanced DNA photocleavage properties. Photodynamic antibacterial action was determined by performing the bacterial cell growth experiments under continuous photolysis conditions using a 5W LED. The construction and design of the LED setup is described in Chapter 2. The effect of photolysis by the 5W, 520 nm cutoff LED in the absence of metal complex on bacterial cell growth was determined by performing the bacterial cell culture with continuous exposure to light. One culture was done without any light exposure and served as a control. Figure 3.34 shows the results of this study. No impact on cell growth was observed when cells were grown with continuous exposure to light. This implies that the photolysis

conditions used in current studies do not by themselves have detrimental effects on cell culture growth.

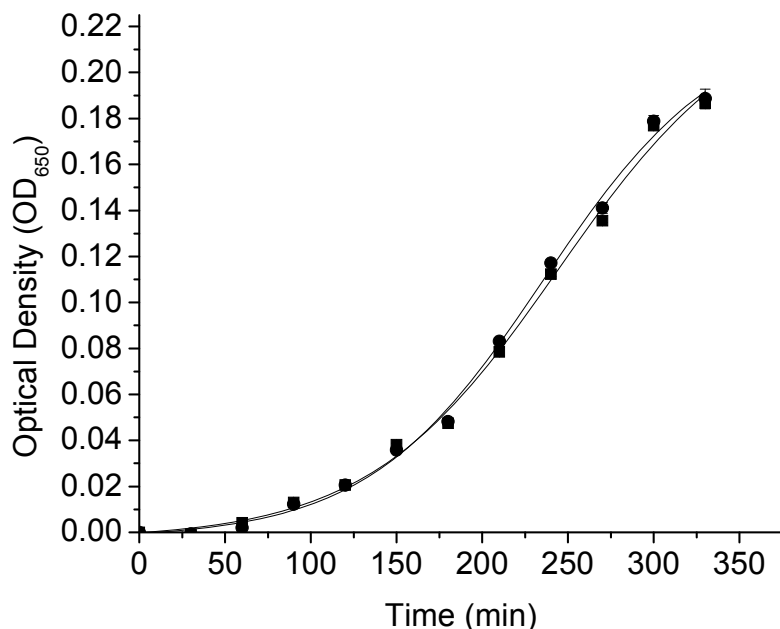


Figure 3.34. Growth curve of *E. coli* JM109 (pUC18) grown with continuous exposure to LED light. Cells were grown under photolysis conditions (●), and Control (no photolysis) (■).

The impact of photoactivation of the [(MePhtpy)RuCl(dpp)](PF₆) complex on bacterial cell growth was investigated. Bacterial cell cultures were grown in the presence of 0.05 mM [(MePhtpy)RuCl(dpp)](PF₆) complex under continuous photolysis conditions using the 5W LED. An increase in cell growth inhibition was observed in the presence of 0.05 mM [(MePhtpy)RuCl(dpp)](PF₆) under continuous photolysis conditions than in the dark (Figure 3.35). This is consistent with our DNA photocleavage studies that showed photobinding and photocleavage. The increase in cell growth inhibition could be due to the DNA photobinding or photocleavage as a result of the production of singlet oxygen on photoactivation of the metal complex. DNA has previously been reported as a site of action for photobactericidal activity of a chromophore, methylene blue, against *E. coli*.¹⁷⁸ However we cannot rule out the possibility of the reaction of singlet oxygen with other biomolecules. Hartman and coworkers have reported that, generation of singlet oxygen in sufficient quantities near the bacterial outer membrane can

cause damage to vital cellular structures such as DNA, RNA, and cell wall.⁷⁹ This could provide a means to allow the complex to enter the cell and target DNA.

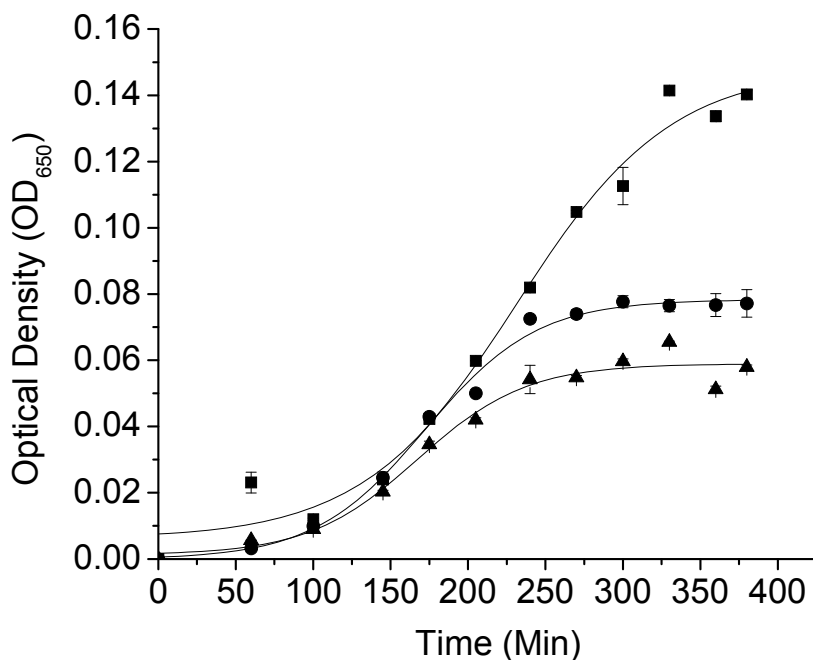


Figure 3.35. Growth curve of *E. coli* JM109 (pUC18) at 0.05mM [(MePhtpy)RuCl(dpp)](PF₆) in the presence and absence of 5W LED (dpp = 2,3-bis(2-pyridyl)pyrazine, MePhtpy = 4'-(4-methylphenyl)-2,2':6',2''-terpyridine). Cells were grown in dark with 0.05 mM [(MePhtpy)RuCl(dpp)](PF₆) complex (●), under continuous photolysis conditions with 0.05 mM [(MePhtpy)RuCl(dpp)](PF₆) complex (▲), and Control without [(MePhtpy)RuCl(dpp)](PF₆) complex (■).

A number of organic photosensitizers i.e. methylene blue, aminoacridines, proflavin, and acridine orange that have shown photobactericidal activity.^{72,178} Photodynamic antiviral and antibacterial properties of phthalocyanines have also been reported.^{179,180} However [(MePhtpy)RuCl(dpp)](PF₆), is the first inorganic molecule to display photobactericidal activity.

To further explore the nature of the photobactericidal activity of the designed molecule effects of intermittent light exposure were determined. In this experiment the bacterial cell culture was exposed to 0.05 mM [(MePhtpy)RuCl(dpp)](PF₆) complex under intermittent photolysis conditions. Continuous photolysis was performed for the first 180 minutes. Then the

LED was turned on for 30 min and off for 30 min. Growth inhibition was observed when cells were exposed to light, while resumption of cell growth was observed in the absence of light (Figure 3.36). This experiment indicates that the photobactericidal property of the designed metal complex is reversible.

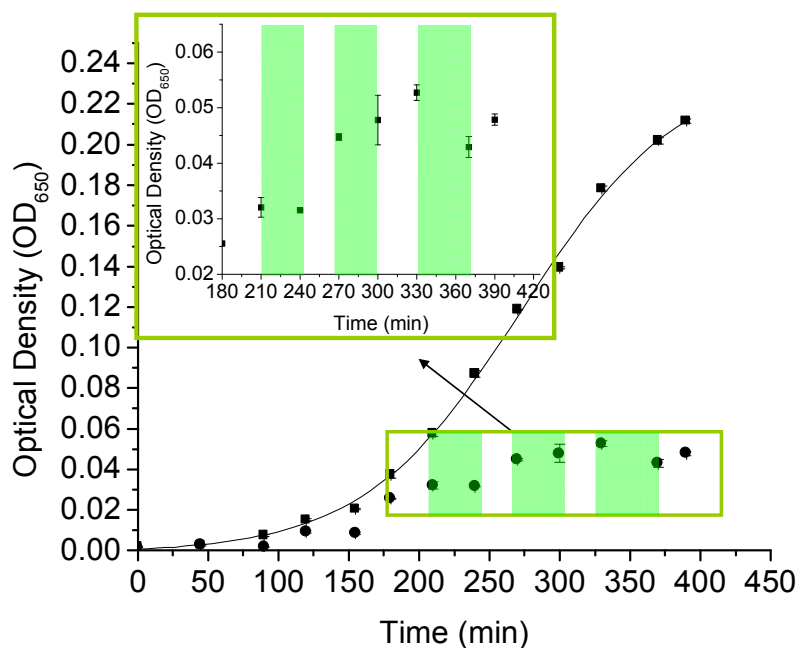


Figure 3.36. Growth curve of *E. coli* JM109 (pUC18) at 0.05mM [(MePhtpy)RuCl(dpp)](PF₆) under intermittent photolysis conditions (dpp = 2,3-bis(2-pyridyl)pyrazine and MePhtpy = 4'-(4-methylphenyl)-2,2':6',2''-terpyridine). Bacterial cell cultures were grown under intermittent photolysis conditions (●), and no photolysis (■). The inset figure shows reversible photoactivity with intermittent photolysis conditions. Green bars represents the time at which LED was turned on.

It is generally accepted that the cytotoxicity of ruthenium complexes is related to their ability to bind to DNA.⁸³ Reversible interaction of these molecules with DNA typically involves noncovalent interaction and is usually defined by electrostatic, intercalative, major or minor groove binding. Agarose gel electrophoresis studies support the non-covalent interaction of [(MePhtpy)RuCl(dpp)](PF₆) with DNA. This metal complex displays a strong metal to ligand charge transfer (MLCT) band at 520 nm. The excited state ³MLCT life time of the metal complex measured is 16 nsec. The energy transfer could occur from the excited triplet state of the molecule to the triplet oxygen species resulting in the ground state sensitizer and singlet

oxygen. Singlet oxygen can diffuse along the DNA helix and cleave DNA. It is also feasible that the designed metal complex photobinds DNA and forms a single DNA-MC bond. The damage caused by the metal complex would be detected by DNA repair enzyme and this could result in the reversibility in cell growth inhibition. However we cannot rule out other possibilities like interaction of excited metal complex with other biomolecules like the cell wall, RNA and proteins.

3.15. Mechanism of Cell Growth Inhibition

3.15.1. DNA Extraction using Quagen Kit

Antibacterial studies have revealed a correlation between DNA binding and antibacterial properties of Ru^{II}Pt^{II} bimetallic complexes and their monometallic precursors. In order to investigate the *in vivo* effect of [(MePhtpy)RuCl(dpp)PtCl₂](PF₆) on DNA structure, cells were grown in the presence of different concentrations of the complex for 5 hrs and plasmid DNA was then extracted from bacterial cells. This was achieved by using a quagen kit which is designed for purification of up to 20 µg of high-copy plasmid DNA from 1–5 mL overnight cultures of *E. coli* in LB medium. The extracted DNA was diluted 10 fold and fractionated by electrophoresis on an agarose gel.

The results of gel electrophoresis on extracted DNA are shown in Figure 3.37. Lane C represents plasmid DNA extracted from the control cell culture, lane 0.025 represents plasmid DNA extracted from the cells grown in the presence of 0.025 mM [(MePhtpy)RuCl(dpp)PtCl₂](PF₆), lane 0.05 represents plasmid DNA extracted from the cells grown in the presence of 0.05mM [(MePhtpy)RuCl(dpp)PtCl₂](PF₆), lane 0.1 represents DNA extracted from the cells grown in the presence of 0.1 mM [(MePhtpy)RuCl(dpp)PtCl₂](PF₆), lane 0.2 represents DNA extracted from the cells grown in the presence of 0.2 mM [(MePhtpy)RuCl(dpp)PtCl₂](PF₆), Lane λ represents the molecular weight marker. With increased concentrations of metal complex, decreased amounts of plasmid DNA were observed. This is consistent with the cell culture studies, which revealed an increase in cell death with increased concentrations of the metal complex. The increase in amount of DNA slows down the

upper end of DNA. However, the slowing down of the plasmid DNA migration on an agarose gel was observed with increased metal complex concentrations. This could be due to binding of metal complex with DNA. This is consistent with our *in vitro* experiments (Section 3.12.2). This experiment confirms that DNA is one of the targets for antibacterial action shown by this metal complex.

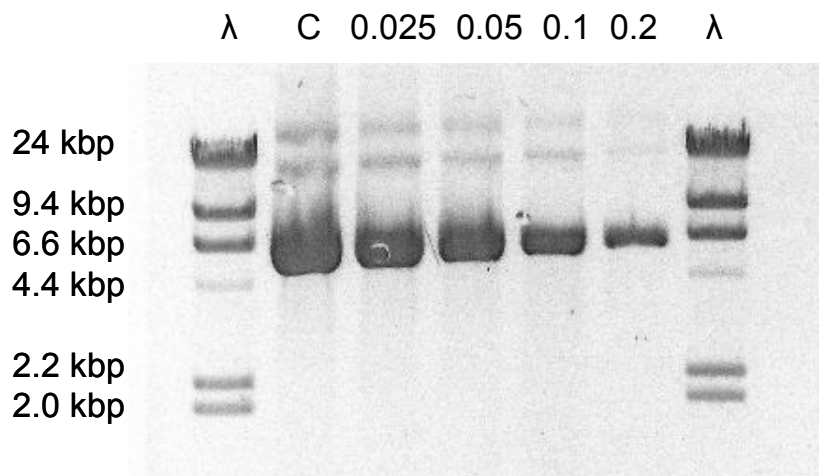


Figure 3.37. Agarose gel electrophoresis studies on DNA extracted from bacterial cells using quagen kit, when cells were grown in the presence of no metal complex (lane C), 0.025 (lane 0.025), 0.05 (lane 0.05), 0.1 (lane 0.1) and 0.2 mM (lane 0.2) $[(\text{MePhtpy})\text{RuCl}(\text{dpp})\text{PtCl}_2](\text{PF}_6)$. DNA (MePhtpy = 4'-(4-methylphenyl)-2,2':6',2''-terpyridine, dpp = 2,3-bis(2-pyridyl)pyrazine). Lane λ represents molecular weight marker.

In order to investigate the mode of action of photobactericidal properties of $[(\text{MePhtpy})\text{RuCl}(\text{dpp})](\text{PF}_6)$, cell culture studies were performed in the presence of metal complex with continuous photolysis and after 5 hrs of cell growth the DNA was extracted from bacterial cells. Plasmid DNA was extracted from bacterial cells using a quagen kit. The extracted DNA was diluted 100 fold and fractionated by electrophoresis on an agarose gel.

Figure 3.38 displays the agarose gel electrophoresis studies on extracted DNA. Lane λ represents the molecular weight marker, lane C represents plasmid DNA extracted from control cell culture, lane MC represents plasmid DNA extracted from the cells grown in the presence of 0.05 mM $[(\text{MePhtpy})\text{RuCl}(\text{dpp})](\text{PF}_6)$, lane hv+MC represents plasmid DNA extracted from the cells grown in the presence of 0.05mM $[(\text{MePhtpy})\text{RuCl}(\text{dpp})](\text{PF}_6)$ under continuous photolysis conditions. This study revealed the slowing in the migration of metal complex (MC) lane

compared to control (C). However the amount of DNA loaded in the wells of gel (MC and hv+MC) was too less to see any photocleavage event.

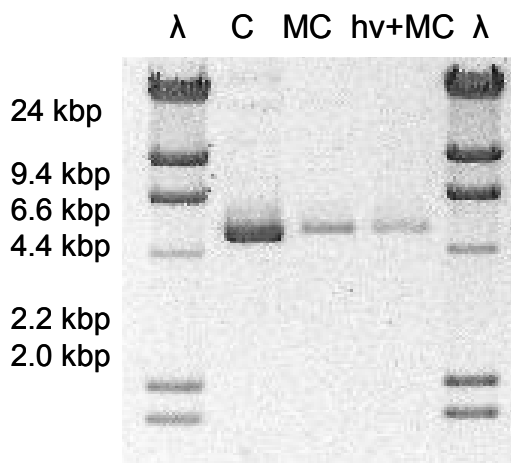


Figure 3.38. Agarose gel electrophoresis studies on DNA extracted from bacterial cells grown in the presence of different concentrations of $[(\text{MePhtpy})\text{RuCl}(\text{dpp})](\text{PF}_6)$ under no photolysis and photolysis conditions (dpp = 2,3-bis(2-pyridyl)pyrazine and MePhtpy = 4'-(4-methylphenyl)-2,2':6',2''-terpyridine). After extraction DNA was diluted 100 fold. DNA extracted from the culture grown in the presence of 0.05 mM $[(\text{MePhtpy})\text{RuCl}(\text{dpp})](\text{PF}_6)$ (lane MC), 0.05 $[(\text{MePhtpy})\text{RuCl}(\text{dpp})](\text{PF}_6)$ with continuous photolysis (lane hv+MC). Lane C represents DNA extracted from the control culture. Lane λ represents the molecular weight marker.

3.15.2. DNA Extraction using Lysis in the Gel Well Protocol

To further investigate the effect of photolysis on DNA structure in the presence of $[(\text{MePhtpy})\text{RuCl}(\text{dpp})](\text{PF}_6)$, the cell lysis in the wells of electrophoresis gel experiment was performed (Figure 3.39). In this study the cells were lysed within the well of a gel by lysis solution and the extract was run through the gel. The lysis in the gel well procedure is described in Chapter 2. This method eliminates the problems due to filtering out damaged DNA fragments during DNA extraction using Quagen kit. Figure 3.39 displays cell lysis in the wells of electrophoresis gel studies when *E. coli* JM109 (pUC18) cells were grown in the presence of 0.05 mM $[(\text{MePhtpy})\text{RuCl}(\text{dpp})](\text{PF}_6)$ under continuous photolysis conditions.

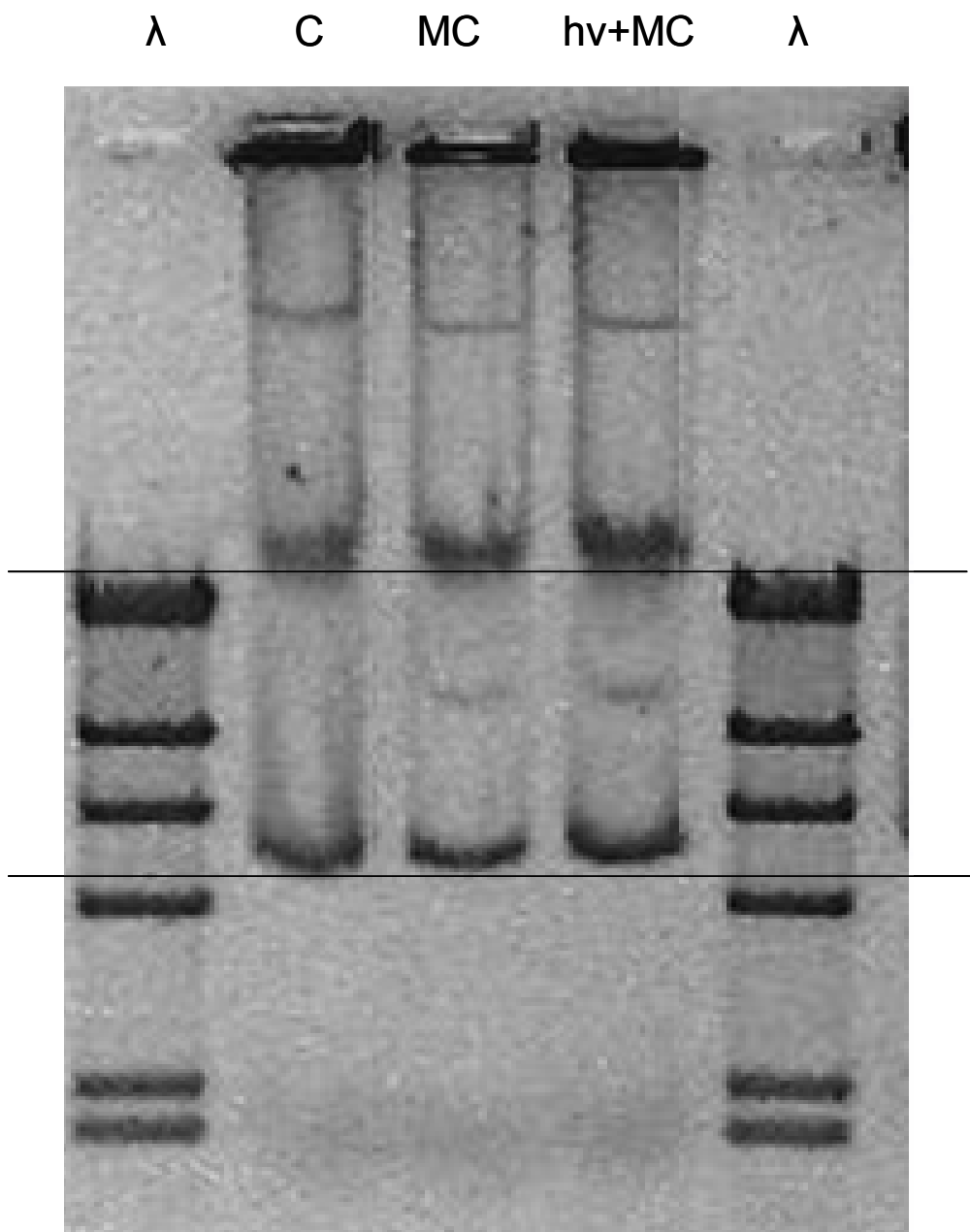


Figure 3.39. Agarose gel electrophoresis studies on DNA extracted from bacterial cells cell lysis in the wells of electrophoresis gel. Cells were grown in the presence of 0.05 mM [(MePhtpy)RuCl(dpp)](PF₆) with and without photolysis conditions (dpp = 2,3-bis(2-pyridyl)pyrazine, MePhtpy = 4'-(4-methylphenyl)-2,2':6',2''-terpyridine). Lane λ represents molecular weight marker, Lane C represents DNA extracted from cell culture done in the absence of metal complex, Lane MC represents DNA extracted from the culture grown in the presence of 0.05 mM [(MePhtpy)RuCl(dpp)](PF₆) (lane 3), lane (hv MC) represents DNA extracted from the culture grown in the presence of 0.05 mM [(MePhtpy)RuCl(dpp)](PF₆) with continuous photolysis (lane 4). Lines are drawn to show the relative positions of the bands in the gel.

Figure 3.39 displays cell lysis in the wells of electrophoresis gel studies when *E. coli* JM109 (pUC18) cells were grown in the presence of 0.05 mM [(MePhtpy)RuCl(dpp)](PF₆) under continuous photolysis conditions. Lane λ represents molecular weight marker, Lane C represents DNA extracted from cell culture done in the absence of metal complex, Lane MC represents DNA extracted from the culture grown in the presence of 0.05 mM [(MePhtpy)RuCl(dpp)](PF₆) (lane 3), lane (hv MC) represents DNA extracted from the culture grown in the presence of 0.05 mM [(MePhtpy)RuCl(dpp)](PF₆) with continuous photolysis (lane 4). Cell lysis in the wells of electrophoresis gel studies revealed slowing down of DNA migration under photolysis conditions (Figure 3.39, lane hv+MC). However the change in the DNA migration is too small. This suggests that either the DNA may not be the primary target of action of the designed molecule or the gel electrophoresis is not a best technique to see the damage caused by [(MePhtpy)RuCl(dpp)](PF₆) under *in vivo* conditions. It has been reported that, although DNA damage occurs upon photolysis in the presence of photosensitizers such as phenothiazene, it may not be the primary cause of bacterial cell death.⁷⁸ The alteration of cytoplasmic membrane proteins, disturbance of cell wall synthesis and the appearance of multilamellar structures near the septum of dividing cells, along with the loss of potassium ion from cells have been suggested as additional causes of cell death in the presence of photosensitizers.⁷⁸ As mentioned above there are also reports of antimicrobial photodynamic inactivation suggesting that the photosensitizer does not have to penetrate the bacterium to be effective. For example, generation of singlet oxygen in sufficient quantities near the bacterial outer membrane can cause damage to vital cellular structures such as DNA, RNA, and cell wall.⁷⁹

CHAPTER 4: Conclusions and Future Work

4.1. Conclusions

The purpose of this work was to design, develop, and study a new class of supramolecular assemblies by coupling a ruthenium-based light absorber to a cisplatin moiety. The ruthenium-based light absorbers of the form [(TL)RuCl(dpp)](PF₆) and ruthenium-based chromophore coupled cisplatin analogs of the form [(TL)RuCl(dpp)PtCl₂](PF₆) with varying TL (terminal ligand) (tpy = 2,2':6',2''-terpyridine, MePhtpy = 4'-(4-methylphenyl)-2,2':6',2''-terpyridine, or ^tBu₃tpy = 4,4',4''-tri-tert-butyl-2,2':6',2''-terpyridine) and BL (bridging ligand) = 2,3-bis(2-pyridyl)pyrazine (dpp) have been designed and developed. The impact of component modification on redox, spectroscopic, photophysical properties, DNA interaction, and antibacterial properties of a series of ruthenium-based chromophores and chromophore coupled cisplatin analogs was studied.

A comparative study of the photophysical, redox, and DNA photocleavage properties upon ligand modification of the heteroleptic complexes, [(MePhtpy)RuCl(dpp)](PF₆), [(tpy)RuCl(dpp)](PF₆), and [(^tBu₃tpy)RuCl(dpp)](PF₆), and the homoleptic complexes, [Ru(MePhtpy)₂]²⁺, [Ru(tpy)₂]²⁺, and [Ru(^tBu₃tpy)₂]²⁺, has been performed. The heteroleptic complexes showed intense metal to ligand charge transfer (MLCT) at lower energy ([[(MePhtpy)RuCl(dpp)](PF₆), 522 nm; [(tpy)RuCl(dpp)](PF₆), 516 nm; [(^tBu₃tpy)RuCl(dpp)](PF₆), 521 nm) compared to the homoleptic complexes, [Ru(MePhtpy)₂]²⁺, 490 nm; [Ru(tpy)₂]²⁺, 476 nm; and [Ru(^tBu₃tpy)₂]²⁺, 480 nm. The heteroleptic complexes displayed longer excited state lifetimes and higher emission quantum yields compared to the homoleptic complexes due to the stabilization of π* orbital on the dpp ligand. Consistent with the previous reports, the homoleptic complexes, [Ru(tpy)₂]²⁺, [Ru(MePhtpy)₂]²⁺, and [Ru(^tBu₃tpy)₂]²⁺ displayed a reversible Ru^{II/III} wave couple at 1.35, 1.30, and 1.12 V, with first reduction at -1.23, -1.20, and -1.37 V, respectively, vs. Ag/AgCl in CH₃CN.^{48,58,135,141,144} The heteroleptic complexes, [(MePhtpy)RuCl(dpp)](PF₆), [(tpy)RuCl(dpp)](PF₆), and [(^tBu₃tpy)RuCl(dpp)](PF₆), displayed a reversible Ru^{II/III} wave couple at -1.10, -1.10, and -1.01 V, with first reduction at -1.16, -1.15, and -1.12 V, respectively, vs. Ag/AgCl in CH₃CN. The

HOMO in both homoleptic and heteroleptic complexes is Ru-based. The LUMO in the heteroleptic complexes is dpp-based compared to the tpy-based LUMO in the homoleptic complexes. The dpp-based reduction occurred at a more positive potential than the tpy-based reduction due to the lower energy π^* orbital of dpp relative to tpy. The photophysical studies showed that the heteroleptic complexes possess higher emission quantum yields and longer excited state lifetimes as compared to the homoleptic complexes due to the stabilization of $^3\text{MLCT}$ state, which is Ru \rightarrow dpp CT in nature.

A series of multifunctional mixed metal supramolecular complexes of the type $[(\text{TL})\text{Ru}(\text{dpp})\text{PtCl}_2](\text{PF}_6)$ with varying terminal ligands have been successfully synthesized using a building block method. The heterobimetallic complexes were fully characterized by using FAB-MS, electrochemistry, electronic absorption spectroscopy, and ^{195}Pt NMR techniques. The FAB-MS spectra of the complexes were characterized by the appearance of the molecular ion peak $[\text{M}-\text{PF}_6]^+$. The fragments observed were characteristic of the loss of counter ions, intact ligands and/or metals. The ^{195}Pt NMR studies of heterobimetallic complexes displayed that these systems possess single ^{195}Pt resonance suggesting the presence of a single Pt containing species. All the bimetallic complexes displayed ligand-based $\pi\rightarrow\pi^*$ transitions in the UV region and MLCT transitions to each acceptor ligand in the visible region, with the Ru \rightarrow BL CT-based transitions occurring at lower energy. The Ru \rightarrow BL CT transitions were red-shifted in comparison to their respective monometallic precursors. These Ru $^{\text{II}}\text{Pt}^{\text{II}}$ bimetallic complexes displayed reversible Ru $^{\text{II/III}}$ couples at 1.10, 1.10, and 1.01 V vs. Ag/AgCl, for TL = tpy, MePhtpy, and $^t\text{Bu}_3\text{tpy}$, respectively. The tpy $^{0/-}$ reduction occurred at -1.43, -1.44, and -1.59 V vs. Ag/AgCl for TL = tpy, MePhtpy, and $^t\text{Bu}_3\text{tpy}$, respectively. These complexes displayed a more positive potential dpp $^{0/-}$ couple (-0.50 -0.55, -0.59 V) relative to their monometallic synthons (-1.15, -1.16, and -1.22 V), consistent with the bridging coordination of the dpp ligand.^{110,129} The tpy-based reduction in the $[(^t\text{Bu}_3\text{tpy})\text{RuCl}(\text{dpp})\text{PtCl}_2](\text{PF}_6)$ complex occurred at a more negative potential relative to those in the other two complexes due to the electron donating nature of the $^t\text{Bu}_3$ group.

This research also presents the first extensive DNA photocleavage studies of relatively unexplored tridentate, tpy containing chromophores. Agarose gel electrophoresis and equilibrium

dialysis experiments were used to investigate the DNA interaction properties of designed molecules. The ruthenium-based chromophores have previously been shown to photocleave DNA through molecular oxygen sensitization.^{67,68,70} The heteroleptic complexes, [(MePhtpy)RuCl(dpp)](PF₆), [(tpy)RuCl(dpp)](PF₆), and [(^tBu₃tpy)RuCl(dpp)](PF₆) were found to photocleave DNA more efficiently than homoleptic complexes, [Ru(MePhtpy)₂]²⁺, [Ru(tpy)₂]²⁺, and [Ru(^tBu₃tpy)₂]²⁺, in the presence of oxygen. The heteroleptic complex, [(MePhtpy)RuCl(dpp)]⁺, was found to be the most efficient in DNA photocleaving agent. Among homoleptic complexes, [Ru(MePhtpy)₂]²⁺ complex was found to photocleave DNA more efficiently than [Ru(tpy)₂]²⁺ and [Ru(^tBu₃tpy)₂]²⁺. The introduction of a methylphenyl group on the terpyridine ligand improves the photophysical properties, increases the lipophilicity, improves the DNA interaction ability and thereby improves the DNA photocleavage property of the supramolecular complex.

The coupling of the cisplatin unit to a ruthenium-based chromophore provides not only the coordinate covalent DNA binding ability due to *cis*-Pt^{II}Cl₂ moiety but also the spectroscopic probe and the potential for photoactivity of these supramolecules. The [(MePhtpy)RuCl(dpp)PtCl₂](PF₆) complex avidly binds to DNA and cleave DNA by molecular oxygen sensitization through the ³MLCT state of the Ru polypyridine unit representing one of only a handful of multifunctional DNA binding and photocleaving agents. The tetrametallic complex, [{(bpy)₂Ru(dpp)}₂Ru(dpp)PtCl₂](PF₆)₆, represents the only Ru^{II}Pt^{II} complex that has previously been shown to bind and photocleave DNA.¹⁰³ The [(^tBu₃tpy)RuCl(dpp)PtCl₂](PF₆) complex displayed minimal coordinate covalent binding to DNA compared to the other two complexes. The presence of the t-butyl groups on the terpyridine moiety lowers Pt coordination to the DNA. This could result from the steric bulkiness of t-butyl groups or groove binding of the metal complex via t-butyl groups. The presence of the methylphenyl group on the tpy ligand improves the interaction of the molecule with DNA, providing more facile DNA binding and photocleavage. The heteroleptic complexes photocleaved DNA through an oxygen mediated pathway. These results demonstrate that the metal complexes exhibiting enhanced DNA photocleavage activity can be designed by two ways: 1) by incorporating the lipophilic ligand to provide improved DNA interaction properties and better photophysical properties to the

supramolecular complex and 2) by Pt(II) coordination to increase the local concentration of metal complex near target, giving higher $^1\text{O}_2$ concentration.

The first *in vivo* studies of the mixed-metal supramolecular complexes of the type $[(\text{TL})\text{RuCl}(\text{dpp})\text{PtCl}_2](\text{PF}_6)$ and their monometallic precursors was performed. The impact on bacterial cell growth upon exposure to different concentrations of designed ruthenium chromophores and $\text{Ru}^{\text{II}}\text{Pt}^{\text{II}}$ bimetallic complexes was studied. The antibacterial properties of designed complexes were compared with that of cisplatin. The agarose gel electrophoresis results indicated that the mixed-metal complexes exhibited a larger change in DNA migration through a gel than does the cisplatin. However slightly higher concentrations of $[(\text{TL})\text{RuCl}(\text{dpp})\text{PtCl}_2](\text{PF}_6)$ (tpy, 0.04 mM; MePhtpy, 0.1 mM; and $^t\text{Bu}_3\text{tpy}$, 0.1 mM) were required to inhibit bacterial cell growth as compared to cisplatin (0.01 mM). The $[(\text{MePhtpy})\text{RuCl}(\text{dpp})](\text{PF}_6)$ showed bacterial cell growth inhibition at the lowest concentration (0.04 mM). A correlation between the DNA binding ability, lipophilicity, and cytotoxicity of the designed metal complexes was observed. The supramolecular complex, $[(\text{MePhtpy})\text{RuCl}(\text{dpp})](\text{PF}_6)$, exhibited high DNA binding constant and high lipophilicity and was found to be the best antibacterial agent. The *in vivo* studies have revealed the evidence of cell death due to DNA-MC interaction. The anti-bacterial property exhibited by these complexes provides a new direction for this mixed metal supramolecular chemistry.

The photodynamic antibiotic property of ruthenium (II) polypyridyl complex, $[(\text{MePhtpy})\text{Ru}(\text{dpp})\text{Cl}](\text{PF}_6)$ was studied. The complex, $[(\text{MePhtpy})\text{RuCl}(\text{dpp})](\text{PF}_6)$, was found to display photodynamic antibacterial properties. To the best of our knowledge the $[(\text{MePhtpy})\text{RuCl}(\text{dpp})](\text{PF}_6)$ complex is the first Ru-based metalloantibiotic reported to show light activated antibacterial property. This complex inhibits cell growth at 0.05 mM concentration. Cell growth inhibition was found to increase with photoactivation. The impact of intermittent photolysis on bacterial cell growth was studied to demonstrate the reversible mode of action of the metal complex. The reversibility in bacterial cell growth was observed on exposure to the $[(\text{MePhtpy})\text{RuCl}(\text{dpp})](\text{PF}_6)$, with cell growth inhibition in the presence of light and cell growth resumption in the absence of light. The reversibility in interaction makes this complex a potential candidate for the development of photodynamic antibiotics.

4.2. Future Work.

The research described in this thesis was focused on the design and development of multifunctional supramolecules with improved DNA interaction and antibacterial properties. This work illustrates that with careful selection of building blocks, the photophysical, DNA interaction, and antibacterial properties of the molecules can be modulated and efficient multifunctional molecules can be designed. While this research describes the approaches used to design and characterize multifunctional molecules, additional work is needed to derive structure activity relationships and to understand the mechanism of action of designed metal complexes.

Variations can be made on ligands and metal centers to have steric and electronic impact on the whole supramolecular assembly. Synthetic modifications of both metal center and ligands are possible, that can lead to variation in the spectroscopic, redox, and biological properties of these polymetallic systems. The use of the symmetric bridging ligand, bpm, for dpp ligand can eliminate the stereoisomers associated with the inequivalent nitrogens of the pyrazine and pyridine rings of dpp. The use of Os for Ru metal center can lead to red shift in absorption as a result of the higher energy $d\pi$ orbitals on osmium, allowing the molecules to absorb in a therapeutic window, a requirement for an efficient PDT agent. Related systems should be explored in detail to derive structure activity relationships.

Based upon the results of this research, ideal metalloantibiotics can be designed. The ruthenium-based chromophores exhibiting noncovalent interactions with DNA and higher membrane permeability could serve as photometalloantibiotics. The log P values of the designed molecules should be in the range of 1 to 3 to have good passive absorption across lipid membranes. Lipophilic substituents on the polyazine ligands not only provide the membrane permeability but also improve the groove binding ability of the complexes. The DNA interaction properties of the molecule can also be improved by introducing planar ligands that can intercalate between bases of DNA.

New methods can be utilized to probe the interaction of designed supramolecules with DNA. Atomic force microscopy (AFM) has previously been used to explore the DNA-MC

interaction. The interaction of metal complex with DNA changes the confirmation of DNA.^{181,182} This change in confirmation can be visualized by AFM and this can determine their mode of binding. AFM has previously been used for imaging single-stranded DNA, double-stranded DNA and DNA–metal complexes.^{182,183} Hyata and coworkers have visualized the structural changes in DNA after γ -irradiation by AFM at nanometer level resolution.¹⁸⁴

Photodynamic antibacterial activity exhibited by the complex, [(MePhtpy)RuCl(dpp)](PF₆), displayed a great potential for ruthenium-based chromophores as photobactericidal agents. Further studies need to be done on similar kinds of molecules. Ruthenium-based chromophores containing bidentate ligands can be designed. By replacing the tridentate terminal ligand with the bidentate ligands, the photophysical properties of the molecules can be improved and possibly also the light activated antibacterial properties.

Although we have observed a direct correlation between DNA interaction and photodynamic bacterial cell growth inhibition, we were not able to confirm these interactions under *in vivo* conditions. Additional work needs to be done to understand the mode of bacterial cell growth inhibition by these supramolecules. The interaction between designed Ru^{II}Pt^{II} heterobimetallic complexes and proteins should be investigated. As cisplatin is known to bind with proteins, therefore protein binding studies can provide us useful information about the mechanism of cell growth inhibition by designed molecules. Polyacrylamide gel electrophoresis studies could be utilized to probe MC-protein interaction. Atomic force microscopy can be utilized to analyze the mode of action of designed molecules. AFM is a high-resolution microscope allows measurements of native biological samples in physiological conditions. Fluorescence spectroscopy could also be utilized to understand the target and mechanism of action of designed supramolecules. To perform fluorescence spectroscopy, fluorescent molecules would have to be developed, for example, by coupling an anthracene moiety to the MePhtpy ligand. These supramolecular complexes will be of the type FT-LA-BAS (FT = fluorescent tag, LA = light absorber, and BAS = bioactive site), illustrated in Figure 4.1. The hydrophobic groups could be introduced to improve the membrane permeability. The proposed fluorescent sensor will interact with DNA through *cis*-PtCl₂ moiety. The interaction of the proposed sensor with DNA and other biomolecules will be monitored by fluorescence spectroscopy.

Given that the designed metal complexes have displayed DNA interaction and antibacterial properties, it is desirable to investigate the anticancer properties of the designed molecules. The MTT (3-(4,5-dimethylthiazol-2-yl)-2,5-diphenyltetrazolium bromide) assay can be used to determine anticancer activity of these molecules. The MTT assay is a standard colorimetric assay for measuring cellular proliferation. The amount of yellow MTT reduced to purple formazan is measured spectrophotometrically. This reduction of MTT takes place only when mitochondrial reductase enzymes are active, and thus conversion is directly related to the number of viable cells.

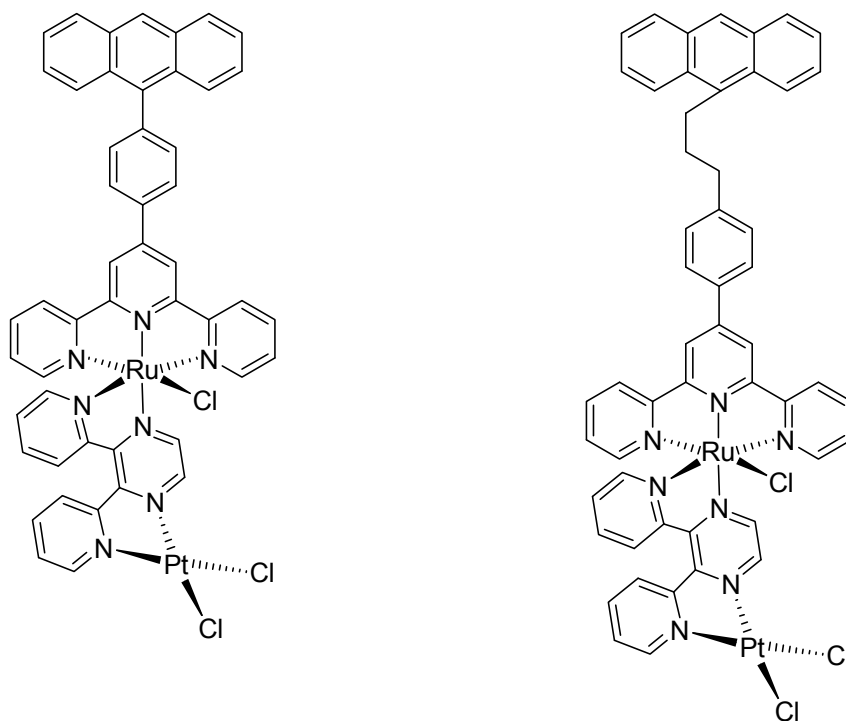


Figure 4.1. Proposed fluorescent sensors.

Finally it is desirable and necessary to determine photodynamic dynamic action of designed molecules using mammalian cells. The complex, $[\{(bpy)_2Ru(dpp)\}_2RhCl_2]Cl_5$, has been shown to kill Green monkey kidney cells upon photolysis, but do not impede cell growth in the absence of light.¹⁸⁵ Similar studies are needed to be done using the designed metal complexes.

References.

1. *Cancer facts and figures* In American Cancer Society, 2008.
2. McAllister, R. M., Horowitz, S. T. and Gilden, R. V., *Cancer*, Basic Books, Newyork, 1993.
3. Cooper, G. M., *The Cancer Book*, Jones and Barlett, Boston, 1993.
4. Whitehouse, M. and Slevin, M., *Cancer the facts*, Oxford University Press, New York, 1996.
5. Levitt, P. M., Guralnick, E. S., Kagan, A. R. and Gilbert, H., *The cancer reference book*, Facts on File, New York, 1979.
6. Wong, E. and Giandomencio, C. M., Current status of platinum-based antitumor drugs *Chem. Rev.* 1999, **99**, 2451-2466.
7. Jamieson, E. R. and Lippard, S. J., Structure, recognition, and processing of cisplatin-DNA adducts *Chem. Rev.* 1999, **99**, 2467-2498.
8. Zang, C. X. and Lippard, S., New metal complexes as potential therapeutics *Current opinion in Chemical biology* 2003, **7**, 481-489.
9. Voet, D. and Voet, J. G., *Biomolecules, mechanisms of enzyme action, and metabolism*, John Wiley & Sons, Inc, 2003.
10. Kumar, C. V., Barton, J. K. and Turro, N. J., Photophysics of ruthenium complexes bound to double helical DNA *J. Am. Chem. Soc.* 1985, **107**, 5518-5523.
11. Barton, J. K., Metals and DNA: Molecular left-handed compliments *Science* 1986, **233**, 727-734.
12. Mei, H. Y. and Barton, J. K., Chiral Probe for A-Form Helices of DNA and RNA: tris(Tetramethylphenanthroline)Ruthenium(II) *J. Am. Chem. Soc.* 1986, **108**, 7414-7416.
13. Friedman, A. E., Chambron, J.-C., Sauvage, J.-P., Turro, N. J. and Barton, J. K., Molecular "light switch" for DNA; Ru(bpy)₂(dppz)²⁺ *J. Am. Chem. Soc.* 1990, **112**, 4960-4692.
14. Rosenberg, b., Camp, V. and Kriagas, T., Inhibition of cell division in *Echerichia coli* by electrolysis products from a platinum electrode *Nature* 1965, **205**, 698-699.
15. Rosenberg, B., L. V. C., Trosko, J. E. and Mansour, V. H., Platinum Compounds: A New Class of Potent Antitumour Agents *Nature* 1969, **222**, 385-387.
16. Cohen, G. L., Ledner, J. A., Bauer, W. R., Ushay, H. M., Caravana, C. and Lippard, S. J., Sequence dependent binding of cis-dichlorodiammineplatinum(II) to DNA *J. Am. Chem. Soc.* 1980, **102**, 2487-2488.
17. Sherman, S. E. and Lippard, S. J., Structural aspects of platinum anticancer drug interactions with DNA *Chem. Rev.* 1987, **87**, 1153-1181.
18. Reedjik, J., Why does cisplatin reach guanine-N7 with competing S-donor ligands available in the cell? *Chem. Rev.* 1999, **99**, 2499-2510.
19. Sundquist, W. I., Ahmed, K. J., Hollis, L. S. and Lippard, S. J., Solvolysis reactions of cis- and trans-diamminedichloroplatinum(II) in dimethyl sulfoxide. Structural characterization and DNA binding of trans-bis(ammine)chloro(DMSO)platinum(1+) *Inorg. Chem.* 1987, **26**, 1524-1528.
20. Bancroft, D. P., Lepre, C. A. and Lippard, S. J., Platinum-195 NMR kinetic and mechanistic studies of cis- and trans-diamminedichloroplatinum(II) binding to DNA *J. Am. Chem. Soc.* 1990, **112**, 6860-6781.

21. Hambley, T., Platinum binding to DNA: structural control and consequences *Dalton Transaction* 2001, 2711-2718.
22. Takahara, P. M., Frederick, C. A. and Lippard, S. J., Crystal Structure of the Anticancer Drug Cisplatin Bound to Duplex DNA *J. Am. Chem. Soc.* 1996, **118**, 12309-12321.
23. Hanigan, M. H., Gallagher, B. C., Taylor, P. T. and Large, M. K., Inhibition of gamma-glutamyl transpeptidase activity by acivicin in vivo protects the kidney from cisplatin induced toxicity *Cancer Res.* 1994, **54**, 5925-5929.
24. Sherman, S. E. and Lippard, S. J., Structural aspects of platinum anticancer drug interactions with DNA. *Chem. Chem. Rev.* 1987, **87**, 1153-1181.
25. Desoize, B. and Madoulet, C., Particular aspects of platinum compounds used at present in cancer treatment *Crit. Rev. Oncol. Hematol.* 2002, **42**, 317-325.
26. Farrell, N., Qu, Y. and Hacker, M. P., Cytotoxicity and antitumor activity of bis(platinum) complexes. A novel class of platinum complexes active in cell lines resistant to both cisplatin and 1,2-diaminocyclohexane complexes *J. Med. Chem.* 1990, **33**, 2179-2184.
27. Johnson, A., Qu, Y., Houten, B. V. and Farrell, N., B{uparrow} Z DNA conformational changes induced by a family of dinuclear bis(platinum) complexes *Nucleic Acid Research* 1992, **20**, 1697-1703.
28. Blasi, P. D., Bernareggi, A., Beggiolin, G., Piazzoni, L., Menta, E. and Formento, M. L., *Anticancer Res.* 1998, **18**, 3113-3117.
29. Perego, P., Caserini, C., Gatti, L., Carenini, N., Romanelli, S., Supino, R., Colangelo, D., Viano, L., Leone, R., Spinelli, S., Pezzoni, G., Mazotti, C., Farrell, N. and Znini, F., A Novel Trinuclear Platinum Complex Overcomes Cisplatin Resistance in an Osteosarcoma Cell System *Mol. Pharm.* 1999, **55**, 528-534.
30. Allison, R. R., Mota, H. C. and Sibata, C. H., Clinical PD/PDT in North America: An historical review *Photodiagn. Photodyn. Ther.* 2004, **1**, 263-277.
31. Ackroyd, R., Keity, C., Brown, N. and Reed, M., The history of photodetection and photodynamic therapy *Photochemistry and Photobiology* 2001, **74**, 656-669.
32. Dougherty, T. J., Gomer, C. J., Henderson, B. W., Jori, G., Kessel, D., Koebrlik, M., Moan, J. and Peng, Q., Photodynamic therapy *Journal of the Cancer Institute* 1998, **90**, 889-904.
33. Dennis, E. J., Dolmans, G. J., Fukumura, D. and Jain, R. K., Photodynamic therapy for cancer *Nature Reviews* 2003, **3**, 380-387.
34. Moore, J. V., West, C. M. L. and Whitehurst, C., The biology of photodynamic therapy *Phys. Med. Biol.* 1997, **42**, 913-935.
35. Foote, C. S., Definition of type I and type II photosensitized oxidation *Photochem. Photobiol.* 1991, **54**, 659-659.
36. Kriska, T., Korecz, L., Nemes, I. and Gal, D., Physico-chemical modeling of the role of free radicals in photodynamic therapy. III. Interactions of stable free radicals with excited photosensitizers studied by kinetic ESR spectroscopy *Biochem. and Biophys. Res. Commun.* 1995, **215**, 192-198.
37. Nemeth, A., Jakus, J., Kriska, T., Keszler, A., Vanyur, R. and Gal, D., Physio chemical modeling of the role of free radicals in photodynamic therapy *Biochem. and Biophys. Res. Commun.* 1999, **255**, 360-366.

38. Gal, D., Shutova, T., Kriska, T. and Nemeth, A., Quantitative spin trapping and triplet quenching by radicals for *in vivo* studies I. The chemical model. *J. Biochem. Biophys. Methods* 2003, **55**, 11-21.
39. Ziolkowski, P., Leszczyszyn, H. G., Symonowicz, K., Bronowicz, A. and Osiecka, B. J., Clinical applications of photodynamic therapy *Adv. Clin. Exp. Med.* 2004, **13**, 359-365.
40. Kalyanasundaram, K., Photophysics, photochemistry and solar energy conversion with tris(bipyridyl)ruthenium(II) and its analogues *Coord. Chem. Rev.* 1982, **46**, 159-244.
41. Stochel, G., Wanat, A., Kulis, E. and Stasicka, Z., Light and metal complexes in medicine *Coord. Chem. Rev.* 1998, **171**, 203-220.
42. Balzani, V., Photochemical molecular devices *Photochem. Photobiol. Sci.* 2003, **2**, 459-476.
43. Balzani, V., Moggi, L. and Scandola, F., in *Supramolecular Photochemistry*, ed. V. Balzani, D. Reidel Publishing Company, Editon edn., 1987, pp. 1-28.
44. Balzani, V. and Scandola, F., in *Comprehensive Supramolecular Chemistry*, ed. D. H. Reinhoudt, Pergamon, New York, Editon edn., 1996, vol. 10, pp. 687-746.
45. Kalyanasundaram, K., *Photochemistry of Polypyridine and Porphyrin Complexes*, Academic Press, San Diego, 1992.
46. Kalyanasundaram, K. and Nazeeruddin, M. K., Photophysics and photoredox reactions of ligand-bridged binuclear polypyridyl complexes of ruthenium(II) and their monomeric analogues *Inorg. Chem.* 1990, **29**, 1888-1897.
47. Balzani, V., Juris, A. and Venturi, M., Luminiscent and redox active polynuclear transition metal complexes *Chem. Rev.* 1996, **96**, 759-833.
48. Juris, A., Balzani, V., Barigelletti, F., Campagna, S., Belser, P. and von Zelewsky, A., Ru(II) polypyridine complexes: photophysics, photochemistry, eletrochemistry, and chemiluminescence *Coord. Chem. Rev.* 1988, **84**, 85-277.
49. Durham, B., Caspar, J. V., Nagle, J. K. and Meyer, T. J., Photochemistry of tris(2,2'-bipyridine)ruthenium(2+) ion *J. Am. Chem. Soc.* 1982, **104**, 4803-4810.
50. Young, R. C., Nagle, J. K., Meyer, T. J. and Whitten, D. G. Electron Transfer Quenching of Nonemitting Excited States of Ru(TPP)(py)₂ and Ru(trpy)₂²⁺ *J. Am. Chem. Soc.* 1978, **100**, 4773-4778.
51. Winkler, J. R., Netzel, T. L., Creutz, C. and Sutin, N., Direct observation of metal-to-ligand charge-transfer (MLCT) excited states of pentaammineruthenium(II) complexes *J. Am. Chem. Soc.* 1987, **109**, 2381-2392.
52. Berger, R. M. and McMillin, D. R., Localized states in reduced and excited-state ruthenium(II) terpyridyls *Inorg. Chem.* 1988, **27**, 4245-4249.
53. Kirchhoff, J. R., McMillin, D. R., Marnot, P. A. and Sauvage, J. P., Photochemistry and photophysics of bis(terpyridyl) complexes of ruthenium(II) in fluid solution. Evidence for the formation of an .eta.2-diphenylterpyridine complex *J. Am. Chem. Soc.* 1985, **107**, 1138-1141.
54. Collin, J. P., Guillerez, S., Sauvage, J. P., Barigelletti, F., De Cola, L., Flamigni, L. and Balzani, V., Photoinduced processes in dyads and triads containing a ruthenium(II)-bis(terpyridine) photosensitizer covalently linked to electron donor and acceptor groups *Inorg. Chem.* 1991, **30**, 4230-4238.
55. Barigelletti, F., Flamigni, L., Balzani, V., Collin, J.-P., Sauvage, J.-P., Sour, A., Constable, E. C. and Thompson, A. M. W. C., Rigid Rod-Like Dinuclear Ru(II)/Os(II) Terpyridine-Type Complexes. Electrochemical Behavior, Absorption Spectra,

- Luminescence Properties, and Electronic Energy Transfer through Phenylene Bridges *J. Am. Chem. Soc.* 1994, **116**, 7692-7699.
56. Beley, M., Collin, J. P., Sauvage, J. P., Sugihara, H., Heisel, F. and Miehe, A., Photophysical and photochemical properties of ruthenium and osmium complexes with substituted terpyridines *Journal of the Chemical Society, Dalton Transactions* 1991, **11**, 3157-3159.
 57. Thummel, R. P., Hegde, V. and Jahng, Y., Influence of remote substituents on the properties of bis(terpyridyl)ruthenium(II) complexes *Inorg. Chem.* 1989, **28**, 3264-3267.
 58. Maestri, M., Armaroli, N., Balzani, V., Constable, E. C. and Thompson, A. M. W. C., Complexes of the Ruthenium(II)-2,2':6',2''-terpyridine Family. Effect of Electron-Accepting and -Donating Substituents on the Photophysical and Electrochemical Properties *Inorg. Chem.* 1995, **34**, 2759-2767.
 59. Abrahamsson, M., Jager, M., Osterman, T., Eriksson, L., Persson, P., Becker, H. C., Johansson, O. and Hammarstrom, L., A 3.0 s Room Temperature Excited State Lifetime of a Bistridentate RuII-Polypyridine Complex for Rod-like Molecular Arrays *J. Am. Chem. Soc.* 2006, **128**, 12616-12617.
 60. Constable, E. C., Harverson, P., Smith, D. R. and Whall, L., The coordination chemistry of 4'-(4-tert-butylphenyl)-2,2' : 6',2''-terpyridine--a solubilising oligopyridine *Polyhedron* 1997, **16**, 3615-3623.
 61. Medlycott, E. A. and Hanan, G. S., Synthesis and properties of mono- and oligo-nuclear Ru(II) complexes of tridentate ligands: The quest for long-lived excited states at room temperature *Coord. Chem. Rev.* 2006, **250**, 1763-1782.
 62. Erkkila, K. E., Odom, D. T. and Barton, J. K., Recognition and reaction of metallointercalators with DNA *Chem. Rev.* 1999, **99**, 2777-2795.
 63. Zeglis, B. M., Pierre, V. C. and Barton, J. K. Metallo-intercalators and metallo-insertors *Chem. Commun.* 2007, 4565-4579.
 64. Clarke, M. J., Ruthenium metallopharmaceuticals *Coord. Chem. Rev.* 2003, **236**, 209-233.
 65. Farrer, B. T. and Thorp, H. H., Redox Pathways in DNA oxidation: kinetic studies of guanine and Sugar oxidation by para substituted derivatives of oxoruthenium(IV) *Inorg. Chem.* 2000, **39**, 44-49.
 66. Grover, N., Gupta, N., Singh, P. and Thorp, H. H., Studies of electrocatalytic DNA cleavage by oxoruthenium(IV). X-ray crystal structure of [Ru(tpy)(tmen)OH₂](ClO₄)₂ (tmen = N,N,N',N'-tetramethylethylenediamine, tpy = 2,2',2''-terpyridine) *Inorg. Chem.* 1992, **31**, 2014-2020.
 67. Chouai, A., Wicke, S. E., Turro, C., Bacsá, J., Dunbar, K. R., Wang, D. and Thummel, R. P., Ruthenium(II) Complexes of 1,12-Diazaperylene and Their Interactions with DNA *Inorg. Chem.* 2005, **44**, 5996-6003.
 68. Patty, K. L. F., Bradley, P. M., Loyen, D. V., Durr, H., Bossmann, S. H. and Turro, C., DNA photocleavage by a supramolecular Ru(II)-Viologen complex *Inorg. Chem.* 2002, **41**, 3808-3810.
 69. Liu, Y., Hammitt, R., Lutterman, D. A., Thummel, R. P. and Turro, C., Marked Differences in Light-Switch Behavior of Ru(II) Complexes Possessing a Tridentate DNA Intercalating Ligand *Inorg. Chem.* 2007, **46**, 6011-6021.
 70. Ding, H.-Y., Wang, X.-S., Song, L.-Q., Chen, J.-R., Yu, J.-H., Chao, L. and Zhang, B.-W., Aryl-modified ruthenium bis(terpyridine) complexes: Quantum yield of ¹O₂

- generation and photocleavage on DNA *Journal of Photochemistry and Photobiology A: Chemistry* 2006, **177**, 286-294.
71. Wainwright, M., Phoenix, D. A., Gaskell, M. and Marshall, B., Photobactericidal activity of methylene blue derivatives against vancomycin-resistant *Enterococcus* spp. *J. Antimicrob. Chemother.* 1999, **44**, 823-825.
 72. Wainwright, M., Photodynamic antimicrobial chemotherapy (PACT) *J. Antimicrob. Chemother.* 1998, **42**, 13-28.
 73. Wainwright, M., Photoinactivation of viruses *Photochem. Photobiol. Sci.* 2004, **3**, 406-411.
 74. Wainwright, M., The development of phenothiazinium photosensitisers. *Photodiagnosis and Photodynamic Therapy* 2005, **2**, 263-272.
 75. Hamblin, M. R. and Hasan, T., A new antimicrobial approach to infectious disease *Photochem. Photobiol. Sci.* 2004, **3**, 436-450.
 76. Demidova, T. N. and Hamblin, M. R., *Int. J. Immunother.* 2004, **17**, 117-126.
 77. Gad, F., Zahra, T., Hasan, T. and Hamblin, M., Effects of Growth Phase and Extracellular Slime on Photodynamic Inactivation of Gram-Positive Pathogenic Bacteria *Antimicrobs. Agents. Ch.* 2004, **48**, 2173-2178.
 78. Malik, Z., Ladan, H. and Nitzan, Y., Photodynamic inactivation of Gram-negative bacteria: Problems and possible solutions *J. Photochem. and Photobiol. B* 1992, **14**, 262-266.
 79. Dahl, T. A., Midden, W. R. and Hartman, P. E., Pure singlet oxygen cytotoxicity for bacteria *Photochem. Phobiol.* 1987, **46**, 345-352.
 80. Hass, B. S. and Webb, R. B., Photodynamic effects of dyes on bacteria. Lethal effect of acedine orange and 460 or 500 nm monochromatic light in strains of *E. coli* that differ in repair capability *Mutat. Res.* 1981, **81**, 277-285.
 81. Hass, B. S. and Webb, R. B., Photodynamic effects of dyes on bacteria. Mutagenesis by acedine orange and 460 or 500 nm monochromatic light in strains of *E. coli* that differ in repair capability *Mutat. Res.* 1979, **60**, 1-11.
 82. Nitzan, Y., Gutterman, M., Malik, Z. and Ehrenberg, B., Inactivation of gram negative bacteria by photosensitized porphyrins *Photochem. Phobiol.* 1992, **55**, 89-96.
 83. Novakova, O., Kasparkova, J., Varna, O. I., Vliet, P. M. V., Reedijk, J. and Brabec, V., Correlation between Cytotoxicity and DNA Binding of Polypyridyl Ruthenium Complexes *Biochemistry* 1995, **34**, 12369-12378.
 84. Ming, L.-J., Structure and Function of "Metalloantibiotics" *Medical Research Reviews* 2003, **23**, 697-762.
 85. Ming, L.-J. and Epperson, J. D., Metal binding and structure-activity relationship of the metalloantibiotic peptide bacitracin *J. Inorg. Biochem.* 2002, **91**, 46-58.
 86. Chang, C. H. and Meares, C. F., Cobalt-bleomycins and deoxyribonucleic acid: Sequence-dependent interactions, action spectrum for nicking, and indifference to oxygen. *Biochemistry* 1984, **23**, 2268-2274.
 87. Allardyce, C. S., Dorcier, A., Scolaro, C. and Dyson, P. J., Development of organometallic (organo-transitionmetal) pharmaceuticals *Appl. Organometal. Chem.* 2005, **19**, 1-10.
 88. Gameiro, P., Rodrigues, C., Baptista, T., Sousa, I. and Castro, B. d., Solution studies on binary and ternary complexes of copper(II) with some fluoroquinolones and 1,10-

- phenanthroline: Antimicrobial activity of ternary metalloantibiotics *International Journal of Pharmaceutics* 2007, **334**, 129-136.
89. Anderberg, P. I., Harding, M. M., Luck, I. J. and Turner, P., Ruthenium Complexes of Analogues of the Antitumor Antibiotic Streptonigrin *Inorg. Chem.* 2002, **41**, 1365-1371.
 90. Cetinkaya, B., Ozdemir, I., Binbasioglu, B., Durmaz, R. and Gunal, S., Antibacterial and antifungal activities of complexes of ruthenium (II) *Drug Res.* 1999, **49**, 538-540.
 91. Jhaumeer-Laullo, S., Bhowon, M. G. and Hosnay, A., Synthesis, catalytic and antibacterial activity of ruthenium complexes of 2,2'-dithiobis[N-(2-hydroxy-naphth-3-yl)benzamides] *J. Indian Chem. Soc* 2004, **81**, 547-551.
 92. Mishra, L., Yadaw, A. K., Srivastavab, S. and Patelb, A. B., Synthesis, spectroscopic, electrochemical and antibacterial studies of new Ru(II) 1,10-phenanthroline complexes containing aryldiazopentane-2,4-dione as co-ligand *New J. Chem.* 2000, **24**, 505-510.
 93. Will, J., Kyas, A., Sheldrick, W. S. and Wolters, D., Identification of (n6-arene)ruthenium(II) protein binding sites in *E. coli* cells by combined multidimensional liquid chromatography and ESI tandem mass spectrometry: specific binding of [(n6-p-cymene)RuCl₂(DMSO)] to stress-regulated proteins and to helicases *J Biol. Inorg. Chem.* 2007, **12**, 883-894.
 94. Triesscheijn, M., Baas, P., Schellens, J. H. M. and Stewart, F. A. Photodynamic therapy in oncology *Oncologist* 2006, **11**, 1034-1044.
 95. Detty, M. R., Gibson, S. L. and Wagner, S. J., Current Clinical and preclinical photosensitizer for use in photodynamic therapy *Journal of Medicinal Chemistry* 2004, **47**, 3897-3915.
 96. Canti, G., Nicolin, A., Cubeddu, R., Taroni, P., Bandieramonte, G. and Valentini, G., Antitumor efficacy of the combination of photodynamic therapy and chemotherapy in murine tumors *Cancer Lett.* 1998, **125**, 39-44.
 97. Crescenzi, E., Chiaviello, A., Canti, G., Reddi, E., Venezizni, B. M. and Palumbo, G., Low dose of cisplatin or gemcitabine plus photofrin/ photodynamic therapy: Disjointed cell cycle phase-related activity accounts for synergistic outcome in metastatic non small cell lung cancer cells (H1299) *Mol. Cancer Ther.* 2006, **5**, 776-785.
 98. Nonaka, M., Ikeda, H. and Inokuchi, T., Effect of combined photodynamic and chemotherapeutic treatment on lymphoma cells in vitro *Cancer Lett.* 2002, **184**, 171-178.
 99. Brunner, H. and Gruber, N., Carboplatin containing porphyrin-platinum complexes as cytotoxic and phototoxic antitumor agents *Inorg. Chim. Acta* 2004, **357**, 4423-4451.
 100. Brunner, H., Schellerer, K. M. and Treittnger, B., Synthesis and invitro testing of hematoporphyrin type ligands in platinum (II) complexes as potent cytostatic and phototoxic antitumor agents *Inorg. Chim. Acta* 1997, **264**, 67-79.
 101. Lee, H. H., Palmer, B. D., Baguley, B. C., Chin, M., Mcfayden, W. D., Wickham, G., Palmer, D. T., Wakelin, L. P. G. and A.Denny, W., DNA directed alkylating agents. 5. Acridinecarboxamide derivatives of (1,2-Diaminoethane)dichloroplatinum(II) *J. Med. Chem.* 1992, **35**, 2983-2987.
 102. Lottner, C., Bart, K. C., Bernhardt, G. and Brunner, H., Soluble tetraarypophyrin-platinum conjugates as cytotoxic and phototoxic *J. Med. Chem.* 2002, **45**, 2079-2089.
 103. Miao, R., Mongelli, M. T., Zigler, D. F., Winkel, B. and Brewer, K. J., A Multifunctional Tetrametallic Ru-Pt Supramolecular Complex Exhibiting Both DNA Binding and Photocleavage. *Inorg. Chem.* 2006, **45**, 10413-10415.

104. Sakai, K., Ozawa, H., Yamada, H., Tsubomura, T., Hara, M., Higuchi, A. and Haga, A., A tris (2,2'-bipyridine)ruthenium(II) derivative tethered to a cis-PtCl₂(amine)₂ moiety: synthesis, spectroscopic properties and visible light induced scission of DNA *Dalton Transaction* 2006, 3300-3305.
105. Sahai, R., Baucom, D. A. and Rillema, D. P., Strongly luminescing ruthenium(II)/ruthenium(II) and ruthenium(II)/platinum(II) binuclear complexes *Inorg. Chem.* 1986, **25**, 3843-3845.
106. Qu, Y. and Farrell, N., Synthesis and chemical properties of a heteronuclear (Pt,Ru) DNA-DNA and DNA-protein crosslinking agent *Inorg. Chem.* 1995, **34**, 3573-3576.
107. Houten, B. V., Illenye, S., Qu, Y. and Farrell, N., Homonuclear (Pt, Pt) and heteronuclear (Ru,Pt) metal compounds as DNA-protein crosslinking agents: Potential Suicide DNA lesions *Biochemistry* 1993, **32**, 11794-11801.
108. Schilden, K. V. D., Garcia, F., Kooijman, H., Spek, A. L., Haansoot, J. G. and Reedijk, J., A highly flexible dinuclear ruthenium(II)-platinum(II) complex: crystal structure and binding to 9-ethylguanine *Angew. Chem. Int. Ed.* 2004, **43**, 5668-5670.
109. Sahai, R. and Rillema, D. P., A ruthenium(II)/platinum(II) binuclear complex bridged by 2,2'-bipyridine *Inorg. Chem. Acta* 1986, **118**, L35-L37.
110. Yam, V. W., Lee, V. W. M. and Cheung, K. K., Synthesis photophysics and electrochemistry of a novel luminescent organometallic ruthenium(II)/platinum(II) binuclear complex and its ruthenium(II)/dichloroplatinum(II) and palladium(II) counterparts. X ray crystal structure of [Ru(bpy)₂(u-2,3-dpp)PtCl₂]²⁺ (2,3-dpp= 2,3-bis(2-pyridyl)pyrazine] *J. Chem. Soc., Chem. Commun.* 1994, 2075-2076.
111. Yam, V. W.-W., Lee, V. W. M. and Cheung, K. K., Synthesis, Photophysics, Electrochemistry, and Reactivity of ruthenium (III) polypyridine complexes with organoplatinum (II) moieties. Crystal structure of [Ru(bpy)₂(u-dpp)PdCl₂]²⁺ *Organometallics* 1997, **16**, 2833-2841.
112. Ruminski, R. R., Nelson, J. M. and Culver, W. S., Synthesis and characterization of Pt(II) and Pt(II)/Ru(II) complexes with the bidentate ligand dpop *Inorg. Chem. Acta.* 2005, **358**, 93-101.
113. Sahai, R. and Rillema, D. P., A novel heterooligomer containing one ruthenium(II) and three platinum(II) metal centers bridged by 2,3-bis(2-pyridyl)quinoxaline *Journal of the Chemical Society, Chemical Communications* 1986, 1133-1134.
114. Barthram, A. M., Ward, M. D., Gessi, A., Armaroli, N., Flamigni, L. and Barigelletti, F., Spectroscopic, luminescence and electrochemical studies on a pair of isomeric complexes [(bipy)₂Ru(AB)PtCl₂][PF₆]₂ and [Cl₂Pt(AB)Ru(bipy)₂][PF₆]₂, where AB is the bis-bipyridyl bridging ligand 2,2':3',2'':6'',2'''-quaterpyridine *New Journal of Chemistry* 1998, **22**, 913-917.
115. Milkevitch, M., Brauns, E. and Brewer, K. J., Spectroscopic and Electrochemical Properties of a Series of Mixed-Metal d₆,d₈ Bimetallic Complexes of the Form [(bpy)₂M(BL)PtCl₂]²⁺ (bpy = 2,2'-Bipyridine; BL = dpq (2,3-Bis(2-pyridyl)quinoxaline) or dpb (2,3-Bis(2-pyridyl)- benzoquinoxaline); M = OsII or RuII) *Inorg. Chem.* 1996, **35**, 1737-1739.
116. Williams, R. L., Toft, H. N., Winkel, B. and Brewer, K. J., Synthesis, characterization and DNA binding properties of a series of Ru, Pt mixed metal complexes *Inorg. Chem.* 2003, **42**, 4394-4400.

117. Fang, Z., Swavey, S., Holder, A., Winkel, B. and Brewer, K. J., DNA binding of mixed metal supramolecular Ru, Pt complexes *Inorg. Chem. Commun.* 2002, **5**, 1078-1080.
118. Brewer, K. J., Swavey, S., Williams, R. L., Fang, Z. and Bullock, E. R., Designing mixed metal supramolecular complexes *Proceedings of SPIE* 2001, **4512**, 53-64.
119. Milkevitch, M., Mixed-metal ruthenium-platinum polyazine supermolecules [electronic resource] : synthesis, characterization and exploration of DNA binding. Virginia Tech, 2000.
120. Milkevitch, M., Shirley, B. W. and Brewer, K. J., Mixed-metal polymetallic complexes designed to interact with DNA *Inorg. Chim. Acta* 1997, **264**, 249-256.
121. Milkevitch, M., Storrie, H., Brauns, E., Brewer, K. J. and Shirley, B. W., A new class of supramolecular, mixed-metal DNA-binding agents: The interaction of Ru(II),Pt(II) and Os(II),Pt(II) bimetallic complexes with DNA *Inorg. Chem.* 1997, **36**, 4534-4538.
122. Swavey, S., Williams, R. L., Fang, Z., Milkevitch, M. and Brewer, K. J., DNA binding of supramolecular mixed metal complexes *Proceedings of SPIE* 2001, **4512**, 75-83.
123. Herman, A., Tanski, J. M., Tibbetts, M. F. and Anderson, C. M., Synthesis, Characterization, and in Vitro Evaluation of a Potentially Selective Anticancer, Mixed-Metal [Ruthenium(III)-Platinum(II)] Trinuclear Complex *Inorg. Chem.* 2008, **47**, 274-280.
124. Winter, M., Editon edn., <http://winter.group.shef.ac.uk/chemputer/>.
125. Gennett, T., Milner, D. F. and Weaver, M. J., *J. Phys. Chem.* 1985, **89**, 2787-2790.
126. Kober, E. M., Sullivan, B. P., Dressick, W. J., Caspar, J. V. and Meyer, T. J., Highly luminescent polypyridyl complexes of osmium(II) *J. Am. Chem. Soc.* 1980, **102**, 7383-7385.
127. Sangester, J., *Octanol-water partition coefficients: Fundamentals and Physical Chemistry*, 1997.
128. Prussin, A. J., Zigler, D. F., Jain, A., Brown, J. R., Winkel, B. S. J. and Brewer, K. J., Photochemical methods to assay DNA photocleavage using supercoiled pUC18 DNA and LED or xenon arc lamp excitation *J. Inorg. Biochem.* 2008, **102**, 731-739.
129. Milkevitch, M., Brauns, E. and Brewer, K. J., Spectroscopic and Electrochemical Properties of a Series of Mixed-Metal d6,d8 Bimetallic Complexes of the Form $[(bpy)_2M(BL)PtCl_2]^{2+}$ (bpy = 2,2'-bipyridine; BL = dpq (2,3-Bis(2-pyridyl)quinoxaline) or dpb (2,3-bis(2-pyridyl)-benzoquinoxaline); M = OsII or RuII) *Inorg. Chem.* 1996, **35**, 1737-1739.
130. McGhee, J. D. and vonHippel, P. H., Theoretical aspects of DNA-protein interactions: co-operative and non-co-operative binding of large ligands to a one-dimensional homogeneous lattice. *J. Mol. Biol.* 1974, **86**, 469-489.
131. Jain, A., Winkel, B. S. J. and Brewer, K. J., In vivo inhibition of *E. coli* growth by a Ru(II)/Pt(II) supramolecule $[(tpy)RuCl(dpp)PtCl_2](PF_6)$ *J. Inorg. Biochem.* 2007, **101**, 1525-1528.
132. A Rapid and Efficient Method for Screening Bacterial Colonies for Recombinant Plasmids *Epicenter Forum* 1995, **2**.
133. Kuhn, H. J., Braslavsky, S. E. and Schmidt, R., Chemical actinometry (IUPAC technical report) *Pure Appl. Chem.* 2004, **76**, 2105-2146.
134. Vogler, L. M., Franco, C., Jones, S. W. and Brewer, K. J., Ruthenium chromophore containing terpyridine and a series of polyazine bridging ligands *Inorg. Chim. Acta.* 1994, **221**, 55-59.

135. Hadda, T. B. and Bozec, H. L., Synthesis and characterization of ruthenium (II) complexes containing the new tridentate ligand 4,4',4''-tri-tert-butyl-terpyridine *Inorg. Chim. Acta* 1993, **204**, 103-107.
136. Sullivan, B. P., Calvert, J. M. and Meyer, T. J., Cis-trans isomerism in [(trpy)(PPh₃)RuCl₂]. Comparisons between the chemical and physical properties of a cis-trans isomeric pair *Inorg. Chem.* 1980, **19**, 1404-1407.
137. Hecker, C. R., Fanwick, P. E. and McMillin, D. R., Evidence for dissociative photosubstitution reactions of (acetonitrile)(bipyridine)(terpyridine)ruthenium(2+). Crystal and molecular structure of [Ru(trpy)(bpy)(py)](PF₆)₂·(CH₃)₂CO *Inorg. Chem.* 1991, **30**, 659-666.
138. Gerli, A., Reedijk, J., Lakin, M. T. and Spek, A. L., Redox Properties and Electrocatalytic Activity of the Oxo/Aqua System [Ru(terpy)(bpz)(O)]²⁺/[Ru(terpy)(bpz)(H₂O)]²⁺. X-ray Crystal Structure of [Ru(terpy)(bpz)Cl]PF₆·nMeCN (terpy = 2,2',2''-Terpyridine; bpz = 2,2'-Bipyridine) *Inorg. Chem.* 1995, **34**, 1836-1843.
139. Miyamoto, T. K., Okude, K., Maeda, K., Ichida, H., Sasaki, Y. and Tashiro, T., Syntheses, Spectroscopic Properties, Crystal Structures, and Antitumor Activities of the Optically Isomeric Mandelate Chelates, mandelato(trans-1,2-diaminocyclohexane)platinum(II) *Bull. Chem. Soc. Jpn.* 1989, **62**, 3239-3246.
140. Hadda, T. B. and Bozec, H. L., Preparation and characterization of ruthenium complexes with the new 4,4',4''-tri-tert-butyl-terpyridine ligand and with 4,4'-di-tert-butyl-bipyridine *Polyhedron* 1988, **7**, 575-578.
141. Hadda, T. B., M., C. and Bozec, H. L., Ruthenium (II) complexes containing the tridentate ligand 4,4',4''-tri-tert-butyl-terpyridine: synthesis and isomerisation study of trans-(trpy*)RuCl₂(L) [L = CO, PR₃, P(OR)₃] *Polyhedron* 1995, **14**, 953-955.
142. Hadda, T. B., Zindane, I., Moya, S. A. and Bozec, H. L., Soluble ruthenium carbonyl complexes containing new sterically hindered bipyridine ligands *Polyhedron* 1996, **15**, 1571-1573.
143. Jing, B.-w., Wang, W.-q., Zhang, M.-h. and Shen, T., Polypyridine ruthenium (II) complexes containing mixed ligands. Synthesis, spectroscopic and photophysical and electrochemical properties *Dyes and Pigments* 1998, **37**, 177-186.
144. Sauvage, J.-P., Collin, J.-P., Chambron, J.-C., Guillerez, S., Coudret, C., Balzani, V., Barigletti, F., Cola, L. D. and Flamigni, L., Ruthenium (II) and osmium(II) bis(terpyridine) complexes in covalently-linked multicomponent systems: synthesis, electrochemical behavior, absorption spectra, and photochemical and photophysical properties *Chem. Rev.* 1994, **94**, 993-1019.
145. Dodsworth, E. S. and Lever, A. B. P., Correlations between electrochemical potentials and optical charge transfer energies in ruthenium bipyridine derivatives *Chem. Phys. Lett.* 1986, **124**, 152-158.
146. Kober, E. M., Marshall, J. L., Dressick, W. J., Sullivan, B. P., Caspar, J. V. and Meyer, T. J., Synthetic control of excited states. Nonchromophoric ligand variations in polypyridyl complexes of Os(II) *Inorg. Chem.* 1985, **24**, 2755-2763.
147. Caspar, J. V., Westmoreland, T. D., Allen, G. H., Bradley, P. G., Meyer, T. J. and Woodruff, W. H., Molecular and electronic structure in the metal to ligand charge-transfer excited state of d₆ transition metal complexes in solution *J. Am. Chem. Soc.* 1984, **106**, 3942-3500.

148. Johnson, S. J., Westmoreland, T. D., Caspar, J. V., Barqawi, K. R. and Meyer, T. J., Influence of variations in the chromophoric ligand on the properties of metal to ligand charge transfer excited states *Inorg. Chem.* 1988, **27**, 3195-3200.
149. Gorelsky, S. I., Dodsworth, E. D., Lever, A. V. P. and Vleck, A. A., Trends in metal to ligand orbital mixing in generic series of ruthenium N-Donor ligand complexes-effect on electronic spectra and redox properties *Coord. Chem. Rev.* 1988, **174**, 469-494.
150. Vogler, L. M., Scott, B. and Brewer, K. J., Investigation of the photochemical, electrochemical, and spectroelectrochemical properties of an iridium(III)/ruthenium(II) mixed-metal complex bridged by 2,3,5,6-tetrakis(2-pyridyl)pyrazine *Inorg. Chem.* 1993, **32**, 898-903.
151. Vogler, L. M., Jones, S. W., Jensen, G. E., Brewer, R. G. and Brewer, K. J., Comparing the spectroscopic and electrochemical properties of ruthenium and osmium complexes of the tridentate polyazine ligands 2,2':6',2"-terpyridine and 2,3,5,6-tetrakis(2-pyridyl)pyrazine *Inorg. Chim. Acta* 1996, **250**, 155-162.
152. Vogler, L. M. and Brewer, K. J., Building Block Approach to the Construction Long-Lived Osmium(II) and Ruthenium(II) Multimetallic Complexes Incorporating the Tridentate Bridging Ligand 2,3,5,6-Tetrakis(2-pyridyl)pyrazine *Inorg. Chem.* 1996, **35**, 818-824.
153. Zhao, S., Arachchige, S. M., Slebodnick, C. and Brewer, K. J., Synthesis and Study of the Spectroscopic and Redox Properties of RuII,PtII Mixed-Metal Complexes Bridged by 2,3,5,6-Tetrakis(2-pyridyl)pyrazine. *Inorg. Chem.* 2008, **47**, 6144-6152.
154. Juris, A. and Prodi, L., Photophysical properties of supramolecular assemblies containing polypyridine complexes and pyrene chromophores *New. J. Chem.* 2001, **25**, 1132-1135.
155. Damrauer, N. H., Boussie, T. R., Devenney, M. and McCusker, J. K., Effects of intraligand electron delocalization, steric tuning, and excited state vibronic coupling on the photophysics of aryl-substituted bipyridyl complexes of Ru(II) *J. Am. Chem. Soc.* 1997, **119**, 8253-8268.
156. Treadway, J. A., Loeb, B., Lopez, R., Anderson, P. A., Keene, F. R. and Meyer, T. J., Effect of delocalization and rigidity in the acceptor ligand on MLCT excited-state decay *Inorg. Chem.* 1996, **35**, 2242-2246.
157. Strouse, G. F., Schoonover, J. R., Duesing, R., Boyde, S., Jones, W. E., Jr. and Meyer, T. J., Influence of electronic delocalization in metal-to-ligand charge transfer excited states *Inorg. Chem.* 1995, **34**, 473-487.
158. Watts, R. J. and Crosby, G. A., Quantum efficiencies of transition metal complexes, III. The effect of ligand substitution on radiative and radiationless processes *J. Am. Chem. Soc.* 1972, **94**, 2606-2614.
159. Avdeef, A., Physicochemical profiling. Solubility, permeability and charge state *Curr. Top. Med. Chem.* 2001, **1**, 277-351.
160. Graham, L. P., *Introduction to medicinal chemistry Second edition*, second edn., 1995.
161. Ruelle, P. and Kesselring, U. W., The hydrophobic effect. 3. A key ingredient in predicting n-octanol-water partition coefficients. *J. Pharm. Sci* 1998, **87**, 1015-1024.
162. Kalsbeck, W. A. and Thorp, H. H., Determining binding constants of metal complexes to DNA by quenching of the emission of Pt₂(pop)₄⁻ (pop = P₂O₅H₂²⁻) *J. Am. Chem. Soc.* 1993, **115**, 7146-7151.
163. Jacqueline K. Barton, Danishefsky, A. T. and Goldberg, J. M., *J. Am. Chem. Soc.* 1984, **106**, 2172-2176.

164. Patel, K. K., Plummer, E. A., Darwish, M., Rodger, A. and Hannon, M. J., Aryl substituted ruthenium bis-terpyridine complexes: intercalation and groove binding with DNA *J. Inorg. Biochem.* 2002, **91**, 220-229.
165. Denny, W. A., Twigden, S. J. and Baguley, B. C., Steric constraints for DNA binding and biological activity in the amsacrine series *Anti-Cancer Drug Design* 1986, **1**, 125-132.
166. Burger, R. M., Cleavage of nucleic acid by bleomycin *Chem. Rev.* 1998, **98**, 1153-1169.
167. Renshaw, E. and Thomson, A. J., Tracer studies to locate the site of platinum ions within the filamentous and inhibited cells of *Escherichia coli*. *J. Bacteriol.* 1967, **94**, 1915-1918.
168. Reslova, S., The induction of lysogenic strains of *Escherichia coli* by cis-dichlorodiammineplatinum (II) *Chem.-Biol. Interact.* 1971, **4**, 66-70.
169. Beck, D. J. and Brubaker, R. R., Effect of cisplatin (II)diamminodichloride on wild type and deoxyribonucleic acid repair-deficient mutants of *Escherichia coli*. *J. Bacteriol.* 1973, **116**, 1247-1252.
170. Munchausen, L. L., The chemical and biological effects of cis-dichlorodiammineplatinum (II), an antitumor agent on DNA. *Proc. Natl. Acad. Sci. U.S.A.* 1974, **71**, 4519-4522.
171. Janovska, E., Novakava, O., Natile, G. and Brabec, B., Differential genotoxic effect of antitumor trans-[PtCl₂(E- iminoether)₂] in *Escherichia coli* *J. Inorg. Biochem.* 2002, **90**, 155-158.
172. Souza, E. C., Loyola, T. L., Rodriguez, M. B., De, M. A., Menezes, B. C., Rey, N. A. and Maia, E. C., Synthesis and characterization of tetracycline-Platinum(II) complex active against resistant bacteria *J. Inorg. Biochem.* 2005, **99**, 1001-1008.
173. Kushev, D., Gorneva, G., Enchev, V., Naydenova, E., Popova, J., Taxirov, S., Maneva, L., Grancharov, K. and Spassovska, N., Synthesis, cytotoxicity, antibacterial and antitumor activity of platinum(II) complexes of 3-aminocyclohexanspiro-5-hydantoin *J. Biological Inorg. Chem.* 2002, **89**, 203-211.
174. Speelmans, G., Rutger, W. H. M., Reedijk, K. and Kruijff, B. D., Cisplatin complexes with phosphatidylserine in membranes *Biochemistry* 1997, **36**, 10545-10550.
175. Mishra, A. K., Mishra, S. B., Manav, N., Saluja, D., Chandra, R. and Kaushik, N. K., Synthesis, characterization, antibacterial and cytotoxic study of platinum (IV) complexes *Bioinorganic & Medicinal Chemistry* 2006, **14**, 6333-6340.
176. Wainwright, M., Phoenix, D. A., Wareing, D. R. A. and Bolton, F. J., Study of photobactericidal activity in the phenothiazinium series. *FEMS Immunol. Med. Microbiol. FEMS Immunol. Med. Mic.* 1997, **19**, 75-80.
177. Wagner, S. J., Virus inactivation in blood components by photoactive phenothiazine dyes. *Transfus Med Rev.* 2002, **16**, 61-66.
178. Menezes, S., Capella, M. A. M. and Caldas, L. R., Photodynamic action of methylene blue: repair and mutation in *Escherichia coli*. *Journal of Photochemistry and Photobiology B: Biology* 1990, **5**, 505-517.
179. Allen, C. M., Weber, J. M. and vanLier, J. E., Sulphophthalocyanins for photodynamic inactivation of viruses in blood products- effect of structural modifications *Photochem. and Phobiol.* 1995, **62**, 184-189.
180. Bonnet, R., Buckley, D. G., Burrow, T., Galia, A. B. B., Saville, B. and Songca, S. P., Photobactericidal materials based on porphyrins and pthalocyanins *Journal of Material Chemistry* 1993, **3**, 323-324.

181. Jeffrey, A. M., Jing, T. W., DeRose, J. A., Vaught, A., Rakesh, D., Lu, F. X. and Lindsay, S. M., Identification of DNA-cisplatin adducts in a blind trial of in situ scanning tunneling microscopy *Nucleic Acids Res.* 21, **1993**, 5896–5900.
182. Bezanilla, M., Drake, B., Nudler, E., Kashlev, M., Hansma, P. K. and Hansma, H. G., Motion and enzymatic degradation of DNA in the atomic force microscope. *Biophys. J.* 1994, **67**, 2454-2459.
183. A.M.Jeffrey, T.W.Jing, DeRose, J. A., A.Vaught, D.Rekesh, Lu, F. X. and Lindsay, S. M., *Nucleic Acids Res.* 21, **1993**, 5896–5900.
184. Murakamia, M., Hirokawa, H. and Hayataa, I., Analysis of radiation damage of DNA by atomic force microscopy in comparison with agarose gel electrophoresis studies *J. Biochem. Biophys. Methods* 2000, **44**, 31–40.
185. Holder, A. A., Zigler, D. F., Tarrago-Trani, M. T., Storrie, B. and Brewer, K. J., Photobiological impact of [$\{(bpy)_2Ru(dpp)\}_2RhCl_2]Cl_5$ and [$\{(bpy)_2Os(dpp)\}_2RhCl_2]Cl_5$ [bpy = 2,2'-bipyridine; dpp = 2,3-bis(2-pyridyl)pyrazine] on Vero cells *Inorg. Chem.* 2007, **46**, 4760-4762.

Appendix

Figure	Page
Figure A-1. ^1H NMR spectrum of $[\text{Ru}(\text{tpy})_2](\text{PF}_6)$ in CD_3CN	A-2
Figure A-2. ^1H NMR spectrum of $[\text{Ru}(\text{MePhtpy})_2](\text{PF}_6)$ in CD_3CN	A-2
Figure A-3. ^1H NMR spectrum of $[\text{Ru}(\text{}^t\text{Bu}_3\text{tpy})_2](\text{PF}_6)$ in CD_3CN	A-3
Figure A-4. ^1H NMR spectrum of $[(\text{}^t\text{Bu}_3\text{tpy})\text{RuCl}(\text{dpp})](\text{PF}_6)$ in CD_3CN	A-4
Figure A-5. ^1H NMR spectrum of $[(\text{MePhtpy})\text{RuCl}(\text{dpp})](\text{PF}_6)$ in CD_3CN	A-5
Figure A-6. Mass spectrum of $[(\text{MePhtpy})\text{RuCl}(\text{dpp})](\text{PF}_6)$	A-6
Figure A-7. Mass spectrum (high mass range) of $[(\text{MePhtpy})\text{RuCl}(\text{dpp})](\text{PF}_6)$ with calculated isotopic pattern (inlay)	A-7
Figure A-8. Mass spectrum of $[(\text{}^t\text{Bu}_3\text{tpy})\text{RuCl}(\text{dpp})](\text{PF}_6)$	A-8
Figure A-9. Mass spectrum (high mass range) of $[(\text{}^t\text{Bu}_3\text{tpy})\text{RuCl}(\text{dpp})](\text{PF}_6)$ with calculated isotopic pattern	A-9
Figure A-10. Mass spectrum (high mass range) of $[(\text{tpy})\text{RuCl}(\text{dpp})](\text{PF}_6)$ with calculated isotopic pattern	A-10
Figure A-11. Mass spectrum of $[(\text{tpy})\text{RuCl}(\text{dpp})\text{PtCl}_2](\text{PF}_6)$	A-11
Figure A-12. Mass spectrum (high mass range) of $[(\text{tpy})\text{RuCl}(\text{dpp})\text{PtCl}_2](\text{PF}_6)$ with calculated isotopic pattern	A-12
Figure A-13. Mass spectrum of $[(\text{MePhtpy})\text{RuCl}(\text{dpp})\text{PtCl}_2](\text{PF}_6)$	A-13
Figure A-14. Mass spectrum (high mass range) of $[(\text{MePhtpy})\text{RuCl}(\text{dpp})\text{PtCl}_2](\text{PF}_6)$ with calculated isotopic pattern	A-14
Figure A-15. Mass spectrum of $[(\text{}^t\text{Bu}_3\text{tpy})\text{RuCl}(\text{dpp})\text{PtCl}_2](\text{PF}_6)$	A-15
Figure A-16. Growth curves of <i>E. coli</i> JM109 (pUC18) at different concentrations of $[(\text{MePhtpy})\text{RuCl}(\text{dpp})\text{PtCl}_2](\text{PF}_6)$	A-16

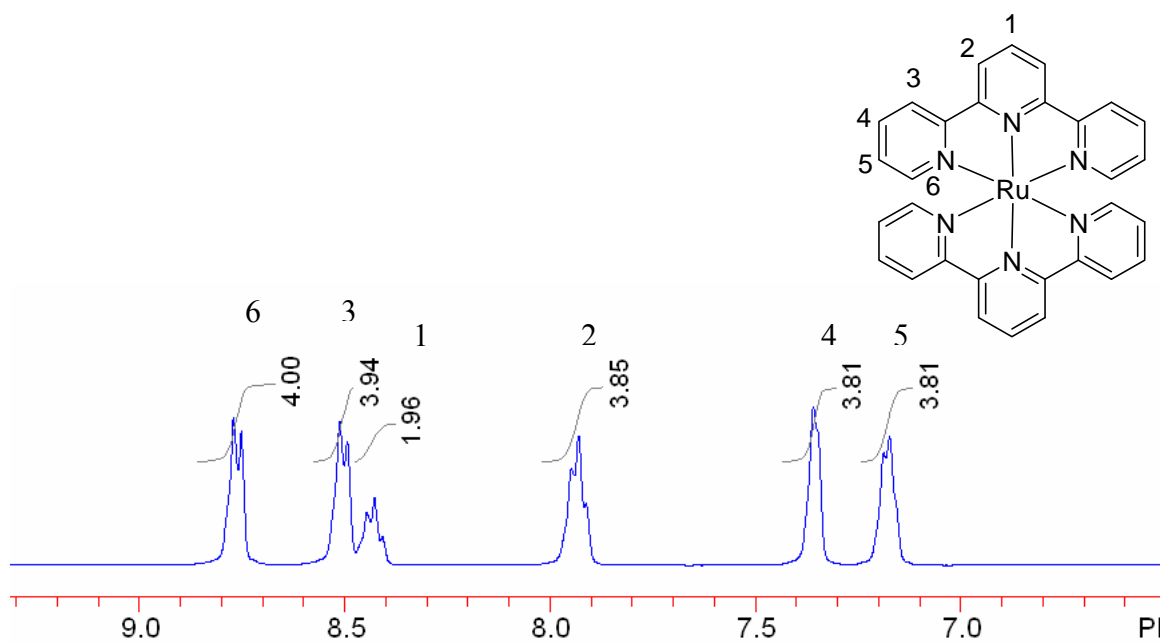


Figure A-1. ^1H NMR spectrum of $[\text{Ru}(\text{tpy})_2](\text{PF}_6)$ in CD_3CN with assignments (tpy = 2,2,2':6',2''-terpyridine). Star denotes peaks due to solvent.

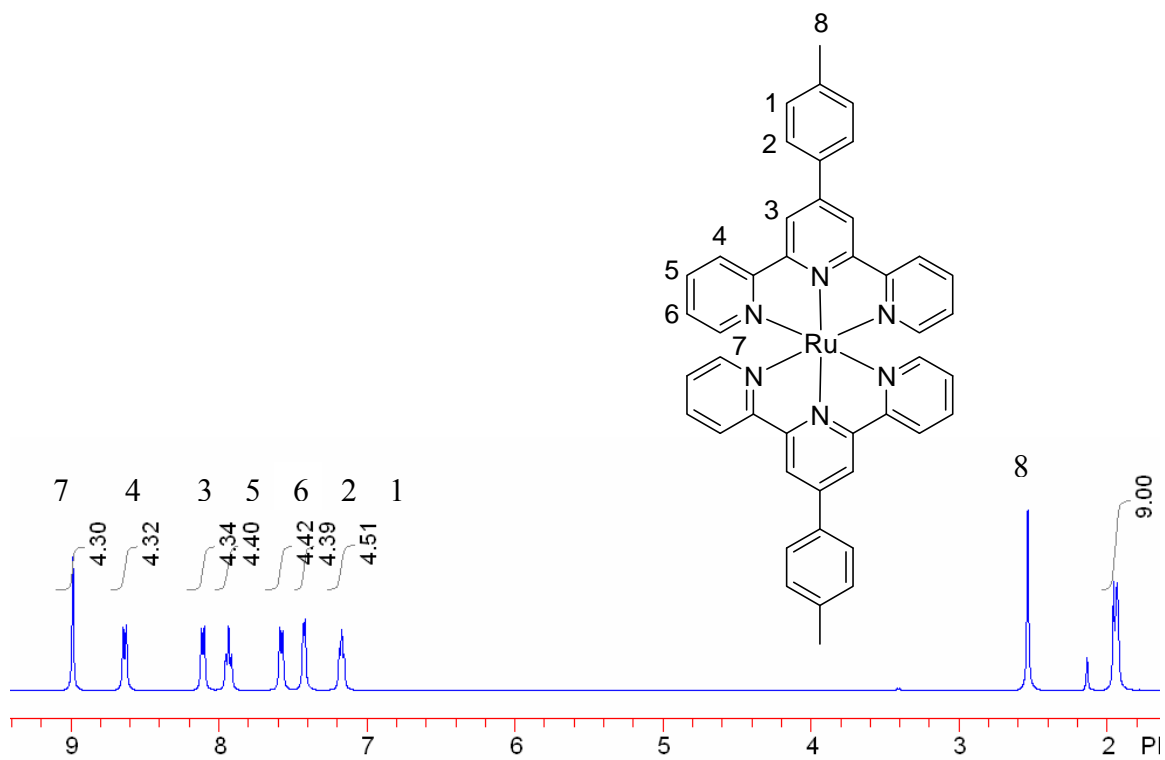


Figure A-2. ^1H NMR spectrum of $[\text{Ru}(\text{MePhtpy})_2](\text{PF}_6)$ in CD_3CN with assignments (MePhtpy = 4'-(4-methylphenyl)-2,2,2':6',2''-terpyridine). Star denotes peaks due to solvent.

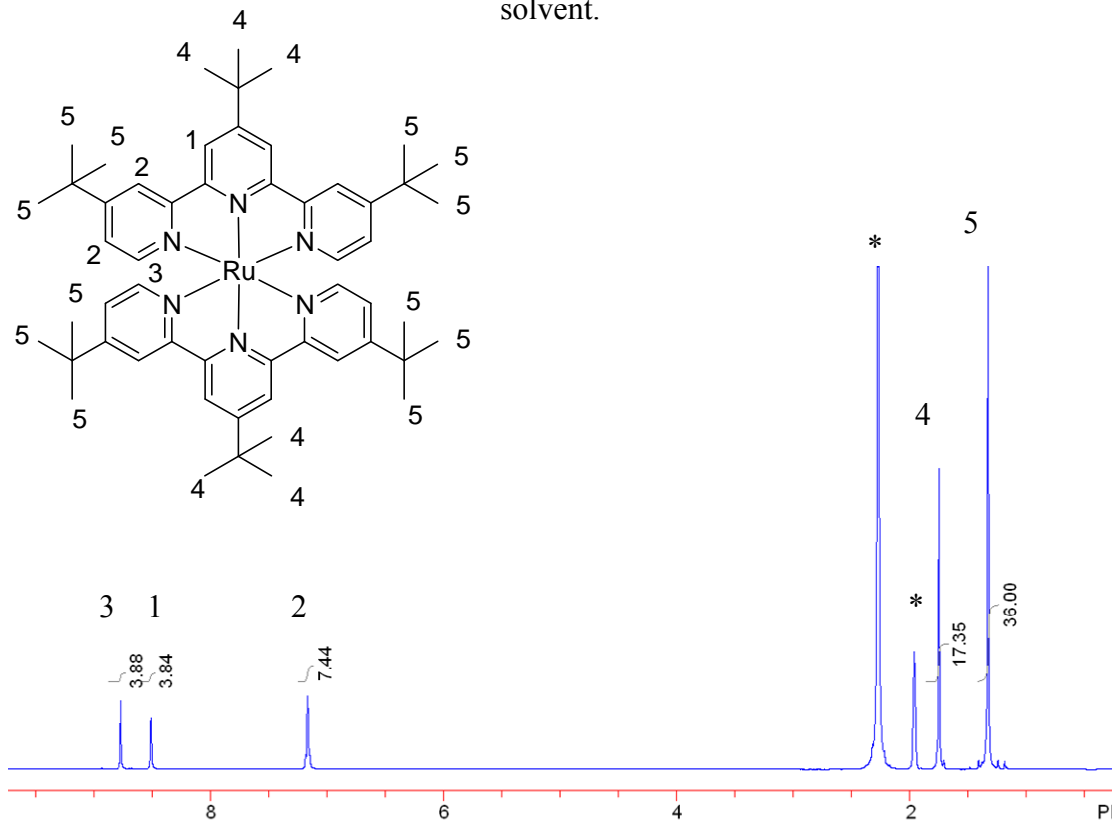


Figure A-3. ^1H NMR spectrum of $[\text{Ru}(\text{}^t\text{Bu}_3\text{tpy})_2](\text{PF}_6)$ in CD_3CN with assignments (${}^t\text{Bu}_3\text{tpy}$ = 4,4',4''-tri-tert-butyl-2,2':6',2''-terpyridine). Star denotes peaks due to solvent.

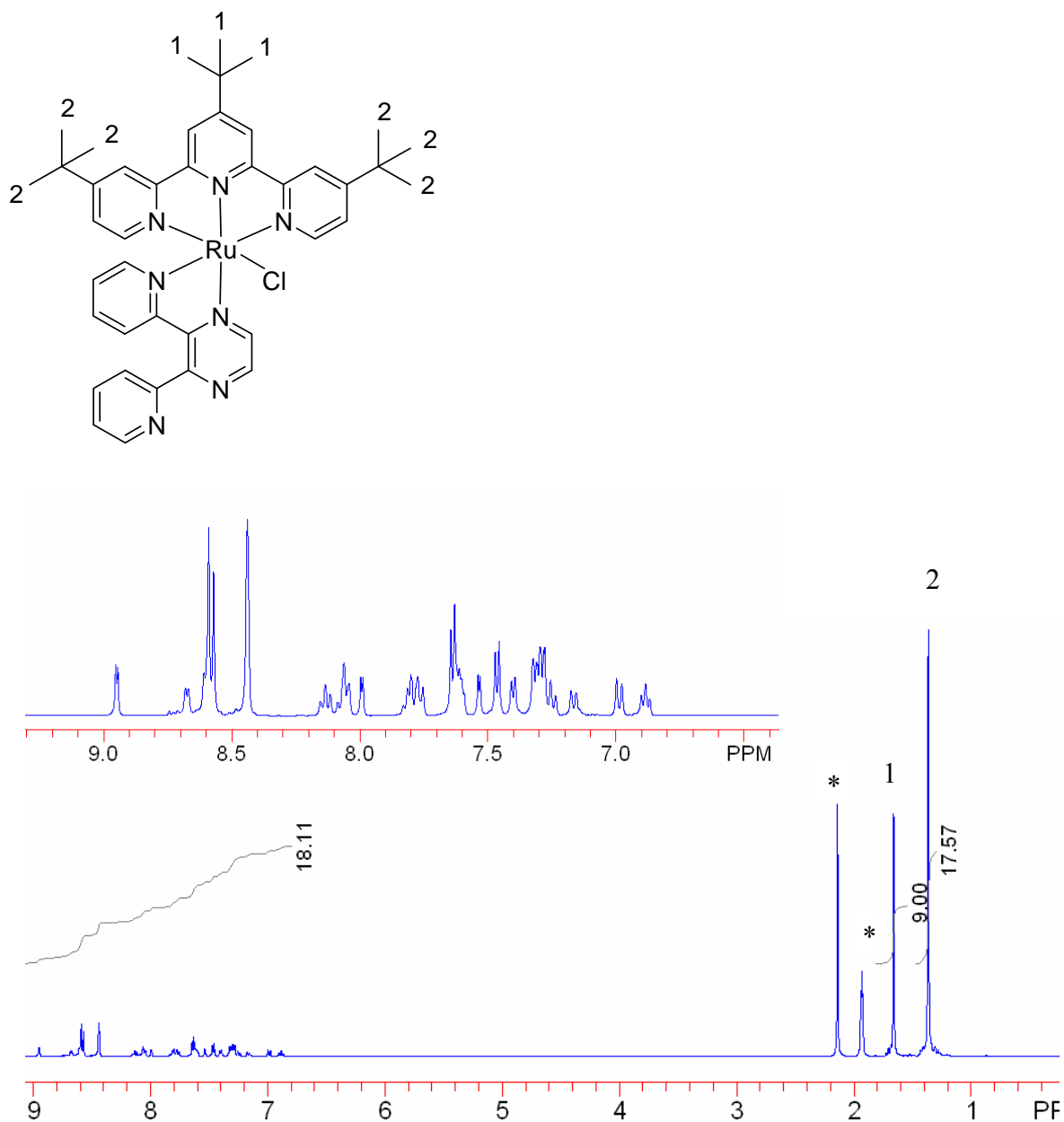


Figure A-4. ^1H NMR spectrum of $[(^t\text{Bu}_3\text{tpy})\text{RuCl}(\text{dpp})](\text{PF}_6)$ in CD_3CN with aromatic region inlay ($^t\text{Bu}_3\text{tpy}$ = 4,4',4''-tri-tert-butyl-2,2':6',2''-terpyridine and dpp = 2,3-bis(2-pyridyl)pyrazine). Star denotes peaks due to solvent.

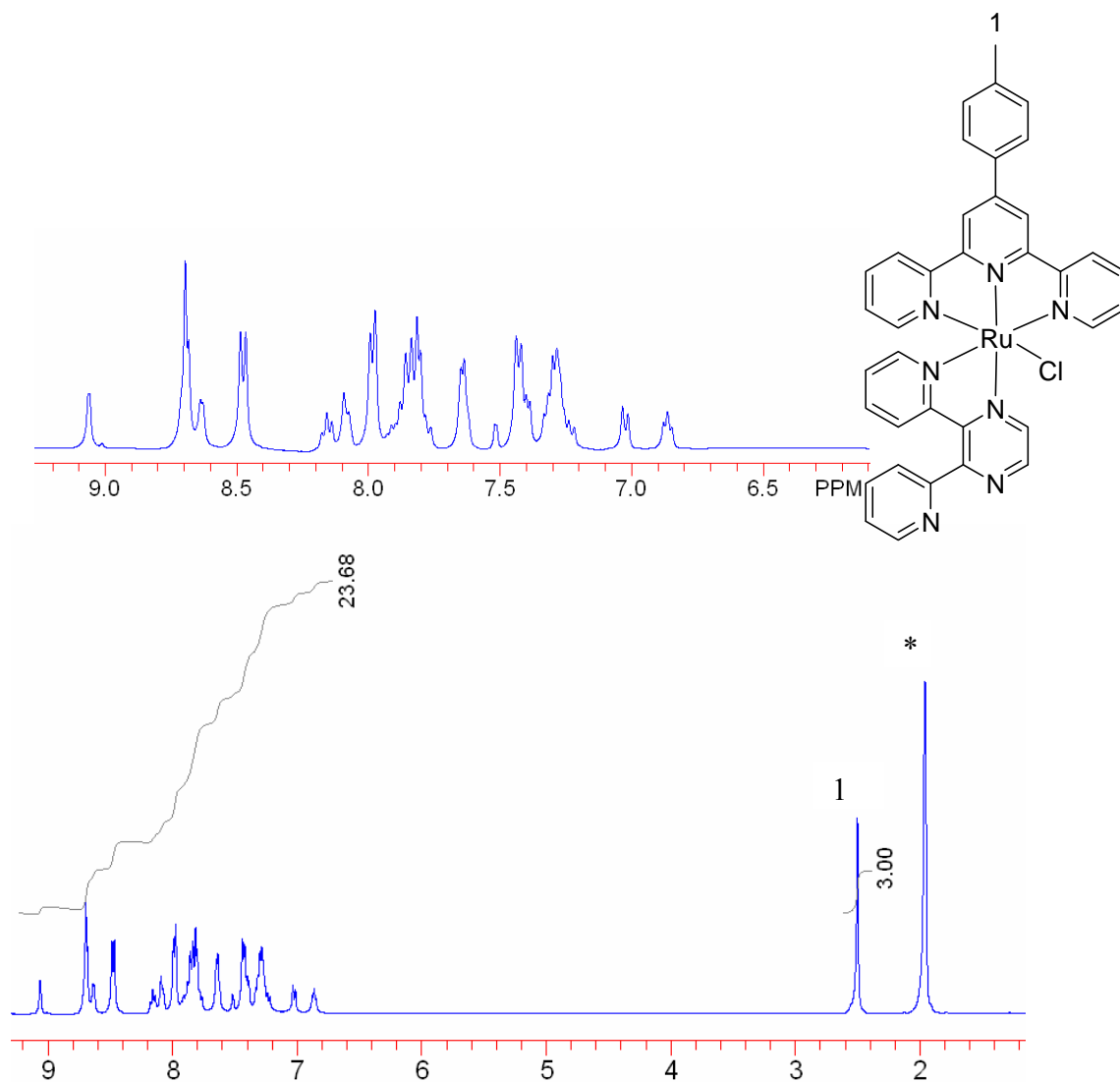


Figure A-5. ^1H NMR spectrum of $[(^1\text{Bu}_3\text{tpy})\text{RuCl}(\text{dpp})](\text{PF}_6)$ in CD_3CN with aromatic region inlay (MePhtpy = 4'-(4-methylphenyl)-2,2,2':6',2''-terpyridine and dpp = 2,3-bis(2-pyridyl)pyrazine). Star denotes peaks due to solvent.

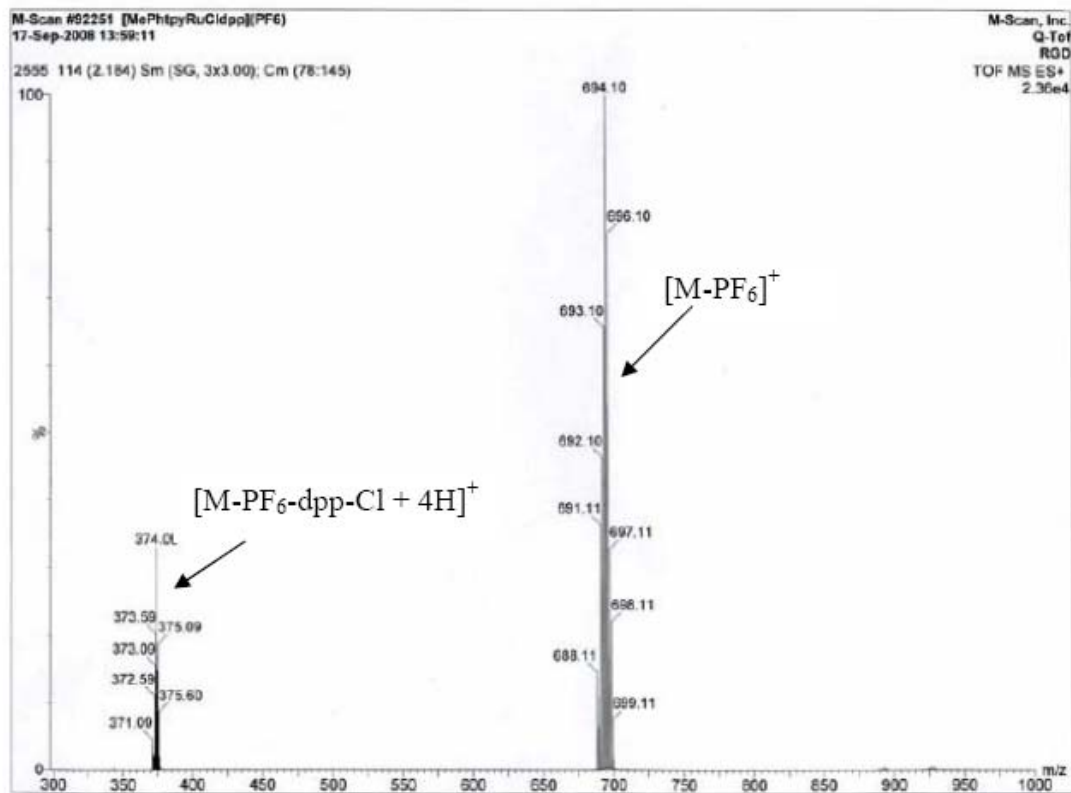


Figure A-6. Mass spectrum of [(MePhtpy)RuCl(dpp)](PF₆) as acquired by M-Scan Inc. (MePhtpy = 4'-(4-methylphenyl)-2,2':6',2''-terpyridine and dpp = 2,3-bis(2-pyridyl)pyrazine).

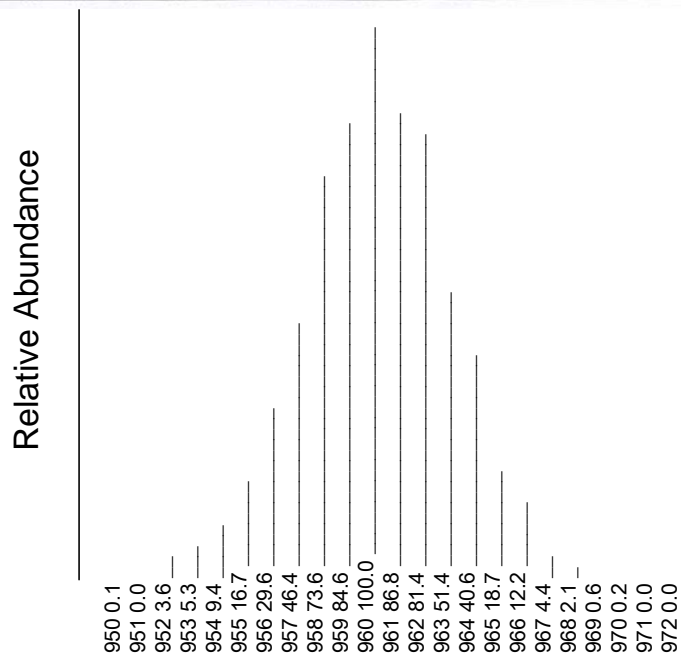
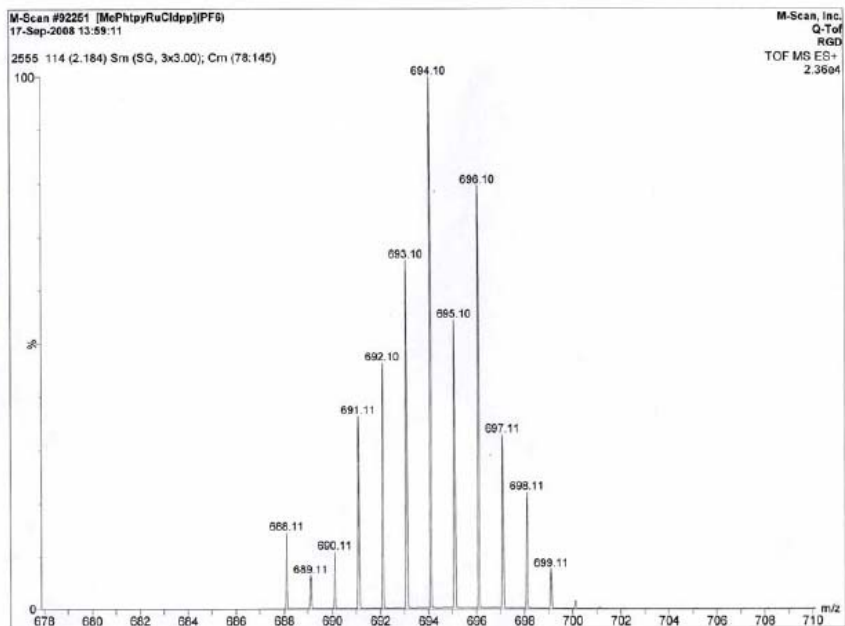


Figure A-7. Mass spectrum of [(MePhpty)RuCl(dpp)](PF₆) (high mass region) showing isotopic distribution pattern, as acquired by M-Scan Inc., with calculated isotopic distribution pattern, as calculated by Sheffield Chemputer. (MePhpty = 4'-(4-methylphenyl)-2,2':6',2''-terpyridine and dpp = 2,3-bis(2-pyridyl)pyrazine).

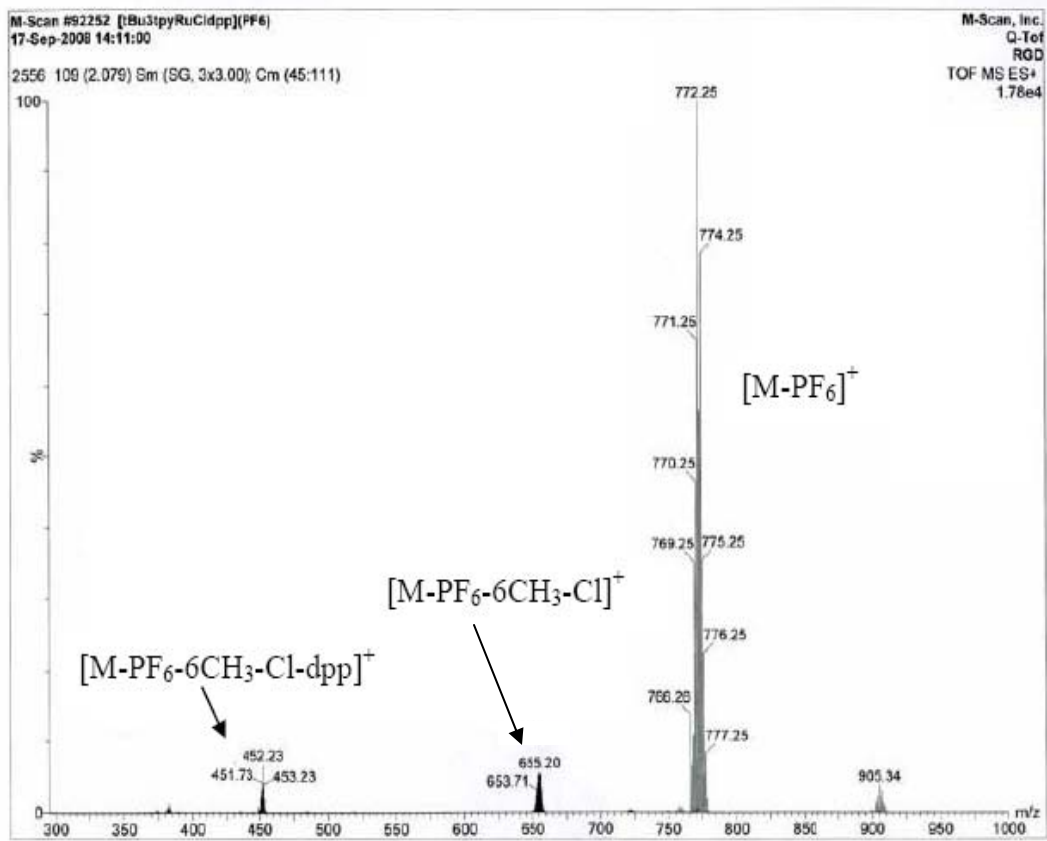
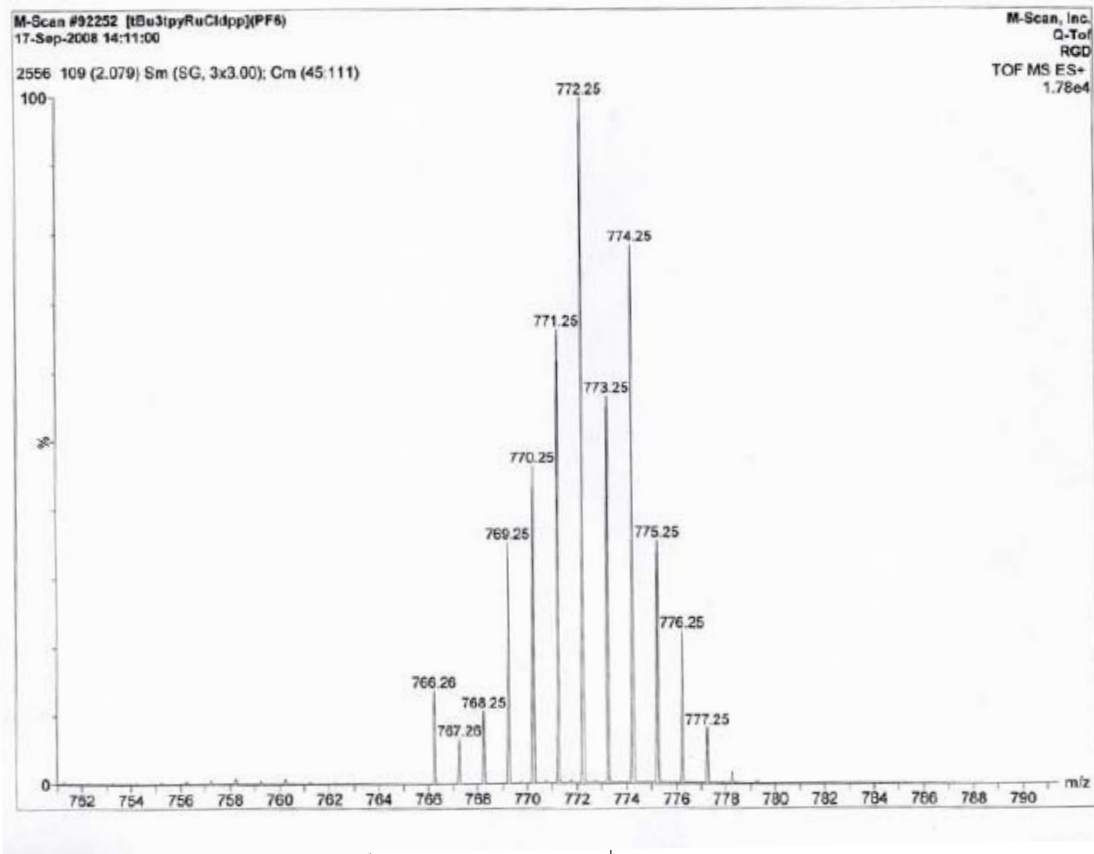


Figure A-8. Mass spectrum of [(^tBu₃tpy)RuCl(dpp)](PF₆) as acquired by M-Scan Inc. (^tBu₃tpy = 4,4',4''-tri-tert-butyl-2,2':6',2''-terpyridine and dpp = 2,3-bis(2-pyridyl)pyrazine).



Relative Abundance

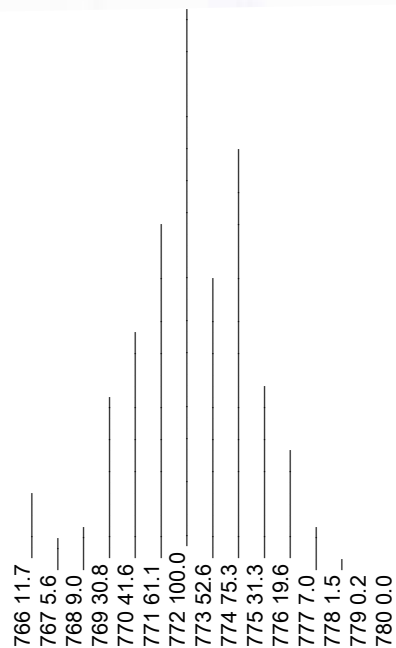


Figure A-9. Mass spectrum of [¹Bu₃tpy)RuCl(dpp)](PF₆) (high mass region) showing isotopic distribution pattern, as acquired by M-Scan Inc., with calculated isotopic distribution pattern, as calculated by Sheffield Chemputer. (¹Bu₃tpy = 4,4',4''-tri-tert-butyl-2,2':6',2''-terpyridine and dpp = 2,3-bis(2-pyridyl)pyrazine).

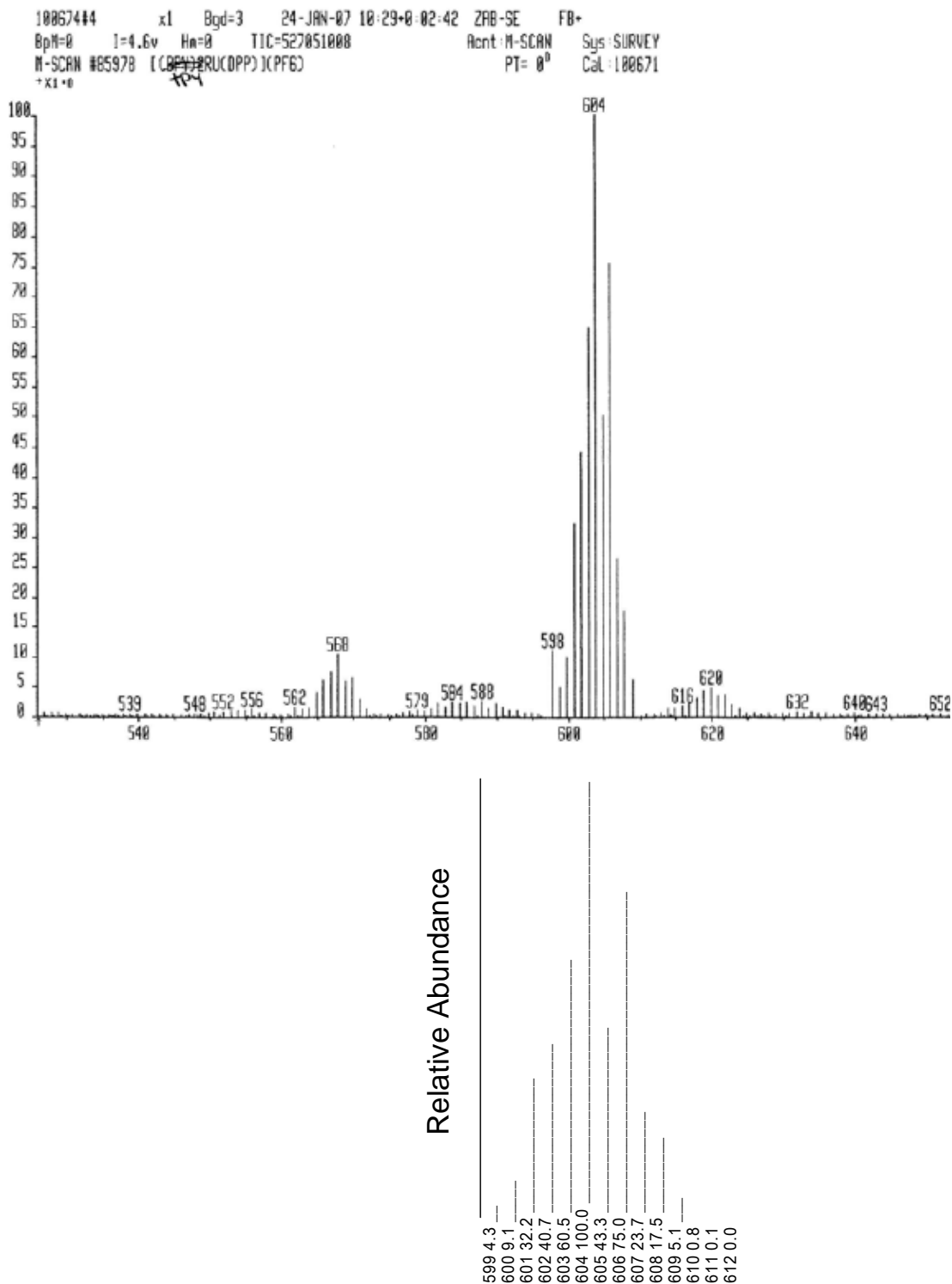


Figure A-10. Mass spectrum of $[(\text{tpy})\text{RuCl}(\text{dpp})](\text{PF}_6)$ showing isotopic distribution pattern, as acquired by M-Scan Inc., with calculated isotopic distribution pattern, as calculated by Sheffield Chemputer. (tpy = 2,2':6',2"-terpyridine and dpp = 2,3-bis(2-pyridyl)pyrazine).

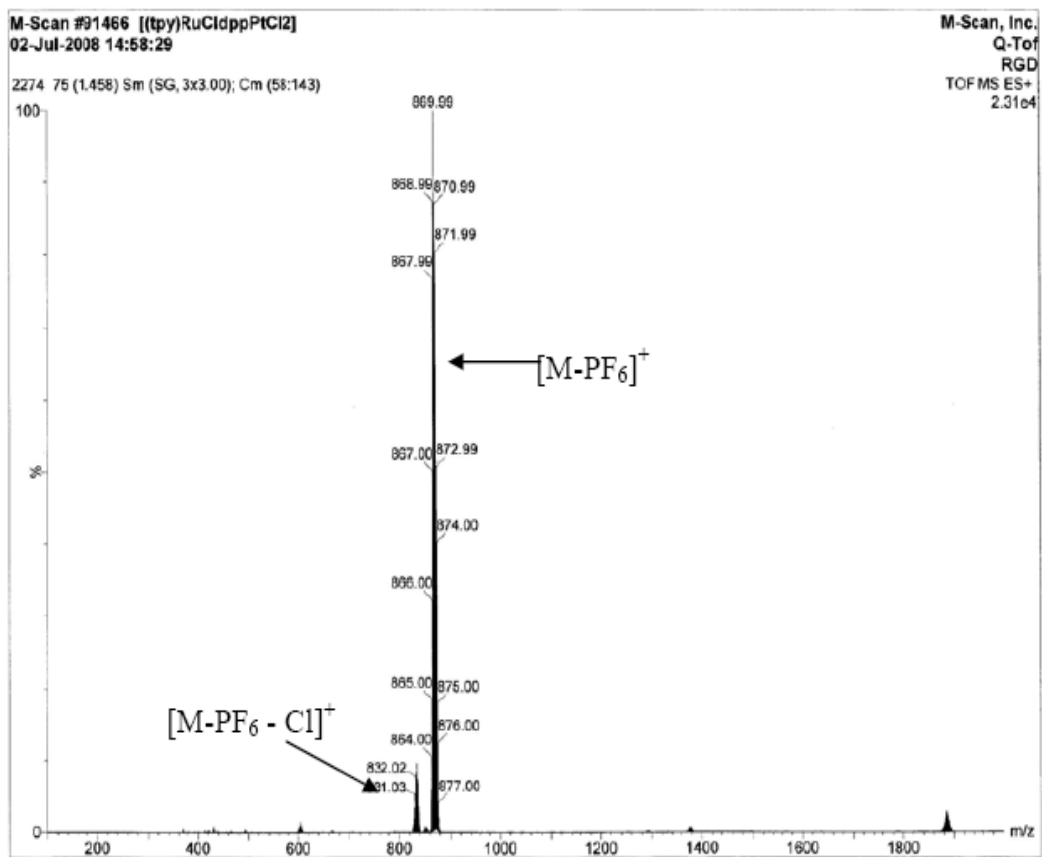


Figure A-11. Mass spectrum of [(tpy)RuCl(dpp)PtCl₂](PF₆) as acquired by M-Scan Inc. (tpy = 2,2':6',2''-terpyridine and dpp = 2,3-bis(2-pyridyl)pyrazine).

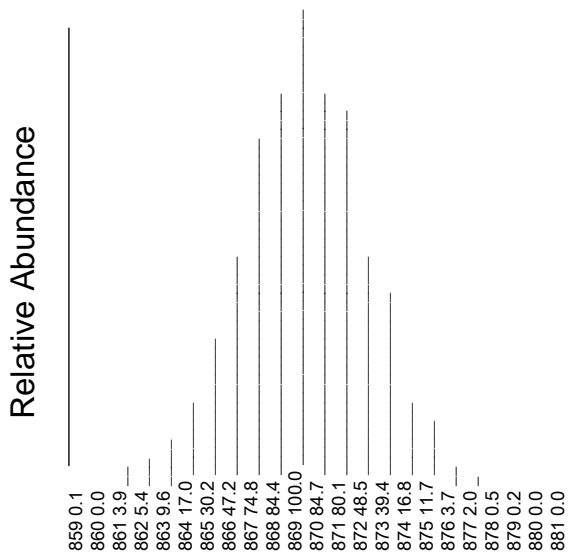
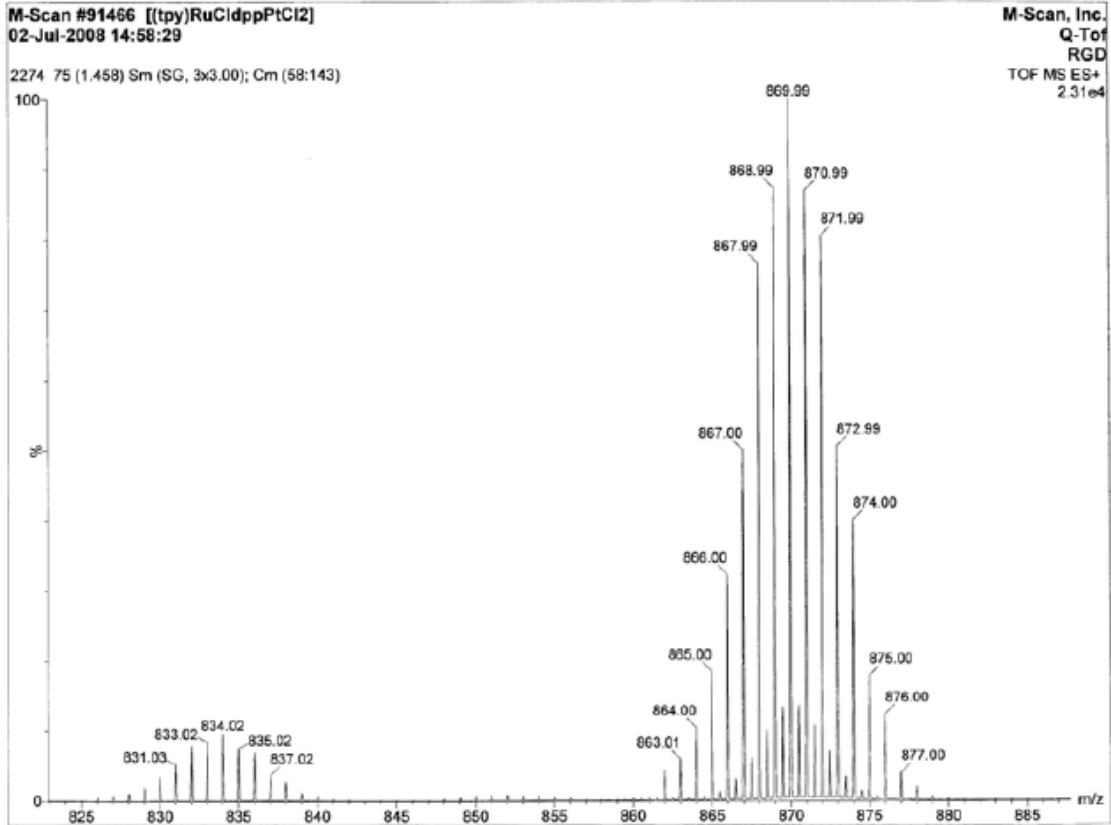


Figure A-12. Mass spectrum of [(tpy)RuCl(dpp)PtCl₂](PF₆) (high mass region) showing isotopic distribution pattern, as acquired by M-Scan Inc., with calculated isotopic distribution pattern, as calculated by Sheffield Chemputer. (tpy = 2,2':6',2''-terpyridine and dpp = 2,3-bis(2-pyridyl)pyrazine).

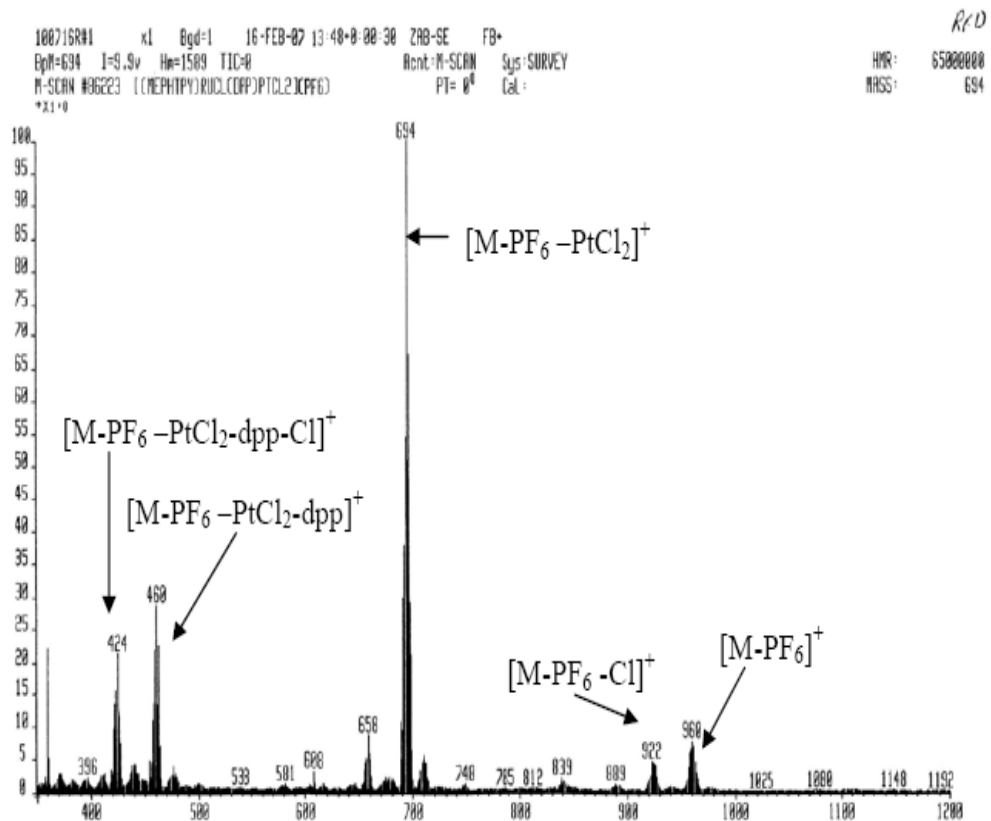


Figure A-13. Mass spectrum of $[(MePhtpy)RuCl(dpp)PtCl_2](PF_6)$ as acquired by M-Scan Inc (MePhtpy = 4'-(4-methylphenyl)-2,2,2':6',2''-terpyridine and dpp = 2,3-bis(2-pyridyl)pyrazine).

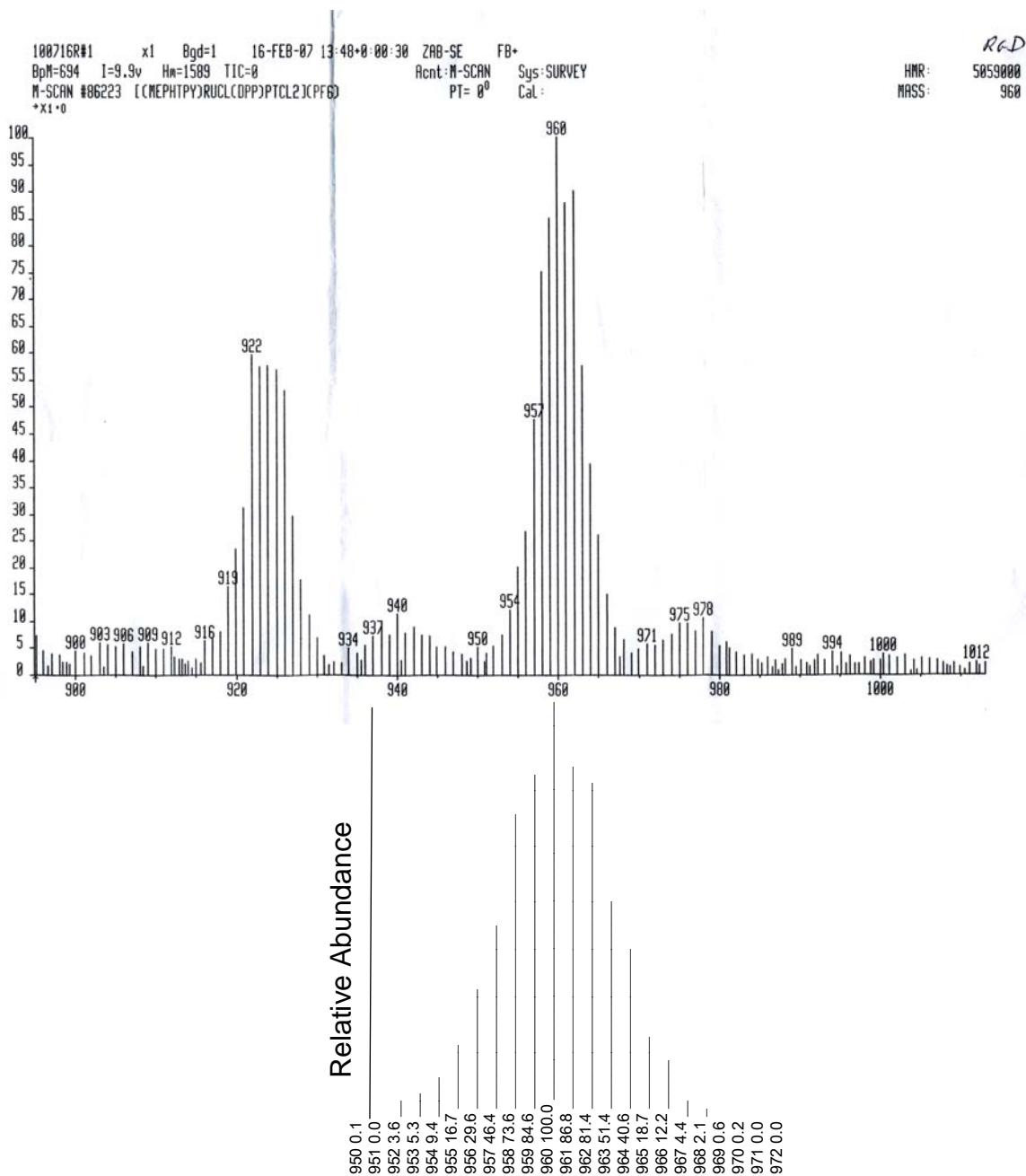


Figure A-14. Mass spectrum of [(MePhtpy)RuCl(dpp)PtCl₂](PF₆) (high mass region) showing isotopic distribution pattern, as acquired by M-Scan Inc., with calculated isotopic distribution pattern, as calculated by Sheffield Chemputer. (MePhtpy = 4'-(4-methylphenyl)-2,2,2':6',2''-terpyridine and dpp = 2,3-bis(2-pyridyl)pyrazine).

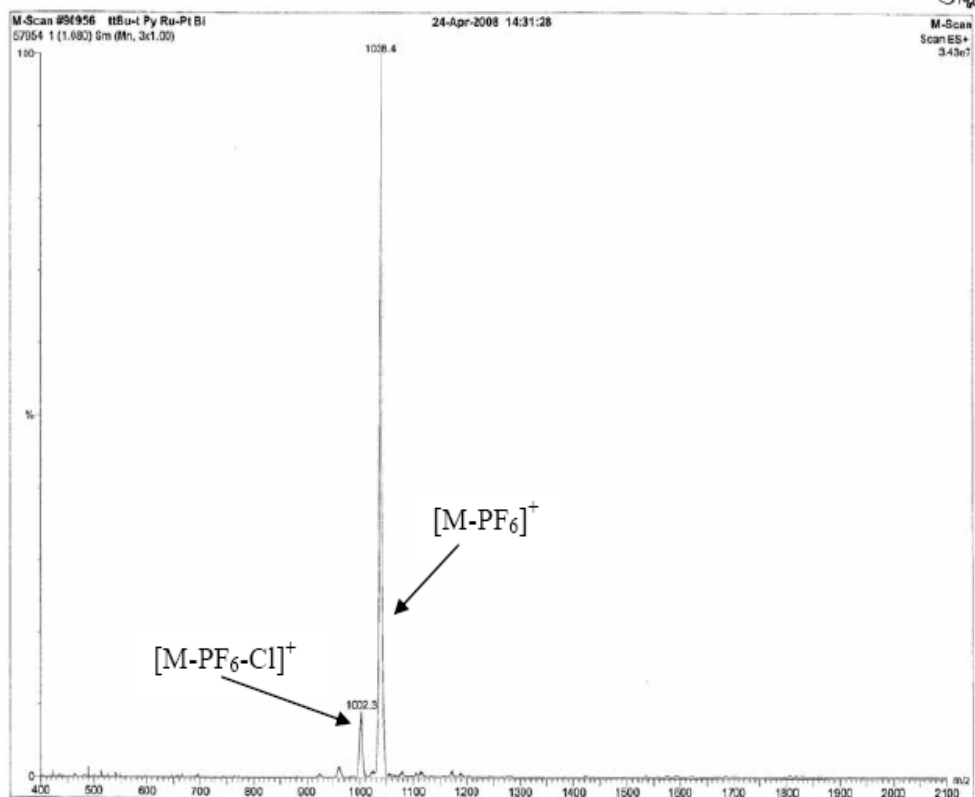


Figure A-15. Mass spectrum of $[{}^1\text{Bu}_3\text{tpy})\text{RuCl}(\text{dpp})\text{PtCl}_2](\text{PF}_6)$ as acquired by M-Scan Inc. (${}^1\text{Bu}_3\text{tpy}$ = 4,4',4''-tri-tert-butyl-2,2':6',2''-terpyridine and dpp = 2,3-bis(2-pyridyl)pyrazine).

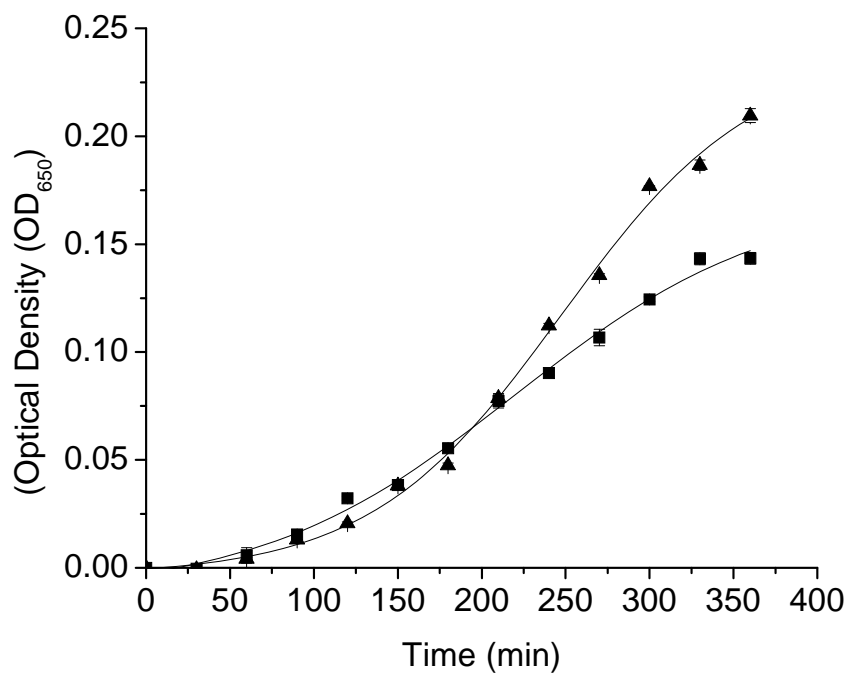


Figure. A-16. Growth curves of *E. coli* JM109 (pUC18) at 0.1 mM concentrations of [(MePhtpy)RuCl(dpp)PtCl₂](PF₆) (dpp = 2,3-bis(2-pyridyl)pyrazine and MePhtpy = 4'-(4-methylphenyl)-2,2':6',2''-terpyridine). Cells grown in the presence of 0.1 mM [(MePhtpy)RuCl(dpp)PtCl₂](PF₆) (▲), and Control (■).

Note: The growth curves shown in Figure A-16 is the repetition of the cell culture studies discussed on page 115.